

Stratigraphy and development of a Holocene barrier spit (Sylt, southern North Sea)

Dissertation
zur Erlangung des Doktorgrades
der Naturwissenschaften im Department
Geowissenschaften
der Universität Hamburg

vorgelegt von
Sebastian Lindhorst
aus
Hamburg

Hamburg
2007

Als Dissertation angenommen vom Department Geowissenschaften der Universität
Hamburg

auf Grund der Gutachten von
und

Prof. Dr. Christian Betzler
Dr. Christian Hass

Hamburg, den 06. Februar 2008

Prof. Dr. Kay-Christian Emeis
Leiter des Departments Geowissenschaften

Summary

This study aims to reconstruct the development of the Holocene northern barrier spit of Sylt, an island located off the southern German North Sea coast. The sedimentary architecture of this spit system was investigated through an integrated approach, using ground-penetrating radar (GPR) and sediment core data. An age assignment of stratigraphical units was obtained through radiocarbon dates. The data obtained made it possible to document the sedimentary architecture with a high resolution. This sheds new light on the sedimentary processes that influence growth and destruction of the spit and helps to sharpen predictions of future developments. The presented method provides an excellent tool for efficient, high-resolution spatial analysis of sedimentary facies and stratigraphy of sandy coastal areas in temperate climates. The models developed for the spit's sedimentary dynamics provide a framework which may also be applied for interpretation of other sedimentary successions which formed in similar settings.

A new stratigraphic model for the northern barrier spit of Sylt is presented, showing that the spit's latest Holocene development is much more complex than previously thought. Morphologically, the spit is composed of a large, recurved main spit (the „Listland“) that terminates with a hooked spit geometry (the „Ellenbogen“) against the northward adjacent tidal inlet. Data shows that both parts of the spit system undergo a different evolution. Increased erosion at the main spit leads to enhanced growth of the hooked spit, which therefore serves as a sediment sink for at least part of the eroded material. The data furthermore reveals that the recent shoreline of the northern spit does not reflect the orientation of the genetically built spit axis which strikes northwest – southeast. This can probably be attributed to a change of controlling factors during the development of the spit.

Whereas the southern part of the Listland consists of backbarrier sediments, overlain by washover sediments, the northern part of the spit comprises of sandy beach sediments. The welding of swash bars is shown to be the predominant process during progradational phases of the main spit system. During these periods, progradation is not restricted to a linear growth along the spit axis, but also comprises a seaward-directed component. Major erosion surfaces, which delimit progradational sediment packages, are interpreted to reflect exceptionally severe storms. Data indicates that the fossilization potential of this sedimentary succession was controlled by a positive net long-term sediment balance, and the position of the groundwater table which controlled eolian deflation. Fossil eolian deflation surfaces, preserved as erosional unconformities in different depths, indicate that the land surface of the spit is controlled by the hydrodynamic coupling of groundwater table and sea-level position. This results either in erosion – by deflation – during falling stages of the sea level, or in vertical aggradation – by trapping of windblown sand – during periods of sea-level rise.

The development of the hooked spit, the Ellenbogen, is controlled by the interplay of alongshore migrating foreshore beach-drifts under fair-weather conditions and strong erosional events, interpreted as the result of rare severe storms. These storms interrupt beach-progradation and lead to a significant retreat of the coastline. Exceptional storms may also excavate scarps in the backshore. Storm scarps play an important role in the development of the fore-dune ridges that are situated on the recent hooked spit. In contrast to the main spit of Sylt, where the sediment budget is negative, the hooked spit experienced significant beach growth during the last decades. This can probably be attributed to enhanced beach nourishment updrift,

along the main spit, and makes the investigated hooked spit a natural laboratory to study the influence of increasing sediment supply in a system developing under the conditions of Holocene sea-level rise.

Radiocarbon dating of mollusk-shell debris makes it possible to present an age model of the late Holocene spit stratigraphy. Around 3700 BP, the initial spit reached a north-south extension comparable to the present day extension. Spit deposits are sands, and clays were deposited in the backbarrier. As a result of a sea-level lowering, erosion occurred between 3500 and 2500 BP, and an eolian deflation surface developed, nowadays located in a depth of 2 to 3 m below mean sea level. Between 2500 and 2000 BP the coast retreated, a process which was probably triggered by exceptional strong storms. Subsequently, the spit recovered by welding of swash bars. Contemporaneously, large wash-over fans formed along the lee-side of the spit. Around 2000 BP, a tidal inlet developed between the Listland and the Ellenbogen. This feature was closed before 1700 BP, due to enhanced spit progradation. Around 1300 BP at the latest, the Ellenbogen hooked spit formed. Around 1000 BP increased erosion on the western coast resulted in enhanced growth of the hooked spit. Contemporaneously, between 1700 and 1000 BP, an eolian deflation surface developed all over the Listland. This surface is nowadays buried by an up to 1.5 m thick eolian succession.

Sediment availability on the spit is an important prerequisite for spit aggradation during phases of sea-level rise. Artificial stabilization of migrating dunes and exceptionally high coastal dunes therefore reduces sediment input into the interdune valleys, impairing or even suppressing vertical spit aggradation as a natural reaction to sea-level rise in these areas. Future sea-level rise will therefore not only cause enhanced erosion on the western coast, but also the flooding of the spit by marine incursion arising from the backbarrier bay.

Zusammenfassung

Ziel dieser Arbeit ist die Rekonstruktion der holozänen Entwicklung des nördlichen Nehrungshakens der Insel Sylt (südliche Nordsee). Grundlage der Untersuchungen sind Georadardaten, Sedimentkerne und Radiokohlenstoffdatierungen. Die integrierende Interpretation dieser Daten erlaubt eine hohe Auflösung der Sedimentstrukturen und neue Einblicke in die grundlegenden sedimentdynamischen Prozesse dieses Barriersystems. Dies ermöglicht neben der Rekonstruktion der Entstehungsbedingungen auch verbesserte Voraussagen zur zukünftigen Entwicklung des Systems, insbesondere unter den veränderten Rahmenbedingungen eines steigenden Meeresspiegels. Die angewandte Methodik wurde im Verlauf der Untersuchungen kontinuierlich verbessert und bietet ein hervorragendes Werkzeug zur hochauflösenden Sedimentkartierung im küstennahen Raum. Die prozessorientierten Modelle, die im Rahmen dieser Arbeit entwickelt wurden, bilden die Sedimentdynamik des untersuchten Nehrungshakens in bisher nicht erreichter Auflösung ab und liefern Ansatzpunkte zur Interpretation vergleichbarer sedimentärer Systeme.

Morphologisch gliedert sich das Untersuchungsgebiet in einen großen Nehrungshaken, das „Listland“, sowie einen kleinen Haken, den „Ellenbogen“, der das Barriersystem gegen das nördlich vorgelagerte Seegatt begrenzt. Das vorgestellte stratigraphische Modell zeigt, dass die spätholozäne Entwicklung des nördlichen Nehrungshakens der Insel Sylt sehr viel komplexer ist, als bislang angenommen wurde. Die Daten belegen die unterschiedliche Genese beider Teile des Nehrungshakens und zeigen, dass eine Zunahme der Erosion entlang der Küste des Listlandes zu einem beschleunigten Wachstum des Ellenbogens führt. Die heutige Küstenlinie entspricht nicht der ursprünglichen Wachstumsrichtung des Nehrungssystems. Dies zeigt die Veränderungen der hydrodynamischen Bedingungen an der Westküste Nordsylts seit der Entstehung des Barriersystems.

Im südlichen Teil des Listlandes überlagern sandige Washover-Fächer Sande und Tone des Rückseitenwatts. Der nördliche Teil des Nehrungssystems besteht vorwiegend aus Sanden, die während der Progradation des Systems im Strandbereich abgelagert wurden. Erosionsereignisse, die das Wachstum des Nehrungshakens unterbrochen haben, sind in Form ausgeprägter Erosionsdiskordanzen überliefert. Es wird gezeigt, dass die Anlagerung intertidaler Sedimentkörper (swash bars) der dominierende Prozess während der Progradationsphasen des Nehrungssystems ist. Das Wachstum des Hakens erfolgt hierbei nicht nur linear entlang der Längsachse des Systems, sondern auch seewärts gerichtet. Markante Erosionsdiskordanzen, die sich bis in eine Tiefe von 10 m unter das Niveau des heutigen Meeresspiegels verfolgen lassen, werden als Signatur seltener, schwerer Stürme interpretiert. Die Daten zeigen, dass das Überlieferungspotential der Sedimentfolge des Nehrungssystems vor allem von einer positiven Langzeit-Sedimentbilanz sowie der Position des Grundwasserspiegels abhängt. Mehrere fossile Deflationsflächen, die in unterschiedlichen Tiefen im Listland als Erosionsdiskordanzen überliefert sind, belegen, dass Grundwasser- und Meeresspiegel hydrodynamisch gekoppelt sind. Die Position des Grundwasserspiegels bestimmt das Deflationsniveau und damit auf lange Sicht das Niveau der Landoberfläche. Ein fallender Meeresspiegel führt zur Absenkung der Landoberfläche durch Deflation, während ein Meeresspiegelanstieg Akkomodationsraum schafft, der bei ausreichender Sedimentzufuhr äolisch verfüllt wird. Veränderungen des Meeresspiegels resultieren somit nicht nur in veränderten Sedimentationsbedingungen entlang des Nehrungshakens, sondern steuern auch die vertikale Position der Landoberfläche.

Unter ruhigen Wetterbedingungen wächst der Ellenbogen durch West-Ost-gerichteten, strandparallelen Sedimentversatz (beach drift). Schwere Stürme unterbrechen diese Phasen, führen zur Ausbildung einer Erosionsdiskordanz und zur Umlagerung von Sediment in den Vorstrandbereich. Außergewöhnlich starke Stürme führen darüber hinaus zur Ausbildung einer Erosionskante (scarp) im Bereich des trockenen Strandes. Diese Erosionskanten dienen als Sedimentfänger und tragen entscheidend zur Ausbildung von Dünenrücken (foredune ridges) bei, die ein markantes morphologisches Merkmal des Ellenbogens darstellen. Die Landfläche des Ellenbogens ist während der letzten Dekaden deutlich gewachsen. Dies steht im Gegensatz zur Situation an der Westküste des großen Nehrungshakens (Listland), der in den letzten Jahrhunderten steter Erosion unterlag.

Ein neues Altersmodell der spätholozänen Entwicklung Nordsylts, basierend auf Radiokohlenstoffdatierungen an Molluskenschalen, ermöglicht eine zeitliche Einordnung der sedimentdynamischen Prozesse. Der Nehrungshaken erreichte danach etwa 3700 Jahre vor heute (v.h.) erstmalig eine Nord-Süd-Erstreckung, die mit der heutigen Ausdehnung vergleichbar ist. Auf der Leeseite des sandigen Hakens kam es zur Ablagerung von Klei. Zwischen 3500 und 2500 v.h. führte ein Absinken des Meeresspiegels zur Ausbildung einer Deflationsfläche. Starke Erosion an der westlichen Küste hatte zwischen 2500 und 2000 v.h. einen deutlichen Küstenrückschritt zur Folge. Für eine starke Erosion zu dieser Zeit sprechen auch bis zu 3 m mächtige Washover-Fächer, die auf der Leeseite des Nehrungshakens abgelagert wurden. Ruhigere Bedingungen und die Anlagerung intertidaler Sedimentkörper (swash bars) erlaubten in der Folgezeit eine Regeneration des Hakens. Etwa 2000 v.h. entwickelte sich zwischen der Position des heutigen Ellenbogens und dem Listland ein Seegatt, welches bereits um 1700 v.h. wieder geschlossen wurde. Der Ellenbogen selbst ist deutlich jünger als das Listland. Die Datierungen zeigen hier ein Alter von etwa 1300 Jahren an. Das deutliche Wachstum des Ellenbogens ab etwa 1000 v.h. ist vermutlich auf eine verstärkte Erosion der Westküste des Listlandes zurückzuführen. Im Listland ist die Zeit zwischen 1700 und 1000 v.h. durch die Ausbildung einer Deflationsfläche geprägt. Diese Oberfläche stellt eine markante Erosionsdiskordanz dar und befindet sich heute unter einer bis zu 1,5 m mächtigen Decke äolisch transportierter Sande.

Die Ergebnisse zeigen, dass die zukünftige Entwicklung des nördlichen Nehrungssystems der Insel Sylt nicht nur von einem Schutz der Westküste abhängt, sondern in beträchtlichem Maße von der Möglichkeit zur Sedimentumlagerung ins Hinterland. Diese ist die wichtigste Voraussetzung für einen natürlichen Niveaueausgleich unter den Bedingungen eines steigenden Meeresspiegels. Die Bepflanzung der Dünentäler, umfangreiche Küstenschutzmaßnahmen sowie die Ortsfestlegung der Wanderdünen haben in der Vergangenheit den Eintrag von windverfrachtetem Sand in die Dünenlandschaft stark verringert. Unter den gegenwärtigen Bedingungen kann deshalb ein Anstieg des Meeresspiegels nicht mehr zu vertikaler Sedimentakkumulation führen. Dies birgt langfristig die Gefahr einer leeseitigen Flutung des Nehrungssystems.

Table of contents

1	Introduction	9
1.1	Study area	10
1.2	Late Holocene sea-level and isostatic adjustment	10
1.3	Aims of the study	11
1.4	Outline of thesis	11
2	The use of ground-penetrating radar (GPR) in coastal settings	13
	ABSTRACT	13
2.1.	Introduction	14
2.2.	Theoretical background of GPR measurements	15
2.3.	Working with GPR in coastal settings – a practical view	19
2.3.1	Possible causes of GPR reflections in coastal sediments	19
2.3.2	Maximum ground penetration	20
2.3.3	Resolution	21
2.3.4	Antenna frequencies and operation modes	23
2.3.5	Survey-design and fieldwork	25
2.3.6	Limitations and pitfalls	25
2.4.	Processing of GPR data	29
2.4.1	Data editing	30
2.4.2	Down-the-trace filter (1D-filter)	30
2.4.3	Trace-to-trace filter (2D-filter)	32
2.4.4	Gain control	33
2.4.5	Topographic correction	34
2.4.6	Velocity estimation and migration	35
2.4.7	Visualization of GPR data	37
2.5.	Interpretation: linking GPR data to sedimentology	38
2.6.	Summary and conclusions	42
3	Swash-bar accretion and storm erosion	45
	ABSTRACT	45
3.1.	Introduction	46
3.2.	Geological setting	46
3.3.	Methods	49
3.3.1	Ground-penetrating radar (GPR)	49
3.3.2	Sediment cores	51
3.3.3	Interpretation of GPR data	51
3.4.	Results	52
3.4.1	Radar sections parallel to the recent shoreline (GPR lines 1 – 3)	53
3.4.2	Radar sections perpendicular to the recent shoreline (GPR lines 4 – 7)	59
3.5.	Discussion	65
3.6.	Summary and conclusions	69

4	Anatomy of a hooked spit	71
	ABSTRACT	71
	4.1. Introduction	72
	4.2. Study area	73
	4.3. Methods	75
	4.4. Results	78
	4.4.1 Geomorphological evolution	78
	4.4.2 Ground-penetrating radar	79
	4.4.3 Sediment cores	89
	4.4.4 AMS ¹⁴ C-dates	91
	4.5. Discussion	92
	4.5.1 Sedimentary architectural elements	92
	4.5.2 Evolutionary model for the hooked spit	97
	4.6. Summary and conclusions	100
5	Stratigraphy and development of northern Sylt	101
	ABSTRACT	101
	5.1. Introduction	102
	5.2. Study area	103
	5.2.1 Geomorphology and geology	104
	5.2.2 Late Holocene development of northern Sylt	106
	5.2.2 Late Holocene sea-level rise and glacial isostatic adjustment	107
	5.3. Methods	107
	5.4. Results	109
	5.4.1 Reflection geometries	109
	5.4.2 Stratigraphic cross sections	118
	5.4.3 Grain-size data	125
	5.4.4 AMS ¹⁴ C-dates	132
	5.5. Discussion	133
	5.5.1 Stratigraphy	133
	5.5.2 Development of northern Sylt	137
	5.6. Summary and conclusions	141
6	Conclusions and outlook	143
	6.1 Methods applied	143
	6.2 Geology of northern Sylt	143
	6.3 Outlook	146
	References	147
	Danksagung	163

1

Introduction

The development of barrier-beach systems is controlled by sediment availability, sea-floor topography and the interactions of waves and currents. Their sedimentary architecture is characterized by a complex facies interfingering, with high energy beach facies and low energy lagoon facies existing close to each other, often only separated by a small dune belt. Small changes in the surrounding conditions can already result in major sediment redeposition and in complete rearrangement of the sedimentary system forcing the barrier to prograde or retrograde. Phases of beach progradation alternate with phases of erosion. As a result, barrier sediments contain a valuable, high-resolution sedimentary record of past sea-level fluctuations and climate changes.

In the past, the knowledge about the sedimentary architecture of barrier-beach settings was contributed mostly by the study of processes on recent beaches and on sediment cores (e.g. Hayes & Boothroyd, 1969; Clifton et al., 1971; Davidson-Arnott & Greenwood, 1976; Hine, 1979; Carter, 1986). But cores, which are the base of most standard sedimentological methods, only allow for a punctual insight into the sediment succession, and the excavation of trenches for sedimentological studies is limited by the high groundwater table in coastal settings. Therefore, internal bedding structures were often left unconsidered because of the insufficient spatial resolution of the methods applied.

Geophysical methods, which enable a spatial insight into the subsurface, provide only a low-resolution image of the subsurface in the majority of cases. From all land-based geophysical methods, only high-resolution reflection seismic and ground-penetrating radar (GPR) offer a spatial resolution that is high enough to detect sedimentary structures in a centimeter to decimeter scale. In contrast to high-resolution seismic surveys, which demand great effort during field-work and processing of the data (Gaertner & Wittka, 1997), the use of GPR for surveying the shallow subsurface is time-economic and cost-effective. Therefore, the advent of GPR in sedimentology during the mid-1990s leads to numerous studies dealing with coastal sediments (e.g. FitzGerald et al., 1992; Clemmensen et al., 1996, 2001; van Heteren et al.,

1996, 1998; van Heteren & van de Plassche, 1997; FitzGerald & van Heteren, 1999; Smith et al., 1999; Bristow et al., 2000; Neal & Roberts, 2000; Anthony & Møller, 2002; Daly et al., 2002; Jol et al., 2002; Neal et al., 2002; Buynevich & FitzGerald, 2003; Møller & Anthony, 2003; Switzer et al., 2005; Clemmensen et al., 2007).

1.1 Study area

The investigated barrier system of Sylt belongs to an island chain lining the coast of the southern North Sea. Sylt is the largest of these islands. Two barrier spits, attached to a core of moraine deposits, shape a highly elongated island, some 37 km long. The stratigraphy of the southern spit system is well investigated (Gripp, 1968; Harck, 1972, 1974; Hoffmann, 1974; Köster, 1979; Ahrendt, 1992; Newig, 1995), and reflects a complex sedimentary architecture, involving at least one small Pleistocene moraine core, south of the main moraine core of Sylt. The northern spit of Sylt is morphologically subdivided into the main spit and a small hooked spit, which forms the northern termination of Sylt. The knowledge about the stratigraphic architecture of the northern spit, however, is based almost completely on cores drilled in the first third of the 20th century (Gripp & Simon, 1940).

Stratigraphic models based on these data, geomorphological investigations, and historical maps imply that this spit system must have experienced a complex development during the last 5000 years. As documented by historical maps and reports, and based on the modern rate of coastal retreat, Sylt experienced a significant coastal retreat during the last centuries (Mager, 1927; Zausig, 1939; Bantelmann, 1967; Newig, 1980, 1995, 2004; Ahrendt & Thiede, 2001; Ahrendt, 1993; Bayerl & Higelke, 1994). Since the mid 20th century, the rate of coastal retreat has been increasing (Ahrendt, 1993). These observations were extended to the widely accepted assumption of a postglacial coastal retreat of more than 10 km during the last 5000 years (Gripp & Simon, 1940; Köster, 1974; Ahrendt & Thiede, 1992). More recent investigations by Lindhorst et al. (in press, Chapter 3), however, revealed that the development of the barrier in the past was rather characterized by the alternation of erosional events and phases of progradation and growth than by a continuously coastal retreat. Additionally, significant sediment redeposition played an important role in shaping the modern barrier spit (Lindhorst et al., in prep., Chapter 4).

1.2 Late Holocene sea-level and isostatic adjustment

Although numerous sea-level curves were compiled for the southern North Sea region, based on archeological, geological, and hydrographical data (Menke, 1976; Jelgersma, 1979; Streif, 1990a, 2002; de Groot et al., 1996; Behre, 2003, 2004, 2007; Gehrels et al., 2006), none of these sea-level curves rely on data from Sylt. The most recent sea-level curve was proposed by Behre (2007), based on the level of mean-high tide. This curve shows a fast rise with a rate of 1.25 cm per year until 7000 BP, when sea-level reached a position of 7 m below recent level. Between 7000 and 3400 BP, the rate decreased to 0.14 cm per year, reaching a sea level of 2 m below the present level. At around 3000 BP sea level dropped 2 m. This sea-level fall was followed by a general sea-level rise at a rate of 0.11 cm per year (Behre, 2003) with a series of superimposed short-term low fluctuations with values between 0.5 and 1.5 m. Data from southern Denmark indicates a continuous sea-level rise between

3500 BP and 1500 BP, and a possible lowering of around 0.5 m between 1500 and 1000 BP (Gehrels et al., 2006). A late Holocene sea-level highstand, as proposed by Mörrner (1976), was not supported by Gehrels et al. (2006).

The nature of the high-amplitude signals, interpreted as short-term sea-level rises and falls by Behre (2003; 2004; 2007), is not unequivocally solved. Menke (1976) found similar fluctuations by investigating coastal sediments at the northwest German North-Sea coast. He noted that those signals were not necessarily triggered by relative sea-level fluctuations, but probably reflected climatic changes. Based on investigations by Overbeck (1975) in raised bogs, Menke (1976) found that more humid periods correlated with potential short-term sea-level highstands. He supposed that these apparent sea-level indicators were rather the signature of periods of intensified storm activity. The hypothesis of Menke (1976) is supported by numeric models of Langenberg et al. (1999), who showed that between 1955 and 1993 the winter high-water level on the German North Sea coast increased by 1-2 mm per year due to a sole atmospheric forcing. Similar effects probably have influenced the mean high-water levels proposed by Behre (2007). This hypothesis is supported by Linke (1981), who found periods with significantly higher storm surges that correlated well with postulated short-term sea-level highstands in the curve of Behre (2007). Based on investigations by Töppe (1994), Streif (2002) found that the level of mean high tide (MHT) showed a significantly higher rise in-between 1881 and 1985, than the level of mean low tide in the same period.

The question of the rate of post-glacial isostatic adjustment and local tectonic movements is not fully answered for the investigated area. Based on the position of the top of the Eemian sediments, Menke (1976) derived a long-term rate of subsidence in the range of 11 cm per century for the northwest German North Sea coast. A map of recent vertical movements compiled by Frischbutter (2001), shows that the study area is located near the zero isobase, indicating no active recent vertical movement.

1.3 Aims of the study

The work is focused on the northern barrier spit system of Sylt, and aims to investigate the sedimentary structures of the Holocene barrier spit of Sylt, to determine the basic sedimentary processes that build up the spit, and to reconstruct the development of this system under the conditions of rising sea-level. Data, obtained with a method combining GPR and shallow cores, reveals the internal sedimentary architecture of Sylt with high spatial resolution. Due to their high resolution, the proposed sedimentary models could serve as a template to recognize similar deposits in the geological outcrop. Radiocarbon dates provide an age framework and make it possible to propose a new model for the palaeogeographic reconstruction, showing the different evolutionary stages of the spit during the last 5000 to 6000 years.

1.4 Outline of thesis

This thesis is subdivided into six chapters. Chapter 1 is the introduction, Chapter 2 focuses on the application of GPR in coastal settings. It contains a brief introduction to the theoretical background of GPR measurements, followed by a vade-mecum for the practical work in the field. The chapter closes with a guideline for processing and interpretation of GPR data. Chapter 3 deals with the accretion of swash bars as

the dominating process in the foreshore and shoreface of the Sylt barrier beach. For the first time the stratigraphical architecture of this part of the spit is shown, which is a record of destructional events interrupting phases of spit growth. Chapter 4 presents the sedimentary architecture of the hooked spit at the northern termination of Sylt. The so called „Ellenbogen“ experienced significant growth during the last decades and obviously serves as a sink for eroded material from the main spit. GPR and core data furthermore reveal the interplay of erosional events and the development of fore-dune ridges. In Chapter 5, the stratigraphy and development of northern Sylt during the latest Holocene are documented and discussed. This chapter reviews the common knowledge about the stratigraphy of northern Sylt and presents a new model for the development of this barrier system. Chapter 6 presents the conclusions of this study. The chapters 3, 4, 5 are based on manuscripts for publication in peer-reviewed journals.

2

The use of ground-penetrating radar (GPR) in coastal settings

ABSTRACT

This work presents a vade-mecum for the use of ground-penetrating radar (GPR) in coastal settings. The presented workflow combines GPR and sedimentological investigations to deduce a high-resolution stratigraphic model of the surveyed area. First, a general introduction to the theoretical background of the GPR measurements, survey design, and field work are addressed. Annotations to limitations and pitfalls using GPR in coastal settings complete this part. The second part comprises of recommendations for data processing and visualization. The third part is focused on techniques for data interpretation. Examples from Holocene barrier islands in the southern North Sea illustrate important points addressed in the text. It is shown that the method of radar-facies interpretation, combined with sedimentological data obtained from shallow cores, provides a useful tool for high-resolution spatial analysis of sedimentary facies – especially in areas with sparsely distributed sediment cores.

2.1. Introduction

Beach systems and therefore barrier systems represent a sedimentary environment of high dynamic, which is influenced by sea-level position, tidal regime, currents and wave conditions. Severe storms are an additional factor affecting the system. As a result, barrier islands can migrate forth and back, phases of beach progradation alternate with phases of erosion. Already small changes in the surrounding conditions can result in major sediment redeposition and in a complete rearrangement of the sedimentary system. This leads to a complex facies interfingering especially in barrier settings, where high energy beach facies and low energy lagoon facies exist close to each other, often only separated by a small dune belt.

In the past, the knowledge about the sedimentary architecture of barrier-beach settings was contributed mostly by the study of processes on recent beaches and on sediment cores (e.g. Hayes & Boothroyd, 1969; Clifton et al., 1971; Davidson-Arnott & Greenwood, 1976; Hine, 1979; Carter, 1986). But sediment cores, which are the base of most standard sedimentological methods, only allow for a 1D insight into the subsurface, and the excavation of trenches for sedimentological studies is limited by the high groundwater table in coastal settings. Internal bedding structures are mostly left unconsidered because of the insufficient spatial resolution of the methods applied. Hence, to obtain a 2D- or 3D-model of the underground, assumptions have to be made which are often afflicted with a high amount of uncertainty.

Geophysical methods enable a 2D- or 3D-insight into the subsurface. The most used methods for land based geophysical surveys are acoustic methods (reflection and refraction seismics), geomagnetic methods, gravity measurements and electric methods (geoelectric investigations and ground-penetrating radar). Among all of them, only high-resolution reflection seismic and ground-penetrating radar (GPR) offer a spatial resolution that is high enough to detect sedimentary structures in a centimeter to decimeter scale. Whereas land based high-resolution seismic surveys demand great effort during field-work and processing of the data (Gaertner & Wittka, 1997), the use of GPR for surveying the shallow subsurface is fast and cost-effective. The equipment is highly portable, which allow to operate in remote areas. Real-time data processing allows for a first estimation of data quality already in the field.

Numerous GPR studies dealing with coastal sediments have been carried out since the mid-1990s, as GPR become a widely accepted method in sedimentology (e.g. Clemmensen et al., 1996, 2001; van Heteren et al., 1996, 1998; FitzGerald & van Heteren, 1999; Smith et al., 1999; Bristow et al., 2000; Neal & Roberts, 2000; Daly et al., 2002; Jol et al., 2002; Neal et al., 2002; Buynevich & FitzGerald, 2003; Møller & Anthony, 2003; Switzer et al., 2005; Clemmensen et al., 2007). They all used GPR to reveal the sedimentary architecture of the investigated area based on radar-data interpretation and additional sedimentary datasets. Furthermore there are a few publications that deal with radar-reflection attributes or statistical analyses to reveal physical sediment properties and to obtain a dataset for further numeric modeling of coastal settings (e.g. Knight & Tercier, 1997; Bano & Girard, 2001).

Although the use of GPR has lots of advantages, disadvantages are also present which sometimes prevent a clear interpretation of the radar data: The exact causes of the radar reflections are often unclear, furthermore, varying propagation velocities of the electromagnetic waves in the subsurface can distort the reflection geometries and multiples can lead to misinterpretations. In addition, not every material is suitable

for the usage of GPR, especially clay and silt as well as peat layers prevent deeper ground penetration. In coastal settings saline groundwater is an additional limiting factor for GPR surveys due to high signal attenuation.

This work shows that the combination of ground-penetrating radar and sediment analyses allow for a time economic high-resolution interpretation of sandy coastal sediments. The advantages, as well as the limits of the method will be defined, providing a guideline for future investigations in this setting.

Examples are from own investigations on the islands of Sylt and Langeoog. Both are Holocene barrier islands, belonging to an island chain that line the coast of the southern North Sea.

2.2. Theoretical background of GPR measurements

GPR is a noninvasive method which is based on the transmission of high-frequency electromagnetic pulses and the reception of energy that was reflected in the subsurface at electromagnetic discontinuities (Bristow, 1995; Blindow et al., 1997; Neal, 2004). The reflected energy is detected by the receiving antenna, where the amplitude of the reflected wave is recorded as a function of time. Several measurements along a profile line lead to a two dimensional image of the velocity discontinuities in the subsurface. Comparable to the method of reflection seismics which is based on acoustic impedance contrasts within the subsurface, the GPR allows to detect electrical discontinuities in the shallow subsurface.

First applications of pulsed electromagnetic waves to investigate the subsurface took place in the 1920s, but it last till the 1970s as geological applications became more frequent (Reynolds, 1997; Neal, 2004; Forkmann, 2006). Commercial GPR systems came into the market with the development of digital acquisition-techniques in the mid-1980s (Annan & Davis, 1992; Jol et al., 1996). Since the middle of the 1990s, GPR has become a standard method for geophysical as well as geological applications. Nowadays, the use of GPR in sedimentology goes far beyond the detection of buried objects or the characterization of sediments by their radar facies (Bristow & Jol, 2003) and more into quantitative analyses of reservoir analogues (e.g. Asprion & Aigner, 1997; Pringle et al., 2000; Kostic et al., 2005) and small scale sequence stratigraphy (Pipan et al., 2003).

In the technical sense, a GPR system consists of three main elements: transmitter, receiver and control unit. In commercial GPR systems, transmitter and receiver do often share one antenna which toggle between transmitting and receiving mode (monostatic configuration). A physical separation of both antenna is common too (bistatic configuration) (Fig. 2.1). Whereas monostatic antennas only allow for surveying in common offset mode (van der Kruk et al., 1999), the latter enable common mid point geometries (Fig. 2.2) and therefore the possibility to obtain additional information, especially concerning the propagation velocity of the electromagnetic waves in the subsurface material (Reynolds, 1997; Jol & Bristow, 2003).

The time between transmission of the electromagnetic pulse and reception of the reflection from the subsurface is referred to as the two-way traveltime (TWT). In the case of GPR, the TWT is measured in nanoseconds (ns). The TWT is a function of antenna separation, distance to the reflector, and radar-wave velocity in the subsurface.

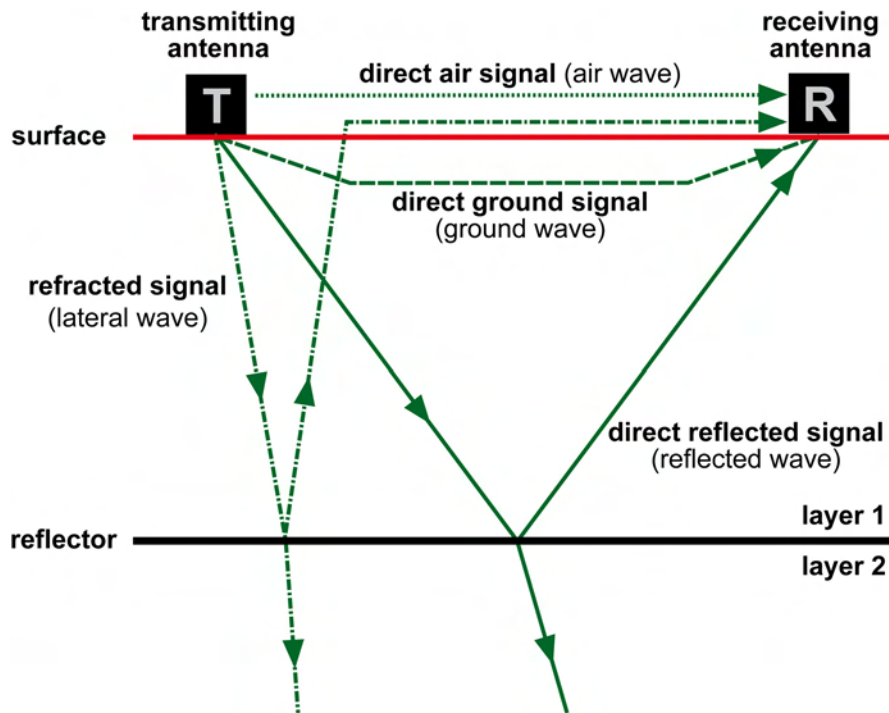


Figure 2.1: Simplified configuration of a bistatic GPR system and possible signal paths in the subsurface. Signals, emitted as short high energy pulse from the transmitting antenna, travel on different paths to the receiving antenna, where signal amplitude is registered as function of time. Different signal paths result in different arrival times. Note that only one part of the energy is reflected at the subsurface electromagnetic discontinuity (reflector), and that some energy is refracted and still travels further. Modified after van der Kruk et al. (1999), Neal (2004), and Annan (2005)

This implies that differences in subsurface radar-wave velocity cause distortions of the radar data – an effect that has to be taken into account during interpretation. By time-depth migration based on a subsurface velocity model, this effect can be minimized.

The direct reflected signal (also reflected wave or primary signal) is not the only signal being detected by the GPR as response to the transmitted pulse. The pulse as well as the reflected signal can travel on different paths between transmitting and receiving antenna (Fig. 2.1). If the separation (antenna offset) between transmitting and receiving antenna is small compared to the target depth, then the dominant signal paths are direct air, direct ground, and direct reflected signal (Annan, 2005). The first signal being registered is the direct air signal, so called air wave. This pulse travels directly from the transmitting to the receiving antenna. The second wave arriving is the direct ground signal (ground wave) which took the direct way through the uppermost ground layers. Air and ground wave obscure primary reflections from shallow subsurface reflectors. During processing both can be partly removed from the data. After Clough (1976), lateral waves are caused by signal reflection on shallow reflectors, followed by refraction of the pulse along the air-ground interface. This occurs only if the reflected signal reaches the surface at a critical angle. Lateral waves show a shorter TWT than primary reflections do (van der Kruk et al., 1999). Reflections associated with lateral waves are therefore not correctly placed in the record with respect to the real depth of the reflector that generates them (Neal, 2004).

The behavior of electromagnetic waves in a medium is primarily controlled by dielectric permittivity, electrical conductivity and magnetic permeability (Neal, 2004). The relative dielectric permittivity represents a measure of the material's ability to store electrical charge. It is in part dependent upon the frequency of the applied electromagnetic field (Powers, 1997).

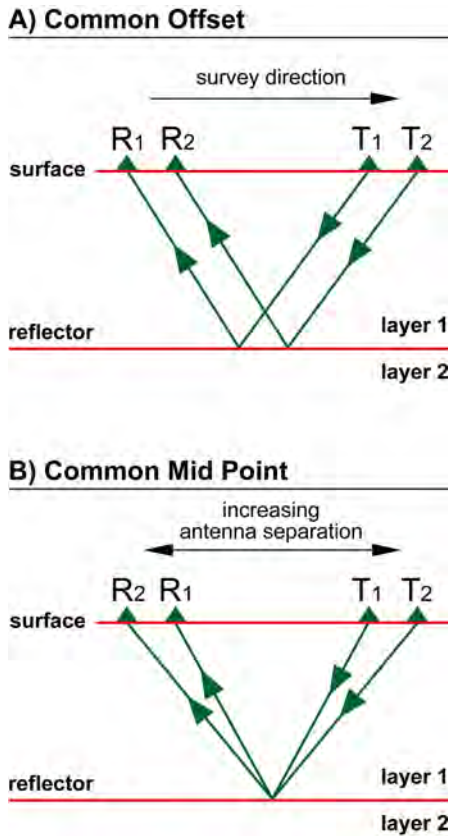


Figure 2.2: Main antenna geometries used in GPR. **A:** Common offset configuration. Separation between transmitting ($T_{1,2}$) and receiving antenna ($R_{1,2}$) is fixed, and both are moved into the same direction along the survey line. A special case of this configuration are monostatic antenna designs, with one single antenna switching between transmitting and receiving mode. This results in a so called „zero-offset section“ with no physical separation between both antennas. **B:** Common mid point configuration. The antenna separation is increased step-wise in-between shots, whereas transmitting and receiving antenna are moved in opposite directions, resulting in multiple covering of each subsurface position. Such datasets allow to estimate subsurface radar-wave velocities. Modified after Neal (2004)

The ability of a material to transport charge in application of a static electric field is represented by the electrical conductivity. Higher conductivity, e.g. caused by dissolved ions in marine saltwater, results in a rapidly increasing signal attenuation. Signal loss can also occur in clays where electric charge is transported by cation exchange on clay minerals (Olhoeft, 1998).

The relative magnetic permeability is the magnetic equivalent of dielectric permittivity. It is a measure of the magnetic field energy that is stored and therefore attenuated by induced magnetization (Powers, 1997). Besides energy losses caused by relative dielectric permittivity, electrical conductivity and magnetic permeability, signal attenuation occurs due to geometric spreading and scattering. Geometric spreading causes a decrease of signal power by the inverse square of distance, because electromagnetic waves propagate through the subsurface in an expanding cone (Neal, 2004). Bano & Girard (2001) found geometric spreading to be the most important factor in signal attenuation in dry sands. Scattering is caused by inhomogeneities in the subsurface (Ziekur, 2000). For materials common in coastal settings, typical attenuation values are depicted in Table 2.1.

After Neal (2004), the velocity of an electromagnetic wave in a host medium (v) can be described by following Eq. (1) as a function of frequency (f), the speed of light in vacuum (c_0), and the sediment’s properties which are defined by relative dielectric permittivity (ϵ_r), relative magnetic permeability (μ_r) and electrical conductivity (σ). Typical values for the electromagnetic wave velocity are provided in Table 2.1.

$$v = \frac{c_0}{\sqrt{\epsilon_r \mu_r \frac{1 + \sqrt{1 + (\sigma / 2\pi f \epsilon)^2}}{2}}} \quad \text{Eq. (1)}$$

Material	Rel. dielectric permittivity	Conductivity	Electromagnetic wave velocity	Attenuation
	-	mS m ⁻¹	m ns ⁻¹	dB m ⁻¹
Air	1	0	0.3	0
Fresh water	80	0.5	0.03	0.1
Seawater	80	30,000	0.01	1000
Ice	3-4	0.01	0.16	0.01
Unsaturated clay	2.5-5	2-20	0.09-0.12	0.28-300
Saturated clay	15-40	20-1,000	0.05-0.07	0.28-300
Unsaturated silt	2.5-5	1-100	0.09-0.12	1-300
Saturated silt	22-30	100	0.05-0.07	1-300
Unsaturated sand	2.55-7.5	0.01	0.1-0.2	0.01-0.14
Saturated sand	20-31.6	0.1-1	0.05-0.08	0.03-0.5
Unsaturated sand and gravel	3.5-6.5	0.007-0.06	0.09-0.13	0.01-0.1
Saturated sand and gravel	15.5-17.5	0.7-9	0.06	0.03-0.5
Freshwater peat	57-80	<40	0.03-0.06	0.3

Table 2.1: Electromagnetic properties of different materials with regard to the frequency range of common GPR systems. Note the contrast between unsaturated and saturated conditions concerning relative dielectric permittivity and conductivity. Table compiled after Neal & Roberts (2000) and Annan (2001)

A simplified form, Eq. (2), is valid only for frequencies > 100 MHz and vertical incidence of the electromagnetic waves (Miltzer & Weber, 1985). Furthermore, Eq. (2) is valid only for clean sands (without iron oxides or clay minerals) and gravels (Neal, 2004). Here the electrical conductivity is minimal and the term $\sigma/2\pi f\epsilon$ is approximately zero (Davis & Annan, 1989; Reynolds, 1997).

$$v = \frac{c_0}{\sqrt{\epsilon_r}} \quad \text{Eq. (2)}$$

If a propagating electromagnetic wave passes a discontinuity with respect to relative dielectric permittivity, relative magnetic permeability or electrical conductivity, a portion of the energy is reflected. Reflection strength is proportional to the magnitude of change. (Reynolds, 1997; van Dam, 2001). The reflection coefficient (R) is a measure of the amount of energy reflected at a bounding surface. After Blindow et al. (1997) it can be determined by the Eq. (3) where ϵ_{r1} and ϵ_{r2} are the relative dielectric permittivity of the adjacent layers 1 and 2.

$$R = \frac{\sqrt{\epsilon_{r1}} - \sqrt{\epsilon_{r2}}}{\sqrt{\epsilon_{r1}} + \sqrt{\epsilon_{r2}}} \quad \text{Eq. (3)}$$

Instead of dielectric permittivity, the propagation velocity (v) of the electromagnetic wave in adjacent layers can be used (Blindow et al., 1997), which leads to Eq. (4).

$$R = \frac{v_2 - v_1}{v_2 + v_1} \quad \text{Eq. (4)}$$

Materials	Porosity	Rel. dielectric permittivity	Reflection coefficient
	%	-	R
air	-	1	- 0,80
seawater	-	80	
air	-	1	- 0,28
dry sand	35	3,1	
air	-	1	- 0,64
saturated sand	35	20,7	
dry sand	35	3,1	- 0,44
saturated sand	35	20,7	
dry sand	35	3,1	- 0,01
dry sand	30	3,27	
saturated sand	35	20,7	+ 0,04
saturated sand	30	17,7	
saturated sand	35	20,7	- 0,20
peat	70	46,5	
dry sand	35	3,1	- 0,43
dry heavy-mineral sand	35	19,9	
saturated sand	35	20,7	- 0,23
saturated heavy-mineral sand	35	53	
round grains	35	23,5	+ 0,08
platey grains	35	16,9	

Table 2.2: Approximations for the reflection coefficient R using Eq. (3). Note the high value for R at the interface between dry and saturated sand, which accounts for the strong reflection from the groundwater table. Compiled after Neal (2004), Annan (2005), and Blindow et al. (1997)

In any case, the reflection coefficient (R) will be in the range of -1 to $+1$, where $|R| = 1$ means a total reflection of the transmitted signal. Typical approximations for R are given in Table 2.2.

The upper frequency range of GPR systems is limited by the frequency at which maximum energy loss occur with respect to water, because water absorbs energy more and more with increasing frequency. The maximum energy loss due to water occurs around a frequency of 17 GHz (Annan, 2005). The lower boundary of the frequency range that is suitable for GPR is around 10 MHz (Neal, 2004). Here signal loss is of unknown origin (Powers, 1997).

2.3. Working with GPR in coastal settings – a practical view

2.3.1 Possible causes of GPR reflections in coastal sediments

Sedimentary bedding is caused by differences in grain compositions, size, shape, orientation and packing of grains (Collinson et al., 2006). In general, all of these changes can cause significant radar-wave reflections (Neal, 2004). GPR is furthermore sensitive to changes in the relative proportions of sediment, freshwater and air (Baker, 1991; Ziekur, 2000).

Van Dam & Schlager (2000) believe that changes in the relative permittivity are the most important factor for causing radar-wave reflections in sediments, because relative permittivity is mainly controlled by the water content of the sediments. As the water content in saturated media predominantly depends on porosity, abrupt changes of grain size or sorting are well reflected in GPR data. The dependence of relative permittivity on the water content is also shown by van Dam et al. (2002), who investigated eolian sands in the Netherlands and found that goethite iron-oxide precipitates significantly lower the electromagnetic-wave velocity in sediments. This

decrease, however, could not be explained by the measured variations in magnetic permeability alone. They conclude that the amount of iron-oxides precipitates appears to correlate with the volumetric water content of the sediments and that the latter caused the observed decrease in radar-wave velocity. Annan (2005) notes that the water content controls the behavior of radar-waves in sediments due to its high polarizability which leads to a high relative permittivity of 80 (compare Tab. 2.1). This causes the strong reflection at bounding surfaces to air with a relative permittivity of 1 and most sediments, which have relative permittivities between 4 and 6 (Davis & Annan, 1989).

The influence of particle size distributions on the dielectric permittivity is shown by Robinson & Friedman (2001), who investigated unconsolidated sediments and found that better sorting increases the effective permittivity. According to them, the observed change is greater than the change in permittivity expected by the significant change in porosity. They conclude that the change in effective permittivity must be directly influenced by the sorting of the material.

According to Neal (2004), ferromagnetic oxides or sulfides, particularly iron and iron-titanium oxides such as magnetite, hematite, and goethite, cause the strongest magnetic response in sediments and are therefore responsible for radar reflections in dry as well as saturated sediments. Buynevich et al. (2004) described heavy-mineral concentrations associated with buried storm scarps from Holocene barrier sequences at the coast of Maine, USA. They conclude that these horizons enriched in ferromagnetic minerals were responsible for distinct GPR reflections in their data. Moore et al. (2004) investigated a prograding coastal barrier in Washington, USA. Associated with layers that cause strong radar-wave reflections, they found enrichments in magnetite. Although a great number of observations exist that link GPR reflections to ferro-magnetic minerals, Olhoeft (1998) remarked that most of the magnetic minerals occurring in nature had never been investigated regarding to their electromagnetic behavior. Hence, their potential to influence radar waves in the subsurface is still unknown.

2.3.2 Maximum ground penetration

The maximum ground penetration of a GPR system is defined as the maximum depth where a buried object can be detected in the subsurface (Noon et al., 1998). Smith & Jol (1995) define the maximum probable depth of penetration more generally as the zone beyond which reflected radar signals are too weak to be detected. This depth is limited by the energy loss electromagnetic waves undergo on their way through the subsurface. Beside the material dependent factors (especially the electrical conductivity), signal attenuation is frequency-dependent (Davis & Annan, 1989), whereas in general the higher the frequency of the transmitted electromagnetic pulse, the shallower the depth of ground penetration that can be achieved (Neal, 2004). Smith & Jol (1995) carried out GPR measurements along the same line in a gravel quarry using different antenna frequencies. They found a linear relationship between antenna frequency and maximum depth of penetration. On GPR studies carried out in barrier settings in the southern North Sea within the scope of this study, the maximum penetration depths reported by Smith & Jol (1995) were not achieved (Fig. 2.3). This is probably caused by the complete water saturation of the sediments in the barrier settings, in contrast to the dry quartz sand they had investigated. Another possible limiting factor is the high content of silt and clay in the sediments investigated for this study.

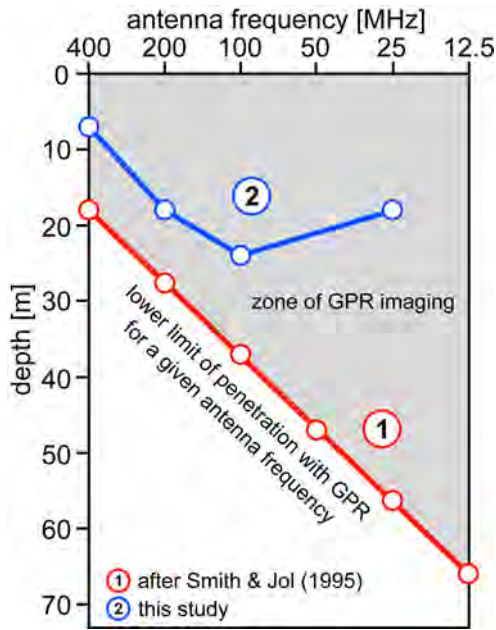


Figure 2.3: Relationship between antenna frequency and depth of penetration in unconsolidated siliciclastic sediments. Red line refers to Smith & Jol (1995) who investigated dry, unconsolidated quartz sands. Blue line represents results from barrier islands in the southern North Sea (this study). The maximum penetration depths of Smith & Jol (1995) are not achieved, probably due to water saturation of the sediment or due to the enhanced content of finer grained material. The lower penetration of the 25 MHz antenna compared to the 100 MHz antenna can probably be attributed to the unshielded antenna design, which results in an enhanced level of background noise. Modified after Smith & Jol (1995)

2.3.3 Resolution

The resolution of GPR data has important implications for their sedimentological interpretation, as it determines the scale of sedimentary structure that can be observed. Knapp (1990) distinguished between two definitions for resolution: The first is the ability to determine the reflector position in space or time, the second relates to the ability to resolve two closely spaced features. These definitions can be adapted directly to GPR (Noon et al., 1998; Neal, 2004). Furthermore, it has to be distinguished between vertical and horizontal resolution.

Vertical resolution is a function of pulse width and therefore frequency, i.e. as frequency increase so does vertical resolution. This is because vertical resolution is controlled by the wavelength (Knapp, 1990). After Eq. (5) wavelength (λ) is governed by wave frequency (f) and velocity (v).

$$\lambda = \frac{v}{f} \tag{Eq. (5)}$$

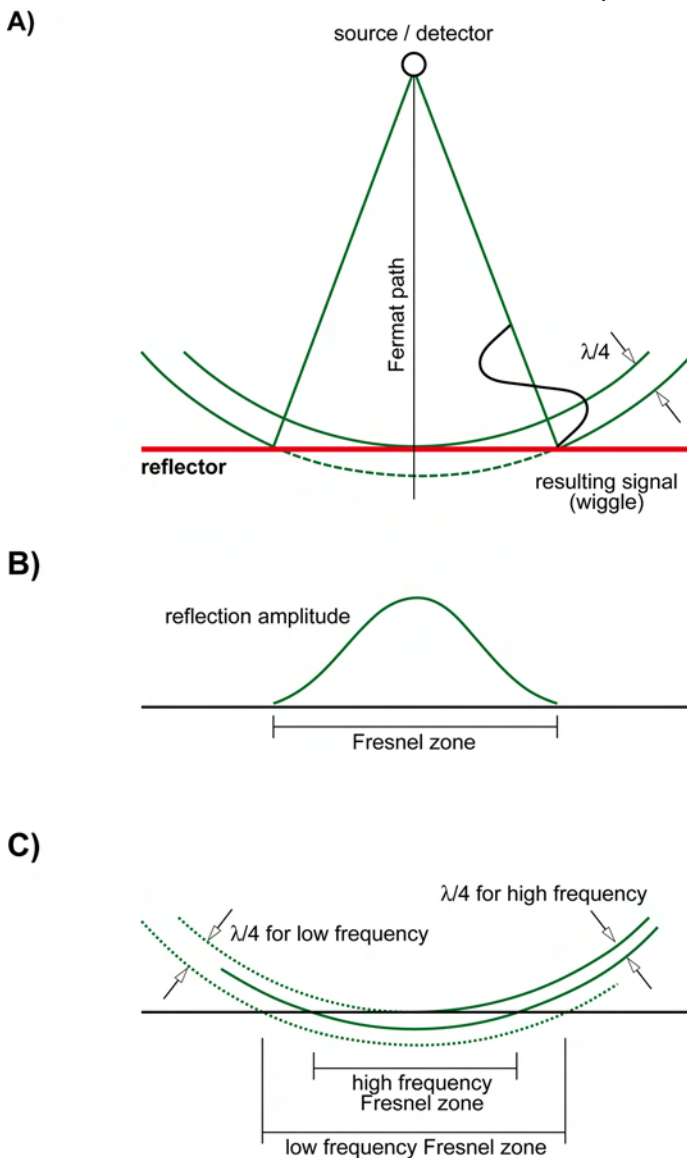
As mentioned above, the propagation velocity of electromagnetic waves in the subsurface is controlled by the material properties. Whereas wave frequency is primarily governed by the antenna frequency, Neal (2004) recommends the use of the returned centre frequency instead of the wave frequency to obtain more realistic estimation of vertical resolution. The returned centre frequency is typically lower than the nominal antenna frequency, because higher frequencies are preferentially attenuated as waves propagate through the subsurface. To obtain a higher vertical resolution it is therefore necessary to enhance the high frequency content of the data, e.g. by using a higher frequency antenna. After Sheriff (1977), wave theory indicates that the best possible vertical resolution is one-quarter of the dominant wavelength. This is the generally accepted Rayleigh criterion, which determines the minimum distance of two nearby reflective surfaces that can be resolved. But this is not the lowermost limit of bed-thickness information to be obtainable from the data. Widess (1973) showed that it is possible to discern the thickness of a bed down to

Material	Rel. dielectric permittivity	Electromagnetic wave velocities m ns ⁻¹	Vertical resolution after Rayleigh (cm)		
			100 MHz	200 MHz	400 MHz
Fresh water	80	0.03	3.8	1.9	1
Dry sand	2.55-7.5	0.1-0.2	25 - 50	12.5 - 25	6.3 - 12.5
Saturated sand	20-31.6	0.05-0.08	12.5 - 20	6.3 - 10	3.2 - 5
Unsaturated silt	2.5-5	0.09-0.12	22.5 - 30	11.3 - 15	5.7 - 7.5
Saturated silt	22-30	0.05-0.07	12.5 - 17.5	6.3 - 8.8	3.2 - 4.4
Unsaturated clay	2.5-5	0.09-0.12	22.5 - 30	11.3 - 15	5.7 - 7.5
Saturated clay	15-40	0.05-0.07	12.5 - 17.5	6.3 - 8.8	3.2 - 4.4
Unsaturated sand and gravel	3.5-6.5	0.09-0.13	22.5 - 32.5	11.3 - 16.3	5.7 - 8.2
Saturated sand and gravel	15.5-17.5	0.06	15	7.5	3.8
Freshwater peat	57-80	0.03-0.06	3.8 - 15	1.9 - 7.5	1 - 3.8

Table 2.3: Approximations for the maximal vertical resolution of GPR at different frequencies, with regard to the Rayleigh criterion. Values are calculated using Eq. (5) and the data of Table 2.1. Note that these values are often not achieved in practice.

one-eighth of the dominant wavelength if data are of excellent quality. Basson (1992) notes that the Rayleigh criterion is seldom achieved in practical use, and that the real resolution of GPR data is often more in the range of one-half of the dominant wavelength. Approximations for the maximal vertical resolution concerning the Rayleigh criterion are depicted in Table 2.3.

The horizontal resolution is determined by the width of the Fresnel zone (Knapp,



1991; van Heteren et al., 1998). The Fresnel zone width, the so called „radar footprint“ in GPR, is a function of wavelength and depth to a particular reflector (Sheriff, 1977), because the energy radiated by the antenna shows a spherical wave front and therefore radial expansion with increasing depth (Fig. 2.4). This lowers horizontal resolution with increasing depth (Neal, 2004). After Neal (2004), the size of the radar footprint (A)

Figure 2.4: The horizontal resolution of GPR is limited by the width of the Fresnel zone which is determined by wavelength and depth of the particular reflector in the subsurface. **A:** The signal travels in an ever expanding cone through the subsurface (wave front). As the vertical resolution is limited to one quarter of the wavelength, the radius of the Fresnel zone at a particular horizontal reflector corresponds to the projected difference of one quarter of the signal wavelength. **B:** The resulting signal amplitude attenuates toward the edges of the Fresnel zone. **C:** A shorter wavelength results in a decreased Fresnel-zone width, which allows for a higher spatial resolution. After Emery & Myers (1996)

	Antenna frequency					
	100 MHz		200 MHz		400 MHz	
	dry sand	saturated sand	dry sand	saturated sand	dry sand	saturated sand
Permittivity	5	24	5	24	5	24
v (m / ns)	0,15	0,06	0,15	0,06	0,15	0,06
Wavelength (m)	1,5	0,6	0,75	0,3	0,375	0,15
Depth (m)						
1	0,88	0,36	0,69	0,28	0,59	0,25
2	1,38	0,57	1,19	0,49	1,09	0,45
3	1,88	0,78	1,69	0,70	1,59	0,66
4	2,38	0,98	2,19	0,91	2,09	0,87
5	2,88	1,19	2,69	1,12	2,59	1,08
6	3,38	1,40	3,19	1,33	3,09	1,29
7	3,88	1,61	3,69	1,53	3,59	1,50
8	4,38	1,82	4,19	1,74	4,09	1,71
9	4,88	2,03	4,69	1,95	4,59	1,91
10	5,38	2,24	5,19	2,16	5,09	2,12
12	6,38	2,65	6,19	2,58	6,09	2,54
14	7,38	3,07	7,19	2,99	7,09	2,96
16	8,38	3,49	8,19	3,41	8,09	3,37
18	9,38	3,90	9,19	3,83	9,09	3,79
20	10,38	4,32	10,19	4,25	10,09	4,21

Table 2.4: Fresnel zone width for different antenna frequencies in given depths. This is the „radar footprint“, which determines the horizontal resolution of GPR data. Data are calculated using Eq. (6), after Neal (2004).

on a buried surface in a given depth (D) can be estimated after Eq. (6) if wavelength (λ) and average relative dielectric permittivity to depth (K) are known.

$$A = \frac{\lambda}{4} + \frac{D}{\sqrt{K - 1}} \tag{Eq. (6)}$$

An essential part of Eq. (6) is the relative dielectric permittivity which determines the shape of the wave field in the matter that the higher the relative dielectric permittivity the more focused the radar beam (Conyers & Goodman, 1997; Reynolds, 1997). Examples for horizontal resolution in dry sand as well as in water saturated sand can be found in Table 2.4.

Forkmann (2006) provided Eq. (7), which allows an estimation of the horizontal resolution (Δx) of GPR in a given depth (h). In contrast to Eq. (6) which additionally requires the relative dielectric permittivity, only the predominant wavelength (λ) has to be known.

$$\Delta x \approx \sqrt{2h\lambda} \tag{Eq. (7)}$$

2.3.4 Antenna frequencies and operation modes

The GPR data for this study were collected using a GSSI (Geophysical Survey Systems Inc.) SIR-3000 GPR system. For this system, different antennas are available, providing a wide frequency range between 16 and 1,6 GHz in total. Whereas the low-frequency antenna (16-80 MHz) is unshielded, all other antennas are electromagnetic shielded. Shielding not only reduces external electromagnetic noise, but also focusses the

radar beam (Annan, 2005). Furthermore, it reduces reflections from objects that are above the surface (e.g. trees, walls, buildings, etc.). On the other hand, an electromagnetic shield increases the antenna dimensions and makes it heavier. Therefore low-frequency antennas are often unshielded. Table 2.5 includes a compilation of used antenna types and their specifications.

The SIR-3000 can be used either in step-mode, in continuous mode or in survey-mode. Whereas the monostatic antennas can be used in all three operating modes, practical use of the bistatic MLF 3200 is only possible in step-mode.

The step-mode, which is recommended by Jol & Bristow (2003) for high data quality, demands a stepwise movement of the antenna by a fixed increment between every measurement. It furthermore enables trace stacking during data collection (Annan & Davis, 1992), which allows reduction of background noise. The step-size depends on the antenna frequency and should not exceed the Nyquist sample interval (Keary & Brooks, 1991), which is one quarter to one half of the predominant wavelength. Annan (2001) provides the following Eq. (8) to calculate the Nyquist sample interval (Δx_{Nyq}):

$$\Delta x_{Nyq} = \frac{c_0}{4f\sqrt{K}} = \frac{75}{f\sqrt{K}} \quad \text{Eq. (8)}$$

The terms f and K refer to the antenna centre-frequency, and the relative permittivity of the subsurface material respectively, c_0 is the speed of light in vacuum. Measuring in step-mode, which allows a good ground-coupling of the antenna because of fixed antenna position during data collection, is very time-consuming: a typical survey with the MLF 3200 (configured to 20 MHz) takes one hour per 100 meters profiling. Furthermore, it requires at least three persons working.

In continuous-mode, measurements are taken with a fixed time increment. This requires movement of the antenna with a constant velocity relative to the surface and therefore conditions that are not achievable on natural ground.

In survey-mode, a survey wheel is added to the system which enables distance triggered data collection. The experiences during the field-work showed, that this is the most economical setting for radar profiling in uneven terrains. A trace increment („step-size“) of 0.05 m turned out to be the best setting for the 200 MHz antenna. It provides high data quality with less trace failures and enables trace stacking during processing because of the small trace increment which is far beyond the Nyquist sample interval.

Model			Range (ground penetration)	
GSSI	Antenna design	Frequency (MHz)	GSSI specification	this study
3206	monostatic / shielded	100	20 m	24 m (735 ns TWT)
5106	monostatic / shielded	200	7 m	18 m (600 ns TWT)
5103	monostatic / shielded	400	4 m	6 m (200 ns TWT)
MLF 3200	bistatic / unshielded	16-80	0 - 50 m	18 m (600 ns TWT)

Table 2.5: Compilation of antennas used for this study. Beside antenna design and rated frequency, the manufacturer specification for range of penetration is provided. Last column gives own values for maximal ground penetration in coastal settings.

2.3.5 Survey-design and fieldwork

Before starting field work, some points concerning aim of the survey and terrain conditions should be addressed to ensure maximum effectiveness. In general, this includes choice of antenna frequency, survey geometry and line orientation.

It is advisable to choose the antenna frequency carefully and with regard to the depth of ground penetration and the resolution which should be achieved. The depth of ground penetration does not depend on the antenna frequency alone, but also on the ground conditions. Only test runs can reveal the maximum accessible depth on unknown terrains. In every case, choosing antenna frequency means to make a compromise between penetration depth and resolution. For extended surveys it is recommendable to collect data with different frequencies, especially in unknown settings. The more general view that low-resolution data provide can allow a first insight into the large scale geological architecture. Subsequently, high-resolution data can add detailed information.

GPR surveys can be performed either in 2D- or 3D-geometries. A 2D-survey consist of one radar line or a group of several radar lines that don't intersect. The obtained information is restricted to the single 2D-lines and no certain spatial information can be achieved. Collecting data in a regular or irregular survey grid, whereas the single 2D-lines intersect, results in a pseudo 3D-survey. This enables spatial interpretation, e.g. predictions about dip direction and dip angle of beds. For pseudo 3D-surveys, line orientation should be parallel and perpendicular to the expected dip direction of the sediments (Jol & Bristow, 2003) in order to minimize geometrical effects on imaged dip and dip direction. However, in practical use, topographic conditions, vegetation or buildings often prohibit the collection of data in well-defined grids.

True 3D-survey geometries enable the application of 3D-migration to remove out-of-the-plane reflections as well as sophisticated interpretation techniques like amplitude mapping and the use of timeslices. For true 3D-surveys, the distance between two parallel running GPR lines should be in the range of the Nyquist sample interval in order to image structures down to the theoretical resolution and to avoid spatial aliasing (Annan, 2001; Grasmueck et al., 2003). This type of survey geometry requires a very precise collecting of elevation data, in best for every shot-position (trace) separately. There exist different attempts using self-tracking laser theodolites and differential GPS to address the problem of exact position estimation during GPR data collection (e.g. Lehmann & Green, 1999; Freeland et al., 2002; Tischler et al., 2002). In general, areas with disturbed topography are only suitable for 3D-surveys to a limited extend.

At least two persons are needed for extensive fieldwork: one to carry the control unit of the GPR and one to trail the antenna. Surveying with the bistatic MLF 3200 requires at least three persons. The expenditure of time depends on the survey geometry and the system that is used for position measurements. Some rough rules of thumbs for estimating the expenditure time are given in Table 2.6.

2.3.6 Limitations and pitfalls

There are different factors that can limit or prohibit the successful usage of GPR in coastal settings. These are primarily factors that enhance signal attenuation in the subsurface, lower ground coupling of the antenna or cause signal ringing. Furthermore,

Survey		Antenna		Persons needed	Estimated time
Type	Size	GSSI model-No.	Frequency		
2D	500 m profiling	3206	100 MHz	2	0.75 h
		5106	200 MHz	2	0.75 h
		5103	400 MHz	2	1 h
		MLF 3200	16 MHz	3	4-5 h
3D	10 m x 10 m	5106	200 MHz	2-3	3 h

Table 2.6: Expenditure of time for radar surveys of different type and size, using different antennas. Time estimations are empirical values out of different radar surveys performed for this study, and include time requirement for GPR line peg out and data collection. The number of people needed is the minimal request. One or two people more often allow for much faster surveying. Depending on the system that is used for position acquisition and mapping of terrain altitudes, additional time is required.

the GPR technique itself can produce interfering signals and artifacts and has therefore to be used attentively.

Materials

As shown above, not every material is equally suitable for GPR surveys. Especially high conductivity materials, like clay and peat, can limit the use of GPR. Already thin clay layers in the shallow subsurface lead to a significant decrease in penetration depth and shadow strata beneath (Fig. 2.5). Because the signal bounces back and forth between the high conductivity reflector and the antenna (Neal, 2004), clay and peat can cause strong ringing in the data. Ringing can totally obscure the primary reflections, leading to a useless dataset. In parts, ringing can be removed by deconvolution (see below). Different possibilities to reduce or remove ringing are discussed by Kim et al. (2007).

Groundwater

Groundwater is often considered as one of the most limiting factors for penetration depth and data quality of GPR surveys (e.g. Asprion, 1998; Alteköster, 2004; Ziekur, 2000). For sediments, this is mainly due to the high relative dielectric permittivity of water, which causes a high reflection coefficient at interfaces between dry and water saturated sediments. In unconsolidated sands with a porosity of 35%, the reflection coefficient is -0.44 at the limit between dry and water-saturated sediments. This means that up to 44% of the incoming energy is to be reflected (Neal, 2004) causing significant signal lowering in the part beneath the groundwater table.

An exception of this general rule is to be observed if the groundwater table lies very shallow beneath or above the surface. This is quite common in the setting of barrier islands, where the freshwater lens stands in a hydrodynamic equilibrium with the surrounding seawater. Our investigations showed, that this situation leads to a very good ground coupling of the GPR. Beside a very high ground-penetration depth, increased resolution is a benefit. The latter is caused by the comparably shorter electromagnetic wavelength in water saturated sediments.

Seawater

Seawater has a conductivity of around 30,000 ms m⁻¹ (van Heteren et al., 1996). This causes attenuation of electromagnetic waves in the range of 1000 dB m⁻¹ (Neal, 2004). The maximal penetration depth in saltwater is given by van Heteren et al. (1996) as 0.3 m. Our studies on Sylt revealed that the contact between marine saltwater and freshwater is marked by a narrow transition zone (Lindhorst et al., 2006) which is well imaged on radar data that were obtained near the coastline (Fig. 2.6). Investigations in the salt marsh on the lee side of the island showed that also ephemeral flooding by seawater hinder the application of GPR. Although the subsurface

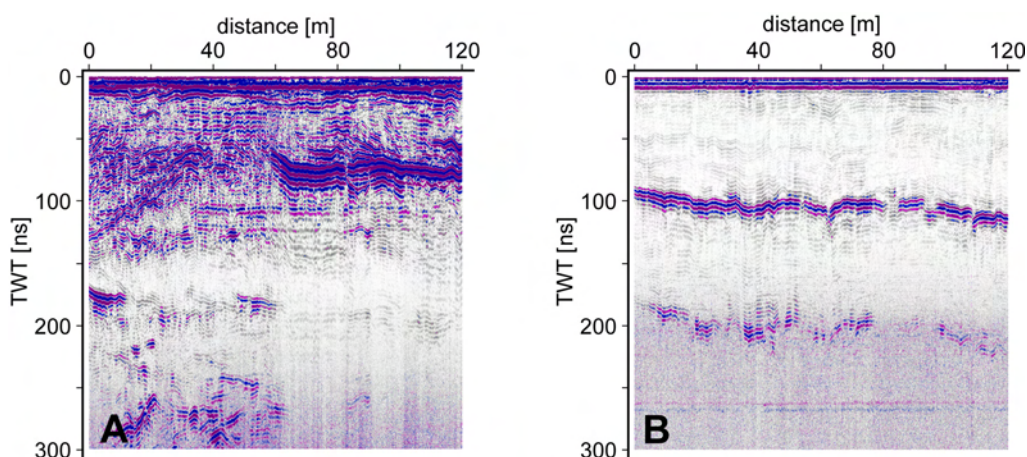


Figure 2.5: GPR image of clay and silt layers measured with a 200 MHz antenna. Data are unprocessed, with the exception of amplitude gain. **A:** Clay layer 2 m (70 ns TWT) below the surface. Thickness of the clay, known from coring, is around 35 cm. Note that strata beneath the clay, from meter 60 of the radar line onwards, are shielded. **B:** Clay layer at a depth of around 3 m (100 ns TWT). From coring it is known that the clay interval is up to 40 cm thick and contains a high portion of sand. Note multiples at a depth of 200 ns TWT, and that strata beneath the clay are shielded.

in the salt marsh area contains a freshwater aquifer, salinization of the uppermost soil layer causes nearly total signal attenuation. Achieved penetration depth here is in the range of 5 to 10 cm. The same effect can be observed on beaches and coastal dunes, where salinization of the sand is caused by seawater spray.

Weather and seasonality

In areas with a high groundwater table, intense rainfalls can improve ground coupling of the GPR antenna by decrease the difference between the relative dielectric permittivity below and above the groundwater table. This results in less energy reflection at the interface between both media and can enhance ground-penetration depth. An example is depicted in Figure 2.7. Here, not only ground coupling is improved by increased humidity of the uppermost soil horizons, but also interfering signals are reduced.

In the setting of oceanic islands, the freshwater aquifer forms a lens-shaped body, which is surrounded by marine saltwater (Fetter, 1972). Especially the enhanced precipitation during the winter months fills up these reservoirs, leading to the development of ephemeral ponds in the interdune valleys. These ponds mark the groundwater table. Observations show a remarkable increase in ground-penetration depth after humid periods, attributed to a better ground coupling of the antenna.

During the winter months, strong ground frost in the upper soil horizon can cause signal ringing due to multiple reflections between the ice layer and the reflectors beneath or inside the ice layer (Fig. 2.8). This results in regular spaced, multiple reflections detected by the GPR. Due to the possible high amplitude of the signal, ringing can obscure most primary signals in the data. To a certain degree, it is possible to eliminate these interfering signals during processing using deconvolution algorithms. Further methods to reduce or remove ringing multiples are discussed by Kim et al. (2007).

Vegetation

Vegetation is an important factor in GPR measurements that can cause strong artifacts in the data. Our field studies showed that especially the dense shrub vegetation of interdune valleys seems to cause high signal attenuation in the uppermost soil horizon. Furthermore, signal ringing can occur, probably due to dense root hairs on vegetated ground. Signal attenuation and signal ringing are more distinct in early spring than in

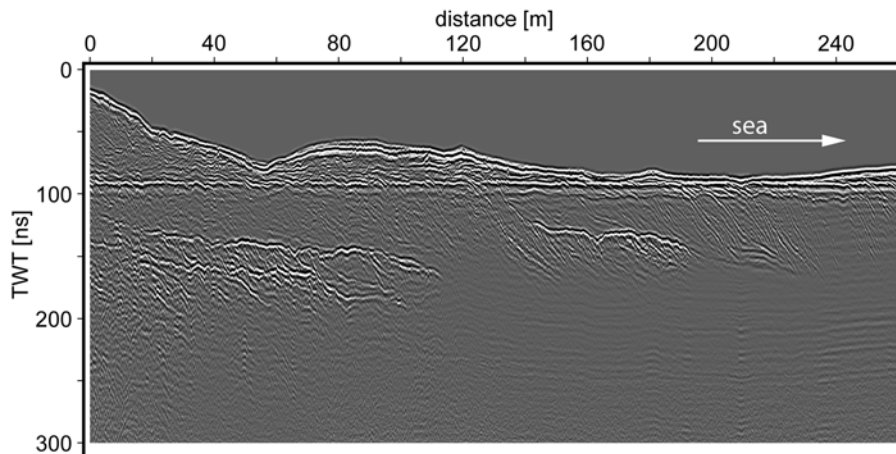


Figure 2.6: This GPR line (200 MHz) runs perpendicular to the coast, the shoreline is to the right. Data are unprocessed, with the exception of amplitude gain and morphology correction. Increasing salinization of the groundwater towards the sea results in decreased penetration depth. Note ringing multiples in the right portion of the line, probably caused by shallow saltwater table.

the late summer. This is possibly a consequence of higher ion-bearing concentrations in the roots and stems caused by increased plant activity after the winter.

Topography

In the field, GPR lines are supposed to be orientated in a manner that steep slopes are avoided as far as possible. Elevation changes along the line can cause significant distortions in the image of the subsurface (Fisher et al., 1996). Lehmann & Green (2000) note that a slope angle $> 6^\circ$ causes problems due to uncorrectable dislocation of subsurface reflections in GPR. This is caused by the fact that radar waves are always radiated in a right angle to the surface. On slopes the radar beam is therefore no longer orientated vertically, but has a significant horizontal component (Neal, 2004). Our field experiences showed that by crossing small dune ridges, the subsurface image is distorted, and structures are overlaid by multiples caused by the steep slopes of the dune. Processing of the data can reduce the artifacts, nevertheless, interpreters have to be aware of dislocated reflections.

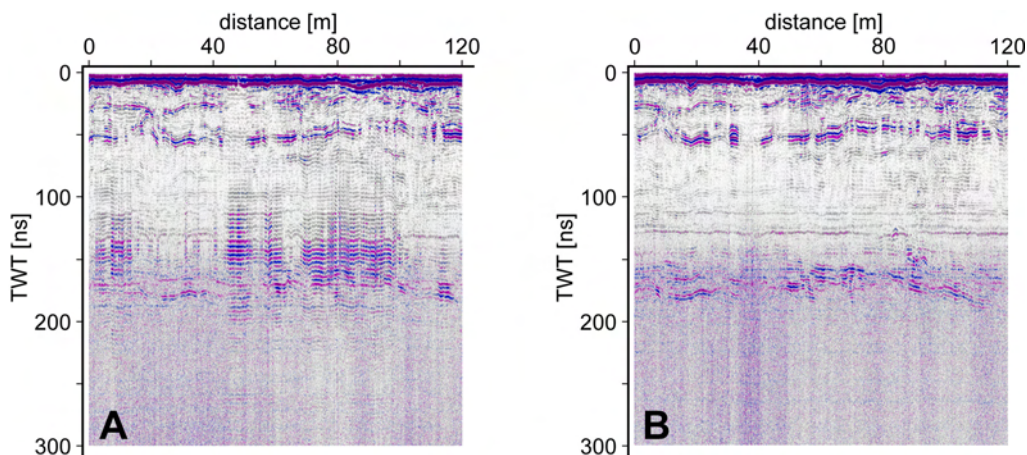


Figure 2.7: Signal quality strongly depends on ground-coupling of the antenna. One additional important factor is the humidity in the shallow subsurface above the groundwater table. **A:** Sediment above the groundwater table is dry after some days without precipitation. Note multiples caused by signal ringing. **B:** Dataset collected one day later after heavy rain in the night shows less interfering signals and better resolution of subsurface structures. The increased data quality is attributed to better ground-coupling of the antenna and less signal attenuation at the groundwater table due to a decreased electromagnetic impedance contrast between sediments above and below.

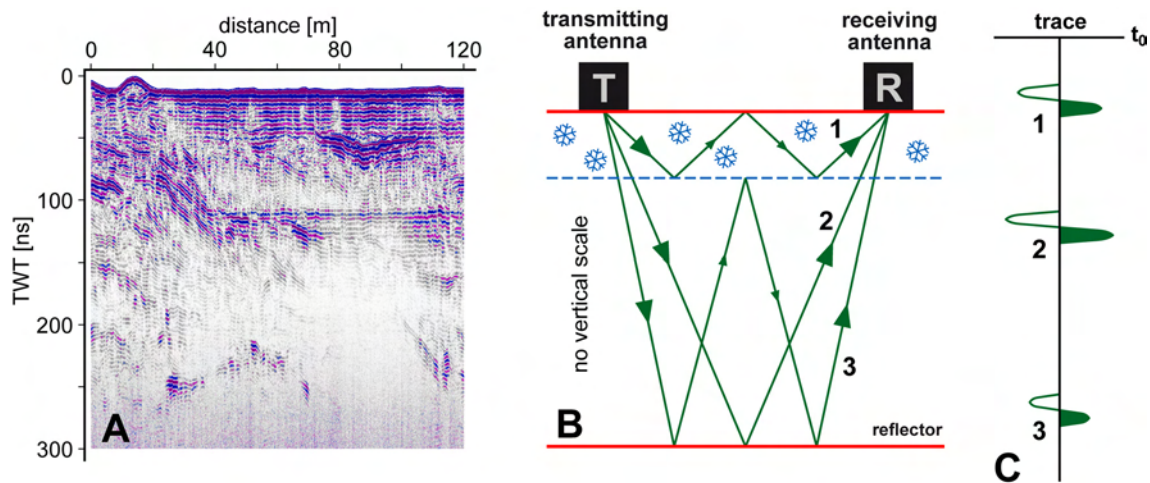


Figure 2.8: **A:** Radar data collected with a 200 MHz antenna during a period of ground frost. The data are not processed with exception of gain and topographic correction. Two types of ringing multiples are visible in the section. First, horizontal multiples that exhibit decreasing amplitudes with increasing depth, best visible in the right part of the line. And second, multiples that multiply every primary reflection. Especially the second type hinder successful interpretation of the data, by masking reflection terminations and exact position of reflectors. **B:** A model showing some possible signal paths that lead to ringing multiples, under the condition that a ground-frost layer exists near the surface. Part of the incoming signal from above is trapped in the ice layer and bounces forth and back between the surface and the lower termination of the frosted zone (signal path 1). This signal contains no information about the target reflector and reaches the receiving antenna prior to the primary reflection (compare Fig. C). Some part of the signal still travels undisturbed through the ice layer (signal path 2). This is the primary signal, containing relevant information about the target reflector. The third signal also provides information about the target reflection, but arrives some time after Signal 2 at the receiving antenna due to the longer signal path in the subsurface (signal path 3). This signal produces an artifact in the data, as it shows a true reflection at the wrong time position (compare Fig. C). **C:** Hypothetical trace showing different arrival times of the Signals 1, 2, and 3.

Technical sources of interfering signals

Shaking of the antenna, tilting or insufficient ground contact are clearly visible in the data: not only as spikes, but also by different trace offsets and as over-gained traces. Such artifacts are often difficult to correct during processing. Especially over-gained traces have to be removed manually before processing, because they can cause strong artifacts during migration. As the cable connected to antenna and control unit is another potential source of interfering signals, it has to be handled carefully during measurements. Twisting or shaking of the cable during data collecting produces spikes, that look similar to that which can be caused by operating of mobile phones. If the cable drags on the ground, it can act as a second antenna, causing ringing multiples in the data. A detailed evaluation of technical factors that can cause interfering signals or artifacts in the data is provided by Alteköster (2004) who investigated the reproducibility of GPR measurements.

2.4. Processing of GPR data

The aim of processing is to obtain a more realistic image of the subsurface (Neal, 2004). In detail, this includes an increase of the signal-to-noise ratio, the removal of interfering signals and the removal of diffractions, multiples and dip displacements to restore real reflector geometries.

Within the scope of this chapter, the term „raw-data“ refers to a dataset that was primarily stored by the control unit of the GPR. Because these data have been already filtered during the collection process, they are no „real“ raw-data in the sense of

„unfiltered“. This real-time processing contains frequency filtering to remove interfering signals and signal amplifying. The bandwidth of the frequency filters depends on the antenna frequency and is normally predefined by the manufacturer. However, the gain-control is dependent on the material and the conditions of the subsurface, so that it is to be adjusted by the user.

The general processing flow (Fig. 2.9) has to be adopted depending on raw-data quality and processing goals. It contains data editing, down-the-trace filtering (also referred to as temporal- or 1D-filters), trace-to-trace filtering (also referred to as spatial- or 2D-filters), signal amplifying (gain control), migration and corrections for varying terrain altitudes.

In most cases, only smooth and careful processing is sufficient. Especially the frequency filters rather add artifacts to the data than improving them. The processing of all radar data was performed using the software ReflexW (Sandmeier, 2006). Details of the different processing steps that were applied to the data will be discussed in the following.

2.4.1 Data editing

The term ‘data editing’ comprises each manual manipulation of the dataset that does not alter the trace content itself. It includes tools for removing single traces or trace ranges. Additionally manipulations of the trace headers, e.g. by adding position data, are part of data editing.

Beside trace header operations, data editing is mostly used to remove unwanted traces that contain a disproportionately high amount of noise, or are distorted otherwise. These traces (often referred to as ‘spikes’) appear as high amplitude signal in the radar section and can negatively affect later processing steps, especially migration. Before data editing, the horizontal resolution of the dataset should be considered. To avoid negative effects, trace editing should be restricted to single traces or trace ranges below the theoretical resolution of used antenna frequency.

2.4.2 Down-the-trace filter (1D-filter)

A so called down-the-trace filter acts independently on each trace. The information of one trace therefore can not alter the information of adjacent or any other traces. These filters are also referred to as time-domain based filters.

Dewow

The goal of dewowing is to remove very-low frequency components from the data. These are commonly associated with inductive phenomena in the antenna (Annan, 2005). Although the very-low frequency components are initially often invisible in the data, they can negatively affect other filters during later processing steps (Sandmeier, 2006).

Frequency filtering

As mentioned above, a frequency filter is applied during data collection. This filter, however, allows a broad bandwidth of frequencies to pass, which normally contain also unwanted signals. Additional frequency filtering during processing can remove these signals, but it is often afflicted with a significant loss in data quality, by smoothing the reflections or adding reverberations to the data.

The aim of frequency filtering is to remove interfering signals with a specific frequency or a distinct bandwidth from the dataset. Concerning the shape of the filter curve, band-pass and notch filter are to be distinguished. Band-pass filters let pass a frequency range which is limited by two cut-off frequencies. Notch filters, on the other hand, aim to remove the frequency range in-between the two cut-off frequencies. Whereas the latter are used to remove specific interfering frequencies, band-pass filtering narrows the frequency content of the dataset. High-pass (also known as low-cut) and low-pass (high-cut) filters are special cases of band-pass filtering, whereby the filtered frequency spectrum is cut only at one end.

A high portion of noise in deeper parts of the GPR line can be reduced by means of a time-dependent frequency filter. This is a band-pass filter with decreasing bandwidth towards increasing time along the filtered trace. This characteristic allows to leave signals near the surface nearly unfiltered, whereas higher-frequency noise in deeper part of the line is removed. Since reflections from deeper strata only contain lower frequencies, the loss in primary reflections should theoretically be minimal. In

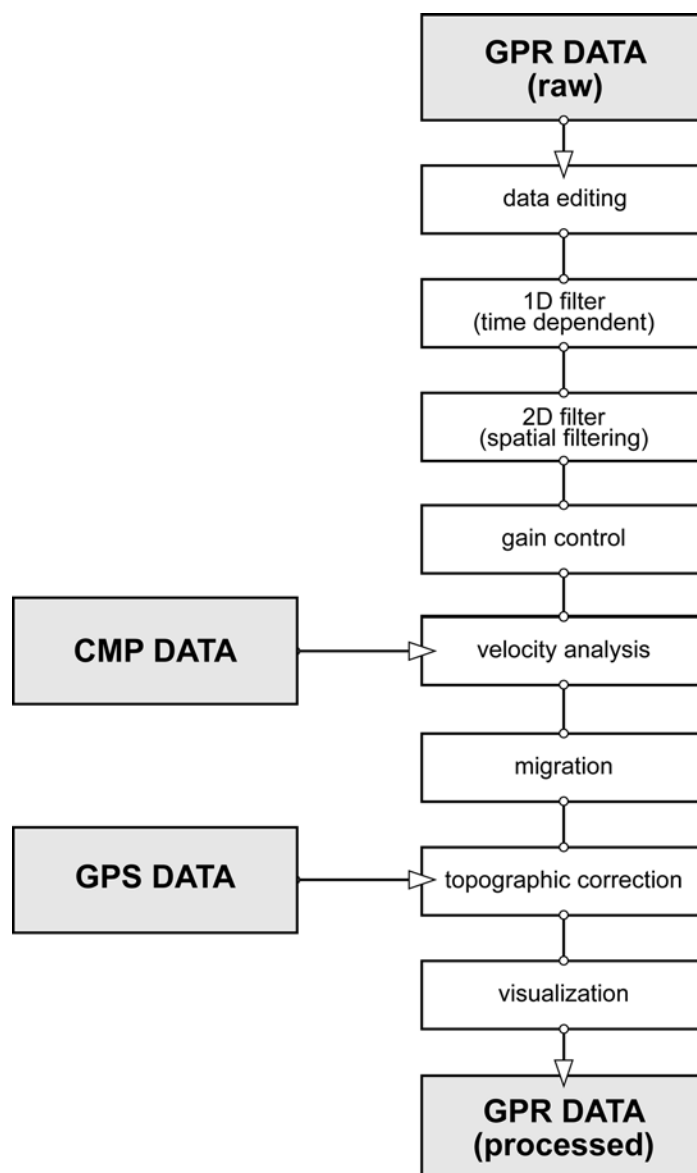


Figure 2.9: Flowchart showing the general processing flow of GPR data.

practice, this filter often adds artifacts to the data or causes unwanted reflection smoothing, which complicates the interpretation process.

Deconvolution

Yilmaz (1987) defines deconvolution as an analytical process, designed to remove reverberation effects caused by a previous filtering operation. This includes the removal of ringing multiples (Neal, 2004). The aim of deconvolution is to shorten the pulse length for improving vertical resolution (Kearey & Brooks, 1991). Annan (1999) recommends not to use deconvolution as an essential processing step, because it can cause artifacts in the data, often without improving the resolution. Nevertheless, deconvolution offers a method to remove ringing multiples, that are caused by heavy conductive reflectors in the subsurface, by vegetation or by ground frost (see above). During the deconvolution process, the addition of white noise to the data is necessary to keep the filter operation stable (Sandmeier, 2006). This often leads to a decreased penetration depth due to increased background noise.

Mean and median filter

These filters lower vertical resolution and are therefore to be used with care. Both filter types can reduce random noise by combining the information of multiple samples. Thereby primary reflections interfere in a constructive manner, and are therefore enhanced in comparison with random noise which attenuates. These filters perform as low-pass filters by suppressing steep reflections. The low-pass effect is the more pronounced the more data samples are considered during each filtering step. The negative effects of these filters can be minimized, if data are collected with a sample-rate few times greater than the expected vertical resolution.

2.4.3 Trace-to-trace filter (2D-filter)

Trace-to-trace filter affects several traces at the same time. Therefore, the information of one trace can alter the information in other traces. Trace-to-trace filters are often referred to as spatial filter. This type of filters should be used with care, as artifacts in the data are easily produced and often hard to identify.

Background removal

This filter performs a subtraction of an averaged trace, which is built by all traces within a defined interval along the line (Sandmeier, 2006). The filter therefore removes all signals that reappear in every trace at the same time position. In most cases, all traces should be considered for creating the average trace, especially to eliminate air and ground wave, and the strong reflection caused by the groundwater table. The average trace can also be created over a user defined range of traces, e.g. to remove unwanted horizontal artifacts like reverberations which are expressed only over a given trace range. The filter should be used carefully, especially if it acts only on a range of traces, suppressing of primary reflections can occur, leading to misinterpretations of the data.

f-k filter

The f-k filter performs a filter process in the so called frequency-wave number domain (f-k domain). The wave number is defined as the reciprocal of the wavelength. Primary signals and noise are often more clearly separated in the f-k domain. This filter allows to remove reflections with certain characteristics, e.g. reflections with a given velocity, dip angle, or dip direction. To transform data from the time-space domain

(t-x domain) into the f-k domain, two-dimensional Fourier transformations are used.

An example for a f-k spectrum is depicted in Figure 2.10. The y-axis is the frequency axis, whereas the x-axis shows wave number against line distance (k-x). The f-k spectrum allows to map different dip values onto different parts of the diagram. It therefore represents a graphical technique to distinguish subsets of data according to their dip direction and the radar-wave velocity in the subsurface. Reflections which down-dip towards ascending distances along the GPR line show positive k-x values, and are therefore mapped on the right side of the diagram. Events with up-dip towards ascending distances along the line are mapped on the left side. Nearly horizontal reflections show small k-x values, and are mapped near the middle of the diagram.

The f-k filter can act as a band-pass or notch filter. The main advantage of the f-k filter compared to the frequency filters mentioned above is the possibility to set filter characteristics not only in the frequency range, but also with respect to geometrical criteria, which allows to selectively remove reflections with a specified amount of dip from the data.

Trace stacking and running average

Trace stacking performs the temporal simultaneous addition of two or more traces in order to enhance the signal-to-noise ratio of the resulting trace (Sandmeier, 2006). Signals that have the same phase in every considered trace are enhanced, whereas signals with changing phase (e.g. random noise) are suppressed (Fig. 2.11).

Trace stacking can be applied without lowering the resolution, provided that the resulting trace increment is smaller than the Nyquist sample interval. For data collected with a 200 MHz antenna and a sample interval of 0.05 m, a stacking of two or three traces can be performed without information loss – particularly for deeper layers where resolution decreases (see Tab. 2.4).

In contrast to trace stacking, the number of traces is not reduced by applying a running average filter. The filter calculates an average trace from all traces in the given window. This average trace is then assigned to the actual trace. The filter suppresses trace dependent noise and emphasizes horizontally coherent energy. It therefore acts as a low-pass filter and results in a smoothed dataset.

2.4.4 Gain control

Gain is a time-variant scaling of the signal amplitude (Yilmaz, 1987). This can help to enhance the visibility of primary reflections. At the same time, however, noise is also amplified. By adding gain to the data, the original amplitude information is lost. Very common is the use of the so called 'automatic gain control' (AGC). Within predefined limits, the AGC adds gain to the data, that is inversely proportional to signal strength (Neal, 2004). The narrower the AGC

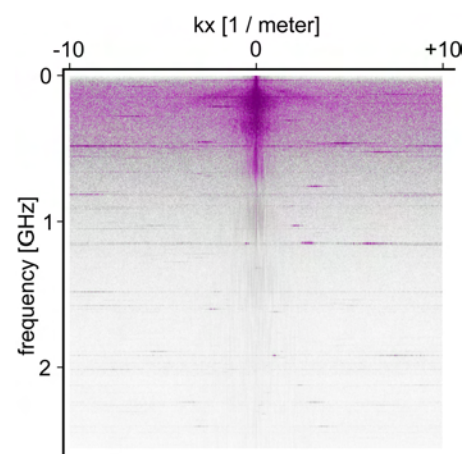


Figure 2.10: f-k spectrum of GPR data provided in Figure 2.7A. The horizontal axis of the diagram refers to wave number against radar line distance (k-x), the vertical axis is the frequency axis. The f-k spectrum allows to visualize the dip of reflections. Signals that are vertically arranged along the middle axis refer to horizontal reflections in the data. The greater the distance from the middle axis, the greater the dip of the reflection.

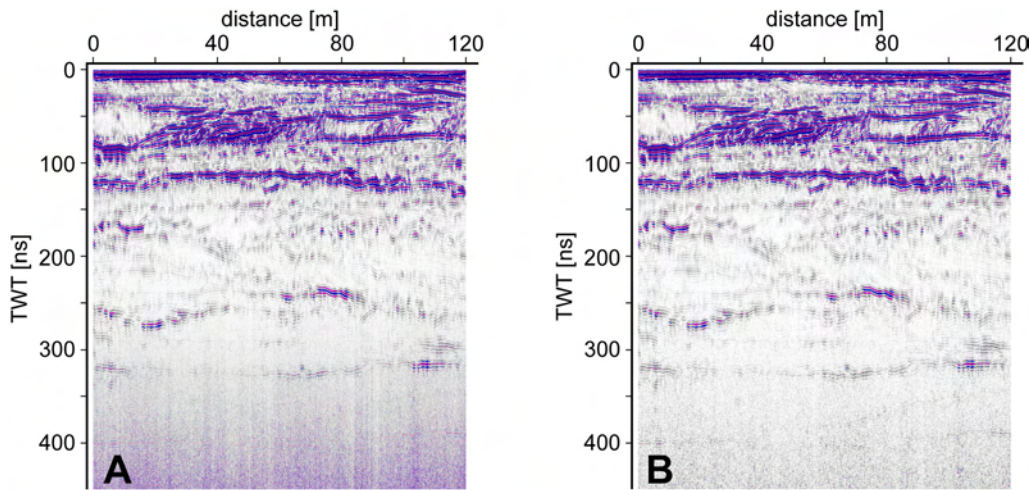


Figure 2.11: Stacking of several traces allows suppression of background noise. This reduces the number of traces in the dataset. In contrast to primary reflections which show a constant polarity in each trace, random noise exhibits polarity changes. By stacking several traces, random noise is partly eliminated, whereas primary reflections interfere in a constructive manner. If stacked trace ranges span more than the Nyquist sample interval for the given frequency, the horizontal resolution of the data decreases. **A:** Radar line obtained with a 100 MHz antenna. Data are unprocessed with exception of gain. Note increasing background noise at greater times. **B:** Same dataset as presented in Figure A after stacking of 5 traces each. Random noise at greater times is reduced and weak reflections become visible.

window is set, the more it attempts to equalize the signal amplitudes along the trace (Yilmaz, 1987; Sandmeier, 2006). Although each information regarding the relative reflection amplitudes is lost, AGC is useful to enhance low amplitude reflections with regard to high amplitude reflections. If relative reflection amplitudes have to be preserved, the use of a manual gain curve is recommended instead of AGC. To compensate horizontal amplitude variations caused by a different ground-coupling of the antenna along the line, a horizontal (x)-scaled gain-curve can be added. Thereby energy differences in-between the traces are equalized, while the amplitude information within the traces, however, will be preserved.

2.4.5 Topographic correction

The distance between the antenna and the ground is always constant during profiling, hence, topographic variations along the GPR line are not taken into account, and reflector depths and reflector geometries are therefore wrongly imaged (Fisher et al., 1996). This means, that a topographic correction is required in order to achieve a correct interpretation of sediment geometries. Two different ways are available: first, relative to a reflection that is assumed to be horizontal along the survey line (e.g. the groundwater table), or second, by the appliance of a topographic dataset which is collected in the field along the line.

The first method is not based on topographic information. It therefore represents a simple time-shift of the traces in the radar line. The aim of this method is to flat a picked horizon which is assumed to be horizontal in nature. This method enables a fast correction of different terrain altitudes, but also holds the risk of adding artifacts to the data, if e.g. lateral changes in the velocity profile occur.

The second method requires a dataset containing topographic information with an adequate accuracy as well as a velocity model for the radar waves in the subsurface. The use of a topographic dataset for topographic correction allows a more sophisticated interpretation of the radar data. This method is recommended for

sedimentological investigations so that it finds detailed description in the following.

There exist different methods to perform a topographic survey in the field. The most common ones are the use of either a differential GPS (dGPS), a total station, or a laser theodolite. All of these have the required vertical accuracy which depends on both, the frequency used to collect the GPR data, and the aim of the survey. For this study two different dGPS systems were used: either a Ashtech ProMark II or a Leica GPS 1200. Whereas the Ashtech systems requires collecting of the topographic data in a separately work step, the Leica enables real-time dGPS surveying during GPR profiling.

The Ashtech system is a passive dGPS, whose vertical accuracy is specified by the manufacturer to be in the range of 10-15 cm. It consists of two GPS receivers which are equipped with an external antenna each. In the field, one GPS (the basis) is stationary, the other (the rover) is used to perform the measurements along the survey line. After an initializing phase (6 to 10 minutes), both of them are collecting data separately from each other, with no real-time data interchange. The system can be used in different survey modes, including stop-and-go and continuous mode. For the purposes of this study, the stop-and-go mode was used because of its much higher accuracy. Step-size depends on the terrain morphology and the frequency of the GPR antenna which is used for surveying. In practical use step-size varies, because it is advisable to collect data points at all significant slope breaks. The intermediate points can be interpolated later by simple algorithms.

The data collected with the Ashtech ProMark II require a processing during which a correction of the recorded positions is performed. Practical experiences in the frame of this study showed that the relative vertical accuracy was high enough for a proper topographic correction of GPR data as long as all data were collected using the same base point for the stationary GPS receiver. On the other hand, a change of the base point results in non comparable data-sets that later have to be shifted to an absolute coordinate system. In this case, it is advisable to measure a point with known coordinates at least after every new initializing procedure.

The Leica GPS 1200 is an active dGPS which provides real-time corrected coordinates. The system consists of one GPS station which is stationary installed on a place with known coordinates (base) and the rover which is used for surveying. The base transmits a correction signal to the rover which can be located in a radius of several kilometers around the base. The vertical accuracy of this system is specified by the manufacturer to be in the range of 0.1 to 0.2 cm. For surveying the GPS antenna can be mounted directly on the GPR antenna without causing detectable disturbances in the radar data. Because this system follows every movement of the radar antenna, a continuous mode of dGPS data collection should be used. Experiences in the field showed that a step-size between 0.5 m and 1.0 m, depending on terrain conditions, is advisable. Smaller step-sizes create datasets that show every movement of the antenna and therefore do not reflect the real terrain morphology.

2.4.6 Velocity estimation and migration

Migration can be regarded as spatial deconvolution of the data (Yilmaz, 1987; Fisher et al., 1992). The goal of the migration process is to restore the true reflection geometries in the subsurface (Annan, 2005), and to remove diffractions, distortions and dip displacements (Neal, 2004). Hence, migration can improve the horizontal resolution of the data by a factor of 3 to 4 (Eidner, 2006).

The Kirchhoff migration in the time domain (Schneider, 1978) and the migration in the frequency-wavenumber domain after Stolt (1978) are the most common migration methods in GPR processing. Whereas the Kirchhoff migration accounts for vertical velocity variations, the migration algorithm proposed by Stolt (1978) requires one constant velocity for the whole line. This was modified by Margrave (2001) allowing the migration with vertical velocity variations using the Stolt method. Both algorithms are accurate for dip angles up to 90° (Neal, 2004 after Yilmaz, 1987 and Sheriff & Geldart, 1995). For successful migration, the GPR data are supposed to represent a so called zero-offset configuration, i.e. transmitting and receiving antenna must be located at the same position (Sandmeier, 2006). Real 3D-datasets enable multi-dimensional migration. 3D-migration algorithms also account for out-of-the-plane reflections and provide a much more clear image of the subsurface.

Every migration algorithm requires the input of the velocity distribution in the subsurface. To obtain a subsurface velocity model, three ways are common in GPR: crosshole radar tomography, common-midpoint measurements, and analysis of diffraction hyperbolas. The first two need special data acquisition configurations, whereas the latter is only performed during processing.

For crosshole radar tomography, at least two stable boreholes are required. Special designed bistatic antennas are used to measure the traveltime of the radar waves in-between the two boreholes. This method allows to detect vertical velocity variations with high accuracy. However, horizontal velocity variations remain unconsidered. Crosshole radar tomography was used e.g. by Hubbard et al. (1997) and Tronicke et al. (2002) to obtain radar-wave velocity variations in unconsolidated gravels and sands. Kostic et al. (2005) used this method to detect velocity variations in unconsolidated sediments of a Quaternary gravel delta. For coastal sediments, the use of crosshole radar tomography is restricted due to the high groundwater table, which hinder borehole stabilization without casing.

Common-midpoint measurements (CMP measurements) are performed in step-mode with bistatic antennas. Between two shots, the separation of transmitting and receiving antenna is increased by a fixed increment. Due to increasing arrival times, the resulting radar section shows horizontal continuous reflections like airwave, ground wave, and subhorizontal reflections in the subsurface as hyperbolas. The known antenna separations and the detected increases in TWT can be used to calculate an average radar-wave velocity (v_1) to the given reflection (Annan & Davis, 1976; Blindow et al., 1997; Reynolds, 1997; van der Kruk et al., 1999; Neal, 2004) following Eq. (9):

$$v_1 = \sqrt{\frac{(x_2^2 - x_1^2)}{(t_{x_2}^2 - t_{x_1}^2)}} \quad \text{Eq. (9)}$$

where t_{x_1} and t_{x_2} are the two-way travel times down to the reflection event at the given antenna separations x_1 and x_2 (Neal, 2004 after Robinson and Çoruh, 1988)

The method requires strong subhorizontal reflectors in the subsurface, which must be traceable along the profile line. High horizontal velocity variations, e.g. caused by steep-dipping strata, can hinder the use of this method. The groundwater table alone is insufficient for velocity estimations, as it only provides information about the velocity in the dry, overlying layer.

Objects in the subsurface that are large with respect to the dominant wavelength, can cause diffraction hyperbolas in the data. These hyperbolas span multiple traces, and their curvature depends on their depth and the average velocity between the antenna and the object. Therefore diffraction hyperbolas also allow for a velocity estimation of radar waves in the subsurface (Young et al., 1995; Fisher et al., 1992). Processing tools for GPR data often enable an interactively semi-automated velocity modeling of GPR data. If multiple diffraction hyperbolas along the line are taken into account, horizontal as well as vertical velocity variations can be detected with adequate accuracy.

If the exact velocity distribution in the subsurface is unknown, migration can be performed as an interactive process, whereby the velocity is iteratively adjusted to optimize the image (Annan, 2005). Due to the high potential of adding artifacts to the data, this should be considered as a last resort only.

One problem in GPR is the magnitude of topography compared to the depth of exploration (Annan, 2005). Therefore, best results should be obtained involving topographic information into the migration process. This has been demonstrated by Lehmann & Green (2000) who provided algorithms for topographic migration, based on the work of Wiggins (1984), and recommended to consider topographic information in the migration process if the surface gradient exceeds 10%.

2.4.7 Visualization of GPR data

Visualizations prepared for interpretation cause other need than visualizations for publishing or presentation. Whereas for the first the main criteria are often visibility, continuity and high resolution, willingly at the cost of clearness and perfect signal-to-noise ratio, the latter more focus on lucidity, well processed data and an economic picture handling. Interpretation is often performed directly on the screen, which allow to modify magnification, vertical exaggeration, contrast and perspective permanently according to work requirements. In contrast, figures for publication are restricted to a fixed view and format, which is usually quite small.

Most GPR-data visualizations are amplitude plots. This means that the amplitude, and in most cases also the signal polarity, are expressed by graphic. Processing programs like ReflexW offer a wide space of visualization tools. Provided that such datasets exist, 2D-, 2.5D- (e.g. fence diagrams), and 3D-graphics are easy to produce. Beside wiggle plots, where traces are plotted as polygonal lines, point plots are also possible, coding data polarity and amplitude according to a predefined colortable.

Nearly every radar line is to be depicted with vertical exaggeration, at least with respect to the disadvantageous relation between profile length and penetration depth of GPR data. But vertical exaggeration can also enhance the visibility of sediment geometries by an artificial increase of small dip angles. On the other hand, vertical exaggeration often leads to smearing of details and over-steeping of structures that have a comparably great dipping angle. As a result, this can cause obscurities and misinterpretations. In practical application, vertical exaggerations between 2 and 5 turned out to be a good choice for interpretation purposes, whereas higher magnification factors, between 5 and 10, are recommendable for publications where the focus is more on the general sediment architecture than on the internal structure.

The nomogram provided in Figure 2.12 shows the relation between apparent and true dip angle for vertical exaggerations of 2-, 5-, 10- and 20-times. If the vertical

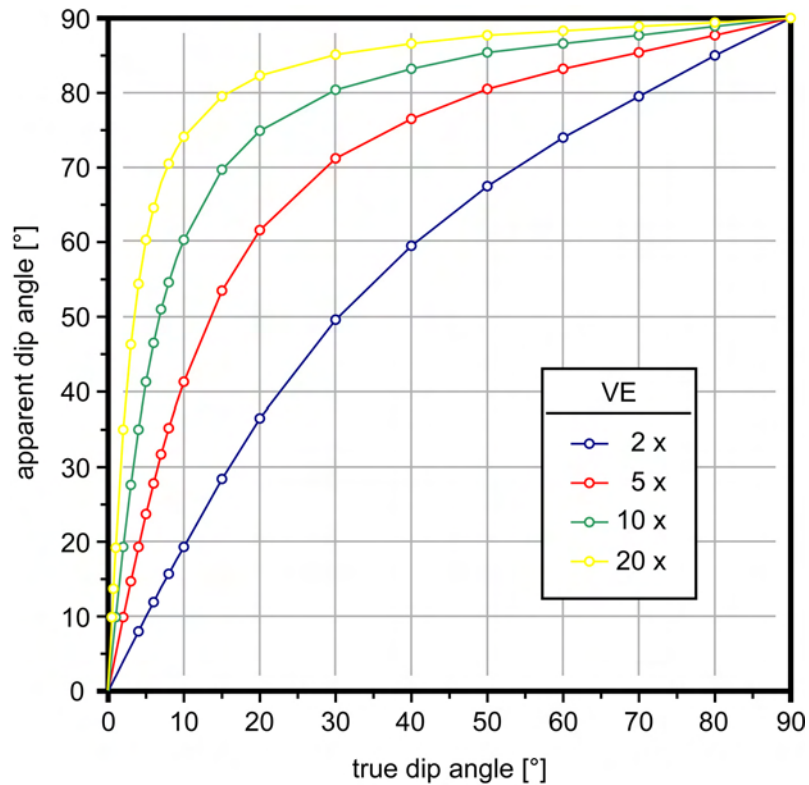


Figure 2.12: Nomogram showing the relation between apparent and true dip angle for vertical exaggerations of 2-, 5-, 10-, and 20-times.

exaggeration (VE) is known, the true dip (α) of a given apparent angle (α') can be calculated by triangle calculations using Eq. (10):

$$\sin(\alpha) = \frac{1}{(VE / \tan(\alpha'))} \quad \text{Eq. (10)}$$

2.5. Interpretation: linking GPR data to sedimentology

Interpreting large GPR datasets is very time consuming. Furthermore, if every reflection in every radar line is interpreted separately, comparisons in-between different lines are often very difficult. Especially in high-resolution datasets, simplifications are necessary, for whose realization the concept of radar-facies interpretation is a useful method. The definition of radar facies furthermore allows to link GPR to sedimentology, as sedimentological characteristics are directly assigned to observed reflection patterns during the interpretation flow. Provided that similar reflection patterns are genetically related, assumptions concerning the sedimentological attributes can be made for GPR sections where no sediment cores are recovered, which is the common case in extensive surveys, where not every radar line can be proved by sediment cores.

The basic principles of radar facies interpretation are adapted from reflection seismic interpretation techniques and based on seismic stratigraphy. Sedimentary sequences, especially in siliciclastic sequence stratigraphy, display a hierarchy of depositional units, starting from individual laminae to whole sedimentary basin fills (Miall, 1991). Therefore, the seismic concept can be directly adopted to the interpretation of GPR

sections which image structures on a much smaller scale than reflection seismic do (Neal et al., 2002; Neal, 2004). The term 'radar stratigraphy' was first used by Jol & Smith (1991) to describe an interpretation technique for GPR data based on concepts developed during the 1970s for the interpretation of seismic data (Neal, 2004). Beres & Haeni (1991) interpreted their GPR data with regard to reflection configurations. They distinguish between chaotic, layered, and reflection free configuration. Gawthorpe et al. (1993) introduced a complete concept of radar stratigraphy, based on the interpretation of reflection terminations. Taking into account the often very complex reflection configuration of GPR sections, Bristow (1995) used a more qualitative approach to interpret sedimentary structures in shallow marine sand stones.

Adapting the concept for seismic interpretation introduced by Mitchum et al. (1977) to the interpretation of GPR data, the term „radar facies“ describes a two- or three-dimensional set of reflections bordered by surfaces termed „radar surfaces“. Reflection configurations are characterized by shape and dip of reflections, relationship between reflections, reflection continuity and amplitude. Bristow et al. (2000) summarize the term radar facies as repeated packages of reflections with similar character and geometry. This also implies that radar facies are frequency dependent due to the limited spatial resolution of GPR at a given frequency.

Radar surfaces are defined by reflection terminations (Gawthorpe et al., 1993). Different types of reflection terminations exist, such as erosional truncation, top lap, onlap, and downlap (Neal, 2004). Radar surfaces represent bounding surfaces and therefore a break in the sedimentary sequence (Reading, 1996). Because of the large number of reflector terminations associated with small-scale sedimentary structures, only more extensive surfaces should be taken into account as bounding surface (Bristow et al., 2000).

Following Mitchum et al. (1977), radar packages can be interpreted as depositional units consisting of genetically related strata, as described by the radar facies. They are bounded top and bottom by unconformities or their related correlative conformities, as defined by seismic surfaces. The relationship between the three terms radar facies, radar surface, and radar package is illustrated in Figure 2.13. For the description of reflection geometries, there exist a fixed terminology which is summarized by Neal (2004) after Campbell (1967), Mitchum et al. (1977), and Allen (1982). Examples for the practical implementation of radar facies to the interpretation of GPR data are provided by Gawthorpe et al. (1993), van Heteren et al. (1998), Bristow et al. (2000), Neal (2004), and Costas et al. (2006).

The general way for interpretation of radar data can be summarized by a workflow (Fig. 2.14), showing all steps from the processed GPR data to the product, the stratigraphic model. The interpretation process starts with the classification of different reflection patterns (Fig. 2.15). As general patterns are difficult to find, this should not be restricted to only one line per time, but should include all lines chosen for interpretation. Because reflection patterns vary with vertical exaggeration, it is recommendable to compare only GPR lines with similar vertical exaggeration. Before defining and describing radar-facies architectural elements out of the reflection patterns, the huge reflection-pattern collection from the previous step has to be condensed down to a few basic recurring patterns. As a general rule of thumb, an extended survey in sandy coastal sediments normally does not contain more than 10 to 15 different radar-facies architectural elements. Defining radar facies is a recursive process, during which the results have to be compared with the data and modified, until every reflection pattern in the GPR data has been assigned to a distinct radar facies.

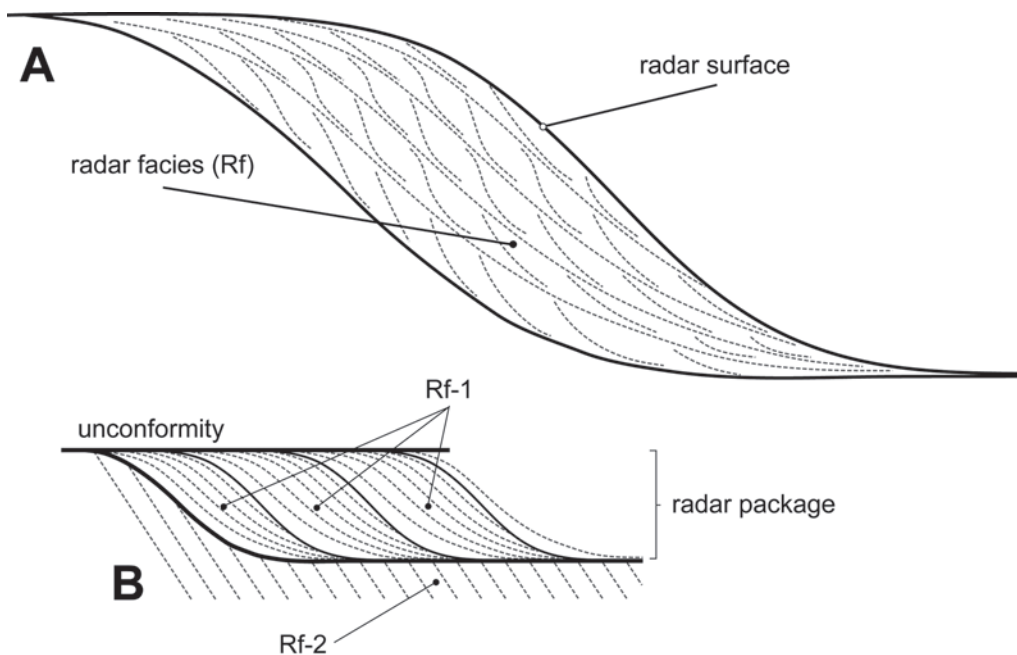


Figure 2.13: **A:** The term „radar facies“ describes a two- or three-dimensional set of reflections with similar character and geometry, limited by surfaces termed „radar surfaces“. Radar surfaces are defined by reflection terminations, and represent a break in the sedimentary sequence. **B:** The term „radar package“ refers to a depositional unit consisting of genetically related strata, as described by the radar facies. Radar packages are bounded by unconformities or their related correlative conformities.

Once the radar-facies architectural elements are defined, the main discontinuities should be outlined in the data (Fig. 2.15). Discontinuities are expressed in GPR data either by reflection terminations or as a single reflection that borders different radar facies. Also a combination of both can occur, if an erosional unconformity separates sediments of different electromagnetic properties. To some extent it is up to the interpreter to decide which are main discontinuities that reflects an important sedimentary process, and which are discontinuities on a smaller scale. The latter then often represent radar-package internal discontinuities, separating similar radar facies.

To link radar facies and sedimentology, appropriate lithofacies data are necessary. These data are commonly obtained by coring and adjacent sedimentological analyses. Coring locations should be chosen with regard to interpretation needs. Therefore, it is recommendable to perform the radar-facies interpretation first, subsequently followed by the decision where to core. The sediment cores should penetrate at least every radar facies once. Also distinct radar surfaces should be a target for coring. For a perfect fit of radar data and litho-facies information, a short radar line is to measure over the planned coring location just before coring. Otherwise the exact localization of the core's position in older radar data will be a challenge.

Description and sampling of the sediment core can follow two different strategies: statistical or facies sampling. Whereas a regular spaced sample interval allows to detect trends that are ascertainable to visual description in the field, it also leads to a huge amount of samples to be analyzed. Another potential problem is the risk of creating samples that overlap discontinuities. On the other hand, irregularly sampling depending on the observed bedding phenomena bears the possibility of overlooking important changes. If the amount of samples is not a criteria, the best choice is a combination of both sampling strategies: regularly, densely sampling over the whole sediment core and additional, irregular spaced samples from both below and above observed discontinuities. Sample interval should be chosen with regard to GPR

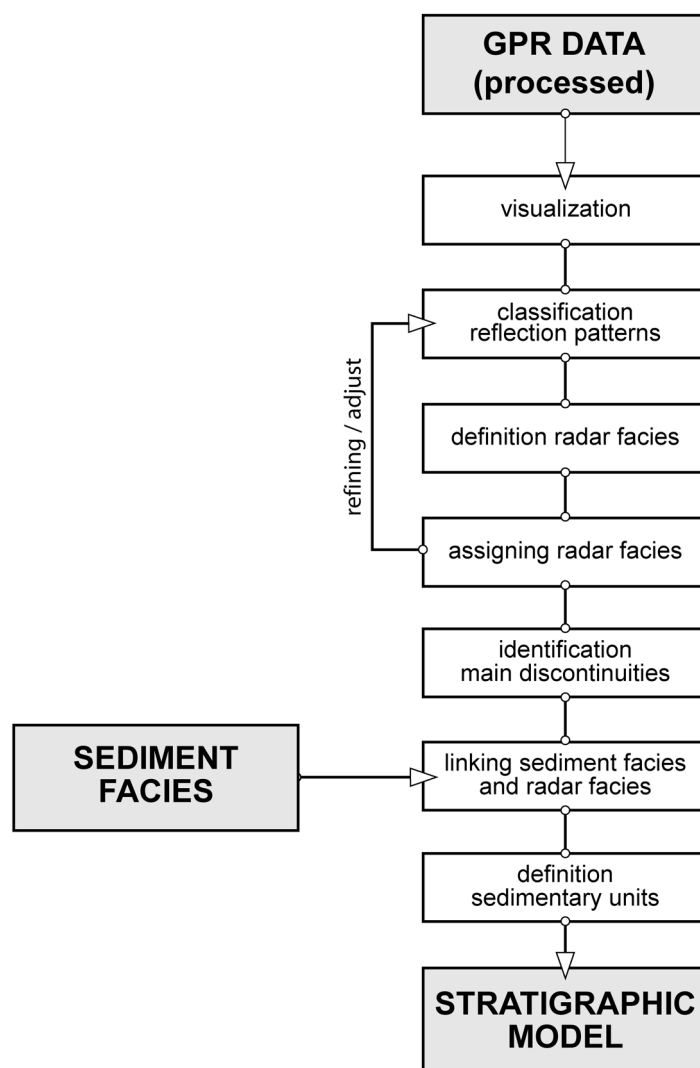


Figure 2.14: Flowchart illustrating the general interpretation flow adopted for GPR data.

resolution. As a raw rule of thumb, the sample interval should not exceed one half of the expected GPR resolution. If the maximal resolution that can be achieved is one quarter of the dominant wavelength (compare Eq. (5)), regularly sampling of at least every 4-5 cm is required (for a 200 MHz antenna and saturated sand).

As fluid content is the most important factor in causing subsurface radar reflections, laboratory analyses should at least contain grain-size analyses to obtain information about changes in grain-size and sorting, which are the controlling factors for pore space in sediments. Furthermore, an estimation of the mineralogical and geochemical composition can provide information about heavy-mineral enrichments and iron precipitations, both of which can be responsible for high amplitude reflections.

In combination with lithofacies data, the previously defined radar-facies architectural elements can be assigned to a distinct sedimentary facies. This allows to map sedimentary units. Depending on radar-line orientation with respect to subsurface structures, the same sedimentary facies can lead to several radar-facies architectural elements. Some authors therefore group their radar facies in elements visible in GPR lines measured parallel, and those visible in lines perpendicular to the predominantly strike direction in the subsurface. Another attempt is presented by Kostic & Aigner (2007), who defined three dimensional GPR elements based on the reflection patterns observed in different oriented 2D-lines.

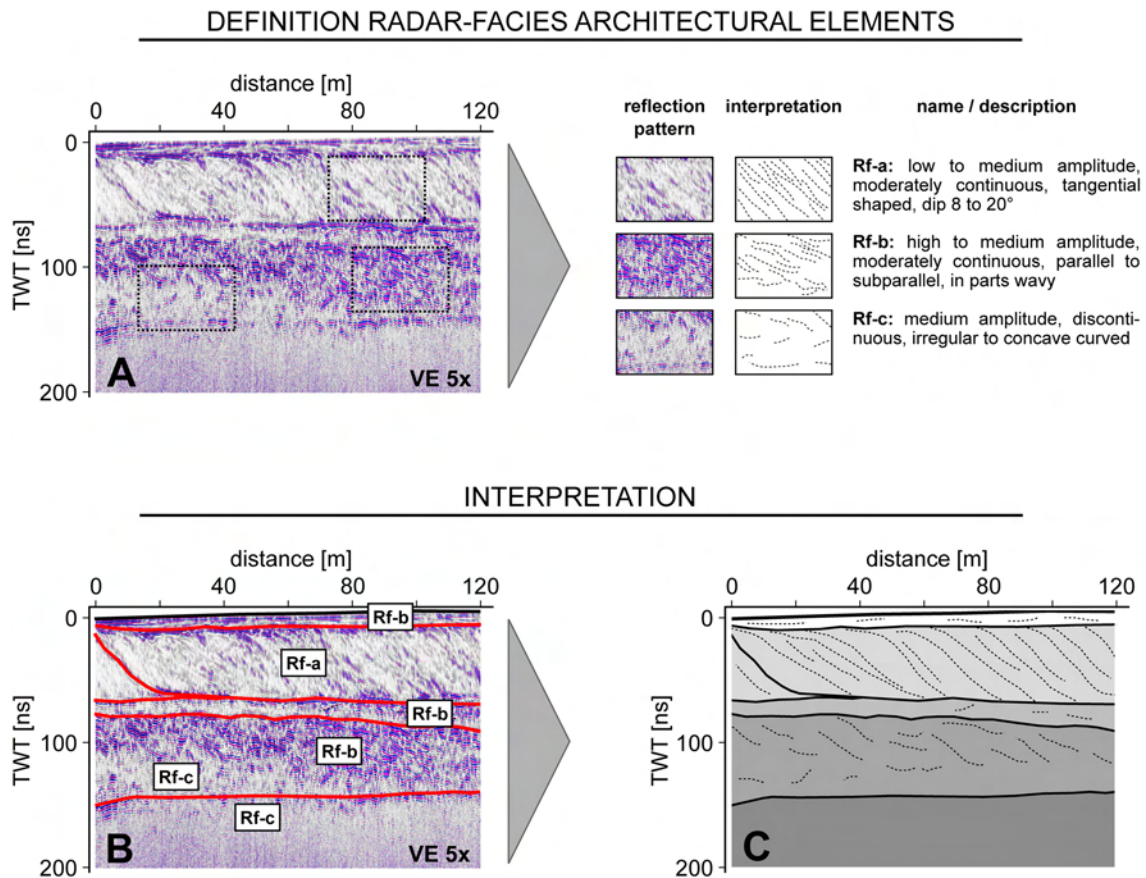


Figure 2.15: The concept of radar-facies interpretation provides a tool for a standardized interpretation of GPR data. **A:** Representative, recurring reflection patterns are selected. They are the base for the definition of different radar-facies architectural elements for the specific survey. Line drawings clarify the reflection pattern, and description gives a short summary of the typical characteristics for each radar-facies architectural element. **B:** Defined radar-facies architectural elements are assigned to the GPR lines and the main discontinuities are defined based on reflection terminations and radar facies. **C:** Radar packages are defined with regard to main discontinuities and interpreted radar facies.

The product of the interpretation process is the stratigraphic model which shows the genetic relationship between the different sedimentary facies deduced from the radar data. Additional data, especially absolute age dates, can enhance the significance of the model and allow to shift the qualitative genetic evolution to a quantitative model.

2.6. Summary and conclusions

The presented method, summarized in Figure 2.16, comprises three different groups of working steps that lead to the stratigraphic model. These are survey, data processing, and data interpretation. As shown in Figure 2.16, results of later working steps can influence earlier steps, so that the method scheme comprises recursive paths. It is also obviously that the stratigraphic model can't be based on GPR data alone, but must also contain the results of sedimentological investigations which provide information about sedimentary facies and absolute age.

It has been shown that the combination of GPR and sedimentological investigations is a powerful tool for sedimentary research in the coastal setting. Beside high-resolution reflection seismic, which is very time consuming, there exists no other technology which enables such fast and high-resolution survey capabilities as GPR. This work

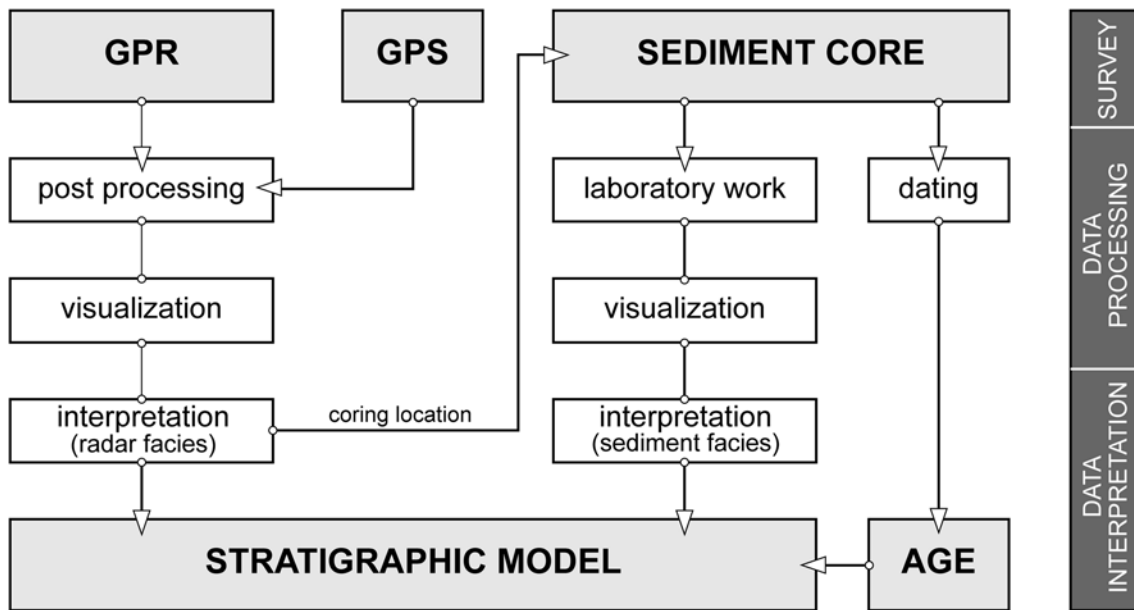


Figure 2.16: Flowchart summarizing the method presented in this work.

also provided a detailed description of potential processing and interpretation steps which can serve as a vade-mecum for future investigations in the coastal setting.

Beside the advantages of the method, the limits and pitfalls are highlighted as well. Near the shoreline, salinization of the ground hinders GPR measurements, clay and silt in the subsurface lead to reduced penetration depth or completely mask deeper strata. And there are several factors that can produce artifacts in the data which have to be identified to avoid misinterpretations.

Only basic principles have been involved and nevertheless, there still remains potential for enhancement: Especially the use of 3D-interpretation techniques, adapted from reflection seismics, bears major potential for future developments, as they enable direct inferences onto the physical sediment properties. These data could be of great value for numeric modeling of coastal environments and for hydrogeological studies.

3

Swash-bar accretion and storm erosion

ABSTRACT

The southern German North Sea coast was shaped by the last post-glacial sea-level rise that caused a significant retreat of the coastline. 5000 years ago, the rate of sea-level rise decreased, providing space for the formation of the Frisian islands which line the coast. This study is focused on Sylt, an island located on the German North Sea coast close to the Danish border. Here, two sandy spit systems developed during the Holocene. Through combining ground-penetrating radar studies and sedimentological investigations based on sediment cores, new aspects on the sedimentary history of this Holocene spit system have been revealed. The data indicates that erosional events alternated with phases of progradation and growth. The welding of swash bars is shown to be the predominant process during progradational phases of the spit system. During these periods, progradation is not restricted to linear growth along the spit axis, but also included a seaward-directed component. Major erosion surfaces, which delimit progradational sediment packages, are interpreted to reflect exceptionally severe storms. The fossilization potential of this sedimentary record was controlled by a positive net long-term sediment balance, and the position of the groundwater table which controlled aeolian deflation. Only with a stable or rising sea level and associated groundwater table position are sediments protected from deflation.

3.1. Introduction

Swash bars are intertidal landward migrating, shore-parallel sediment bodies (King & Williams, 1949; Hine, 1979; FitzGerald et al., 1984; Greenwood et al., 2004; Houser et al., 2006). They typically show high-angle, landward directed planar cross-stratification which is produced through slip-face migration. Although swash bars are a common feature of modern beaches (Hine, 1979; Carter, 1986; Aagaard et al., 1998; Anthony et al., 2004; Masselink et al., 2006; Houser & Greenwood, 2007), sedimentary models of beach depositional systems indicate foreshore seaward-dipping planar bedding as a diagnostic feature of beach sediments (e.g. Thompson, 1937; Clifton, 1969; Davidson-Arnott & Greenwood, 1976; Hunter et al., 1979; McCubbin, 1982; Davis, 1985; Elliott, 1986; Hiroki & Terasaka, 2005). Few authors document swash bars as an architectural element of prograding beaches (e.g. Hayes & Boothroyd, 1969; Massari & Parea, 1988; Nielsen et al., 1988; van Heteren et al., 1998; Gupta & Allen 1999; Bristow et al., 2000).

The aim of this study, which is focused on the German North Sea island of Sylt, is to investigate the sedimentary structures of a Holocene barrier spit by means of ground-penetrating radar (GPR) combined with sedimentological analyses of sediment cores. The data reveal the internal sedimentary architecture of the spit with a high spatial resolution and allow the reconstruction of the controlling sedimentary processes. Swash bars are the dominant accretional element of the spit deposits of Sylt. We present a sedimentological model that shows how the spit formed through westerly- and northerly-directed progradation, episodically interrupted by erosional events triggered by storms.

3.2. Geological setting

Sylt belongs to the North-Frisian Islands (Fig. 3.1A). It is located 15 km off the German mainland coast, at the border with Denmark, and contains a core of Saalian and Elsterian moraines (Fig. 3.1B), as well as re-worked tertiary sediments (Gripp & Becker, 1940; Schwarzer, 1984). Large sandy spit systems (Fig. 3.1B) developed at the northern and southern ends of the island's core during the Holocene (Gripp & Simon, 1940; Dietz & Heck, 1952a). According to the definition of Hayes (1979), the island is currently subjected to a semidiurnal lower to upper mesotidal regime with a tidal range of 1.8 – 2.2 m (Backhaus et al., 1998). Westerly winds between 248° and 315° are dominant (Müller, 1980; Ahrendt, 2001). On the landward side of the northern spit there is a broad tidal bay (the „Sylt-Rømø Basin“) which is part of the Wadden Sea. The Sylt-Rømø Basin is connected to the North Sea by a tidal inlet (the „Lister Tief“) and bordered to the North and to the South by artificial dikes, which connect the islands of Sylt and Rømø to the mainland.

The thickness of the Holocene sediment cover in the German Bight reaches a few meters only near the coast of Sylt (Hoffmann, 1971; Köster, 1974). In terms of sequence stratigraphy, the system is accommodation-dominated. Sediments deposited along the coast consist of reworked glacial and Holocene sediments (Anwar, 1974). The stratigraphy of the southern spit of the island is well-known (Gripp, 1968; Hoffman, 1974), but knowledge of the sedimentary architecture of the northern spit is based almost completely on a series of cores drilled in the first third of the 20th century. Based on these data, Gripp & Simon (1940) provided the widely accepted stratigraphic model for this part of the island. Reconstruction of the paleogeographic

evolution in historical times, as presented by Newig (1980, 2004) and Ahrendt & Thiede (1992), relies on historical maps and includes major uncertainties, as the first map based on trigonometric measurements dates back to the year 1793 (Ahrendt & Thiede, 2001).

Figure 3.2 shows a north – south striking cross section of the spit according to Gripp & Simon (1940) with a succession of Pleistocene and Holocene sediments onlapping towards the South onto the Pliocene sands and the ground moraine deposits

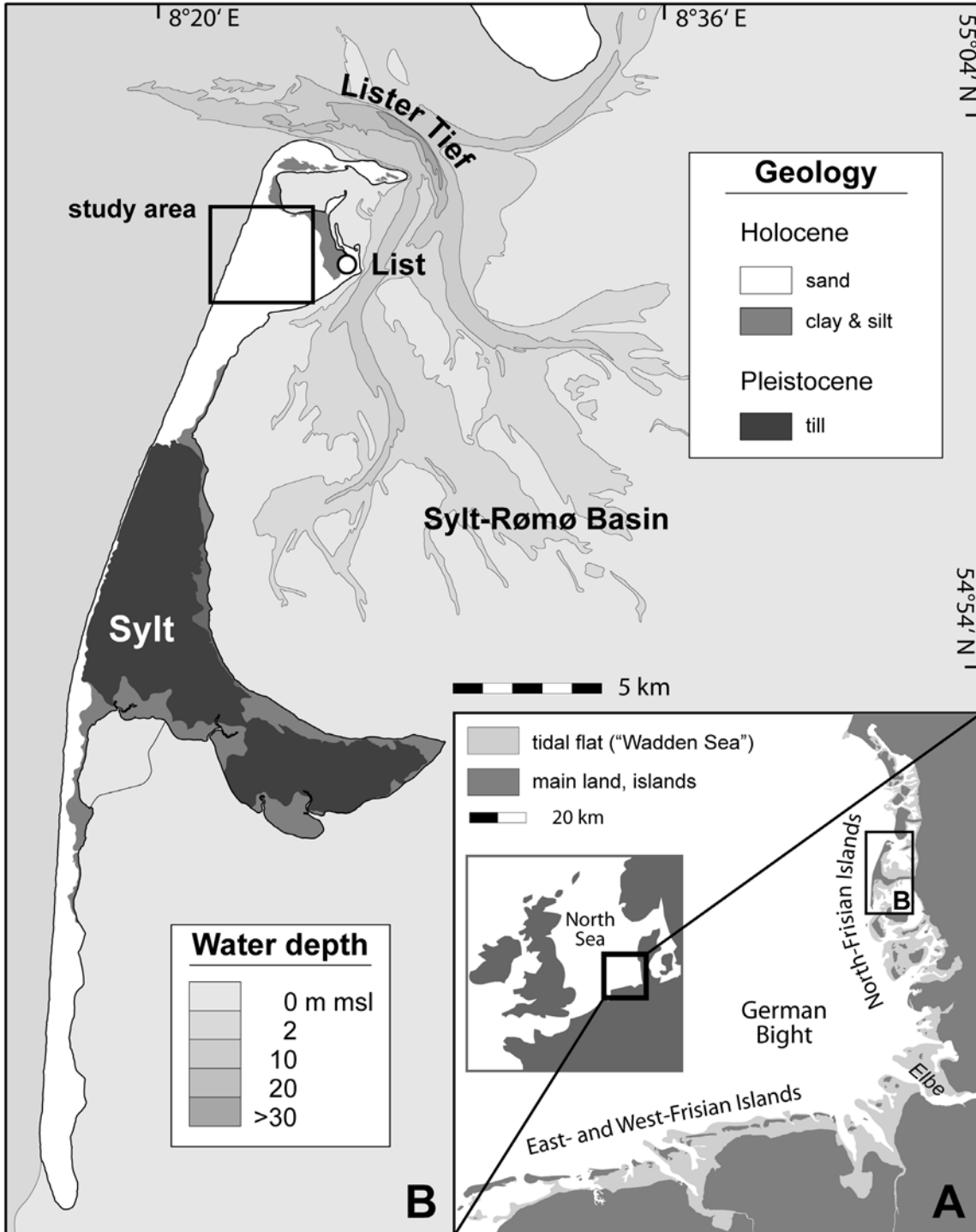


Figure 3.1: **A:** Overview of the islands along the southern North Sea coast with location of Sylt. Inlet map shows adjacent regions of north-western Europe. **B:** Simplified geological map of Sylt after Dietz & Heck (1952b) showing the island's core which consists mostly of Pleistocene moraine deposits, and the two spit systems which extend to the North and to the South. The square marks the position of the study area. Bathymetric data are from Neide (1977a, 1977b).

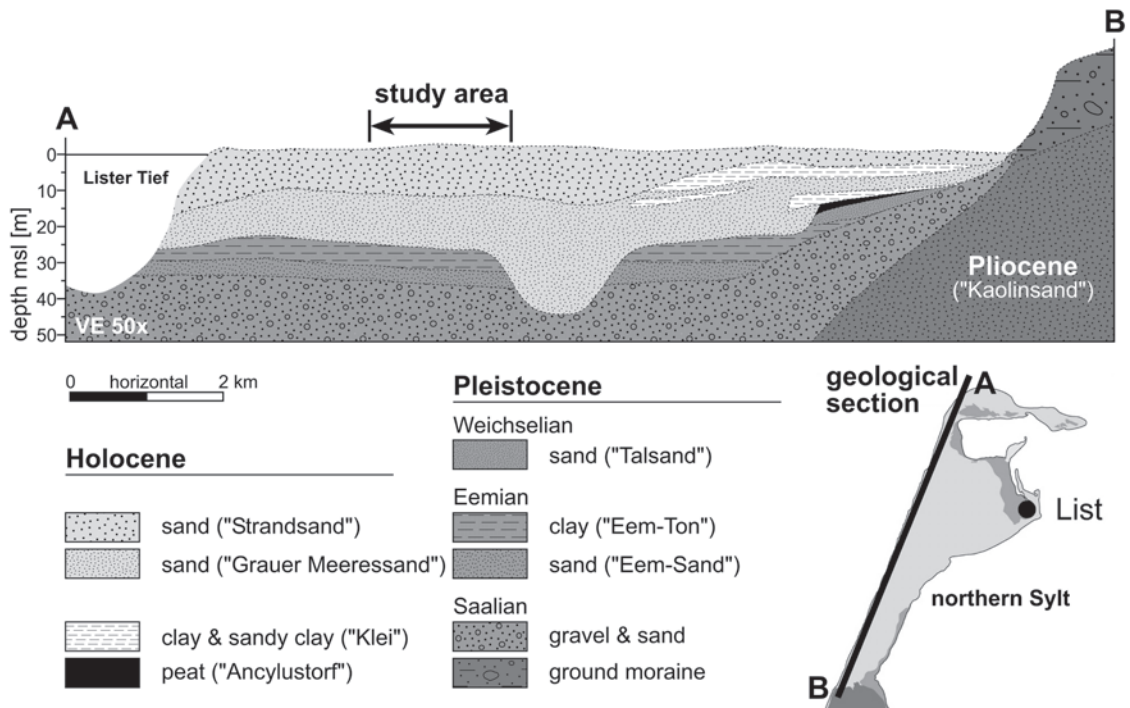


Figure 3.2: Geological cross section of northern Sylt based on sediment cores, after Gripp & Simon (1940). The position of the line is shown in the small inset map. The spit system consists of sand with intercalations of peat and clay. Sediments below the Holocene succession are clays, sands and gravels of Pleistocene age. Note the pre-Holocene sediments of the island's core.

of the island's core. Holocene sediments unconformably overlie Eemian clay, Elsterian ground moraines, sands and gravels of Saalian age, as well as Weichselian sands. The base of the Holocene is located at a depth of 20 to 25 m below mean sea level (bsl), with the exception of an incised valley fill, where the Holocene sediments reach down to a depth of around 45 m below recent mean sea-level (Bayerl & Higelke, 1994; Ahrendt & Pesch, 2001).

Gripp & Simon (1940) distinguish between two Holocene marine sand units, based on a distinct color change from greenish-gray in the lower part of the succession („Grauer Meeressand“ unit) to yellow in the upper part („Strandsand“ unit). Several clay layers and a peat layer occur interbedded in the lower sand unit near the island core. Such horizons have been described for several Holocene successions along the North Sea coast, and are interpreted to reflect short-term sea-level fluctuations (Gripp & Simon, 1940; Hoffmann, 1980; Bartholdy & Pejrup, 1994). The color change from dark grey to yellow is attributed to the oxidation of pyrite, and is not thought to represent a primary sedimentary contact (Gripp & Simon, 1940). The marine sands are interpreted as deposits of a spit which stepped back during its northward growth, in response to sea-level rise.

The youngest sedimentary unit of northern Sylt consists of eolian dune sands. Based on a geomorphological approach, this system was investigated by Priesmeier (1970). He assumed that dune growth and migration was cyclic: every 300 years a new generation of sand dunes accumulates along the western coast and subsequently starts migrating eastward. After 900 to 1000 years, the dunes traversed the northern spit and reach the tidal bay on the leeward side of the island. The marine and eolian Holocene sediments of northern Sylt are up to 70 m thick. Today, the surface consists of dunes, mainly stabilized by plants, and broad interdune flats which are mostly deflated down to the groundwater table. During the wet winter months, ephemeral freshwater ponds develop.

Only a few absolute age assignments exist for the deposits of the northern spit of Sylt. According to Harck (1974), the peat in the lower marine sand unit (Fig. 3.2) is assigned to the Boreal period (9000 – 8000 BP). A clay layer that interfingers with the upper marine sand unit was drilled north of List at a depth of 2 – 3.5 m bsl. It dates back to 3640 – 3750 BP (Bayerl et al., 1998a). Stone tools found on northern Sylt point to a Neolithic age for this part of the spit (Harck, 1972, 1974). In northern Germany, the Neolithic period is dated back to approximately 6500 – 4200 years BP (Behre, 1995; Litt et al., 2001).

Based on geological, archeological, and hydrographical data, Behre (2003, 2004, 2007) presented a curve for the relative post-glacial sea-level rise. It shows a rapid sea-level rise with a rate of 1.25 m/100 a back to 7000 years ago, when sea level reached a position 12 m below recent sea level. Between 7000 and 3400 years BP, the rate decreased to 0.18 m/100 a and sea level reached 2 m below the present one. Between 3400 and 3000 years BP sea level dropped by 2 m. The time between 3000 a BP and today is characterized by a series of small sea-level rises and falls of between 0.5 and 1.5 m.

3.3. Methods

3.3.1 Ground-penetrating radar (GPR)

The stratigraphic architecture of the spit was analyzed by means of GPR surveys and shallow sediment cores. GPR is a non-invasive method which is based on the transmission of high-frequency electromagnetic pulses and the reception of energy that is reflected back from subsurface reflectors (Bristow et al., 1996; Blindow et al., 1997; Neal, 2004). Comparable to the method of seismic reflection which is based on acoustic impedance contrasts within the subsurface, GPR allows the detection of electrical discontinuities in the shallow subsurface. For the GPR surveys, a Geophysical Survey Systems Inc. radar system SIR-3000 was used in combination with antennas with frequencies of 20, 40, 80, 100, 200, and 400 MHz. Generally penetration depth in geological materials increases with decreasing antenna frequencies (Jol, 1995; Smith & Jol, 1995; Neal, 2004). However, in this study, frequencies lower than 100 MHz did not yield an improvement in penetration depth. This was probably the result of pore-water salinity increasing with depth, which caused higher signal attenuation. GPR lines presented here were all measured with a 200 MHz antenna.

To obtain optimal ground penetration, with minimized tilting effects caused by non-vertical radar beam orientation, GPR surveys were restricted to more or less flat surfaces. Slope angles exceeding 6 to 10° were avoided to prevent uncorrectable distortions of underground geometries (Lehman & Green, 2000). The wide interdune flats on Sylt allowed for individual line lengths up to 800 m. The vegetation consists of shrubs with *Impetrum nigrum* (black crowberry), *Pyrola rotundifolia* (round-leaved wintergreen), and *Oxycoccus macrocarpon* (cranberry). Signal ringing occurred in GPR lines measured during the winter months, when an ice layer covered the surface, and during spring surveys when plant activity was increased. This is probably a consequence of higher ion-bearing liquid concentrations in the roots and stems. At the same time, signal attenuation in the uppermost soil horizon was higher. In both cases, it was possible to eliminate the interference during the post processing using deconvolution algorithms.

Radar data were collected by using a survey wheel as distance trigger. The space in-between shot-points (trace increment) was set to 5 cm. 2048 samples were collected at each shot providing a wide scope for later processing. Manufacturer settings for frequency filtering and no stacking were applied during data collection.

Frequency filtering, down-the-trace, and trace-to-trace stacking, using the software ReflexW (Sandmeier, 2006), were applied to enhance the signal-to-noise ratio. Migration was performed by the fk-migration algorithm after Stolt (1978), which allow for a fast migration of 2D lines based on a constant velocity. The aim of the migration process is to trace reflected energy back to their origin, and thus to restore true reflector shapes.

A topographic correction was applied to each line in order to restore different terrain altitudes, and therefore reflector geometries. The data required for the topographic correction were obtained using a differential global-positioning system (either Ashtek ProMark II or Leica GPS 1200). Vertical accuracy of the Ashtek and Leica systems is up to 0.15 m, and 0.01 m respectively (manufacturer specifications).

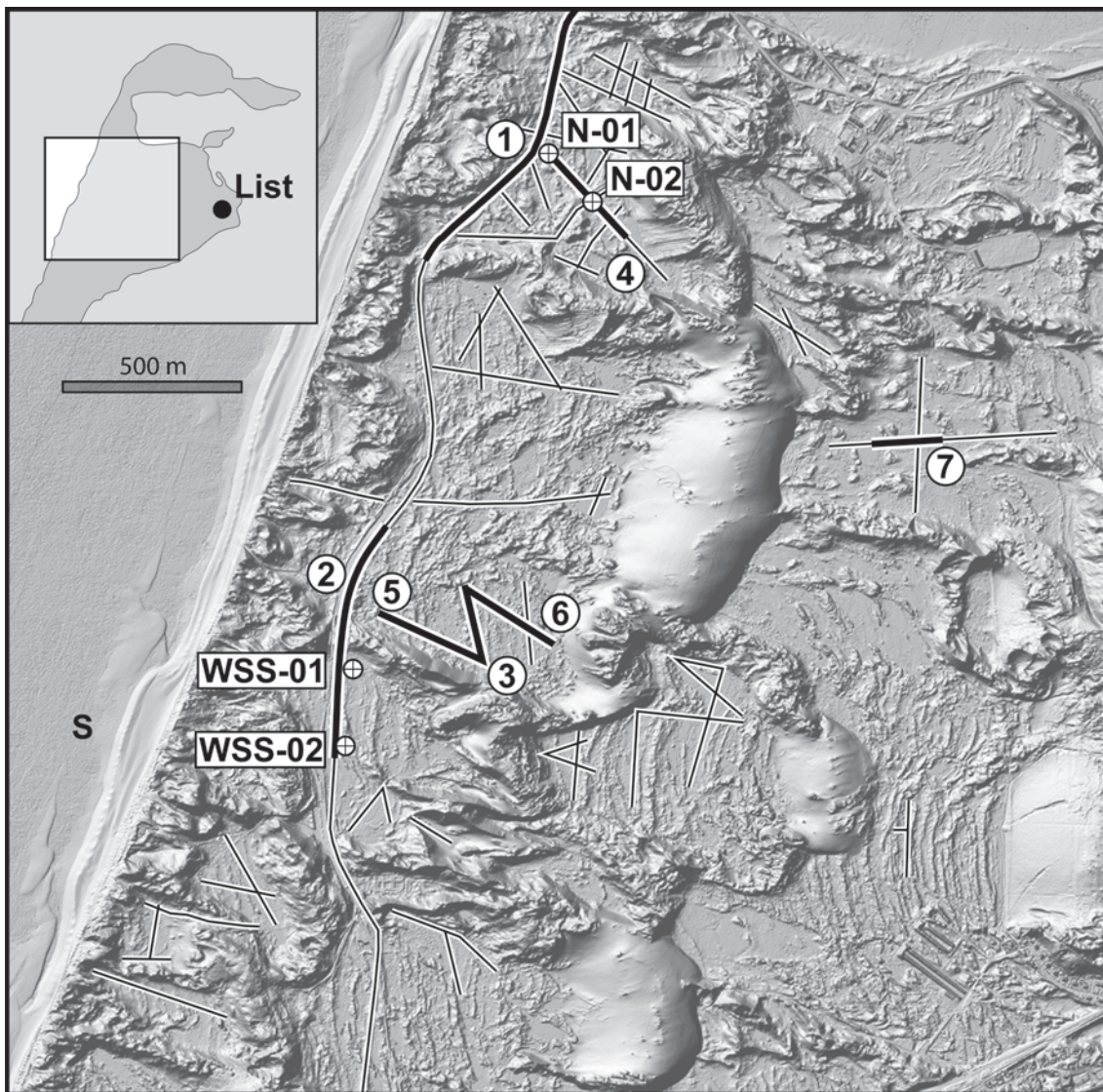


Figure 3.3: Shaded relief of the study area showing the position of radar lines and sediment cores considered for this work. Bold lines and numbers refer to line segments discussed in the text. The map is based on a digital terrain-model which has a cell size of 1 m and a vertical accuracy of 0.2 m (data provided by Amt für ländliche Räume, Husum). Data were obtained by means of airborne Lidar during low tide, which reveals images of the system of recent swash bars along the coast (S).

Common midpoint measurements are generally used to obtain a radar-wave velocity model of the subsurface. This method failed in the working area because prerequisites were not fulfilled, such as a laterally largely homogenous substrate with nearly sub-horizontal strata or occurrence of a shallow reflector which can be traced over at least a few tens of meters (Kruk et al., 1999; Jol & Bristow, 2003). The local velocity of the radar waves in the sediments was determined by the analysis of diffraction hyperbolas and direct correlation of sediment core data with radar data. Values of radar-wave velocities range between 0.055 and 0.065 m/ns, with an average around 0.06 m/ns in the water-saturated sands. In the dune sands which are located above the groundwater table, the velocity range was between 0.10 and 0.15 m/ns, with an average of approximately 0.12 m/ns. These values correspond to radar-wave velocities determined in previous studies for saturated and dry sands respectively (Blindow et al., 1997; Jol & Bristow, 2003). Some of the GPR lines used in this study were measured on an up to 3 m thick road embankment. The average radar-wave velocity of this material was approximately 0.12 m/ns.

3.3.2 Sediment cores

To link ground-penetrating radar results with sedimentological data, vibracores were drilled down to a depth of 6.50 m below the surface at selected positions along the radar lines (Fig. 3.3). For the first meter a 50 mm open core probe was used, and a 36 mm gouge auger for the remainder. A visual analysis of color, grain size, sorting and rounding was performed in the field. For further laboratory analyses the cores were subsampled every 5 cm (1 cm thick samples). A Quantachrome Cilas 1180L laser diffraction particle size analyzer was used for grain-size analyses. Prior to analysis, samples were treated with dilute hydrogen peroxide and acetic acid to dissolve the non-siliciclastic content. The Cilas 1180L provides a size range from 0.04 to 2500 μm . Grains coarser than 2000 μm were removed from samples by a standard sieve, prior to measuring. Grain-size classes and sample statistics were performed by means of the computer program Gradistat (Blott & Pye, 2001) as well as self-programmed routines. All statistical grain-size parameters mentioned in the text are based on the graphical method by Folk and Ward (1957).

3.3.3 Interpretation of GPR data

Sedimentary sequences contain a hierarchy of depositional units, starting from individual laminae to whole sedimentary basin fills (Campbell, 1967). Therefore, concepts of interpreting seismic data can be directly adopted for the interpretation of GPR sections which image structures on a much smaller scale than reflection seismics (Neal et al., 2002; Neal, 2004). Gawthorpe et al. (1993) introduced a complete concept of radar stratigraphy, based on the interpretation of reflection terminations. Taking into account the often very complex reflection configuration of GPR sections, Bristow (1995) used a more qualitative approach to interpret sedimentary structures in shallow marine sand stones of the Lower Greensand formation, Southern England.

Adapting the concept of seismic interpretation introduced by Mitchum et al. (1977) to the interpretation of GPR data, the term „radar facies“ describes a two or three-dimensional set of reflections bordered by surfaces termed „radar surfaces“. According to Bristow et al. (2000), the term radar facies is summarized as ‘repeated packages of reflections with similar character and geometry’. In all, ten different radar facies

(Rf) were identified in the radar sections (Fig. 3.4). The identified radar facies were divided into three groups. Whereas the first group contains radar facies that display inclined reflections, the second group consists of those that exhibit predominantly horizontal reflections. In the third group, irregular reflections dominate. The description of reflection geometries follows the terminology summarised by Neal (2004), after Campbell (1967), Mitchum et al. (1977), and Allen (1982). For interpretation of GPR data, lines with different vertical exaggeration were used. Major unconformities and sediment packages are better visible on higher exaggerated lines. Whereas the interpretation of internal sediment structures, which are important for the determination of facies and depositional environment, is only possible on less vertical exaggerated GPR lines. All dip angles provided in this work are corrected for vertical exaggeration.

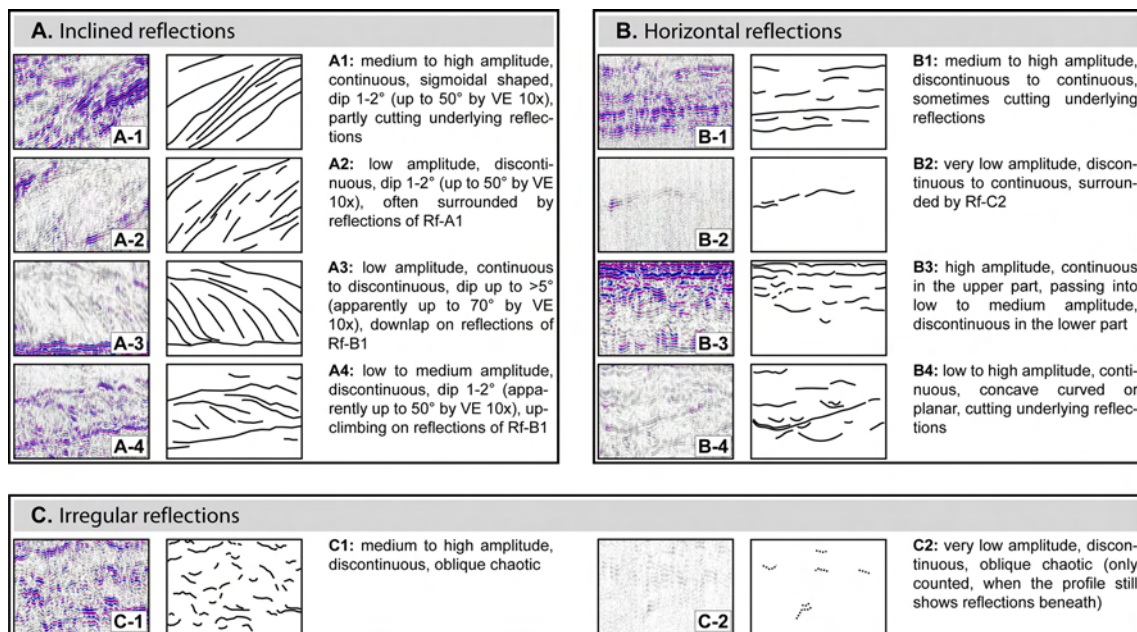


Figure 3.4: Radar-facies architectural elements identified in the radar sections. Based on geometrical criteria, the radar facies were divided into three categories: inclined reflections, horizontal reflections and irregular reflections. Please note that radar data are provided with a vertical exaggeration of 10-times.

3.4. Results

The southern boundary of the study area (Fig. 3.1B) was defined by the occurrence of a shallow intercalated clay which adversely affected the image quality of the GPR lines. These clays correspond to those known from the „Grauer Meeressand“ unit (Gripp & Simon, 1940) (Fig. 3.2). To the North, the area was limited by the occurrence of salty groundwater close to the surface.

In the study area, the radar data show good resolution down to 200-300 ns two-way traveltime (TWT) which corresponds to 6 – 9 m. A maximum penetration depth down to 21 m (700 ns TWT) was achieved. The latter corresponds to the assumed thickness of the freshwater aquifer on northern Sylt, namely 22 m (Dietz & Heck, 1952a). Bressau (1984), however, assumed an extension of the freshwater aquifer down to 45 m bsl. Near the shoreline, the contact between freshwater and saltwater rises due to increasing salinization of the pore-water. The transition from freshwater to saltwater is indicated in the radar data by a narrow, but diffuse zone, which leads to total signal attenuation caused by the high conductivity of the marine saltwater. The depth of this contact is not stable, as the freshwater lens of the island stands in

a hydrodynamic equilibrium with the saltwater beneath. Radar observations show a vertical shift of approximately 0.5 m on the landward side of the island and of up to 1.0 m on the seaward side during one tidal cycle.

Based on their quality and position in the study area, seven radar lines were chosen to document the subsurface sediment geometries and detailed sedimentological data were provided with four vibracores. The positions of the radar lines and cores are shown in Figure 3.3. All depth-readings in the GPR lines refer to German mean sea-level (msl), which for northern Sylt is approximately 0.80 m below mean high tide (Behre, 2003). For completeness, the TWT in ns is also indicated for each profile.

3.4.1 Radar sections parallel to the recent shoreline (GPR lines 1 – 3)

The longest radar section is oriented parallel to the recent shoreline of the spit. It was measured on a concrete-slab road without asphalt cover. The road is partly bearing on an embankment which is elevated up to 3 m above the surrounding land. Two segments of this line are depicted in Figures 3.5 and 3.6. GPR Line 3 (Fig. 3.8) is oriented more or less parallel to the road profile and was measured on natural ground.

GPR Line 1

GPR Line 1 has a maximum ground penetration of 280 ns TWT (Fig. 3.5A). This corresponds to a depth of 9 m. The thickness of the road embankment, which has a higher radar-wave velocity than the sediments below, varies between 20 and 50 ns TWT.

Sediments down to 3 m bsl are bundled into packages (Fig. 3.5B). Each package is limited by high-amplitude reflections dipping with 1-2° between 2 m above mean sea level (asl) and 2 m bsl. Dip is less than 0.5° in greater depths (Rf-A1). The packages have low-amplitude internal reflections (Rf-A2) which exhibit concordant bedding and northerly-directed downlaps onto the reflections that limit the package or are nearly transparent (Rf-C2). In some packages, lenticular bedding occurs. In the uppermost part of the GPR line there are cut-and-fill structures (Rf-B4).

There exist four major erosion surfaces in the line, which are indicated by bold lines in Figure 3.5B. These surfaces truncate underlying strata and are expressed by either Rf-B1 or Rf-B2 reflections. One of these erosion surfaces forms a 200 m wide erosional incision between 3 and 7 m bsl. Reflections above the erosion surfaces often show downlap configuration.

GPR Line 2

The GPR data of Line 2 (Fig. 3.6A) show reflections down to a depth of 320 ns TWT, which in this case corresponds to 10.5 m below the surface. Figure 3.6B shows the dominant pattern, represented by northward-dipping, medium to high amplitude sigmoidal reflections (Rf-A1). These reflections separate bodies which are transparent (Rf-C2) or show weak northward-dipping reflections (Rf-A2). At the top of these bodies, there are cut-and-fill structures (Rf-A4). The sigmoidal reflections of Rf-A1 flatten out at a depth of 2 to 3 m bsl and can be traced for up to 200 m. Horizontal spacing in-between individual sigmoidal reflections varies from 3 to 80 m. At a depth of around 1 m bsl, some sedimentary bodies (Rf-A4) occur at the bottomsets of the sigmoidal reflections, which exhibit an internal layering with dips toward the South, i.e. contrarily to the sigmoidal reflections.

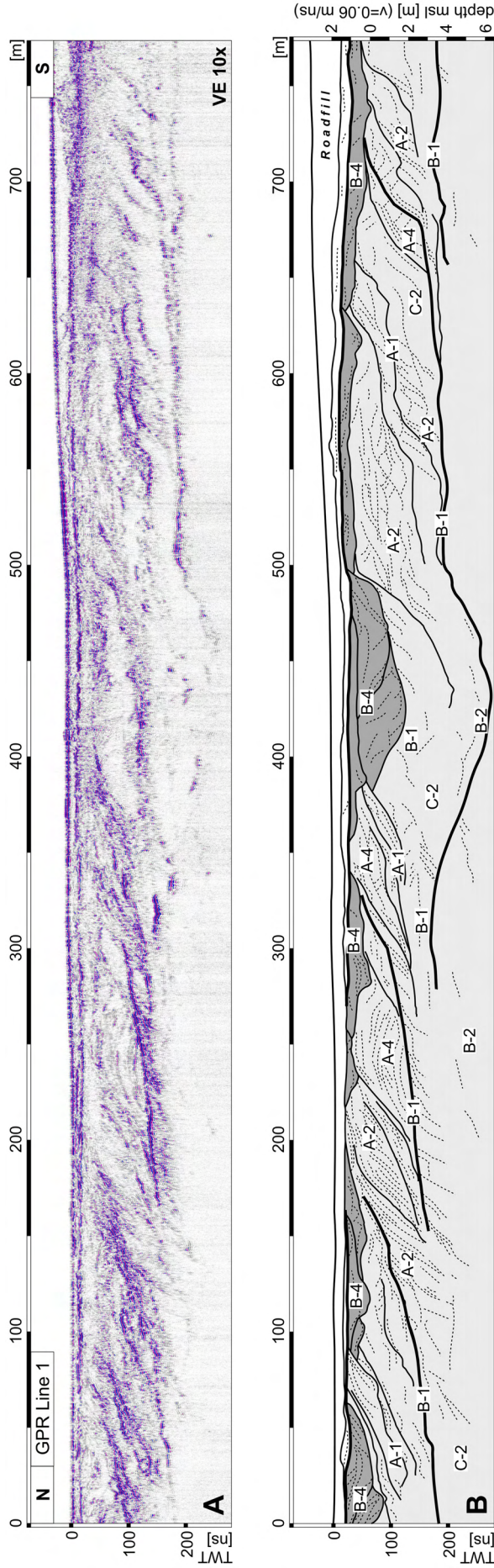




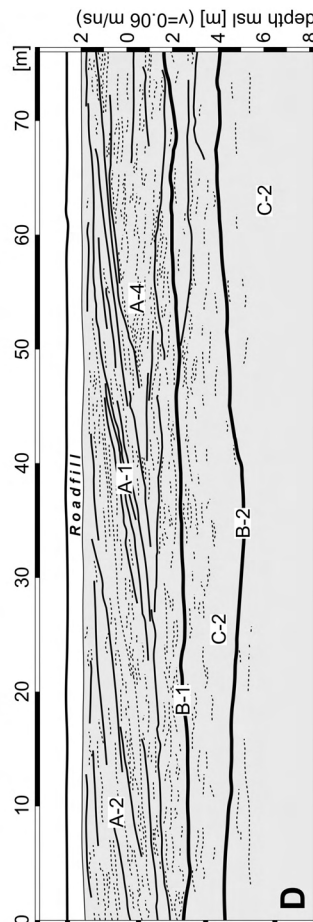
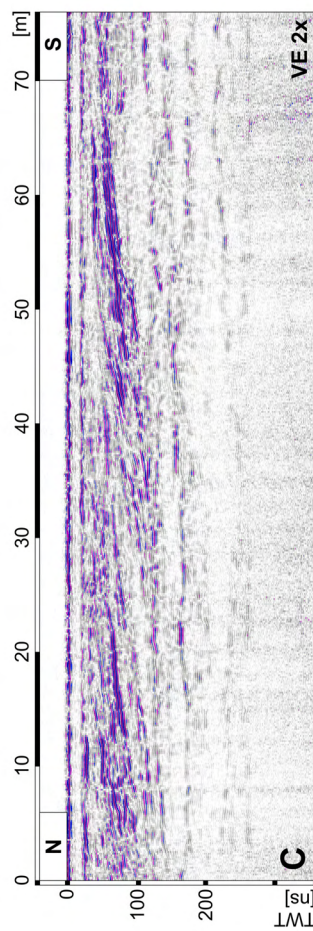
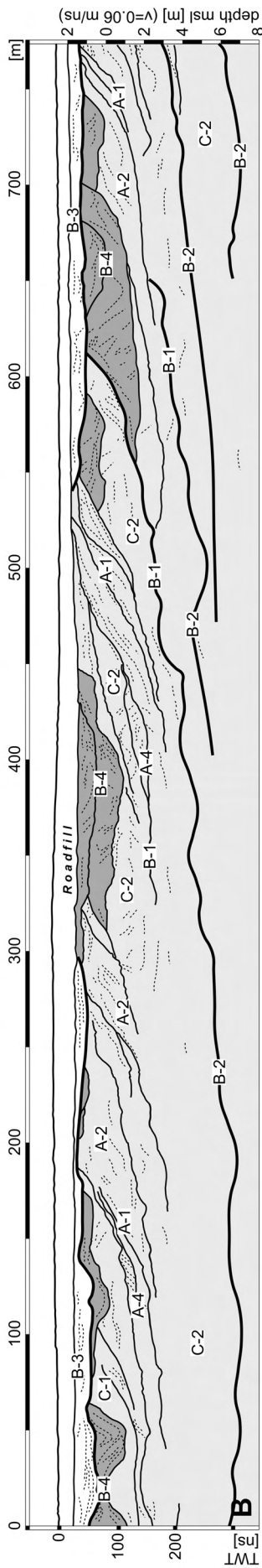
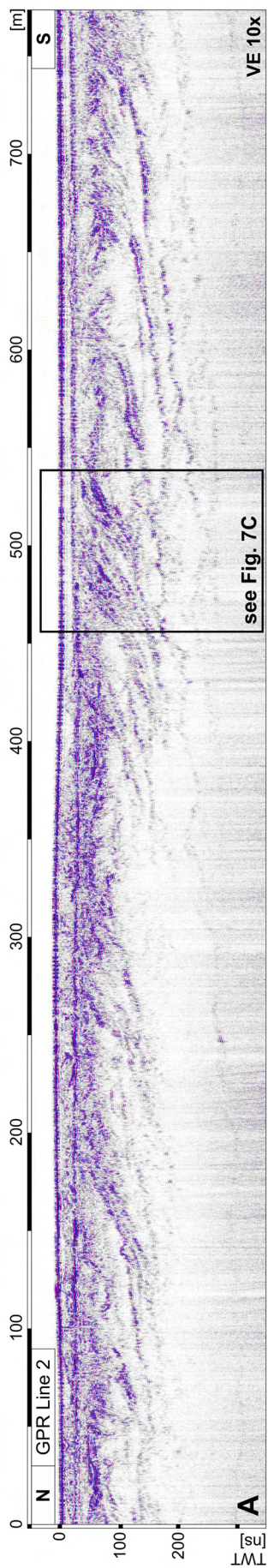


Figure 3.5: A: GPR Line 1, measured on the northern segment of the road. For exact location see Figure 3.3. The left-hand axis presents the TWT in ns, the right-hand axis provides the position of the GPR line relative to msl in meters. A mean radar-wave velocity of 0.06 m/ns was assumed for depth correction below 2 m asl. Please note the vertical exaggeration of radar line. B: Line drawing and interpretation of the radar data provided in Figure 3.5A. Solid lines represent erosion and bounding surfaces, dashed lines trace internal structures and subordinate planes. Background colors indicate different sedimentary units accordingly to the legend. Note that the sedimentary succession is banded into sigmoidal packages and shows a northerly-directed progradation. See Figure 3.4 for radar-facies definition.

Figure 3.6 (next page): A: GPR Line 2, measured on a segment on the road, towards the South of GPR Line 1. For exact location see Figure 3.3. For description of scales and applied radar-wave velocity see Figure 3.5. B: Line drawing and interpretation of the radar data provided in Figure 3.6A. Note that the reflections are banded into sigmoidal packages that show northerly-directed progradation. This corresponds to the reflection patterns previously shown in GPR Line 1. C: One segment of the GPR Line 2 shown with low vertical exaggeration (2x). The location of this detail view is marked in Fig 6A as box. D: Line drawing and interpretation of the radar data shown in Figure 3.6C, revealing internal structures of the sigmoidal bodies. These structures mostly show a subhorizontal dip or a dip contrarily to that of the high amplitude reflections which bound the package. See Figure 3.4 for radar-facies definition and Figure 3.5 for key to interpreted sedimentary units.

Legend (valid for all GPR lines)

-  young eolian cover, in parts with soil development
-  wash-over system with cut and fill structures, interpreted as scour channels, and landward directed wash-over sediments
-  foreshore and shoreface deposits: welded swash bars down to a depth of approximately 3 m below msl, and fine grained sediments in greater depths
-  older spit sediments, undifferentiated



In addition to the Rf-A1 reflections, a second type of sigmoidal reflection occurs. These reflections have a spacing of several hundreds of meters, and reach down to a depth of 7 m bsl. Dip is less than 1° down to a depth of 5 m bsl, and 0.25° to sub-horizontal in greater depths, where these reflections can be traced for up to 1000 m. They are of medium amplitude in the dipping part (Rf-A1) and of medium to low amplitude in the sub-horizontal part (Rf-B1 and Rf-B2).

A 75 m wide segment of the GPR Line 2 is depicted in Figure 3.6C. Down to 2 m bsl, medium to high amplitude reflections (Rf-A1) dip to the North and bound packages of low amplitude reflections (Fig. 3.6D). These low amplitude reflections are subhorizontal (Rf-A2) or dipping with less than 1° to the South (Rf-A4), and have a wavy to concave shape. The lower part of the line exhibit only low amplitude reflections, showing a wavy to sub-parallel configuration (Rf-B1, Rf-B2 and Rf-C2).

Two sediment cores were taken at a distance of approximately 5 m from where GPR Line 2 was measured. Core WSS-01 was located 739 m, and Core WSS-02 411 m away from the starting point of the radar line 2 (Fig. 3.3). Characterizing grain-size parameters for the two cores are summarized in Table 3.1. Core WSS-01 is 650 cm long (Fig. 3.7A), Core WSS-02 485 cm (Fig. 3.7B).

Figure 3.7A shows the mean grain size based on the graphic method (Folk and Ward, 1957) versus depth in sediment core WSS-01. There is a coarsening-upward trend up to 380 cm core depth (1.80 m bsl). This is followed by a relatively stable interval of slightly coarser sediments. From about 100 cm core depth (1.00 m asl), there is a fining-upward trend. Three significant zones of finer sediments occur in the lower part of the core at depths of 635, 553, and 433 cm (4.35, 3.53, and 2.33 m bsl). These are the finest grained intervals in the core.

Figure 3.7B shows the mean grain size based on the graphic method (Folk and Ward, 1957) versus terrain depth of sediment core WSS-02. Trendwise, this core largely resembles Core WSS-01 at a slightly higher mean variability. Five finer zones at 363, 308, 173, and 53 cm core depth (1.63 and 1.08 m bsl, 0.27 and 1.47 m asl) and at the surface punctuate the upper 400 cm of this core. Core WSS-01 does not have these corresponding finer zones.

In both cores sorting and mean grain size is linearly correlated with coarser sediments being better sorted than finer sediments. As the cores WSS-01 and WSS-02

Core		Mean grain size (phi)					
ID	length	maximum		minimum		average	
N-01	580 cm	1.69	medium sand	4.41	very coarse silt	2.06	fine sand
N-02	480 cm	1.66	medium sand	2.66	fine sand	1.81	medium sand
WSS-01	650 cm	1.56	medium sand	2.77	very fine sand	1.77	medium sand
WSS-02	485 cm	1.57	medium sand	3.47	fine sand	1.84	medium sand

Core		Sorting (phi)					
ID	length	maximum		minimum		average	
N-01	580 cm	0.55	moderately well sorted	2.56	very poorly sorted	0.96	moderately sorted
N-02	480 cm	0.53	moderately well sorted	1.69	poorly sorted	0.69	moderately well sorted
WSS-01	650 cm	0.46	well sorted	1.84	poorly sorted	0.72	moderately sorted
WSS-02	485 cm	0.57	moderately well sorted	2.27	very poorly sorted	0.85	moderately sorted

Core		Skewness of the frequency distribution (phi)					
ID	length	maximum		minimum		average	
N-01	580 cm	-0.13	coarse skewed	0.75	very fine skewed	0.36	very fine skewed
N-02	480 cm	0.11	fine skewed	0.67	very fine skewed	0.25	fine skewed
WSS-01	650 cm	0.16	fine skewed	0.66	very fine skewed	0.31	very fine skewed
WSS-02	485 cm	0.30	very fine skewed	0.62	very fine skewed	0.36	very fine skewed

Table 3.1: Characteristic grain-sizes parameters for sediment cores presented in Figure 3.7.

were not taken directly on the GPR line, the correlation between the GPR reflections and the granulometric data is less than in the cores N-01 and N-02 (Figs. 3.7C, 3.7D). For all cores, no linear correlation between GPR reflections and granulometric data could be observed. As semiquantitatively investigated with a magnetic separator, there is, however, a certain correlation between the strength of reflections and the abundance of dark opaque ferromagnetic minerals. Intervals enriched with dark opaque minerals show stronger GPR reflections.

GPR Line 3

This line, shown in Figure 3.8A, has a maximum ground penetration down to 400 ns TWT which corresponds to 12 m below the surface. The uppermost part of the line

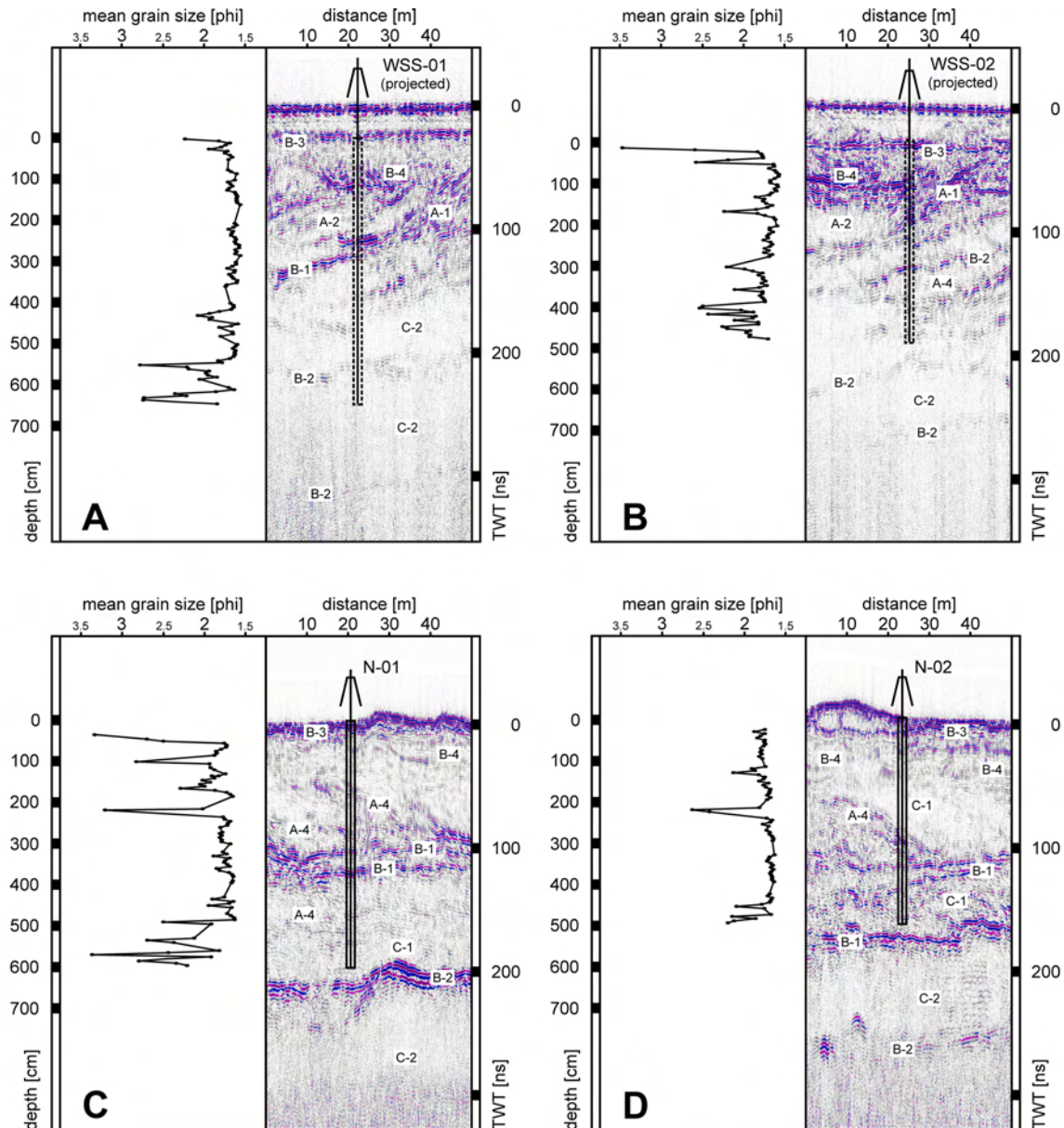


Figure 3.7: Mean grain size and associated radar-facies architectural elements of the vibracores taken at selected locations along the radar lines. Presented cores are: **A:** WSS-01, **B:** WSS-02, **C:** N-01 and **D:** N-02. For core locations see Figure 3.3. Left side of each diagram shows the mean grain size (in phi) plotted against core depth. The right side shows part of the associated radar line and the depth is in ns TWT. Horizontal length of given radar section is 50 m each, vertical exaggeration 10-times. Core position and recovered length of core are indicated. Identified radar facies are labeled at selected positions following the radar-facies code provided in Figure 3.4. Please note that the positions of the cores WSS-01 and WSS-02 are projected (indicated by dashed lines in Figs. 3.7A, 3.7B), because core locations are situated 5 m off the road where related radar lines were taken.

contains Rf-B3 reflections. An unconformity at a depth of approximately 1 m asl forms the lower border of this interval.

The part of the line between 1 m asl and 2 m bsl contains predominantly reflections of Rf-B4. Reflection strength is high in the bottomsets (Rf-B1) and lowers upslope. The dip of the reflections is around 10° down to a depth of approximately 1 m bsl and then flattens rapidly to subhorizontal at 2 m bsl. These reflections, which in some parts truncate underlying sediments, are laterally traceable for up to 130 m. At the north-northwest end of the line there are Rf-A2 reflections. This part of the GPR line is bordered by a steep unconformity, dipping towards the north-northwest.

Between 2 and 6 m bsl, the line contains northwest- to westward-dipping high-amplitude reflections (Rf-B1) that separate bodies with discontinuous subhorizontal or concave low to medium amplitude reflections (Rf-C1 and Rf-C2). Below 6 m bsl, very

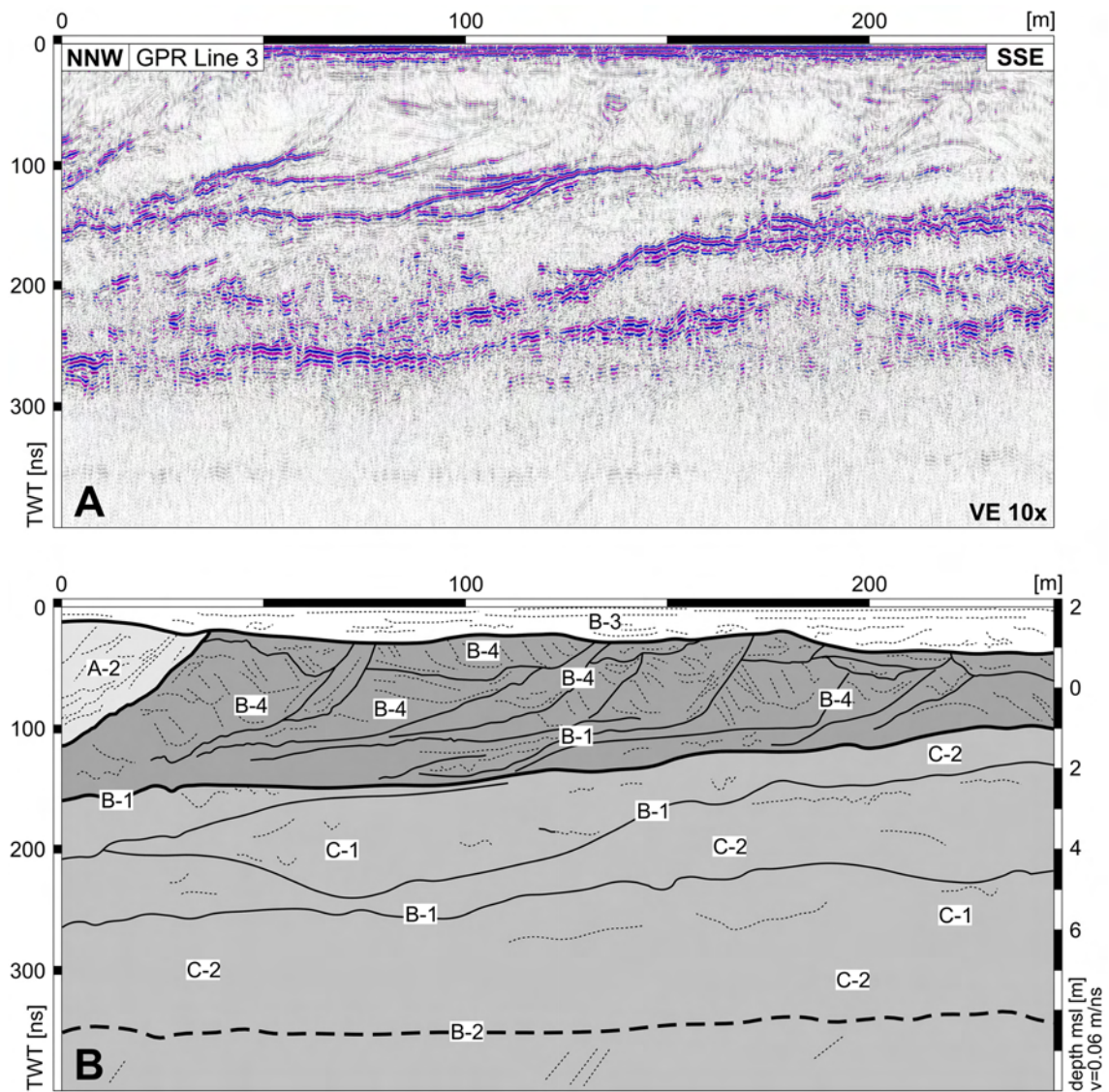


Figure 3.8: **A:** GPR Line 3 measured parallel to the recent shoreline on natural ground. For exact location see Figure 3.3. For description of scales and applied radar-wave velocity see Figure 3.5. **B:** Line drawing and interpretation of the radar data provided in Figure 3.8A. Three intervals can be distinguished based on the radar-facies architectural elements. An upper interval contains subhorizontal reflections. The middle interval exhibits low to high amplitude reflections, dipping towards the north-northwest. These reflections bind mostly contrarily dipping low amplitude reflections into sigmoidal shaped packages. The lower interval shows high amplitude reflections that bind packages with subhorizontal or concave reflections. Large erosional discontinuities are marked with bold lines. See Figure 3.4 for radar-facies definition and Figure 3.5 for key to interpreted sedimentary units.

weak reflections of irregular shape or no reflections (Rf-C2) can be seen. It is assumed that the base of this interval is marked by an unconformity at a depth of 8 m bsl.

The bottom part of the line shows very weak reflections. It starts with a reflection of low amplitude (Rf-B2) that can be followed laterally along the entire section. This reflection seems to truncate underlying layers which dip to the north-northwest with around 8 to 10°.

3.4.2 Radar sections perpendicular to the recent shoreline (GPR lines 4 – 7)

The possibility of carrying out west – east oriented GPR surveys on the northern spit of Sylt is limited. North – south striking relict dunes (Fig. 3.3) require corrections for different terrain altitudes, and lower data quality and penetration depth because of their steep slopes (Lehmann & Green, 2000). Therefore, selection of the positions for GPR surveys which are oriented perpendicular to the shoreline was determined by the terrain morphology.

GPR Line 4

Figure 3.9A shows a GPR line that runs from northwest to southeast. The data show ground penetration down to 300 ns TWT, which corresponds to 9 m below the surface. The uppermost part of the section, down to 1.5 m asl, is characterized by Rf-B3 reflections (Fig. 3.9B). Below this part, down mean sea level, a major cut-and-fill structure extends along the entire section (Rf-B4). Beneath the cut-and-fill structure, two distinct intervals can be distinguished.

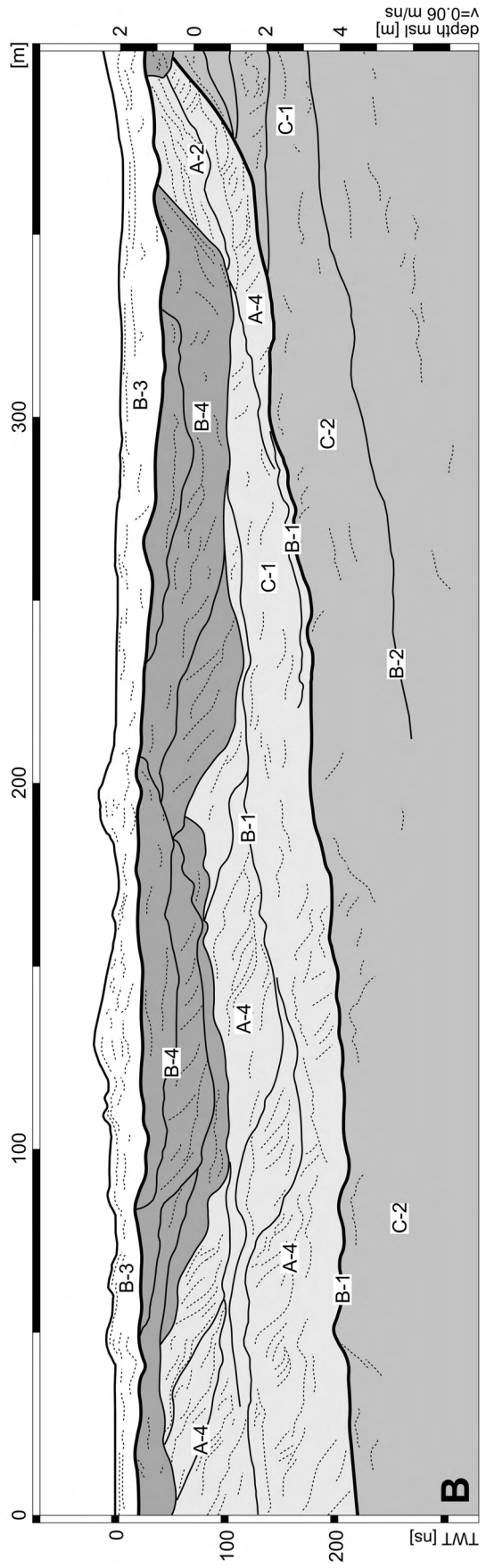
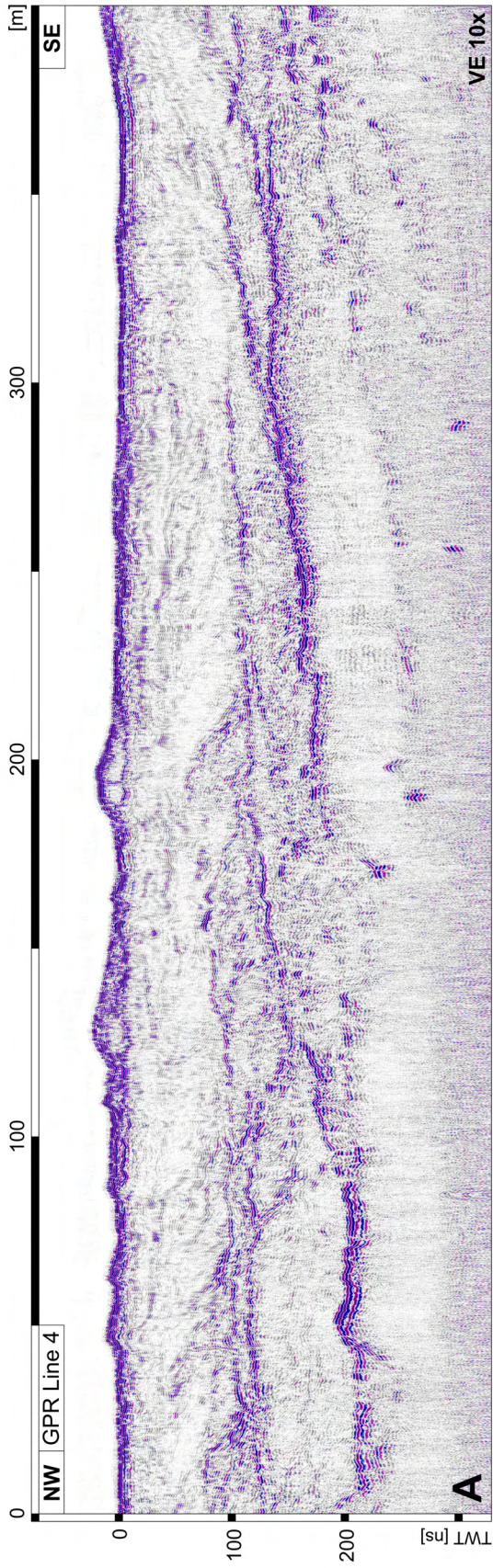
The upper interval is predominantly characterized by Rf-A4 and consists of medium amplitude reflections that delimit bodies of low amplitude reflections. Whereas the medium amplitude reflections dip at 1° to the northwest, the low amplitude reflections show a contrary dip to the southeast at 5 to 10°. Individual packages of Rf-A4 climb up in a southeast direction.

The lower interval of the line is characterized by reflections of low amplitude which dip to the northwest at approximately 1° (Rf-B1). Furthermore, irregular reflections of low amplitude (Rf-C1) and transparent reflection-free areas (Rf-C2) are imaged.

Both intervals are separated from each other by an unconformity (bold line in Fig. 3.9B), which dips at less than 1° to the northwest, reaching a maximum depth of 4 m bsl at the northwest end of the line. This unconformity is expressed by reflections of medium to high amplitude (Rf-B1) which truncate strata of the lower interval.

Two sediment cores were taken on GPR Line 4. Core N-01 (Fig. 3.7C) is located 25 m, and Core N-02 (Fig. 3.7D) 210 m from the northwest end of the GPR Line 4 (Fig. 3.9). Core N-01 is 580 cm long, and Core N-02 480 cm. Characterizing grain-size parameters for the two cores are summarized in Table 3.1.

Figure 3.9 (next page): **A:** GPR Line 4 which runs perpendicular to the recent shoreline in the northern part of the study area. For location see Figure 3.3. For description of scales and applied radar-wave velocity see Figure 3.5. **B:** Line drawing and interpretation of the radar data shown in Figure 3.9A. For key to radar-facies architectural elements see Figure 3.4. Based on radar-facies architectural elements, four different units can be distinguished. In the uppermost part of the line, subhorizontal reflections occur. Beneath there are major cut-and-fill structures. In the lower part of the line, an unconformity separates two distinct levels. The part above the unconformity shows northwestward-dipping reflections that bound packages with an internal southeastward-dipping reflection pattern. Only weak reflections are imaged below the unconformity, showing mostly subhorizontal layering. See Figure 3.4 for radar-facies definition and Figure 3.5 for key to interpreted sedimentary units.



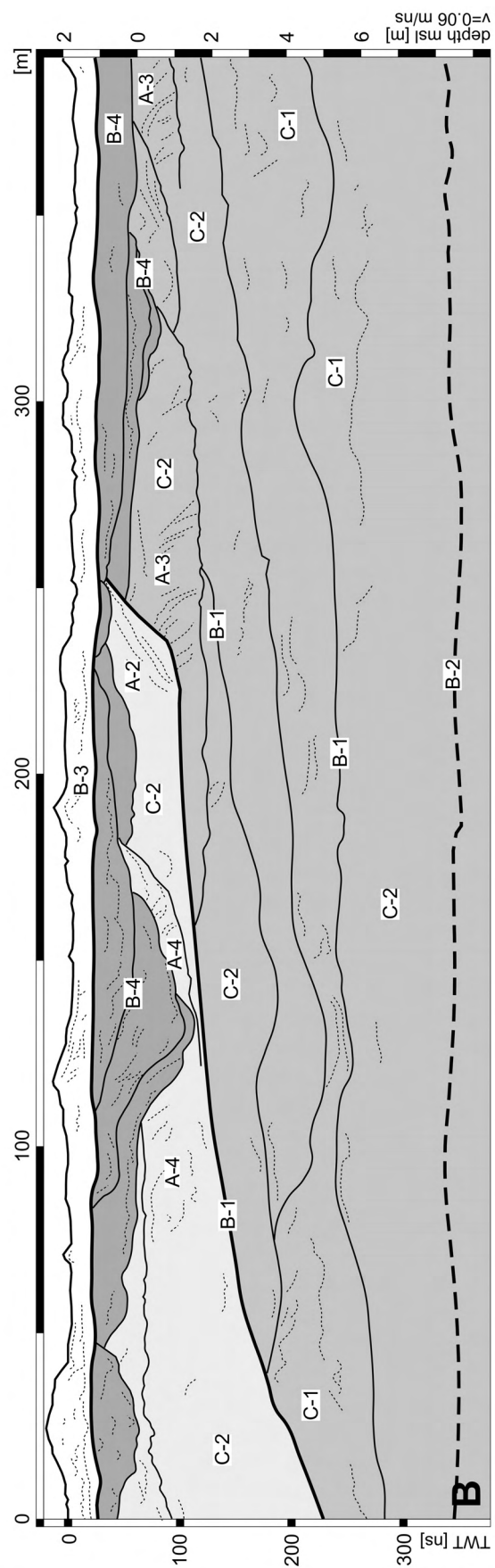
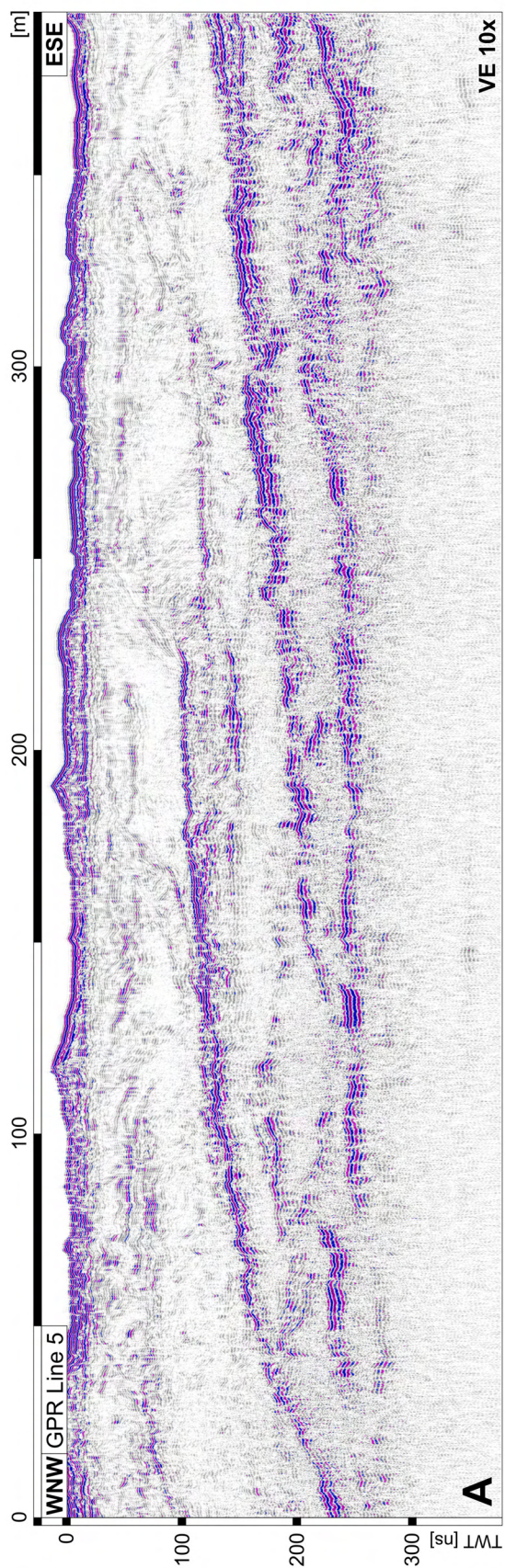


Figure 3.7C shows the mean grain size based on the graphic method (Folk and Ward, 1957) versus terrain depth of sediment core N-01. Figure 3.7D shows the data of Core N-02. From the base of Core N-01 until 470 cm core depth (2.70 m bsl) there is a coarsening-upward of grain size. Between 470 cm core depth and the prominent fine-grained interval at 220 cm core depth (0.20 m bsl), both cores reveal a very slight fining trend. N-02 generally shows slightly coarser sediments than N-01 throughout the core. From about 220 cm core depth both cores show larger fluctuations of the mean grain sizes than in the previous section. Other fine-grained intervals occur at 85 cm core depth (1.15 m asl) as well as at the surface in Core N-01.

In both cores, sorting and mean grain size are linearly correlated with coarser sediments that are generally better sorted than finer sediments.

GPR Line 5

GPR Line 5 (Fig. 3.10A) strikes west-northwest – east-southeast and shows ground penetration down to 360 ns TWT which corresponds to approximately 11 m below the surface. The section is partitioned by two unconformities (bold lines in Fig. 3.10B). Whereas the shallower unconformity (1.5 m asl) is expressed only by reflector terminations, another unconformity is marked by reflections of medium amplitude (Rf-B1) that truncate underlying strata and dip shallowly towards the west-northwest, reaching a depth of 5 m bsl at the west-northwest end of the line.

The shallowest part of the radar line, down to the first unconformity, is characterized by mostly subhorizontal reflections of Rf-B3. Below the unconformity, cut-and-fill structures occur (Rf-B4), which reach down to 1 m bsl in maximum and extend along the whole line. The part of the line above the second unconformity is characterized by the radar-facies architectural elements Rf-A4 and Rf-C2: medium amplitude reflections that dip to the west-northwest with approximately 5 to 7°, bounding bodies with weak internal reflections dipping to the east-southeast and areas where no reflections are imaged.

The part of the line below the second unconformity is characterized by medium to high amplitude reflections that dip to the west-northwest (Rf-B1). At their west-northwest end these reflections are truncated by the second unconformity. Between the reflections, wavy shaped, low to medium amplitude reflections are visible (Rf-C1). No reflections are imaged between 5 and 8 m bsl (Rf-C2), whereas weak reflections (Rf-B2) occur at a depth of 8 m bsl.

GPR Line 6

The west-northwest – east-southeast striking radar section depicted in Figure 3.11A shows ground penetration down to 370 ns TWT, which corresponds to 11 m below the surface. Reflections are imaged down to a depth of 280 ns TWT.

The first meter of the line contains a series of subhorizontal reflections (Rf-B3). The base of this interval (bold line in Fig. 3.11B) is erosive, truncating underlying reflections.

Figure 3.10 (previous page): A: GPR Line 5 which is west-northwest – east-southeast orientated. For location see Figure 3.3. For description of scales and applied radar-wave velocity see Figure 3.5. B: Line drawing and interpretation of the radar data shown in Figure 3.10A. The uppermost part is characterized by subhorizontal reflections. Below 1 m asl, the section is divided into two parts by an erosional unconformity (bold line). The part on the west-northwest side of the unconformity is characterized by cut-and-fill structures and irregular weak reflections. The part on the east-southeast side of the unconformity exhibits cut-and-fill structures and medium amplitude reflections dipping to the west-northwest. The latter bind packages of southeast- to eastward-dipping reflections. See Figure 3.4 for radar-facies definition and Figure 3.5 for key to interpreted sedimentary units.

The depth interval between 1.5 m asl and 2 m bsl is dominated by cut-and-fill structures in the upper part (Rf-B4). The lower part is characterized by low amplitude reflections. These reflections delimit bodies with reflections that are dipping up to 10° towards the east-southeast. Two different radar facies are imaged here: Rf-A3 in the eastern part of the line and Rf-A4 in the western part. A steep unconformity, which dips more than 10° towards the north-northwest, separates both radar facies from each other. Another unconformity is imaged at a depth of approximately 2 m bsl. This unconformity is expressed by high amplitude reflections (Rf-B1) that truncate underlying reflections.

In the part of the line below 2 m bsl there are subhorizontally to weakly west- to northwestward-dipping medium to high amplitude reflections (Rf-B1), which bundle weak reflections of predominantly irregular shape (Rf-C1) into packages. In the

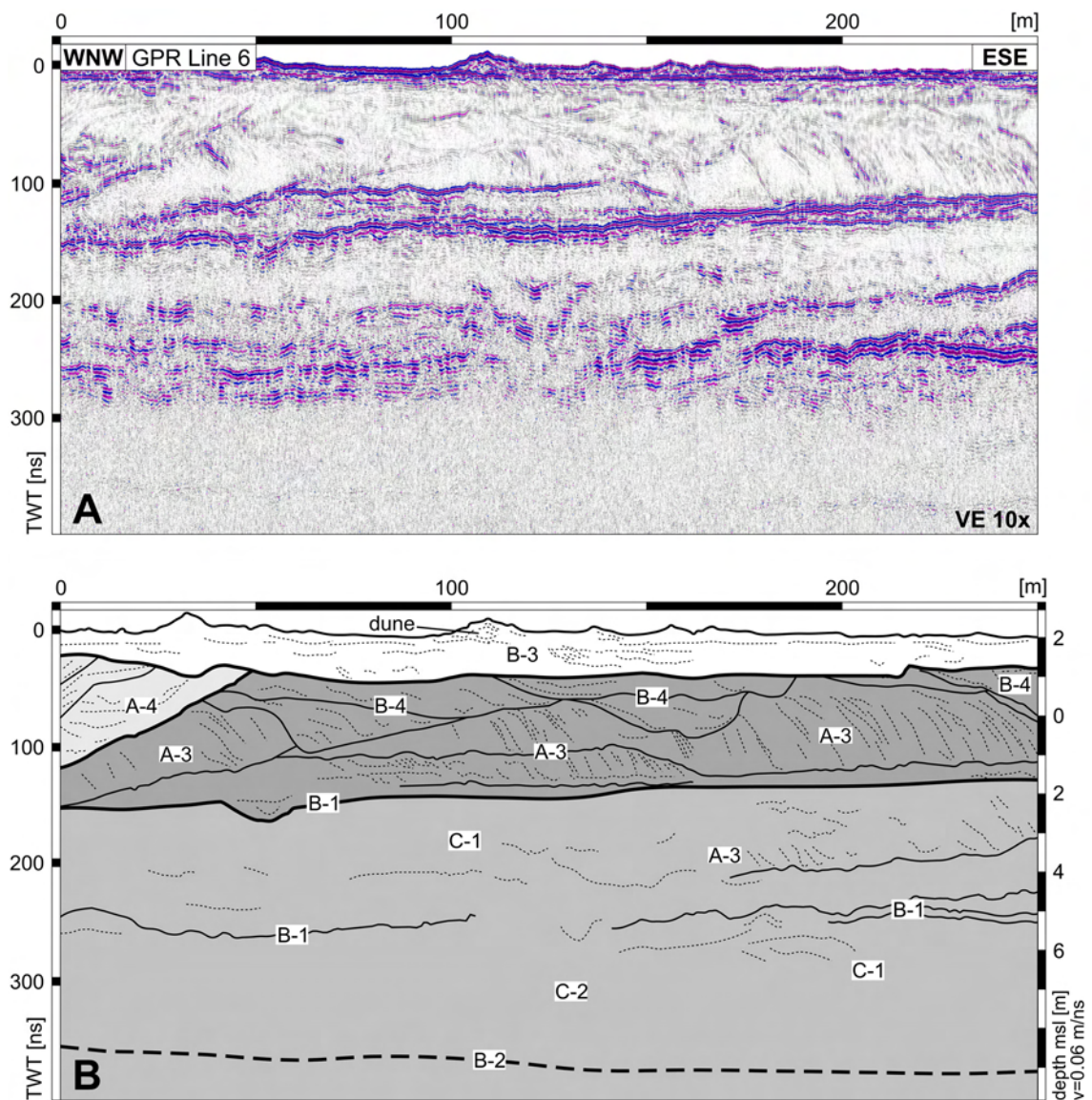


Figure 3.11: **A:** GPR Line 6, running perpendicular to the recent shoreline. For exact location see Figure 3.3. For description of scales and applied radar-wave velocity see Figure 3.5. **B:** Line drawing and interpretation of the radar data provided in Figure 3.11A. Based on the reflection pattern, different units can be distinguished. The uppermost part of the line is characterized by subhorizontal reflections. The middle part is dominated by cut-and-fill structures and low amplitude reflections dipping to the east-southeast. The lower part of the section shows reflections gently dipping to the west-northwest. Please note the steep northwest- and westward-dipping unconformity near the west-northwest end of the line. See Figure 3.4 for radar-facies definition and Figure 3.5 for key to interpreted sedimentary units.

southeast third of the line, at a depth of 3 m bsl, weak reflections with an opposite (east-southeast) dip of approximately 10° are imaged (Rf-A3).

Whereas no reflections are imaged at a depth range between 5.5 and 9 m bsl (Rf-C2), there is a very weak reflection beneath (Rf-B2). Narrow bandpass filtering (30 to 80 MHz) can enhance this reflection at the expense of data quality in the upper part of the section and shows that this reflection is one of high continuity and detectable along the entire line. A comparable reflection, at the same depth range, is imaged in the GPR Lines 3 and 5 (Figs. 3.8, 3.10).

GPR Line 7

A ground penetration down to 300 ns TWT, which corresponds to 9 m below the surface, is achieved in GPR Line 7 which is the easternmost section presented. A segment of this west – east striking line is provided in Figure 3.12A.

In the uppermost part of the line, between 2 and 1 m asl, planar Rf-B3 reflections occur (Fig. 3.12B). The base of this interval is erosive, truncating underlying reflections. A bold line in Figure 3.12B marks this horizon as an unconformity, whereas the unconformity is expressed in the data only by reflection terminations and not by a distinct reflection.

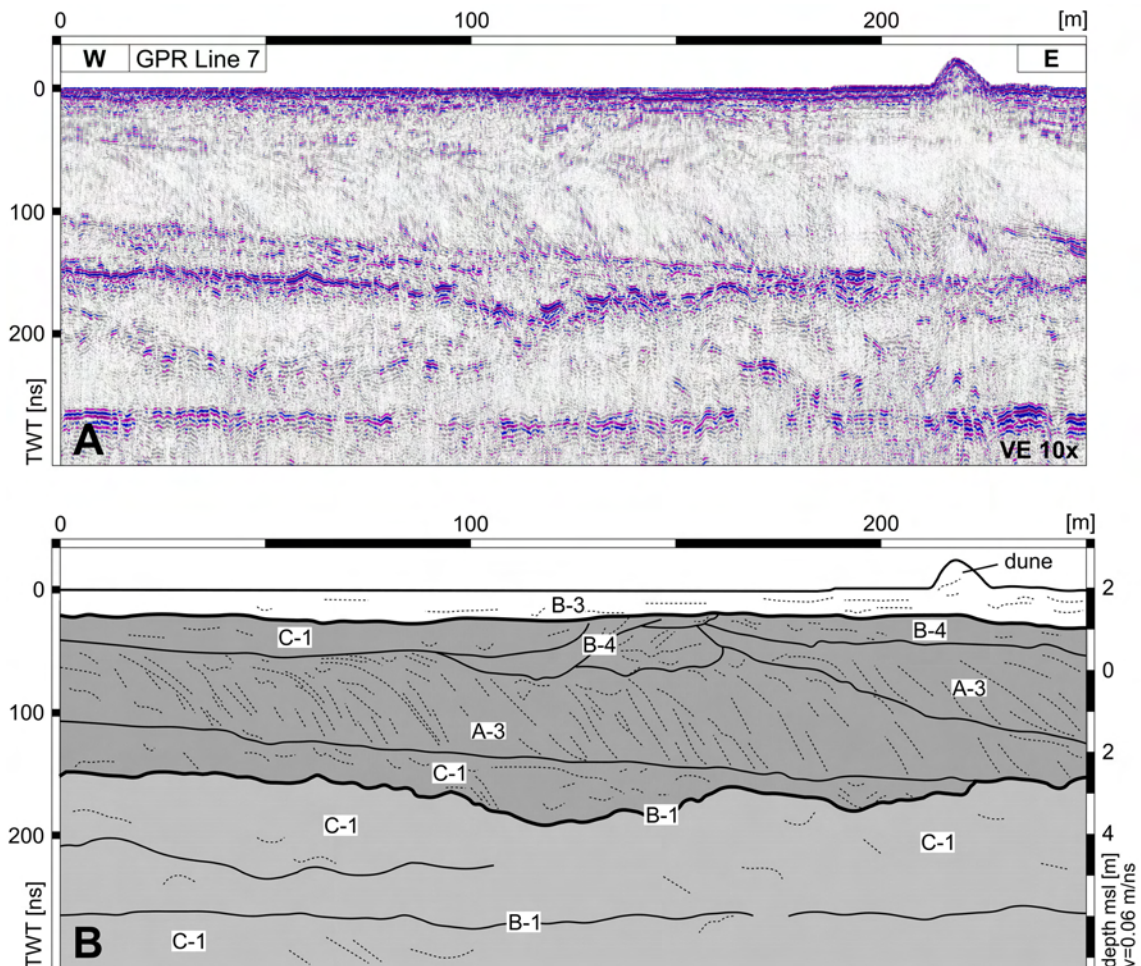


Figure 3.12: **A:** GPR Line 7 which runs perpendicular to the recent shoreline. The line is located in the eastern part of the study area (Fig. 3.3). For description of scales and applied radar-wave velocity see Figure 3.5. **B:** Line drawing and interpretation of the radar data shown in Figure 3.12A. Three different layers can be distinguished. The upper layer shows subhorizontal reflections. The middle layer is dominated by eastward-dipping low to medium amplitude reflections and cut-and-fill structures. The lower layer shows subhorizontal reflections of wavy or concave shape. See Figure 3.4 for radar-facies definition and Figure 3.5 for key to interpreted sedimentary units.

The middle part of the GPR line, between 1.5 m asl and 2 m bsl, is characterized by cut-and-fill structures (Rf-B4) in the upper section. In the lower part Rf-A3 reflections predominate. This part of the section consists of an up to 3 m thick body showing eastward-dipping medium to high amplitude reflections, which delimit weak to medium amplitude reflections dipping towards the East. The middle interval is delimited against the lower interval by medium amplitude reflections that truncate underlying structures. These reflections, which dip weakly towards the East, can be traced along the line at a depth of approximately 2 m bsl. They are marked as unconformities in Figure 3.12B.

The lower part of the line, below 2 m bsl, is characterized by medium to high amplitude reflections, showing a wavy (Rf-B4) or irregular geometry (Rf-C1). Cut-and-fill structures are imaged down to a depth of 4 m bsl. At the base of the line, there is a medium to high amplitude subhorizontal reflection (Rf-B1).

3.5. Discussion

The shore-parallel orientated GPR lines 1 and 2 (Figs. 3.5, 3.6) are characterized by northward-directed progradation of sigmoidal bodies, each delimited by an erosion surface. Two distinct types of surfaces of erosion occur. One type cuts down to approximately 7 m bsl, and can be traced over a distance of more than 1000 m. The other type reaches down to 2 – 3 m bsl, and fades out in the GPR lines after 150 – 200 m. Shore-normal orientated GPR lines show that both types of erosion surfaces climb up from west to east (Fig. 3.9). The sigmoidal bodies have a lower part with wavy to subhorizontal stratification consisting of fine to medium sand. These sediments are moderately to poorly sorted. The middle part of the bodies shows subhorizontal to weakly southward-dipping strata in the shore-parallel lines. GPR Lines oriented normal to the shoreline indicate that this layering is consistently dipping into an east- to southeast-direction. Sediments in this part of the succession are mostly medium, moderately to well sorted, sands. At the top of the bodies horizontal and flat-concave layers as well as cut-and-fill structures can be identified. In this part of the bodies, the sediment is generally finer grained. Sorting is poorer than in the bodies middle part. Tracing of the infill of these structures to the East shows that they merge into bodies with a persistent easterly-directed bedding (Figs. 3.11, 3.12).

The series of bedding styles that is imaged within individual bodies is interpreted to represent a beach depositional system with shoreface sediments in the lower part, swash-bar deposits in the middle part and channel-fills in the upper part. The subhorizontal bedding in the upper part of some of the bodies is attributed to a backshore environment. Cut-and-fill structures are interpreted as channels which cross-cut the upper foreshore and the backshore beds. These channels feed a washover-fan system as imaged in the easternmost line (GPR Line 7). This facies association resembles the architecture of scour channels and washover fans described by Schwartz (1982) in the beach system of the Outer Banks (North Carolina).

Today, even during large storms, dune breakthroughs and washover events are very uncommon on Sylt. This is probably a consequence of coastal protection, i.e. dune stabilization, which allowed to form up to 26 m high dunes lining the modern coast.

Beach progradation occurred under fair-weather conditions through welding of swash bars, a process described in detail by Hine (1979) for recent spit beaches

along Cape Cod (USA). The seaward limit of swash bars is interpreted to represent storm-driven erosion surfaces. Infrequently occurring severe storms triggered profound erosion, which is reflected in the deeper cutting surfaces. These major storm events also controlled the development of scour channels feeding the washover fans on the leeward side of the spit.

The topmost part of the GPR lines is formed by an up to 1 m thick cover of eolian sediments with an easterly-directed low angle dip. The base of these units is erosional, cutting into the underlying structures. This erosional unconformity exist throughout the entire study area, at nearly the same depth. It is interpreted to reflect a former deflation surface, lying approximately 1 m below the recent deflation surface. Subhorizontal or landward-dipping sediments above the deflation surface can be seen as the remnants of dunes.

A simple conceptual model which shows the evolution of the described depositional system is presented in Figure 3.13. The model consists of six stages which reflect the whole cycle of beach erosion, recovery, progradation, channel incision, and finally preservation of the sedimentary succession by a rise of the deflation surface. The deflation surface is formed by the groundwater table which is hydrodynamically coupled to the sea-level. The sedimentary architecture of the spit shows that the growth of the spit system was primarily towards the North, but also westerly-directed.

During Stage 1, a severe storm causes profound erosion of the spit. Coastal dunes are affected by storm waves and overwash – an erosional scarp develops at the foot of the coastal dunes. Eroded sediments are transported seaward and stored in the deeper shoreface or in nearshore bars. On the landward side of the coastal dunes, washover sediments are deposited. Heavy minerals are concentrated above the erosion surface as lag deposits during the waning stages of the storm, when storm-wave erosion decreases (Hayes & Boothroyd, 1969; Buynevich et al., 2004).

This observation corroborates descriptions of Smith et al. (1999) and Buynevich et al. (2004). Smith et al. (1999) investigated barrier sediments on the southwest coast of Washington (USA) and found scarp-like GPR reflections that were associated with sediment layers enriched in Magnetite. Buynevich et al. (2004) described heavy minerals associated with storm erosion surfaces that caused strong reflections in GPR data from barrier sediments on the coast of Maine (USA).

During a major storm event, the seaward shift in breaker position and strong increase of seaward sand transport may heavily affect the bar and beach prism. Exceptionally large storms erode beaches and transport coarser beach sediment via undertow and rip currents out of the nearshore zone. Eventually, the beach profile steepens and forms an eroded scarp (Hayes & Boothroyd, 1969; Niederoda et al., 1985). Carter (1986), however, assumes that sediment eroded from the dune cliff

Figure 3.13 (next page): Model describing the interplay between erosion and sedimentation that leads to the sedimentary architecture imaged in the GPR data. For detailed discussion see text. Six evolutionary stages are distinguished. **A:** Profound erosion by severe storm associated with scarp development and overwash sedimentation. **B:** Beach recovery by return of sediment that was temporarily stored in the deeper foreshore or in longshore bars. Restart of eolian accumulation at the dune scarp. **C:** Continued swash-bar accretion leads to beach progradation. If the time interval between two severe storms is long enough, net spit growth takes place. **D:** If the beach plain is broad enough, this part of the spit system will not be destroyed during the next severe storm, but erosive channels develop due to washover events. **E:** Stable sea-level conditions lead to the development of a deflation surface due to the hydrodynamic coupling of the groundwater table to the sea level position. Migrating dunes can pass on top of the deflation surface. **F:** A rising sea-level creates accommodation space which is filled by trapping of eolian sand. A new deflation surface develops after a return to stable sea-level conditions.

during storms is temporarily stored in nearshore bars and not distributed further offshore. During storms, high turbulence prevents the coarser grains from settling, and erosive waves and currents may reach the foredunes upon prevailing strong storm events and remobilize finer grained sediments there.

Stage 2 comprises the waning stage of the storm and the early after-storm period. At this time, the sedimentation is characterized by settling of fine-grained material that has been suspended during the storm. This sediment forms the thin, fining upward layer on top of the erosion surface, identified in the sediment cores and the GPR surveys.

Early post-storm settling of fine-grained material occurs below the fair-weather wave base only. After a storm, the fair-weather system recovers and the scarps flatten. Coarser material that was stored in the deeper shoreface during the storm, returns to the nearshore zone in the form of swash bars. The bars are welded onto the beach under fair-weather wave action (Niederoda et al., 1984). At the base of the dune scarp, accumulation of eolian sediment starts. Thus, the storm signal that is fossilized and recorded in the GPR lines may consist of the finer foredune sand. This sand was transferred onto the coarser beach system, and subsequently buried again by coarser swash-bar sediments which had returned after the storm event. It is assumed that the returning sediment filled depressions and leveled scarps quite rapidly. As a result, less structured homogeneous sediments presumably cover storm-affected beach prisms before regular fair-weather sedimentation resumed.

Stage 3 is characterized by the return to enduring fair-weather conditions which allows a progradation of the spit system due to continued welding of swash bars. This leads to a northward and westward (seaward) growth of the spit beach, mostly during the summer months. At least 650 m of westward expansion, and 3200 m of northward progradation are recorded by our data.

During winter storms, welded swash bars are partially eroded. These erosion surfaces are well imaged in the GPR data as high amplitude reflections. Similar to the severe storm layers described in Stage 1, enrichments in ferromagnetic minerals are assumed as the cause for the high radar reflectivity.

These findings contradict the hypothesis, first expressed by Gripp & Simon (1940) and later adopted and extended by Köster (1974) and Ahrendt & Thiede (1992), that the evolution of the island during the last 5000 years is characterized by a continuous retreat of this spit and moraine core configuration as a response to post glacial sea-level rise. This hypothesis is based on dramatic modern coastal retreat of approximately 1.25 m per year at an increasing rate from the middle of the 20th century (Ahrendt, 1993), and on the interpretation of historical maps of the North Sea coast (Newig, 1980; 2004; Ahrendt & Thiede, 1992).

Stage 4 indicates the reaction of the depositional system to a renewed severe storm. Beside the sediment availability, the net rate of spit progradation is mainly controlled by the length of the time interval between two severe storms. If this interval is long enough, a broad beach plain develops due to continued swash-bar accretion, followed by stabilization of foredune ridges. The next severe storm will not result in a complete destruction of this part of the spit, but erosive channels develop as a result of washover events.

Stage 5 reflects a stable base level over longer periods of time. This leads to the development of a deflation surface which corresponds to the groundwater table.

The presence of migrating eolian dunes during this stage of the spit evolution can only be assumed.

A rise in sea level, followed by the return to stable base-level conditions marks Stage 6. Due to the hydrodynamic coupling of the groundwater table to sea level, such a rise creates new accommodation space which allows trapping of eolian sand and the conservation of the bottomsets of migrating dunes. As the sea level returns to stable conditions, a new deflation surface develops. The situation, graphically presented for Stage 6, corresponds to the sedimentary architecture that is imaged in the GPR data.

Preservation of the sediment packages described in this study depends mainly on sediment supply, recurrence interval of severe storms, and sea-level position. The rate of sediment supply, compared to the amount of material that is eroded during extreme storms, leads to a net long-term sediment balance. Only if this balance is positive over a longer period of time, the beach prograde and spit growth can occur. Furthermore, to protect the sediments from deflation, it is necessary that the sea level, and thus the groundwater table, is stable or rising. A lowering of the sea level would lead to a lowered deflation surface.

3.6. Summary and conclusions

Ten radar facies, each characterized by distinct reflection patterns and geometries, are differentiated in the Holocene spit sediments. Linking radar facies with sedimentological data allows the development of a new sedimentological model for spit evolution and shows that swash bars are an important building block of the spit. Swash-bar bodies are delimited by erosional surfaces, which are interpreted as resulting from storm events. These storms triggered erosion, sediment reworking, and sediment export out of the nearshore zone. Sediment transfer back to the beach was achieved through swash-bar growth during fair-weather periods. Swash-bar accretion resulted in a northward, as well as a substantial westward, sediment progradation.

There are several outcomes from these results. First, we show that the evolution of the spit is much more complex than previously expressed, and not only characterized by a continuous eastward retreat. The data indicate that at least 700 m of seaward beach progradation occurred. There are, however, no age dates available to pinpoint this period of spit growth. Second, the example of the dominance of swash-bar bedding over seaward-dipping planar foreshore bedding doesn't seem to be a very common pattern in the geological record of beach deposits. It is beyond the scope of this study to reconstruct the controlling factors that determine whether swash bars are present and recorded in beach deposits. In any case, it remains to be proved if more extended GPR studies of other Holocene beaches and spits would reveal that swash-bar deposits are more common in the geological record of beaches than previously thought. Third, the observation that spit growth can be achieved through swash-bar accretion may be a key for developing a concept of enhanced coastal protection under future conditions of accelerated sea-level rise. Sand nourishment in a distal beach area may be more efficient than beach nourishment in the backshore setting, as practiced along the coast of Sylt nowadays.

4

Anatomy of a hooked spit

ABSTRACT

Holocene barrier islands line the coast of the southern North Sea. The largest of these barrier systems is the island of Sylt near the border between Denmark and Germany. This study focuses on a hooked spit, the Ellenbogen, which is attached to the northern recurved spit of Sylt. (The development of the investigated sedimentary system is closely related to the northward adjacent tidal inlet – the Lister Tief. Here, strong tidal currents and a steep bathymetry prevented a further northward-progradation of the main spit. This triggered a switch from northerly- to an easterly-directed net sediment transport. Ground-penetrating radar (GPR) and shallow sediment cores reveal the sedimentary architecture in great detail, and make it possible to propose a model for the development of the hooked spit. The data show that growth of the hooked spit is controlled by the interplay of alongshore migrating foreshore beach-drifts under fair-weather conditions and strong erosional events, interpreted as the result of rare severe storms. These storms interrupted the phases of beach-progradation, leading to a significant retreat of the coastline. Exceptional storms may also excavate scarps in the backshore. Storm scarps play an important role in the development of the fore-dune ridges that are situated on the hooked spit nowadays. AMS ^{14}C -ages indicate an age of at least 1300 years for the hooked spit, which is much older than stated in previously published models. In contrast to the main-spit of Sylt, where the sediment budget is negative, the Ellenbogen experienced significant beach growth during the last decades. This can probably be attributed to enhanced beach-nourishment updrift along the main-spit, and makes the investigated hooked spit a natural laboratory to study the influence of increasing sediment supply in a system developing under the conditions of Holocene sea-level rise.

4.1. Introduction

Hooked spits form at the downdrift termination of drumstick barriers, where wave refraction at the associated tidal inlet causes deflection of longshore sediment transport, and forces the spit to bend away from the sea and to line the tidal inlet.

Hayes (1975, 1980) proposed that the recurved parts of a spit are the product of lateral channel-margin sedimentation along a tidal inlet and synchronous inlet migration. Sediment transport takes place in the marginal flood-channel by flood-directed migrating sand waves. Investigating recent beach processes on Cape Cod, Massachusetts, Hine (1979) found that beach progradation in the hooked portion of a recurved spit is dominated by berm-ridge development, producing predominantly landward-dipping strata. His model comprises the formation of broad intertidal bars that are partially eroded by waves at neap high-tide. Subsequently, on the steep erosional beach face, a new berm develops leading to beach progradation. Kumar & Sanders (1974) presented a model based on investigations on Fire Island (New York), that summarizes the sedimentary facies of a migrating spit. They distinguished between welded ridge facies, composed of sea- and landward-dipping strata, and channel-margin platform facies, dominated by steeply seaward-dipping strata.

The rise of ground-penetrating radar (GPR) in sedimentology allowed for a spatial, and more detailed investigation of subsurface structures and led to numerous studies dealing with the internal structure of prograding barrier spits (e.g. FitzGerald et al., 1992; van Heteren & van de Plassche, 1997; van Heteren et al., 1998; Smith et al., 1999; Anthony & Møller, 2002; Daly et al., 2002; Jol et al., 2002).

Commonly, the morphology of hooked spits is characterized by vegetated beach ridges (van Straaten, 1965; Oertel, 1975; Hine, 1979; FitzGerald et al., 1992; Tanner, 1995) that mark former coastline orientation (Hine, 1979; Bristow et al., 2000). According to Pye (1990) and Psuty (1992), the development of fore-dune ridges on a prograding beach is attributed to higher wind energy and positive sediment budgets of beach and dune. An example is described by Eliot et al. (1998) who investigated the beach-ridge system of Desperate Bay in western Australia that has an eolian accumulated cap. Hesp (1988, 1999) found that in addition to sediment supply, vegetation is an important factor in fore-dune ridge growth as it baffles windblown sand.

To unravel the sedimentary geometries which formed during the formation and growth of a hooked spit, GPR, sediment cores and radiocarbon datings were used. The study area is part of the barrier system of Sylt, an island in the southern German North Sea. Whereas the coast of Sylt showed continuous retreat during the last centuries (Gripp & Simon, 1940; Köster, 1974; Ahrendt & Thiede, 1992; Ahrendt, 1993; Newig, 1980, 1995, 2004), the hooked spit, attached to the northern end of Sylt, has experienced significant growth. Nowadays, the investigated hooked spit is characterized by a system of dune ridges that are oriented parallel to the predominant wind direction. In the subsurface of the spit, shovel-blade shaped bodies, up to 3 m thick, and around 100 m width occur, separated by major erosional unconformities. We propose an integrated model for the formation of these geometries and a template which may serve to recognize similar deposits in the geological outcrop.

4.2. Study area

This study is focused on the northern termination of the north – south striking spit of Sylt, a barrier island 15 km off the German North Sea coast near the border to Denmark (Fig. 4.1). The island is situated in a semidiurnal upper microtidal to lower mesotidal regime after the definition of Hayes (1979), with a tidal range of 1.6 to 2.2 m (Hundt, 1957; Pejrup et al., 1997; Backhaus et al., 1998). The average wave height is between 1.00 and 1.25 m and builds up to 5 m during storms. Westerly winds are dominant (Hundt, 1957; Müller, 1980; Ahrendt, 2001). Sylt contains a core of Elsterian and Saalian moraine deposits as well as Tertiary sediments (Gripp & Becker, 1940; Schwarzer, 1984). Two Holocene barrier spits, attached to the North and to the South, form a highly elongated island some 38 km long (Fig. 4.1B). On the landward side of the northern spit there is a broad tidal bay, the Sylt-Rømø Basin, which covers an area of around 400 km² (Bayerl & Köster, 1998). The bay is bordered to the South by the Hindenburg-Damm, an artificial dam constructed in 1927, and to the North by the Rømø-Damm, constructed in 1949. Due to the dams, water exchange between the basin and the North Sea is nowadays restricted to a 2.8 km wide and maximal 40.5 m deep tidal inlet, the Lister Tief (Fig. 4.1B). Here maximal current velocities of 1.3 m / s were measured (Backhaus et al., 1998). After Bayerl et al. (1998a), the sediments in the Sylt-Rømø Basin are predominantly sands with a median between 0.125 and 0.25 mm (3 to 2 phi), whereas the median grain-size decreases with increasing distance of the tidal inlet. Only 3 % of the area are mudflat with more than 50 % silt and clay.

The northern end of the barrier island has a hooked spit geometry and is named „Ellenbogen“. It has a dumbbell shape, extending around 4.5 km in west – east direction and between 0.5 and 1.5 km in north – south direction. The hinge is very narrow and morphologically marked by a dune chain of up to 13 m height. High dunes also developed at the western coast, whereas west – east extending dune ridges characterize the rest of the Ellenbogen (Fig. 4.2A). The Ellenbogen is connected to the Listland by a small dune ridge, which was flooded during past strong storm surges. The youngest dune break-through in this area dates back to the year 1928.

Little is known about the sedimentary architecture of the Ellenbogen. Cores show that the base of the Holocene, situated at a depth of approximately 25 – 28 m below present mean sea level (bsl), consists of clays which are probably Eemian in age (Gripp & Simon, 1940; Ahrendt & Pesch, 2001). Gripp & Simon (1940) found that Eemian clays are partly eroded in the middle of the Ellenbogen, which is interpreted as an indicator for a paleo tidal inlet beneath the Ellenbogen. Holocene sediments of the hooked spit are gravels and sands (Gripp & Simon, 1940; Dietz & Heck, 1952a).

According to Dietz & Heck (1952a), the currents flowing in the Lister Tief inhibit northward growth of the barrier island spit and trigger formation of the hooked spit geometry of the Ellenbogen. The sediment supply to the hooked spit is from the South, through northward flowing longshore currents. The sediment sources are the retreating moraine cliffs, and since 1972, beach sands replenished along the main spit. Along the beach of the Lister Tief tidal inlet, the influence of the longshore currents decreases. The eastward sediment transport along the northern coast of the Ellenbogen is attributed to waves (Hundt, 1957).

The northern spit of Sylt formed approximately at 5000 – 6000 BP; this age assignment relies on dating of peat layers and stone-age tools (Harck, 1972, 1974, Willkomm, 1980, Behre, 1995; Litt et al., 2001). There are no absolute age dates

for the Ellenbogen hooked spit available. Based on historical maps, Newig (1995) noted that the Ellenbogen did not exist in the 17th century and proposed that it was formed during a storm surge which occurred between 1634 and 1793, as it is depicted in a map that dates to the latter year. Maps from the 17th century, however, already show shoals at the recent position of the Ellenbogen (Newig, 1995). Hundt (1957) argued that the Ellenbogen formed due to increased sediment delivery resulting in an accelerated spit growth. Priesmeier (1970) explained the formation of the Ellenbogen

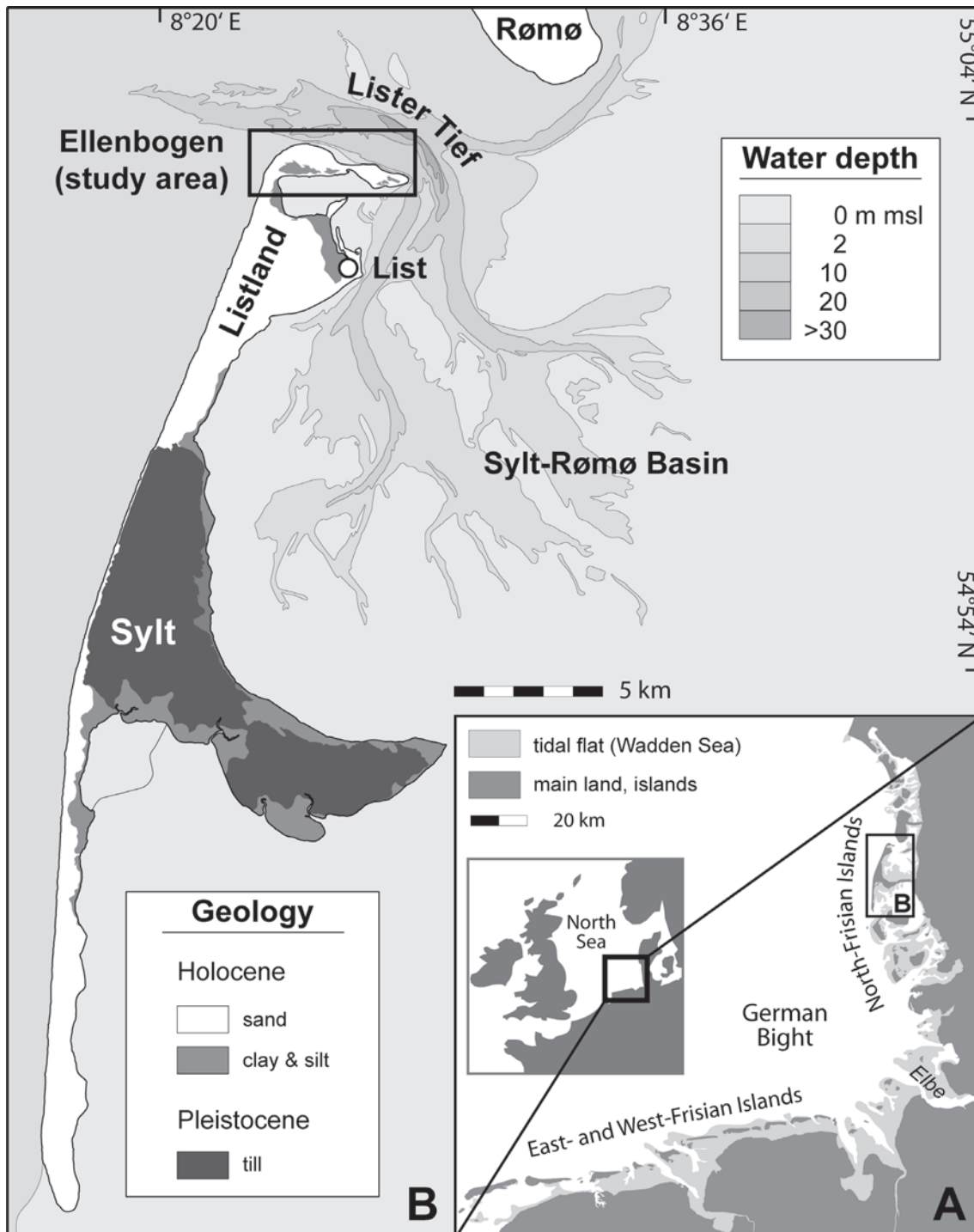


Figure 4.1: **A:** The German Bight in the southern North Sea with the chain of the East-, West-, and North-Frisian Islands. Location of Sylt is marked with a box. **B:** Geological map of Sylt, simplified after Dietz & Heck (1952b). The core of the island consists of predominantly Pleistocene moraine deposits. Two Holocene spit systems extend to the North and to the South. The water exchange between the Sylt-Romo Basin and the North Sea is limited to the tidal inlet of the Lister Tief, which is up to 40.5 m deep north of Sylt. The study area is marked by a black box; bathymetric data are from Neide (1977a, 1977b).

as a result of sediment redeposition from a former ebb delta which was situated towards the South and destroyed during a strong storm.

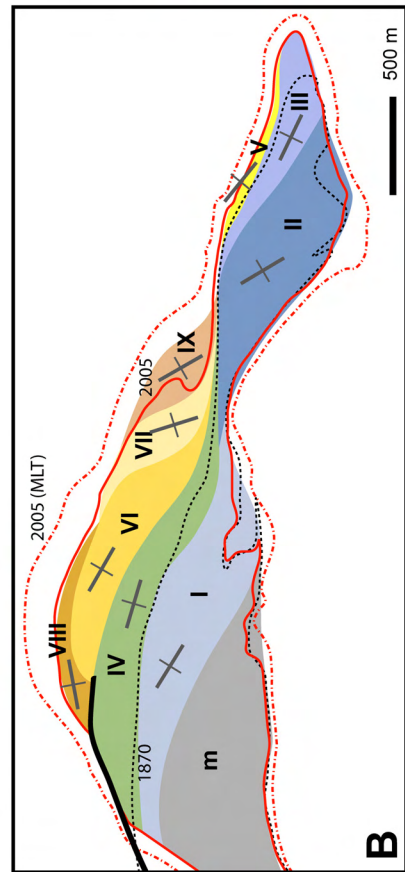
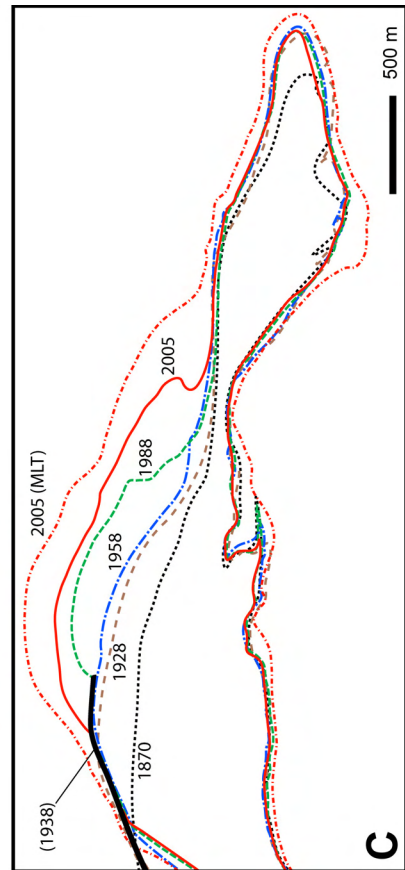
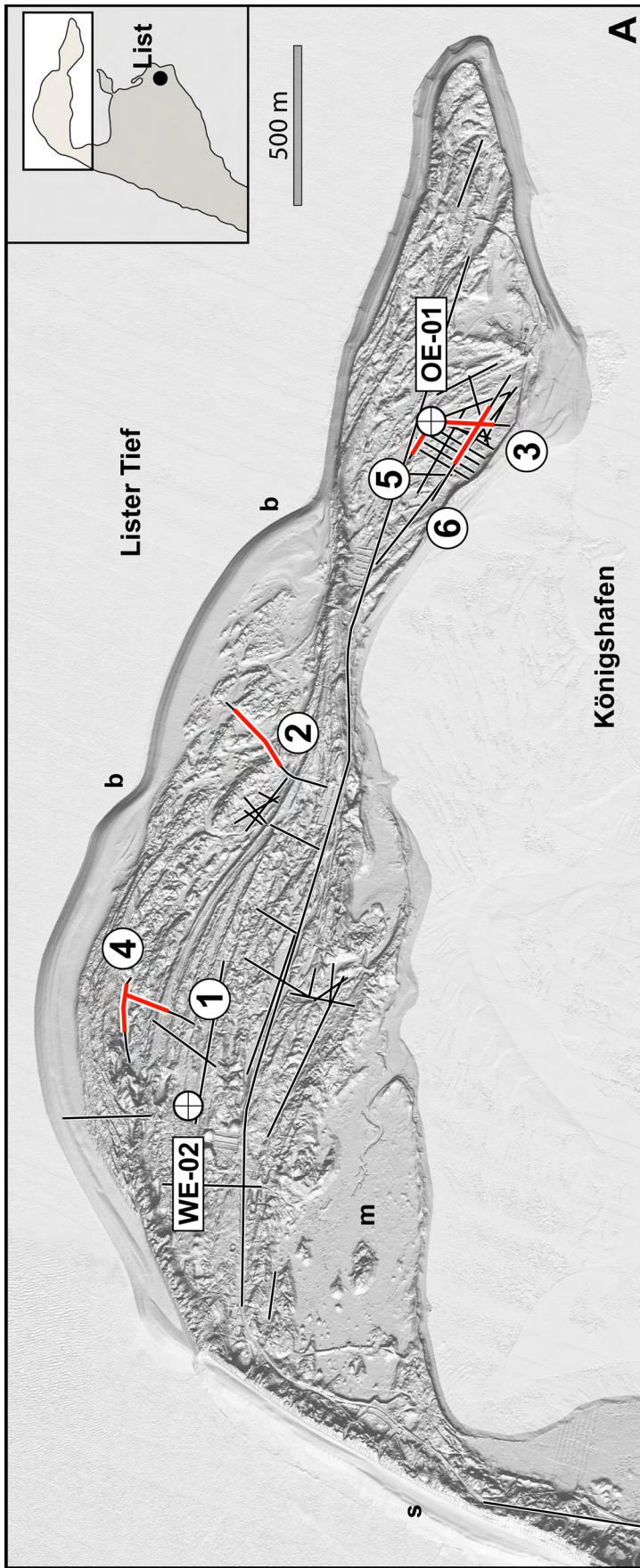
4.3. Methods

The stratigraphic architecture of the Ellenbogen was analyzed by means of GPR and shallow sediment cores. Age estimations are based on radiocarbon dating. GPR provides a noninvasive method for surveying the shallow subsurface in centimeter to decimeter resolution. GPR is based on the transmission of high-frequency electromagnetic pulses. At electromagnetic discontinuities in the subsurface, the energy is partially reflected back to the surface, where it is detected as a function of travelttime. Electromagnetic discontinuities are mainly caused by changes in porosity, and therefore of fluid content, or changing lithological composition. Detailed introductions to GPR are provided e.g. by Blindow et al., 1997, Annan, 2001, 2005, Jol & Bristow, 2003, and Neal, 2004. For GPR surveys carried out for this study, a Geophysical Survey Systems Inc. radar system SIR-3000 was used in combination with antenna frequencies of 100 and 200 MHz. In general, the penetration depth in geological materials increases with decreasing antenna frequency (Jol, 1995; Smith & Jol, 1995; Neal, 2004). Nevertheless, in our setting, the 100 MHz antenna did not yield an increase in penetration depth compared to the 200 MHz antenna, probably due to increasing pore-water salinity with depth, and therefore higher signal attenuation.

Radar data were collected in continuous mode with a survey wheel as distance trigger. Trace increment was set to 5 cm. 2048 samples were collected for each shot, providing a wide scope for later processing. Manufacturer settings for frequency filtering and no stacking were applied during data collection. As non-vertical radar-beam orientation causes distortions in the data and lower penetration depth, GPR surveys were restricted to more or less flat surfaces, as far as possible. Slope angles exceeding 6 to 10° were avoided to prevent uncorrectable distortions of underground geometries (Lehman & Green, 2000). Although the dunes on the Ellenbogen are densely covered with plants, no adverse effects on the GPR data were observed.

Processing contains correction of time-zero offset, frequency filtering, down-the-trace and trace-to-trace stacking, background removal, and migration with the fk-migration algorithm after Stolt (1978). For processing of data the software ReflexW (Sandmeier, 2006) was used. A topographic correction was applied on each radar line in order to restore different terrain altitudes, and therefore reflector geometries. The data required for the topographic correction were obtained using a differential global-positioning system (either an Ashtek ProMark II or a Leica GPS 1200). Vertical data accuracy of the Ashtek system is up to 0.15 m, and up to 0.01 m for the Leica system (manufacturer specifications).

Migration and time-depth conversion require the exact radar-wave velocity in the given subsurface material. Common midpoint measurements, usually aimed to obtain a radar-wave velocity model of the subsurface, failed in the working area, because prerequisites were not fulfilled, such as a laterally largely homogenous underground with nearly sub-horizontal strata and occurrence of a shallow reflector which can be traced over at least a few tens of meters (Kruk et al., 1999; Jol & Bristow, 2003). Hence, the velocity of the radar waves in the investigated sediments was determined by diffraction-hyperbola analysis and by the direct correlation of sediment core to



Year	Type	Source
2006	aerial photograph	Alfred-Wegener-Institut für Polar- und Meeresforschung
2005	aerial photograph	Alfred-Wegener-Institut für Polar- und Meeresforschung
2003	aerial photograph	Alfred-Wegener-Institut für Polar- und Meeresforschung
2002	digital elevation model	Amt für ländliche Räume, Husum
2001	aerial photograph	Landesamt für den Nationalpark Schleswig-Holsteinisches Wattenmeer, Tönning
1998	aerial photograph	Landesamt für den Nationalpark Schleswig-Holsteinisches Wattenmeer, Tönning
1988	aerial photograph	Landesamt für den Nationalpark Schleswig-Holsteinisches Wattenmeer, Tönning
1958	aerial photograph	Amt für ländliche Räume, Husum
1938	technical drawing	Müller & Fischer, 1938
1928	aerial photograph	Amt für ländliche Räume, Husum
1870	drawing	Müller & Fischer, 1938

Table 4.1: Sources of historical coastlines presented in Figures 4.2 and 4.3

radar data. Obtained values for radar-wave velocities show an average of around 0.065 m / ns for groundwater saturated sands, and an average of 0.12 m / ns for dry sands. These values are in the range of radar-wave velocities determined in previous studies for saturated and dry sands respectively (Knödel et al., 1997; Jol & Bristow, 2003; Neal, 2004).

To link ground-penetrating radar with sedimentological data, vibracores down to a depth of 11 m below the surface were drilled at selected positions (Fig. 4.2A). We employed a 50 mm open core probe for the first meter, and a 36 mm gouge auger for the remainder. A visual estimation of sediment color, grain size, sorting and rounding was performed in the field. The cores were subsampled every 2 and 5 cm respectively (1 cm thick samples) for further laboratory analyses. Grain-size analyses were obtained using a Quantachrome Cilas 1180L laser diffraction particle-size analyzer. Prior to analysis, samples were treated with diluted hydrogen peroxide and acetic acid to dissolve the non-siliciclastic content. The Cilas 1180L has a measuring range from 0.04 to 2500 μm . Grains coarser than 2000 μm were removed from the samples before the measurement using a standard sieve. Grain-size statistics were performed by the computer program Gradistat (Blott & Pye, 2001) and self-programmed routines. All statistical grain-size parameters mentioned in the text are based on the graphical method (logarithmic) by Folk & Ward (1957).

Radiocarbon dating using the AMS ^{14}C -method was performed by Leibniz-Labor für Altersbestimmung und Isotopenforschung, Kiel (Leibniz-Laboratory for Radiometric Dating and Stable Isotope Research, at Kiel). Dated materials include shell fragments from marine mollusks, obtained by manual picking from the core material. Conventional ^{14}C -ages were calibrated using the program Calib 5.0 (Stuiver & Reimer, 1993). Marine calibration data are from Hughen et al. (2004). All dated mollusks lived near the beach, within the upper 5 m of the water column. Therefore, no reservoir corrections were applied to the data, because the local marine reservoir effects are unknown and may differ from the global reservoir age correction (Nadeau, Leibniz Laboratory, Kiel, pers. comm.). Due to this lack of reservoir correction, calibrated ^{14}C -ages provided in this work can be regarded as maximum ages.

Figure 4.2 (previous page): **A:** Terrain model of the study area, based on airborne LIDAR measurements by ALR (Husum) in 2002. LIDAR measurements were taken during low-tide. Note swash bars on the western coast (s), active beach-drift fronts (b) and the salt marsh (m). Thin lines show GPR database of this study, bold lines mark GPR lines 1 to 6 discussed in the text. Circles indicate locations of sediment cores (Core OE-01: UTM coordinates 464554 / 6100164; Core OE-02: UTM coordinates 462397 / 6100933) **B:** Ridge-set distribution of the Ellenbogen derived from the terrain model. Crossed lines indicate the prevailing strike direction of fore-dune ridges for each set. Black line at the northwestern corner of the Ellenbogen marks the rock revetment constructed in 1938. **C:** Evolution of mean high-tide (MHT) shoreline position at the Ellenbogen between 1870 and 2005. For 2005, the mean low-tide level (MLT) is indicated in addition by a dashed line.

Geomorphological data used in this study are based on an airborne LIDAR-derived terrain model (Fig. 4.2A) provided by the Amt für ländliche Räume (ALR, Husum, Germany). The horizontal grid space is 1 m, vertical accuracy is around 0.2 m. Coastline reconstructions for the last centuries (Figs. 4.2B, C) are additionally based on historical maps and several aerial photographs (Tab. 4.1).

4.4. Results

4.4.1 Geomorphological evolution

The most prominent morphological feature of the Ellenbogen is a system of fore-dune ridges (Fig. 4.2A) which are arranged in several ridge sets (Fig. 4.2B). Ridge-set limits are geomorphologically marked by truncation of older fore-dune ridges. Striking of fore-dune ridges is west-northwest to east-southeast on the western Ellenbogen, turning to more northwest – southeast on the eastern Ellenbogen. A reconstruction of historical coastline changes on the Ellenbogen is depicted in Figure 4.2C. It shows that the southern coast of the Ellenbogen as well as the eastern headland were mostly stable during the last 140 years. The northern coast of the western Ellenbogen, however, experienced significant coastal progradation, which has expanded the area of the Ellenbogen by around 30 percent since 1958 (Fig. 4.2C). At the same time, the northern coast of the eastern Ellenbogen remained nearly unchanged. The western coast, which has retreated about 50 m since the mid 19th century, has been partly protected by a rock revetment since 1938 (Hundt, 1957; Fig. 4.2B). Whereas the eastern part of this revetment is nowadays protected on the seaward side by several fore-dune ridges, the western part still marks the coastline on the northwest edge of the Ellenbogen. Here, no significant beach growth occurred since the construction of the revetment in 1938.

A close-up of the northern coast of the Ellenbogen which shows the detailed coastline changes between 1998 and 2006 is depicted in Figure 4.3. Sediment that is transported to the North alongshore the western coast of the island is trapped north of the revetment. From here it is moved along the coast of the Ellenbogen towards the East, where significant net beach growth occurs. The tracing of historical coastlines shows that no net beach growth occurred north of the revetment. Here,

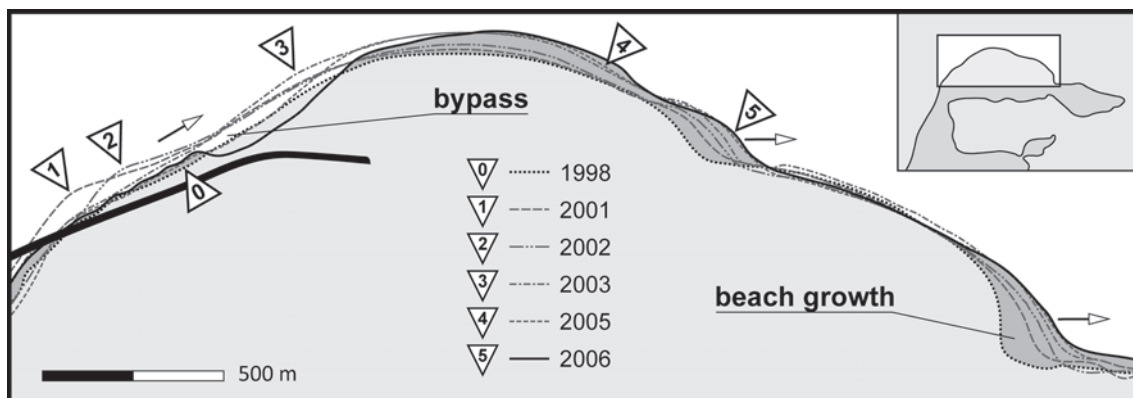


Figure 4.3: Close-up of the northern Ellenbogen showing evolution of MHT coastline position between 1998 and 2006, derived from georeferenced aerial photographs (compare Tab. 4.1). Arrows indicate direction of sediment transport and beach progradation. Note that beach progradation is restricted to the northern and eastern coast, whereas the northwest coast of the Ellenbogen is characterized by sediment bypass. The thick black line indicates the location of the rock revetment.



Figure 4.4: Easterly-directed view of the northern beach of the Ellenbogen with two fore-dune ridges (1, 2) separated from each other by a swale (3). The ridge to the right (1) is up to 5 m high and stabilized by *Ammophila arenaria*. The other ridge (2) lies more seaward and reaches a height of up to 1 m. Plant cover is denser on this younger ridge. Stranded goods in the swale (3) and at the base of the higher ridge indicates ephemeral overwash of the lower ridge (2) and flooding of the swale during storm surges. For scale see group of persons near the center of the photograph.

sediment is obviously only temporarily trapped, because the coastline of the year 2005 nearly corresponds to the one of 1998.

The evolution of fore-dune ridges is well illustrated along the beach of the northern Ellenbogen (Fig. 4.4), where two ridges are separated from each other by a swale. The seaward ridge is up to 1 m high and has a sparse overgrowth of the marram grass *Ammophila arenaria*. The more landward ridge is up to 5 m high and densely overgrown. Stranded goods in the swale and at the base of the higher ridge indicates ephemeral overwash of the lower ridge during storm surges.

4.4.2 Ground-penetrating radar

Six radar lines with a total length of 1,050 m were chosen out of around 16,000 m of GPR survey lines to document the subsurface sediment geometries of the Ellenbogen. Three lines (GPR lines 1, 2, 3) run perpendicular and three (GPR lines 4, 5, 6) parallel to the modern coastline (Fig. 4.2A). All radar data were collected using a 200 MHz antenna. GPR lines are shown with 5-times vertical exaggeration. Depth-readings refer to present German mean sea level (msl), which for northern Sylt is around 0.80 m below mean high-tide (MHT) (Behre (2003).

After Neal et al. (2002) and Neal (2004), the seismic stratigraphic interpretation concepts of Mitchum et al. (1977) can be directly adapted to the interpretation of GPR data. Based on the interpretation of reflection terminations, Gawthorpe et al. (1993) introduced a concept of radar stratigraphy. With regard to the often very complex reflection configuration of GPR sections, Bristow (1995) used a more qualitative approach to interpret sedimentary structures in shallow marine sandstones. Following Bristow et al. (2000), who summarized the term radar facies as 'repeated packages of reflections with similar character and geometry', 10 different radar facies were identified in the radar sections (Fig. 4.5). The identified radar facies were subdivided into three groups.

The first group contains radar facies with inclined reflections, the second group consists of radar facies that exhibit predominantly horizontal or curved reflections. In the third group, irregular reflections dominate. The terminology for reflection-geometry descriptions follows the terminology summarized by Neal (2004) after Campbell (1967), Mitchum et al. (1977), and Allen (1982).

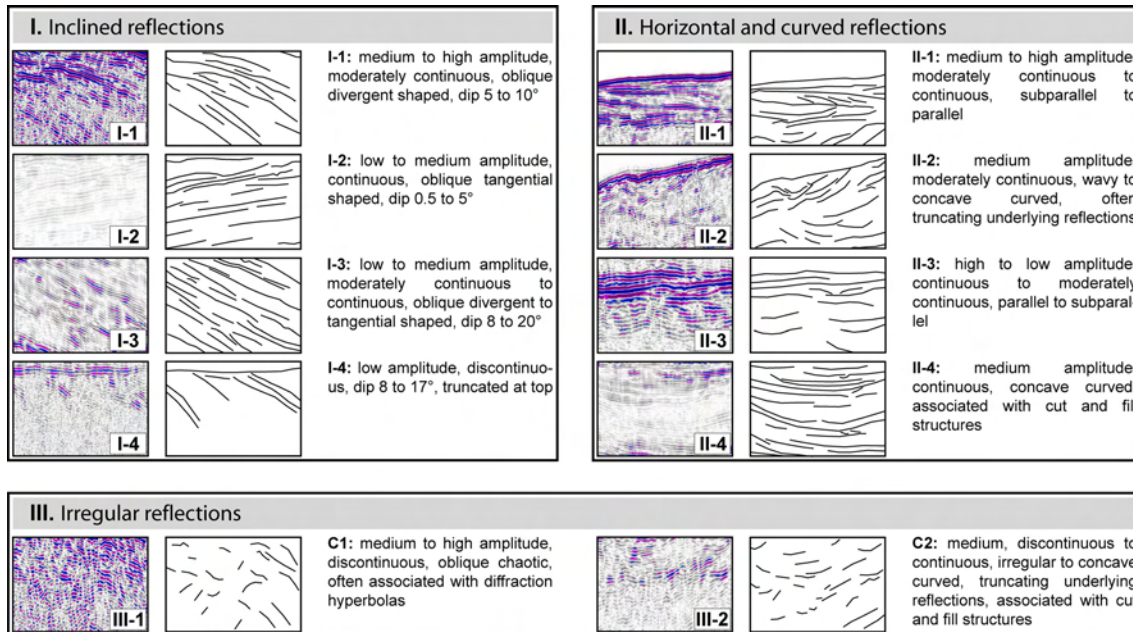


Figure 4.5: Radar-facies architectural elements identified in the radar sections. Based on geometrical criteria, the radar facies are split into three categories: inclined reflections, horizontal and curved reflections, and irregular reflections. Please note that GPR lines in this work are provided with a vertical exaggeration of 5-times.

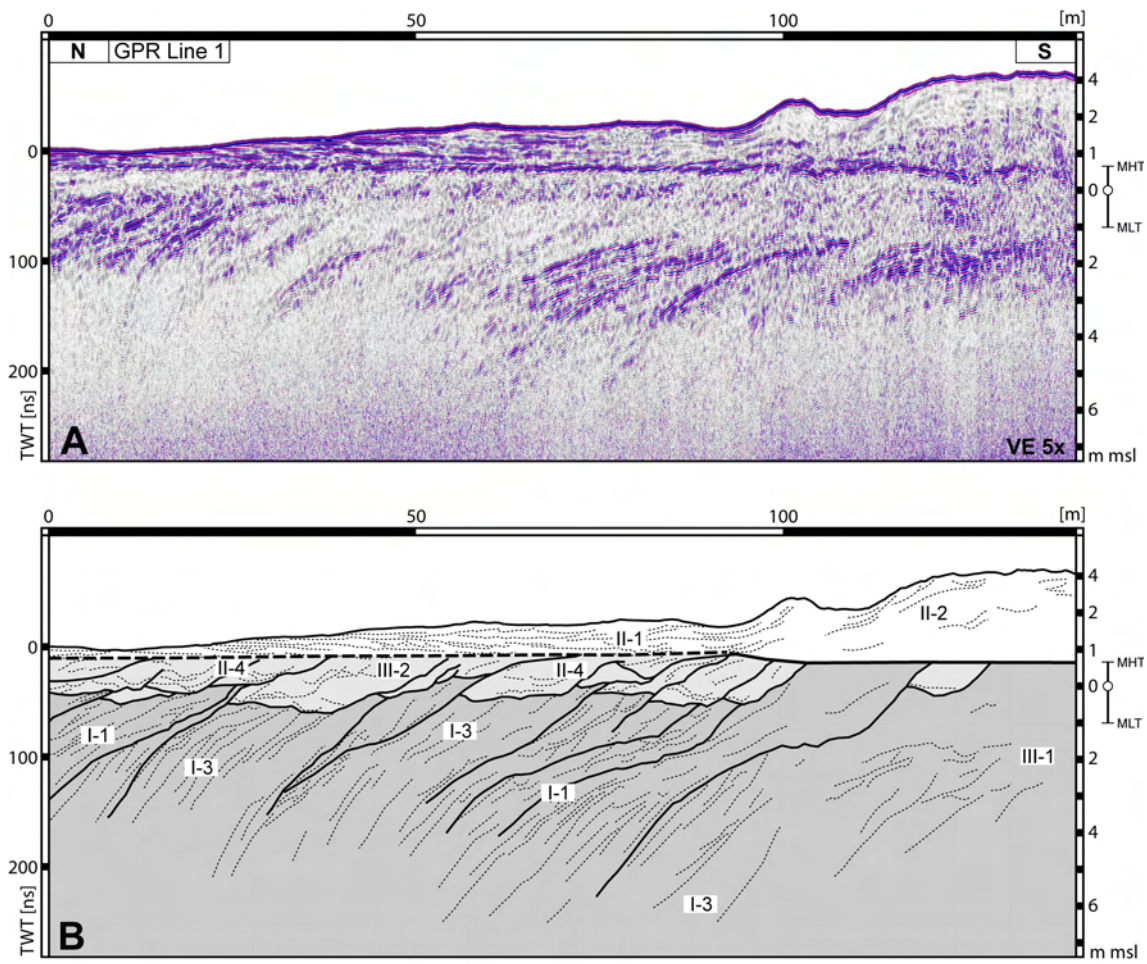
GPR Line 1

The north – south striking GPR Line 1 (Fig. 4.6A) has a maximum ground penetration of 260 ns two-way-traveltime (TWT). This corresponds to a depth of around 6 m bsl. In the northern part of the line, penetration depth decreases, probably because the base of the saline groundwater layer climbs up seaward. To the southern end of the GPR line, dunes of up to 4 m height distort the radar signal and limit penetration depth. In general, the data quality in this section is excellent down to a depth of 4 m bsl. Radar wave velocities are much higher in the dry sands in the upper meter of the profile than below the groundwater table. The depth scale provided in Figure 4.6 is split accordingly.

Based on the radar-facies architectural elements identified in the radar line, two different units can be distinguished (Fig. 4.6B). The upper unit contains subparallel to concave Rf II-2 reflections. On the northern flanks of the dune ridges, these reflections are partly cut by the terrain surface. Rf II-2 reflections are imaged in the higher dunes towards the southern end of the radar line. Reflections of the upper unit interfinger with reflections of the lower unit at a depth of 0.7 to 1.0 m asl. Only between meter 95 and 140 of the radar line, reflections of the lower unit are cut by overlying reflections.

The lower unit contains predominantly Rf I-1 and Rf I-3 reflections with a persistent 6.5° northward-dip down to a depth of 1.5 m bsl. In greater depths, the dip increases to values between 13 and 23°. Several erosive sigmoidal-shaped unconformities, dipping at 5 to 7°, are imaged as high amplitude reflections (Rf I-1). Unconformities are marked as solid lines in Figure 4.6B. Between 1 m asl and 1 m bsl, cut-and-fill structures are imaged by Rf III-2 reflections. These cut-and-fill structures are partly truncated at their northern side.

Reflection amplitudes vary along the GPR line. Highest amplitudes are recorded from the subparallel reflections (Rf II-1) of the upper unit and the sigmoidal shaped unconformities (Rf I-1) in the lower unit between 1 and 3.5 m bsl.



Sedimentary units (for all GPR profiles)

- eolian sediments of the backshore and fore-dune ridges
- cut-and-fill structures in the backshore caused by storm surges
- beach-drift sediments; dipping alongshore E-directed in the intertidal and coast normal beneath. Sediments are bundled into packages by erosion unconformities.
- SE-dipping strata interpreted as sediments of a sandy shoal (only Figs. 4.8, 4.10, 4.11)

Figure 4.6: **A:** North – south striking GPR Line 1. For exact location see Figure 4.2A. The left-hand axis presents the TWT in ns, the right-hand axis provides the position of the line relative to msl in meters. A mean radar-wave velocity of 0.06 m / ns was assumed for depth correction below 1 m asl. Note vertical exaggeration of radar line. **B:** Line drawing and interpretation of the radar data provided in A. Solid lines represent major erosion and bounding surfaces, dashed lines trace internal structures and sub-ordinate planes. Background colors refer to different

sedimentary units accordingly to the legend. Note that the sedimentary succession below 1 m asl is bundled by bounding surfaces and shows a northerly-directed progradation. Indices refer to radar-facies architectural elements (Fig. 4.5).

GPR Line 2

GPR Line 2 (Fig. 4.7A) shows a maximum ground penetration of 220 ns TWT (8.5 m), corresponding to a depth of around 4.5 m bsl. The data are of good quality down to a depth of around 170 ns TWT (2.5 m bsl). Penetration depth decreases along the radar line from southwest to northeast. This probably can be attributed to a seaward increase of the groundwater salinity. To the southwestern end of Line 2, dunes of up to 4 m height distort the radar signal in the subsurface. Beneath the dune slopes, reflections of Rf III-1 are imaged in the subsurface (Fig. 4.7B). The groundwater table, visible as a high-amplitude reflection in the raw data, was partly removed during processing, but is still visible in the GPR line. Its position is marked by an

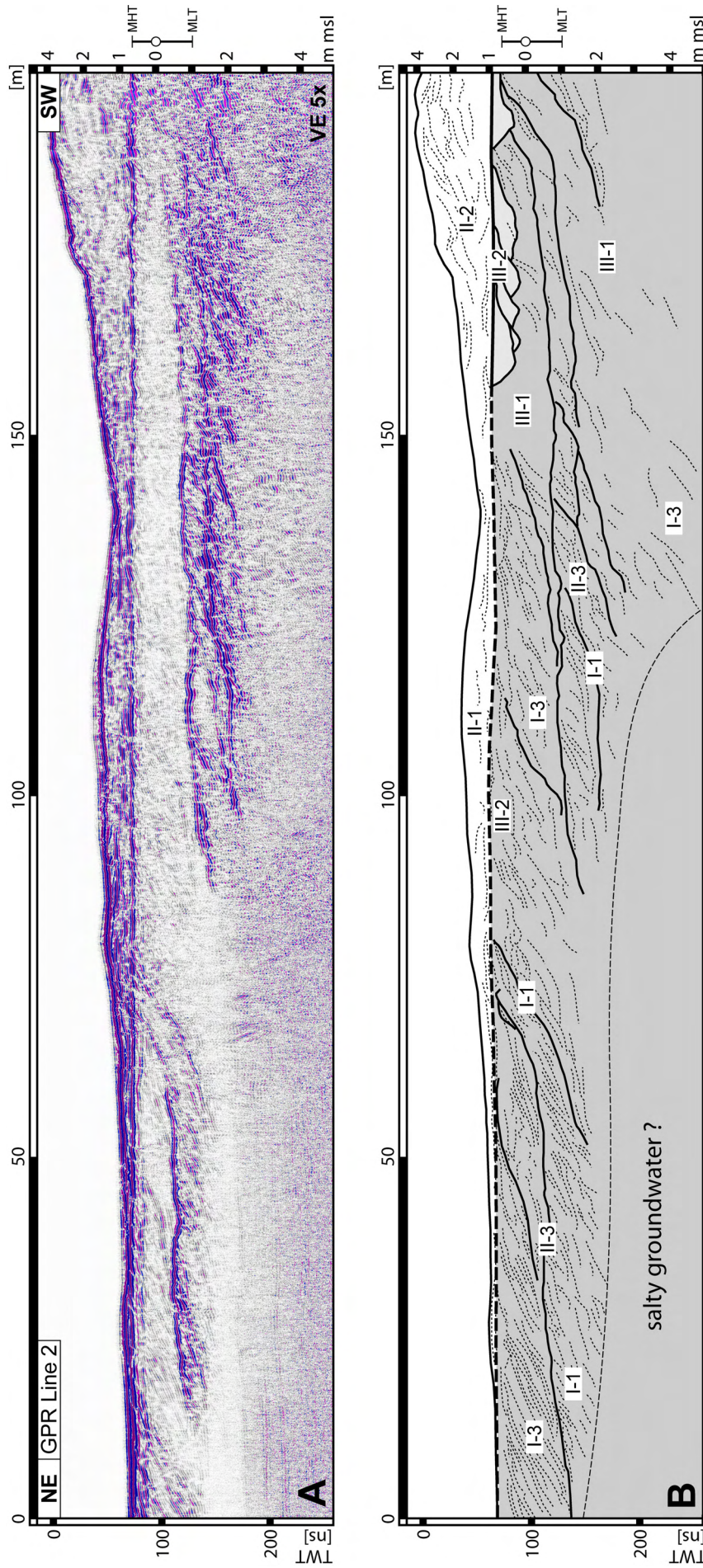


Figure 4.7: A: Northeast – southwest oriented GPR Line 2. Note strong reflections from dominant bounding surfaces between 1 m bsl and 1 m asl. B: Line drawing and interpretation of GPR line provided in A. The line is dominated by northeastward-dipping reflections that are bundled into shovel-blade shaped bodies by erosional unconformities at a depth of around 1 m bsl. Individual bodies show a lateral extension of up to 100 m. Internally high-amplitude reflections dominate (Fig. 4.7A). The erosional unconformities are traceable up to a depth of 1 m asl. Their proximal part forms an erosional scarp which is buried under a dune ridge. For legend and description of scales compare Figure 4.6. Exact radar-line location is depicted in Figure 4.2A.

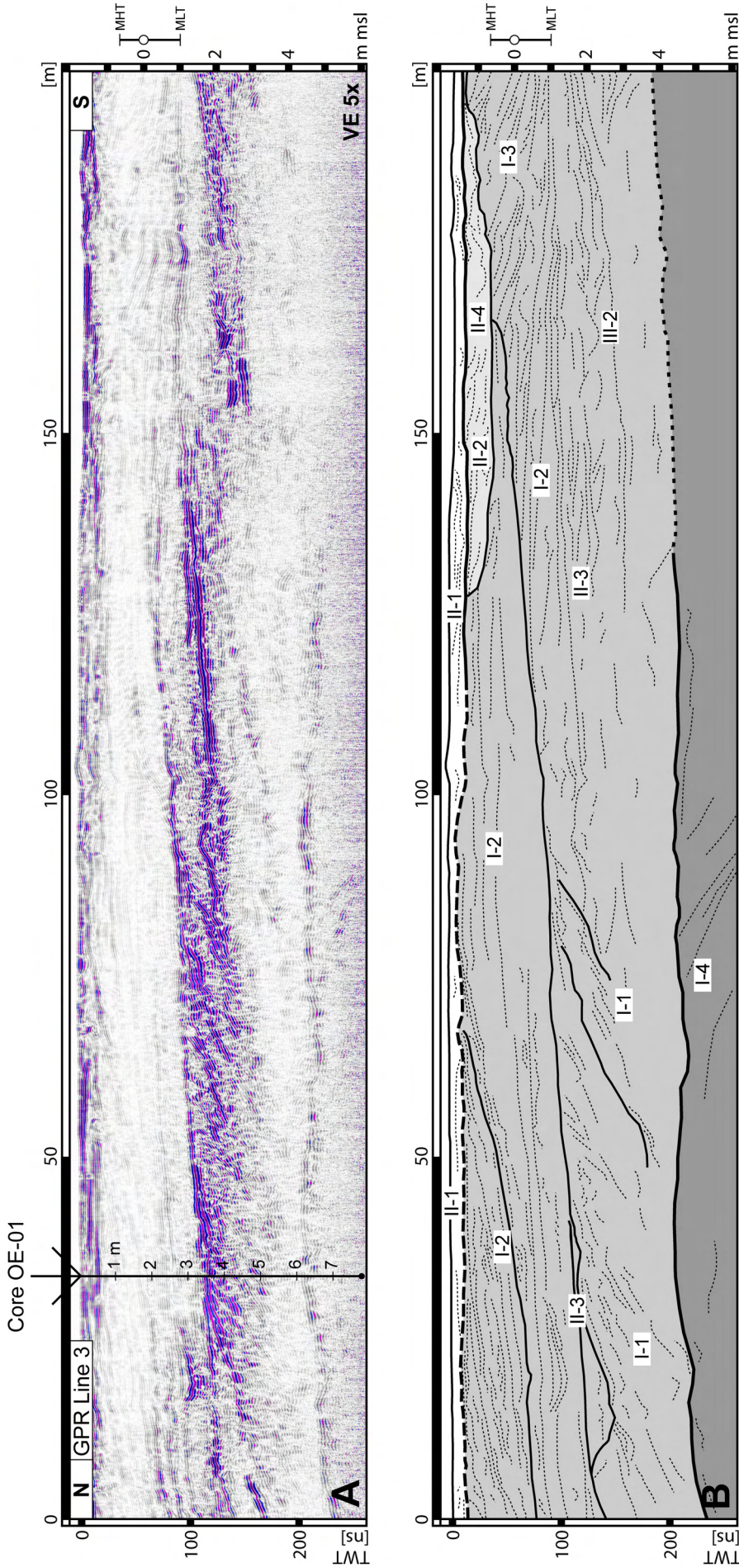


Figure 4.8: **A:** The north – south striking GPR Line 3. The position of Core OE-01 is marked. Depth readings at the core position refer to core depth. **B:** Line drawing and interpretation of GPR line provided in A. Dominant architectural element of this GPR line is an erosional unconformity at a depth of around 1 m bsl. This unconformity dips towards the North and separates gently from steeply dipping strata above the lower high amplitude strata. At a depth of 4 to 5 m bsl there is a second erosional unconformity. Below this unconformity only weak reflections are detected, indicating southward-dipping strata. For legend and description of scales see Figure 4.6, for exact radar-line location Figure 4.2A.

apparent break in reflector dip at a depth of around 1 m asl because of different radar-wave velocities in dry and saturated sediments. To account for this difference in radar-wave velocity, the depth scale was split at 1 m asl and condensed by a factor of 2 for values above groundwater level.

The position of the groundwater table parallels a change in the radar-facies architectural elements at 1 m asl. Above this horizon, subparallel or concave, partly gently northeastward-dipping reflections of Rf II-1 dominate between meter 0 and 150 of the radar line. The higher dunes between meter 150 and the end of the radar line are characterized by Rf II-2 reflections.

Below the groundwater table, down to the depth of the present mean-sea level, concave Rf III-2 reflections predominate between 150 m and the southwestern end of the radar line. They form cut-and-fill structures. The part of Line 2 between 0 and 150 m shows northeastward-dipping reflections of either Rf I-1 or Rf I-3 with a predominant dip of 3.5° . Rf I-3 reflections beneath 1 m bsl are bundled into shovel-blade shaped bodies, that form the dominant elements of GPR Line 2. They are up to 2 – 3 m thick and show a lateral extension of up to 100 m. Internally, geometrical elements of higher order constitute these bodies. The upper limit of these packages is formed by unconformities that show a northeasterly-dip of 3.5° down to the depth of msl (Rf I-1), and less than 0.5° in greater depths (Rf II-3). The lower border is marked by reflections that show a slightly steeper dip than the upper terminating reflection, and no significant flattening of the dip angle in greater depths. These reflections cross cut the position of the groundwater table and are traceable up to the level of 1 m asl (see Fig. 4.7B at meter 75). Underlying reflections are truncated.

Highest reflection amplitudes occur at a depth range of 0.5 m to 2.0 m bsl, and are associated with Rf I-1 reflections, truncating underlying structures. Another high amplitude reflections are imaged above 1 m asl in the northeast half of the line (Rf II-1).

GPR Line 3

A ground penetration of 250 ns TWT (8 m) was achieved in the north – south striking radar line 3 (Fig. 4.8A), which corresponds to 6 m bsl. Data are of good quality down to a depth of around 200 ns TWT (4 m bsl). Penetration depth is decreased to values around 170 ns TWT (4 m bsl) in the southern third of the GPR line, probably due to rising groundwater salinities. Three major architectural elements are to be observed in GPR Line 3.

The upper element consists of the topmost part of the line with subparallel Rf II-1 reflections, reaching down to a depth of around 1 m asl, all along the line. The lower limit of this unit is only partly truncating underlying reflections. Because of the latter, this contact is not continuously marked as unconformity.

Beneath the uppermost unit, there is a composite body which consists of 3 wedge-shaped elements with Rf I-2 reflections, thickening to the South. The upper two wedges display a faint internal northward-dipping layering. The third, lower wedge has a more complex internal stratigraphy. In general, the northward-dipping layers have a steeper dip (Rf I-1 reflections). The wedge is also characterized by southward-dipping Rf I-3 and trough-shaped Rf III-2 reflections at the southern end of the line.

The base of this middle architectural element dips towards the North gently. This contact has an irregular relief and it truncates underlying reflections. The lowermost stratigraphic unit of line 3 shows low amplitude Rf I-4 reflections, dipping towards the South.

Reflection amplitudes show strong variations in Line 3. Whereas highest amplitudes are restricted to the Rf I-1 reflections in the depth range of 0.5 to 2 m bsl, reflections above and beneath are of low to very low amplitude.

GPR Line 4

Ground penetration of the GPR Line 4 (Fig. 4.9A) is down to 200 ns TWT (5.5 m), down to a depth of 4 m bsl respectively. Data are of good quality down to a depth of 170 ns TWT (3.5 m bsl). Higher groundwater salinities probably are responsible for a slight east – west decrease of the penetration depth.

Based on the radar-facies architectural elements, three different units can be distinguished which are separated by truncation surfaces that are located at the depth of approximately 1 m and 0.5 m asl respectively (Fig 9B).

The upper unit is characterized by subhorizontal Rf II-1 reflections. In the middle part of the radar line (around 75 m) reflections are slightly convex. Shallow cut-and-fill structures are expressed by reflections of Rf II-4. They extend up to 20 m along the radar line and reach a depth of 0.6 m asl.

The middle unit of line 4 between 1 to 0.5 m asl, is composed of subparallel reflections (RF II-1) and wavy to concave curved Rf II-2 reflections. The unconformity at the base of the unit gently dips towards the East.

The lower unit of line 2 contains a series of composite bodies delimited by eastward-dipping Rf I-1 reflections, which extend at least down to a depth of 4 m bsl where reflections are lost in the background noise. Rf I-1 reflections dip at less than 2° between 0.5 and 2.5 m bsl, and at around 7° in greater depths. Low amplitude reflections within the bodies are attributed to Rf I-2.

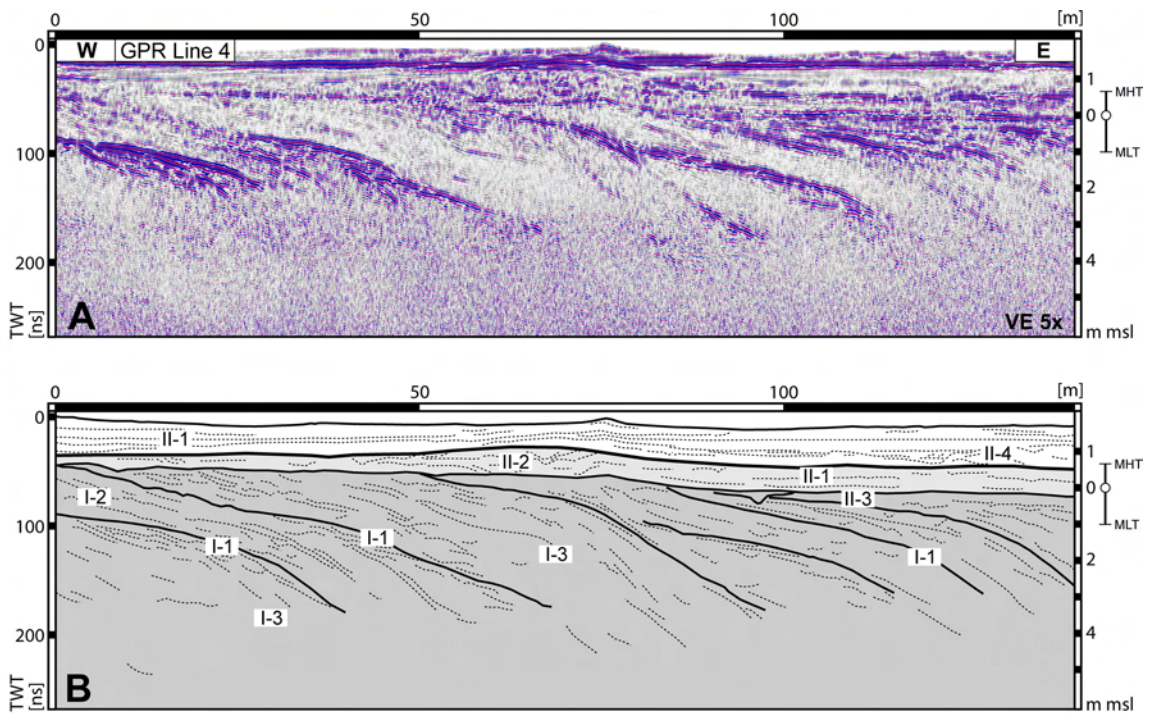


Figure 4.9: A: West – east oriented GPR Line 4. B: Line drawing and interpretation of GPR line provided in A. Above an unconformity at a depth of around 0.5 m asl, horizontal strata occur. Below these strata, a channel is imaged which reaches a thickness of up to 1.5 m. This channel is lengthwise cut in this section. Predominant architectural element of this line are eastward-dipping sediment packages that are bundle by erosional unconformities. For legend and description of scales compare Figure 4.6. Exact radar-line location is depicted in Figure 4.2A.

GPR Line 5

The west – east striking GPR Line 5 (Fig. 4.10A) shows a ground penetration down to 300 ns TWT (8 m). This corresponds to a depth of 6.5 m bsl. Data quality is good down to a depth of 200 ns TWT (4.5 m bsl). On the basis of the radar-facies architectural elements, four different units can be distinguished in this radar line (Fig. 4.10B).

Nearly horizontal reflections of Rf II-1 are the predominant elements in the upper unit, which reaches down to a depth of 1.5 m asl at maximum. The lower limit of this unit is formed by reflections that truncate underlying structures, and is therefore marked as unconformity in Figure 4.10B.

The second unit extends from 1.5 m asl down to 2 m bsl. It is characterized by eastward-dipping Rf I-2 and Rf I-3 reflections. In some parts, irregular and concave reflections of Rf III-2 are present. Rf I-2 reflections are bundled into packages by surfaces that truncate underlying structures, and exhibit a slightly upward curved shape. The contact between the second unit and reflections beneath is formed by a surface that truncated underlying structures, and can be traced along the radar line. This surface is marked as uniformity in Figure 4.10B and is slightly dipping towards the East. Note that there is a thin layer of planar bedded reflections just above the unconformity (Fig. 4.10B).

The third unit of Line 5 is a westward thickening composite wedge with eastward-dipping Rf I-2 and Rf I-3 reflections predominating, bundled into packages by reflections that show an upward curved shape. Compared to the second unit, reflection

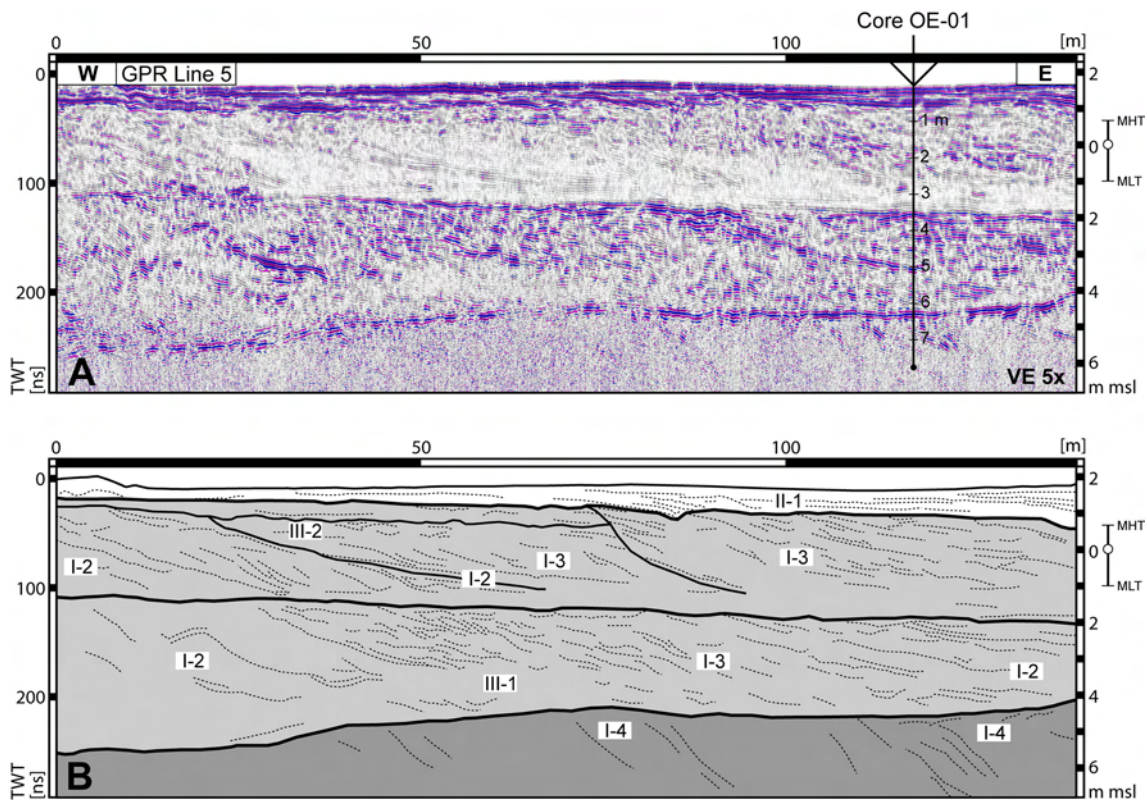


Figure 4.10: **A:** The west – east striking GPR Line 5. The position of Core OE-01 is marked at meter 120 of the line, whereas provided depth readings refer to core depth. **B:** Beside the uppermost, horizontally stratified interval the line is dominated by eastward-dipping strata. Erosional unconformities at depths of 1 m asl, 2 m and 4 to 5 m bsl subdivide the sedimentary succession. Please note that strata below the lowermost unconformity show a significant steeper dip. For legend and description of scales see Figure 4.6; exact radar-line location is depicted in Figure 4.2A.

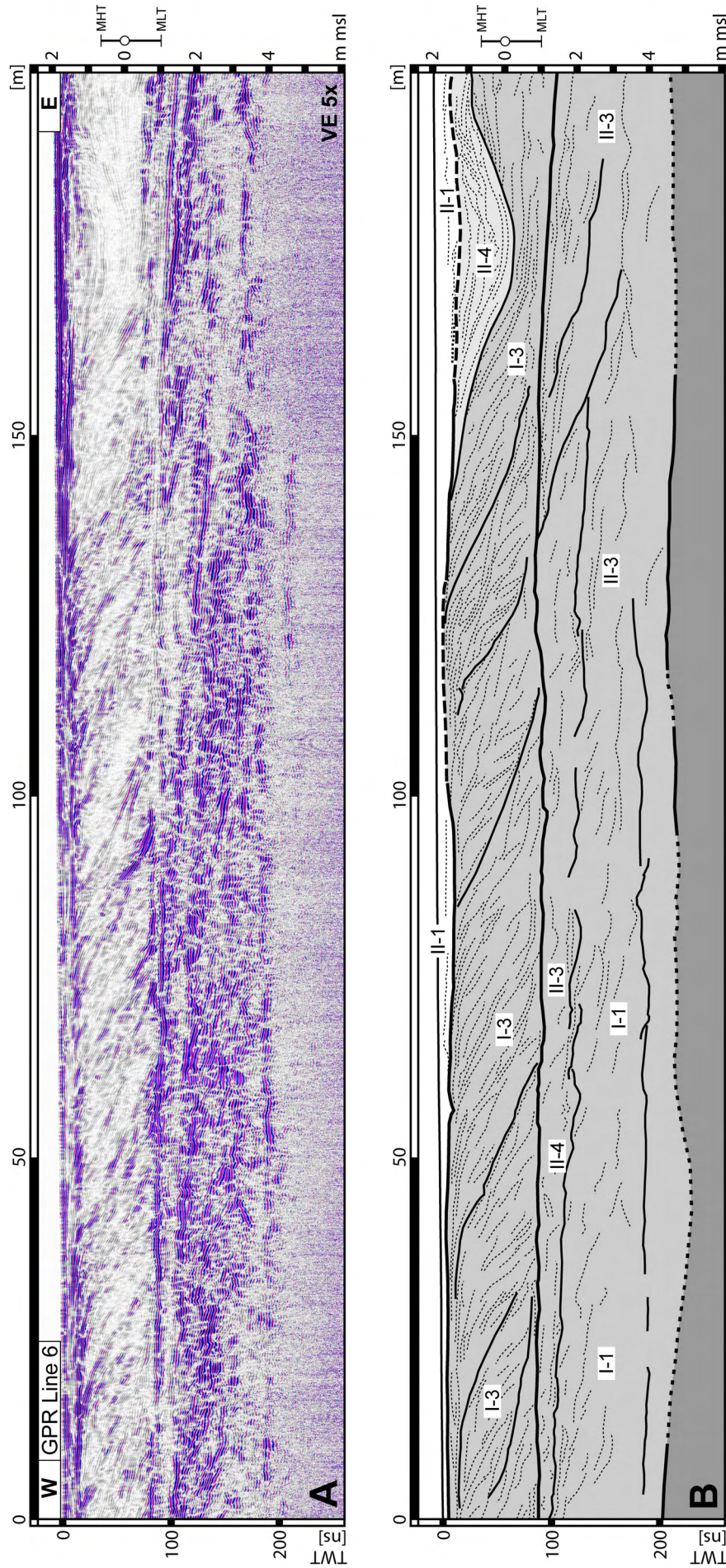


Figure 4.11: **A:** The west – east oriented GPR Line 6. Note the interval of high amplitude reflections between 1 and 3.5 m bsl. **B:** Line drawing and interpretation of the radar line provided in Figure 4.11A. A dominant erosional unconformity occurs at a depth of 1 m bsl, gently dipping towards the East. Strata above this unconformity show a steep eastward-dip and are subdivided by unconformities of higher order. Strata below 1 m bsl gently dip towards the East or show wavy shape. At a depth of 4.5 m bsl, weak reflections indicate a horizontal surface that can be correlated with an erosional unconformity imaged in GPR lines 3 and 5 (Figs. 4.8, 4.10) in the same depth. Legend and description of scales are provided in Figure 4.6. The exact radar-line location is depicted in Figure 4.2A.

amplitudes are slightly higher in this unit. The third unit is delimited against the lowermost unit by a surface that truncates underlying structures. This unconformity shows an irregular relief, and rises from 5.5 m bsl at the western end of the radar line up to 4 m bsl at the eastern end.

The fourth and lowermost unit only contains weak reflections that are truncated at their top (Rf I-4). Dip of reflections is towards the East, and slightly steeper than in the upper units.

GPR Line 6

This west – east oriented line (Fig. 4.11A) has a maximum ground penetration of 220 ns TWT (7 m). This corresponds to a depth of 5 m bsl. Data are of good quality down to 180 ns TWT (4 m bsl). In addition to a cut-and-fill structure between 140 and 200 m of the radar line, three different units can be distinguished above 4 m bsl based on the reflection geometries. Below 4.5 m bsl, only few reflections are imaged.

The first unit which reaches down to 1.3 m asl consists of subhorizontal reflections (Rf II-1). There is no well-defined lower limit of this unit, and radar-facies interfingering with the reflections of the second unit is present (expressed in Fig. 4.11B by a bold dashed line).

The second unit, between 1.3 m asl to 1 m bsl, is characterized by Rf I-3 reflections dipping to the East at around 6° . Reflections are of low to medium amplitude and bundled into packages by sigmoidal or tangential shaped reflections. Between 140 and 200 m of the radar line, there are concave shaped reflections (Rf II-4) that cut into the reflections of this unit down to 0.2 m bsl. This cut-and-fill structure can laterally be traced on other GPR lines. It forms an elongated trough with the long axis striking northeast – southwest. The second unit is delimited against the unit beneath by a surface that cuts underlying reflections, and is therefore marked as unconformity in Figure 4.11B. Note horizontal low amplitude reflections just above the unconformity between meter 100 and 200 of the line.

The third unit extends down to 4.5 m bsl. High amplitude reflections predominate (Rf II-3 and I-1). The Rf I-1 reflections gently dip to the East with less than 1° down to a depth of 3.5 m bsl, and are subhorizontal in greater depths. Most reflections are wavy and of Rf II-3, but concave reflections (Rf II-4) also occur. The uppermost part of the third unit, between meter 0 and 150 of the line, is characterized by subhorizontal reflections of Rf II-3 and II-4. These reflections are bordered against other reflections of this unit by an erosive surface, dipping towards the East down to a depth of 2.5 m asl (Fig. 4.11B).

Beneath the third unit, there are only minor reflections imaged, so that no further statements can be made. A horizontal reflection at a depth of 4.5 m bsl, visible between 110 and 155 m of the radar line, probably correlates to similar reflections imaged in the GPR lines 3 and 5 at comparable depths (compare Figs. 4.8 and 4.10).

Higher reflection amplitudes are restricted in this radar line to the first and to the third unit. The second unit, between 1.3 m asl and 1 m bsl, is characterized by low to medium amplitude reflections. Here, amplitude variations are much less than in the third unit.

4.4.3 Sediment cores

Two sediment cores, OE-01 and WE-02 were taken on the Ellenbogen (Fig. 4.12). These cores provided not only sedimentological data but also material for age dating of shells using AMS ^{14}C . For exact coring locations see Figure 4.2A.

Core OE-01

Core OE-01 is located 38 m from the northern starting point of GPR Line 3 (Fig. 4.8A), and 118 m from the western starting point of GPR Line 5. The core is 7.85 m long and reaches down to a total depth of around 6.0 m bsl. Characterizing grain-size parameters for Core OE-01 are summarized in Table 4.2.

Variations of the mean grain size define five intervals (Fig. 4.12A). The lowermost interval between the bottom of the core and 620 cm (4.4 m bsl) consists of interbedded medium and fine sands. The second interval is between 620 and 350 cm (4.4 m to 1.7 m bsl), showing a slightly coarsening trend, interrupted by some abrupt changes between medium sand and fine sand beds. Compared to the first interval, the second interval is finer grained (around 2.5 phi) and characterized by more stable grain-size conditions. The third interval, between 350 cm and 300 cm (up to 1.2 m bsl) shows an fining-upward trend. The fourth interval, between 300 cm and 20 cm, exhibits an coarsening upward, followed by stable grain-sizes conditions in its upper part. Medium sand, around 1.8 phi, predominate here. The fifth interval comprises the uppermost 10 cm of the core. It shows significantly finer sediments (around 5.0 phi) than the rest of the core.

Sorting and mean grain size in Core OE-01 are in general linearly correlated, and the five intervals are also reflected in the sorting data (Fig. 4.12B). Coarser-grained sediments are better sorted than finer-grained sediments. The first interval shows no significant sorting trend, but the curve shows abrupt changes between sediments of different sorting. The second interval exhibit an overall upward trend towards better sorting of the sediment. Sediments in the third interval show abrupt changes in sorting, but no clear trend though. The sediments in the fourth interval are characterized by an upward trend towards better sorting. The most poorly sorting in Core OE-01 is found in the uppermost interval.

The previously described curves for mean grain size and sorting notwithstanding, the skewness of the frequency distribution of Core OE-01 (Fig. 4.12C) only allow to define two different intervals instead of five. There is a lower interval which extends up to a depth of 350 cm (1.7 m bsl) and comprises the previously defined intervals 1 and 2. Here, skewness data show a predominantly fine to very fine skewed grain-

Core		Mean grain size (phi)		
ID	length	maximum	minimum	average
OE-01	785 cm	0.52 coarse sand	5.60 coarse silt	2.44 fine sand
WE-02	680 cm	1.39 medium sand	2.93 fine sand	1.71 medium sand

Core		Sorting (phi)		
ID	length	maximum	minimum	average
OE-01	785 cm	0.43 well sorted	2.99 very poorly sorted	1.14 poorly sorted
WE-02	680 cm	0.44 well sorted	2.11 very poorly sorted	0.62 moderately well sorted

Core		Skewness of the frequency distribution (phi)		
ID	length	maximum	minimum	average
OE-01	785 cm	-0.22 coarse skewed	0.71 very fine skewed	0.34 very fine skewed
WE-02	680 cm	-0.13 coarse skewed	0.73 very fine skewed	0.20 fine skewed

Table 4.2: Characteristic grain-size parameters for sediment cores presented in Figure 4.12

size distribution, reflecting a predominance of finer grain sizes in the distribution curve. There exist significant variations, a clear trend, however, is not to be observed. The upper interval extends from 350 cm depth to the surface and comprises the previously defined intervals 3 to 5. Here the skewness of the frequency distribution

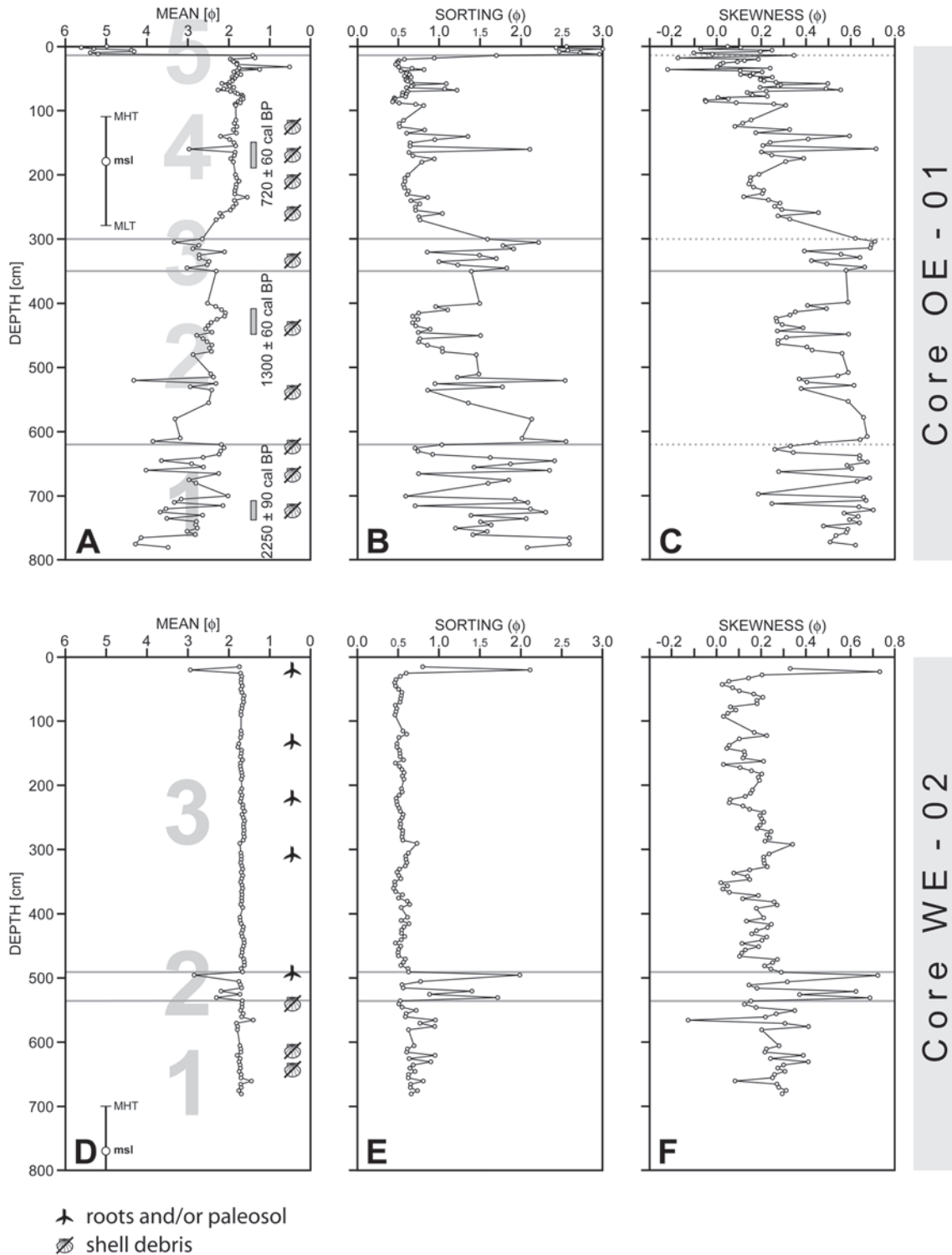


Figure 4.12: Grain-size data of Cores OE-01 (A-C) and WE-02 (D-F). For exact core locations see Figure 4.2A. **A, D:** Mean-grain size for Core OE-01 and Core WE-02 respectively. Bar on left side of grain-size curves provide recent intertidal range with respect to msl; available ¹⁴C-ages are shown on the right side of the curve with bar indicating sampled interval. The core intervals described in the text are labeled with grey numbers in the back. **B, E:** Sorting of the investigated sediment samples based on grain-size in logarithmic phi scale. **C, F:** Skewness of the frequency distribution, based on grain-size classes in logarithmic phi scale.

shows an upward trend towards less skewed sediments. This reflects an increase in symmetry of the grain-size distribution.

Core WE-02

Core WE-02 is located on the western Ellenbogen on top (7.7 m asl) of a west – east striking dune ridge (Fig. 4.2A). The core is 6.8 m long and reaches down to a depth of 0.9 m asl. Characterizing grain-size parameters for Core WE-02 are summarized in Table 4.2.

Based on variations of the mean grain size (Fig. 4.12D), three different intervals can be distinguished in this core. The first interval, between the bottom of the core and 535 cm (2.35 m asl), is characterized by minor variations in mean grain size. Exceptions are two samples with coarser sediments at 565 cm and 660 cm. The second interval, between 535 cm and 495 cm (2.35 and 2.75 m asl), contains three samples that are significantly finer grained than the rest of this interval. The third interval, between 495 cm and the top of the core, has a uniform grain size, and is characterized by medium sands in the range of 1.60 to 1.77 phi.

Variations of mean grain sizes are parallel to the sorting trends (Fig. 4.12E). Like in Core OE-01, sorting and mean grain size of this core are in general linearly correlated, with coarser sediments being better sorted than finer sediments. The first sedimentary interval is characterized by interbedded layers of moderately-well to moderately sorted sediments, the second interval exhibits strong variations, and its sediments are generally less well sorted. The third interval, is characterized by minor sorting variations. With exception of the fine-grained sample at 20 cm depth, which is very poorly sorted, the sediments in the third interval are moderately-well sorted (around 0.54 phi).

Skewness of the frequency distribution (Fig. 4.12F) reflects the three intervals defined before (Fig. 4.12F). The first interval, up to 535 cm depth (2.35 m asl), is characterized by a slightly upward trend towards a more symmetrical grain-size distribution. The second interval, between 535 and 495 cm depth (up to 2.75 m asl), is characterized by abrupt changes between nearly symmetrical and strong positively skewed grain-size distributions. The third interval, from 490 cm depth to the surface, exhibits an overall trend towards a more symmetrical grain-size distribution. It also shows variations of the skewness data, but of minor amplitude.

Bioclasts occur in the lower part of the core up to 500 cm (2.2 and 2.7 m asl). In the upper part there are rootlets and several dark grey stained layers of 1 – 2 cm thickness.

4.4.4 AMS ¹⁴C-dates

The results of the AMS ¹⁴C-investigations are depicted in Table 4.3. All dated samples are from Core OE-01. Associated GPR lines 3 and 5 (Figs. 4.8, 4.10) show how the ages relate to the sedimentary units. For the northeastward-dipping strata above the major unconformity, at a depth of 1 – 2 m bsl, an age range of 660 – 775 cal BP (averaged to 720 ± 60 cal BP) was determined. Strata beneath the unconformity date back to 1241 – 1366 cal BP (averaged to 1300 ± 60 cal BP). And southeastward-dipping strata beneath the second major unconformity, which is located at a depth of 4 – 5 m bsl, are deposited probably between 2160 and 2335 cal BP (averaged to 2250 ± 90 cal BP).

Interval	Sample	Lab. ID	¹⁴ C age	Res. corr.	95.4 % (2σ) cal age ranges		
Core OE-01							
						rounded	
150 - 190 cm	mollusk	KIA 31638	775 ± 25 yr BP	not applied	660 - 775 cal BP	720 ± 60 cal BP	1175 - 1290 AD
410 - 450 cm	mollusk	KIA 31639	1350 ± 30 yr BP	not applied	1241 - 1366 cal BP	1300 ± 60 cal BP	584 - 709 AD
710 - 740 cm	mollusk	KIA 31640	2190 ± 30 yr BP	not applied	2160 - 2335 cal BP	2250 ± 90 cal BP	386 - 211 BC

Table 4.3: Radiocarbon ages obtained by AMS ¹⁴C-dating of marine mollusk shells from Core OE-01 (compare Fig. 4.12A). Calibration of conventional ¹⁴C-ages was performed using the software Calib 5.0 (Stuiver & Reimer, 1993). Marine calibration data are from Hughen et al. (2004). As the local reservoir effects are unknown, no reservoir corrections were applied to the data.

4.5. Discussion

4.5.1 Sedimentary architectural elements

The tracing of former shorelines based on historical maps reveals that the fore-dune ridges on the Ellenbogen are oriented more or less parallel to the shoreline. Hence, the ridge orientation can be used to define the orientation of the GPR lines with respect to the former coastline.

Beach normal sections (A – A' in Fig. 4.13) are characterized by unconformities (F in Fig. 4.13) that show a seaward dip of 3 to 4° down to the depth of msl, less than 0.5° at the level of msl, where they can be traced up to 150 m, and around 1° at their distal end. These unconformities truncate underlying strata (G) and are often associated with a morphological ridge (A) at their steep, landward termination. Several unconformities are arranged in echelon along coast normal sections. Strata above these unconformities (D) are nearly horizontal to gently seaward-dipping, and dip angle increases towards the sea. Some minor unconformities interrupt these prograding sequences. At the base of this seaward-dipping strata, directly overlying the major unconformities, there is an up to 0.3 m thick package of horizontal strata (E) that appears nearly transparent in the data. Strata below the major unconformities exhibit a comparable steep seaward dip and cause high amplitude reflections in the GPR data. The basal contact of these strata is poorly imaged in the GPR data, but it can be assumed that it exhibits a downlap configuration onto an unconformity which is imaged in GPR lines on the eastern Ellenbogen at a depth of 4 to 5 m bsl (Figs. 4.8, 4.10, 4.11). The uppermost part of the profiles shows horizontal or gently seaward-dipping strata (B) with a predominantly conformable contact to steep dipping strata beneath. Only in some parts truncation of dipping strata is imaged. Cut-and-fill structures (C) are imaged between 1 m bsl and 1 m asl.

Several coast parallel sand ridges occur in the backshore zone of the northern Ellenbogen beach (Fig. 4.4). With increasing distance from the shoreline, the ridges are higher, and covered more and more by the marram grass *A. arenaria*. According to Huiskes (1979) and Willis (1989) *A. arenaria* grows best when regularly covered by windblown sand, and Figure 4.4 shows that the grass colonizes the ridges in a very early stage. Such a vegetation cover of the ridges in the past is reflected by the occurrence of the rootlets and grey stained thin layers, interpreted as paleosols in Core WE-02, which was drilled through one of these ridges. Grain-size data from the core show that ridges are composed of moderately-well sorted medium sands, which exhibits only minor variations in grain-size and sorting. The core is located in an area, where, based on the disappearance of bioclasts in the core above 500 cm, a change from a marine to a terrestrial sedimentation eventually occurred between 1870 and 1928 (Fig. 4.2C), as dated by historical maps. Ridge top is nowadays located at 7.7 m asl, which implies that ridge growth have been very fast. It is proposed that ridge

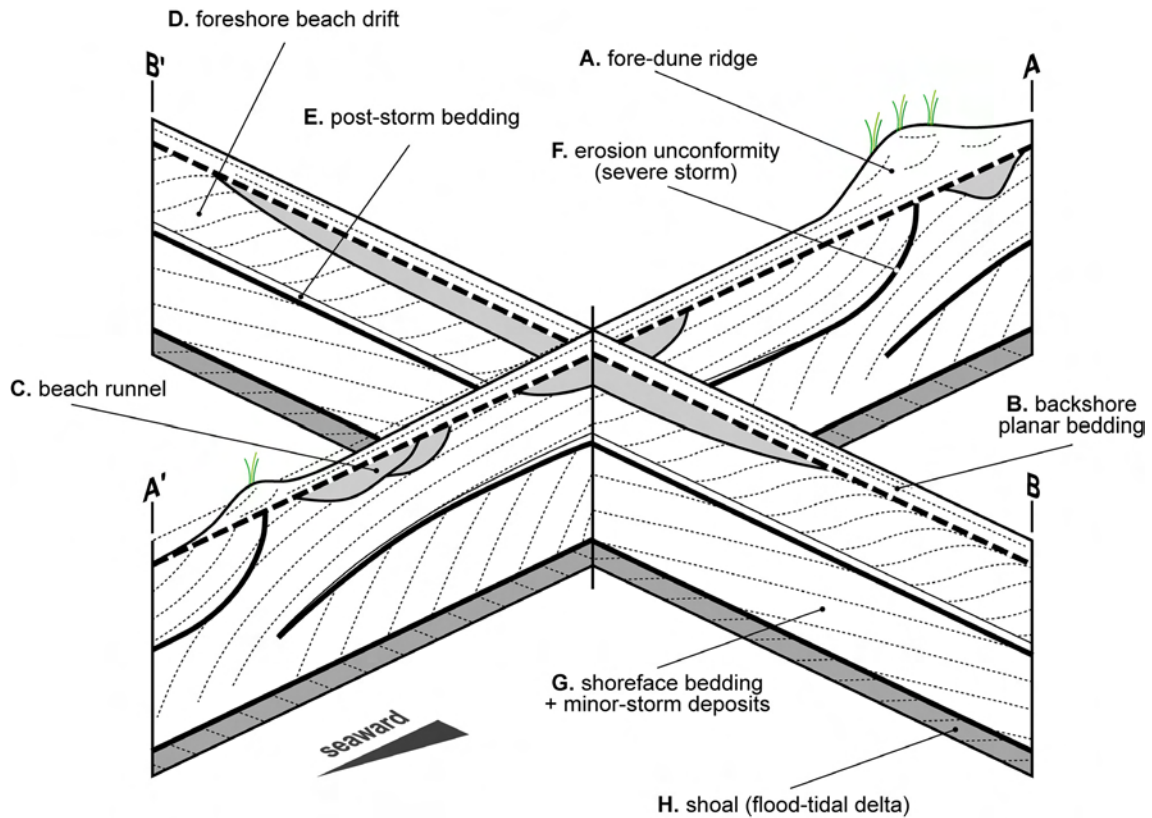


Figure 4.13: Simplified model showing the main sedimentary architectural elements of the Ellenbogen. Line A – A' runs perpendicular, B – B' parallel to the shoreline. Alongshore-dipping strata in the upper part and beach-normal dipping strata in the lower part are separated from each other by erosional unconformities. These unconformities dip into a seaward direction and show a scarp at their proximal termination. Several unconformities are arranged in echelon. Trapping of sand at the scarps leads to the development of fore-dune ridges that are stabilized by plants. Beach runnels are attributed to ephemeral storm events.

growth is an eolian process, achieved through sediment trapping by the marram grass *A. arenaria*.

The west – east striking ridges on the Ellenbogen are always situated above the steep proximal termination of a major unconformity in the subsurface (Fig. 4.7). The erosional scarps in the subsurface probably account for the initial trapping of windblown sand and the formation of an embryonic dune ridge.

Sections oriented parallel to the coast (B – B' in Fig. 4.13) reveal that the major unconformities (F in Fig. 4.13) extend along the coast, separating horizontal to gently alongshore-dipping strata (G) above, from steep alongshore-dipping strata (D) below. In both sedimentary units, above and below the unconformity, there are small unconformities imaged. At the base of the upper unit (G), directly overlying the unconformity, there is a horizontally stratified layer up to 0.3 m thick that appears nearly transparent to the GPR (E). Coast-parallel sections show that the cut-and-fill structures (C), which are described for the beach normal sections, extend along the beach over a great distance, forming channel shaped structures. The near-surface part of coast parallel sections is characterized by horizontal strata (B) that show truncation in some parts.

Whereas strata above the major unconformities, down to approximately 1 m bsl, exhibit low reflection amplitudes, the strata beneath show significantly stronger reflections (Figs. 4.7, 4.8, and 4.11). A comparison of grain-size data from Core OE-01 (Fig. 4.12) with GPR Lines 3 and 5 (Figs. 4.8 and 4.10) show that high amplitude

Architectural element		Environment	Depth range (msl)	Characteristic radar-facies elements		Sedimentary Characteristics
				shore normal	shore parallel	
A	fore-dune ridge	backshore / dunes	above 1 m	II-2; (II-1); (II-4)	not observed	Beds: subparallel to parallel or wavy to concave curved, truncations are common Unit: shore-parallel ridge, up to 1500 m long, 50 m wide, and 10 m high
B	backshore planar bedding	backshore	above 0.7 m	II-1	II-1	Beds: horizontal or gentle seaward dipping, parallel, seldom concave curved Unit: up to 1 m thick, extending along beach, interfingers with fore-dune ridge
C	beach runnel	backshore	-1 m to 1 m	II-4; III-2	III-2; II-2; II-1	Beds: wavy to concave curved, subparallel to irregular, truncations are common Unit: base erosive, forms cut-and-fill structure parallel shore, up to 200 m long, 30 m wide, and up to 2 m thick, seaward limit often truncated by younger runnel
D	beach drift	foreshore	-1 m to 0.7 m	I-3; I-2; I-1; (III-1)	I-2; I-3	Beds: oblique divergent to tangential, or sigmoidal shaped, partly subparallel in shore-normal direction, dip 5-10° alongshore, and 0.5 to 5° seaward Unit: overlies major erosion unconformities, prograding sequence interrupted by unconformities of smaller scale (see text), lower meter coarsening upward
E	post-storm bedding	foreshore to shoreface	up to -0.5 m; lower border not observed	II-3	II-3	Beds: parallel erosion unconformities Unit: up to 0.3 m thick, directly overlies erosion unconformity, fining upward
F	erosion unconformity	backshore to shoreface	up to 1 m; lower border not observed	single I-1 reflection (proximal) and II-3 (distal)	single I-1 reflection (proximal) and II-3 (distal)	truncates underlying structures, dip 3-4° down to msl (proximal part), 0.5° (middle), 1° (distal), traceable over 150 m shore-normal and up to several hundred meters alongshore, in shore-normal direction unconformities are arranged in echelon
G	shoreface bedding + storm deposits	shoreface	-5 m to -1 m	I-1; I-3; II-3; III-1	I-1; I-2; I-3; II-3; III-1	Beds: shore-normal: oblique divergent to tangential, or sigmoidal shaped, wavy; alongshore: predominantly parallel to subparallel, wavy, dip 5-8° shore-normal and 0.5 to 5° alongshore Unit: truncated at top by unconformity, poorly sorted, coarsening upward
H	shoal	flood-delta	up to -4 m; lower border not observed	I-4	I-4	Beds: landward dipping at 8-17°, topsets eroded, bottomsets not observed Unit: probably incorporated during spit progradation, dimensions unknown, coarsening upward, poorly sorted

Table 4.4: Sedimentary architectural elements defined for the Ellenbogen hooked spit. Identifying capitals refer to simplified model of the main sedimentary architectural elements of the Ellenbogen, depicted in Figure 4.13.

reflections between 1 and 3 m bsl correlate with an interval of strong variations in grain size and sorting. By contrast, the transparent interval between 1.5 m asl and 1 m bsl shows more stable grain-size conditions. As greater variations of grain size and sorting can account for higher radar-wave amplitudes due to the higher electromagnetic impedance between two consecutive sediment layers, abrupt changes in grain size and sorting are interpreted as the cause of the high radar-wave amplitudes.

In the lines analyzed, brusque changes of sediment texture (Fig. 4.12) are thought to reflect marine sedimentation under different hydrodynamic conditions that might have been triggered by variations of the wave energy. Taking into account the minor erosional unconformities imaged in the radar data, the strata below 1 m bsl are concerned as a record of alternating fair-weather and storm conditions (G in Fig. 4.13).

At the western Ellenbogen, the high amplitude interval lies below 1 m bsl and below 1.5 m bsl at the eastern Ellenbogen. At the western Ellenbogen, this depth coincides with the level of recent mean low-tide (MLT). Here, GPR lines are located in an area where the change from marine to terrestrial sedimentation occurred not longer than 60 years ago (Fig. 4.2C). At the eastern Ellenbogen, GPR lines lie in an area that is situated near or above msl since 720 ± 60 years, as indicated by

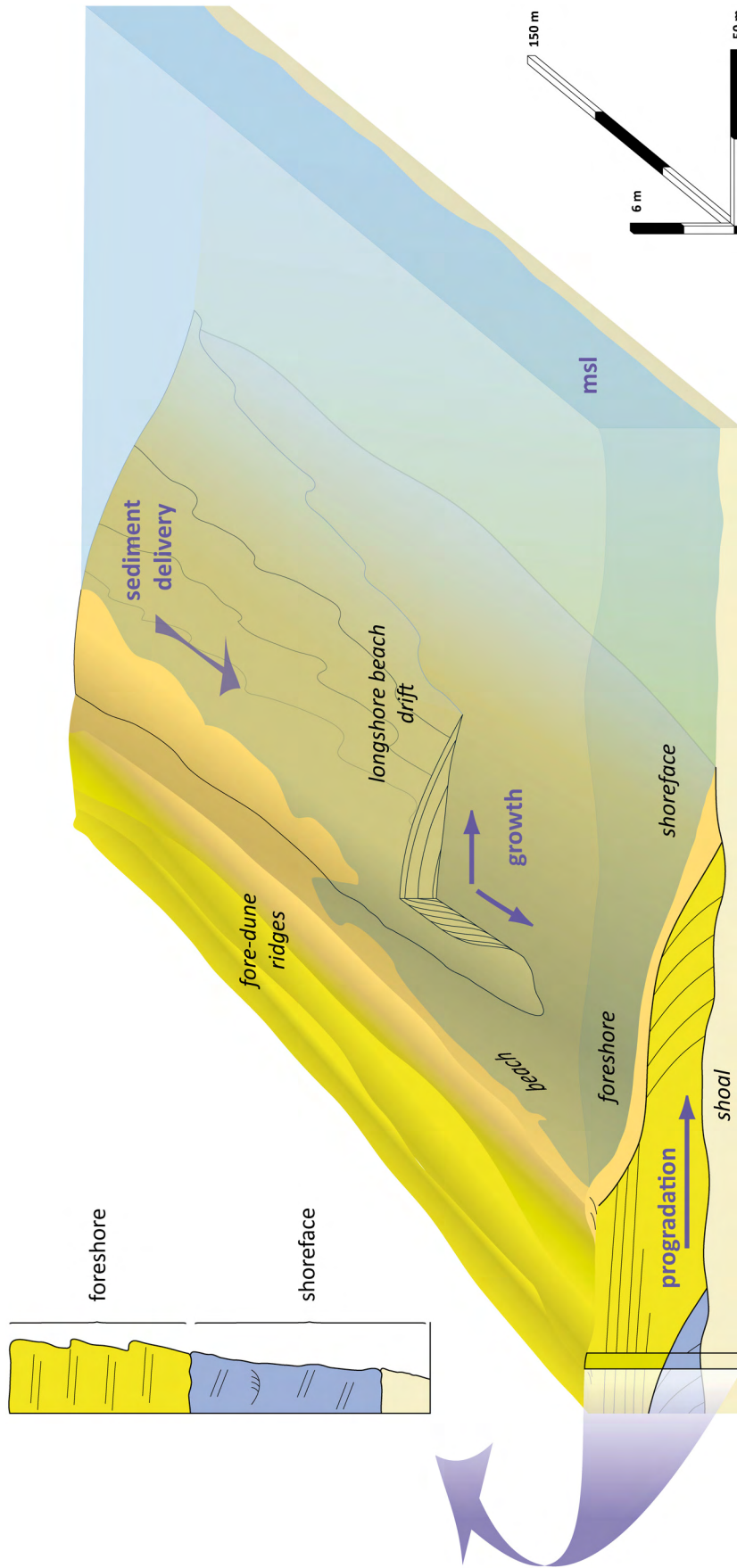


Figure 4.14: Model showing the sedimentary environment of the hooked spit. Beach drifts migrate alongshore, leading to significant growth of the Ellenbogen. Erosional unconformities are attributed to rare severe storms that erode the beach and form erosional scarps in the backshore. The development of fore-dune ridges is initiated with the trapping of sand at these scarps. Situated adjacent to a tidal inlet, the beach profile of the Ellenbogen is very steep, suppressing the development of a barred beach system.

calibrated ^{14}C -dating in Core OE-01 (Tab. 4.3; Fig. 4.12A). For the high amplitude interval, the data indicate an age of 1300 ± 60 years, respectively. Therefore, the greater depth of the high amplitude interval in this area is interpreted to reflect a lower sea level at the time of deposition. This is in line with postulated sea-level curves for the southern North Sea (Behre, 2003, 2004, 2007; Gehrels et al., 2006; Mauz & Bungenstock, 2007), which indicate a sea level 0.5 to 1.0 m lower than today for the time around 1300 BP.

Whereas mean grain size and sorting of a sediment are predominantly controlled by transport mechanisms (Füchtbauer, 1988; Chamley, 1990), the skewness of the frequency distribution is more influenced by the depositional environment (Taira & Scholle, 1979; Füchtbauer, 1958). Skewness data from Core OE-01 show a predominance of finer skewed sediments in the distribution curve up to 300 cm depth (1.2 m bsl), and an increase in symmetry of the grain-size distribution from 300 cm depth upward. Whereas the first is interpreted as the result of predominantly settling of suspension load, the latter represents increasing wave influence to the grain-size distribution. This reflects a shallowing upward sequence.

The described sedimentary architecture, summarized in Table 4.4, is interpreted to have formed in a beach depositional system, with a net progradation eventually interrupted by strong erosional events (Fig. 4.14). Beach progradation in the foreshore zone (down to 1 m bsl) is the result of alongshore sediment transport by beach drifts, resulting in alongshore-dipping strata. These deposits show only little variations in grain-size and sorting. Sediments deposited below MLT have a coast-normal dip which indicates a seaward-directed sediment export from the foreshore. Here, high GPR reflection amplitudes indicate abrupt changes in wave energy that are attributed to an alternation of fair-weather and storm conditions. Erosional unconformities reflect storms of different magnitude. The major unconformities are attributed to rare severe storms, that caused a profound erosion of the beach and probably formed an erosional scarp in the backshore.

Comparable scarps in backshore sediments, interpreted as products of storms, were described by Bristow et al. (2000) in GPR data from beaches in Norfolk (UK). Storm scarps in the backshore zone were also presented by Hayes & Boothroyd (1969) at recent beaches of New Hampshire and northeast Massachusetts (US) after severe storms, and Buynevich et al. (2004, 2007) described a GPR dataset from the Hunnewell barrier beach (Maine, US) showing buried storm scarps with a dip of $3\text{--}5^\circ$ steeper than the usual beach.

The erosional scarps are assumed to initiate the formation of an embryonic dune by trapping of blown sand. Storms of smaller magnitude, that occur several times a year, do not form erosional scarps, but leave a foot print preserved as a minor unconformity in the prograding sequence of the beach. These storms can also account for episodic sediment redistribution from the foreshore to the shoreface, resulting in strong variations of grain-size and sorting.

The sedimentary unit below the prograding beach sequence of the spit is only imaged in radar lines of the eastern hooked spit. Here, GPR lines reveal an erosional unconformity at a depth of 4 to 5 m bsl. This surface has an irregular relief and no predominant direction of dip. The data reveal that strata below this unconformity are dipping at around 8 to 17° towards the southeast. Core OE-01 (Fig. 4.12) shows several small-scale changes between coarser and finer sediments. These variations are also expressed in the different degrees of sorting of the sediment. Based on

sediment geometries and grain-size distribution, these deposits are interpreted as submarine sand bodies which migrated towards the southeast.

The genesis of this sedimentary unit has to remain speculative with the available data. One possible interpretation is that the succession formed in a sandy shoal related to the flood delta of a former tidal inlet. This hypothesis is supported by the occurrence of a landward directed dip of the strata, which probably represent flood-oriented sand waves of a flood-tidal delta (see Hayes, 1975, 1980, and Boothroyd, 1985). Such bodies nowadays exist eastward of the Lister Tief. Calibrated ^{14}C -dating (Tab. 4.3) gives an absolute age of 2250 ± 90 years for these sediments in Core OE-01. At least the eastern part of the Ellenbogen seems to be located at the position of older shoals that were subsequently incorporated into the spit system by beach-drift sedimentation. We therefore assume that the early growth stages of the hooked spit were dominated by upward shoaling of sand bodies, a process known as one of the common mechanisms for barrier island growth (Davis, 1994 after Davis & Hine, 1989 and Gibbs & Davis, 1991). Calibrated ^{14}C -dating of the beach-drift sediments above the unconformity indicates an age of 1300 ± 60 years. Therefore it can be speculated that the development of the eastern hooked spit took place sometime between 2250 ± 90 and 1300 ± 60 BP. This implicates that the recurved Ellenbogen spit is much older than previously thought.

4.5.2 Evolutionary model for the hooked spit

The evolution of the analyzed depositional system can be integrated into a hypothetical model, which is presented in Figure 4.15. This model consists of four stages reflecting the entire cycle of spit erosion by a severe storm, beach recovery, beach-drift progradation interrupted by normal storms, and eventually the formation of a fore-dune ridge.

During Stage 1, a beach is eroded by a severe storm, and an erosional scarp develops. The storm surge excavates a scarp extending landward into the supratidal backshore zone. Eroded material is transported seaward (Ingle, 1966) to the tidal inlet of the Lister Tief by rip currents and wake. Wave action suspends the finer fraction (Brenninkmeyer, 1976). The GPR data show that the erosional profile is steep on the western Ellenbogen (Figs. 4.6, 4.9) and flattens towards the middle part of the Ellenbogen (Fig. 4.7). This possibly reflects less wave energy within the Lister Tief tidal inlet.

Stage 2 is characterized by settling of suspension load and beach recovery, reflecting waning of the storm, and the early post-storm period. Sediments settled from suspension during the waning stage of the storm are imaged in the GPR data as thin planar bedded layers on top of the erosional unconformity (compare Fig. 4.11A between meter 120 and 170 of the line). Grain-size data here indicate a fining-upward trend for this sediment layer reflecting decreasing wave energy. A comparable process is described by Kumar & Sanders (1976) who investigated shoreface storm deposits off Fire Island, New York, composed of basal lag sediments overlain by finely laminated sand interpreted as having been rapidly deposited during the waning phase of a severe storm. Because of the deep tidal inlet that faces the coast of the hooked spit (Fig. 4.1B), we may assume that, in this setting, sediment eroded during storms can not be temporarily stored in nearshore bars as assumed by Carter (1986). Therefore, the early post-storm beach recovery by welding of bars as described by Hayes & Boothroyd (1969) and Niedoroda et al. (1984) is unlikely in the investigated

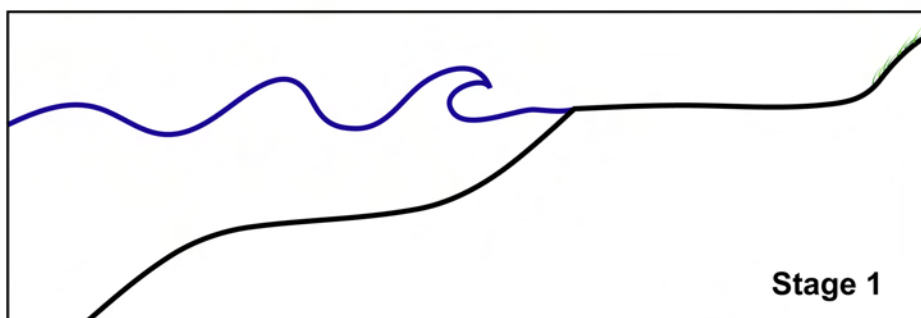
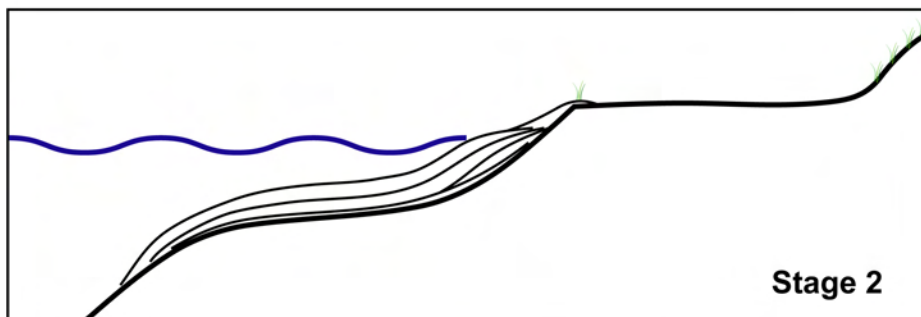
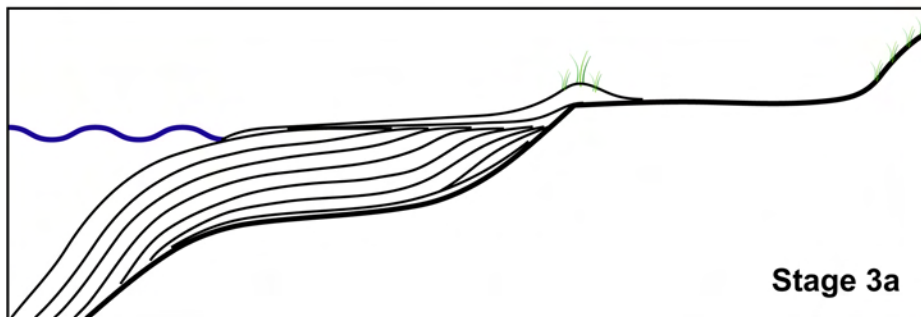
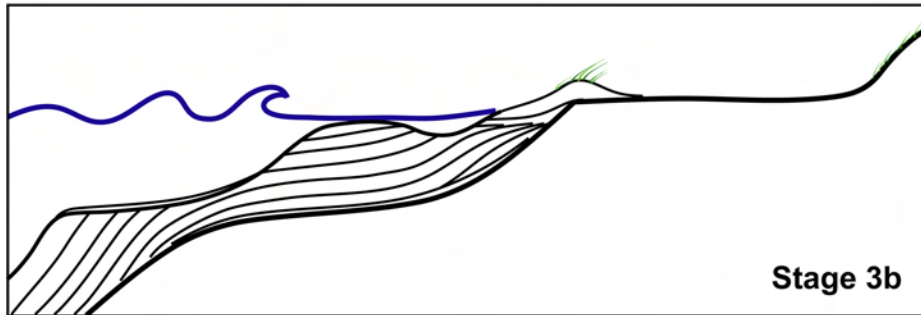
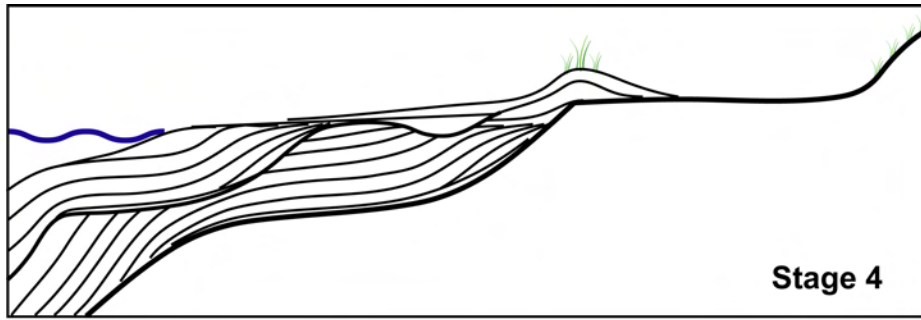
setting. Instead, beach recovery at the Ellenbogen seems to be a process of alongshore sediment movement by beach-drifts. In the backshore, the early post-storm period is characterized by trapping of windblown sand at the proximal termination of the erosional scarp. This initiates the formation of an embryonic dune. Since this part of the beach is desalinated by precipitation, and behind the reach of fair-weather waves, the marram grass *A. arenaria* grows on the embryonic dunes. This fast growing plant (Huiskes, 1979) stabilizes the young dune and plays an important role in trapping of windblown sand (Willis et al., 1959; Willis, 1989).

During Stage 3, beach drifts move in easterly-direction alongshore the northern Ellenbogen under enduring fair-weather conditions. This leads to a net beach progradation (Stage 3a). Due to sorting by waves, foreshore sediments are better sorted than sediments of the shoreface. This is reflected in the GPR data. Within individual sediment layers of the beach drift, there is a proximal – distal change from weaker to stronger reflections. Annually occurring winter storms interrupt the phases of beach progradation (Stage 3b), and erode older deposits. These storms do not produce a scarp, but export material from the foreshore to the shoreface; a process described in detail by Cheel & Leckie (1992) for cretaceous sandstones of the Wapiabi Formation in Canada. The offshore-directed relocation of foreshore sediments was also observed by Aigner & Reineck (1982), who investigated shallow-marine sands of the southern North Sea. Duke (1990) assumed that oscillatory motions triggered by waves, rather than bottom currents due to swell, are responsible for seaward-directed sediment export during storms. The relocation of material causes abrupt changes of grain size in the subtidal part of the beach drift sediments, imaged in the GPR data as high amplitude reflections due to the strong electromagnetic impedance between adjacent beds. Two different hydrodynamic regimes are therefore fossilized in the shoreface sediments: storm waves and fair-weather waves. Annual winter storms can also account for the cut-and-fill structures interpreted as channels which locally occur in the lower part of the backshore zone (compare Figs. 4.6 and 4.7).

Stage 4 of the beach development is characterized by a continued trapping of windblown sand at the former scarp. Sand trapping eventually leads to the development of a fore-dune ridge. The GPR data show that the fore-dune ridges of the Ellenbogen are always directly coupled to the proximal termination of an erosional scarp. The position and lateral shape of these dune ridges therefore traces the former storm coast lines of the recurved spit.

For the formation of the individual fore-dune ridge sets observed on the Ellenbogen (Fig. 4.2B), two different mechanisms are possible. First, a change of the predominant current regime around the recurved spit, or second, an exceptional severe storm. Both processes would lead to profound spit reworking and to the truncation of several

Figure 4.15 (next page): Model describing the interplay between storms and fair-weather conditions that lead to the sedimentary architecture of the hooked spit. **Stage 1:** A severe storm affects the beach. Eroded material is transported seawards by rip-currents, finer grains are suspended. The erosional unconformity terminates with a scarp in the backshore. **Stage 2:** As the storm weakens, suspended material settles and forms a layer of fine material that overlies the erosional unconformity. In the early post-storm period, trapping of sand starts at the backshore scarp and forms an embryonic dune. Alongshore sediment transport and the approach of a beach-drift front restore the fair-weather beach profile. **Stage 3a:** Enduring fair-weather conditions permit sediment transport by beach drift, and the beach progrades. First, plants stabilize the embryonic dune and lead to further trapping of blown sand. **Stage 3b:** Annual winter storms erode the beach, and the eroded material is exported from the foreshore to the shoreface where it sediments a coarse-grained / fine-grained layer. **Stage 4:** The embryonic dune develops into fore-dune ridge through sediment baffling by the grass cover. A broad beach plain develops, protecting the ridge from erosion during the next severe storm.



fore-dune ridges. GPR profiles 5 and 6 document that ridge-set borders are coupled with a significant erosion. High amplitude reflections in the middle part of the profiles are separated from the overlying low amplitude reflections by an unconformity.

4.6. Summary and conclusions

Linking geomorphological, GPR, and sediment core data we present a model for the growth dynamics of a hooked spit. The investigated hooked spit of the Ellenbogen is the termination of a larger recurved spit system. The data show that growth of the hooked spit is controlled by the interplay of fair-weather beach-drift migration and erosion by storms of different magnitude. Whereas sediment transport by beach-drift migration serves as the main important factor for beach progradation, storms are responsible for the relocation of material from the foreshore to the shoreface. Fore-dune ridges, oriented parallel to the shoreline, are a common feature on recurved spits. The development of such ridges is initialized by the formation of a scarp in the backshore that serves as a trap for windblown sand. Colonization by plants stabilizes the embryonic dune and supports the further growth of the ridge by continued trapping of windblown sand.

This growth mechanism results in a series of sediment bodies (Tab. 4.4). Data shown in this study are representative for similar deposits in the geological outcrop. The backshore portion of such sedimentary system is characterized by parallel or gently concave curved beds that form up to 1 m thick units. Cut-and-fill structures in these sediments can reach down to 1 m bsl, and extend up to 150 m along the shoreline. In the upper backshore, the planar backshore-bedding interfingers with fore-dune ridges. In the shoreface portion of a hooked spit, oblique divergent or tangential to sigmoidal shaped strata predominate. These beds dip at 5 to 10° alongshore and show a dip of 0.5 to 5° into seaward direction. Unconformities attributed to minor storms interrupt these sequence that results from beach-drift migration. The shoreface is characterized by strata that exhibit an oblique divergent to tangential shape in shore-normal direction and predominantly parallel to subparallel alongshore. Dip is 5 to 8° shore-normal, and 0.5 to 5° alongshore. These strata form a unit that is truncated at the top by major erosional unconformities caused by severe storms. Major unconformities extend over 150 m in shore-normal direction at a depth of msl and separate foreshore and shoreface strata. The landward termination of these unconformities is a backshore scarp that serves as a trap for wind-blown sand, initializing the formation of a fore-dune ridge.

Our results also shed light on the development of the Ellenbogen. Between 2250 ± 90 and 1300 ± 60 BP, the hooked spit of the Ellenbogen developed, incorporating at least one sandy shoal during progradation. Thus, the hooked spit is significantly younger than the main spit of the Sylt, which formed between 5000 and 6000 BP. It results that both systems are not directly linked and that the formation of the Ellenbogen hooked spit, that nowadays serves as a downstream sink for eroded material from the main spit, times the beginning of net erosion of the barrier island spit. During the last decades, sediment delivery to the hooked spit increased by a factor of 2 to 3, probably due to extended beach nourishment at the main spit. The effects of this increase in sediment supply can be studied in great detail and makes the Ellenbogen spit an ideal natural laboratory for studies dealing with sediment dynamic and beach development in a microtidal to lower mesotidal regime.

5

Stratigraphy and development of northern Sylt

ABSTRACT

The barrier system of Sylt is part of the island chain that lines the coast of the southern North Sea. Sylt consists of a Pleistocene moraine core and two barrier spits, attached to the North and south. This study is focused on the northern barrier spit. Numerous studies dealing with development and stratigraphy of this spit system were published in the past. All are based on sediment cores drilled in the first third of the 20th century. In contrast, this study focuses on an extensive ground-penetrating radar survey and sediment core data, allowing a spatial interpretation of sediment geometries and facies distributions. An age framework is provided by radiocarbon dating of mollusk shells. A new stratigraphic framework for the northern barrier spit of Sylt is presented, showing that the spit has undergone a much more complex development during the latest Holocene than previously thought. The sedimentary architecture of the spit is the result of several stages characterized by either spit growth or erosion, and reflects sea-level fluctuations as well as strong climatic impacts. The stratigraphic model also reveals that the present-day shoreline of the northern spit does not reflect the orientation of the genetically built spit axis which strikes northwest – southeast. Ground-penetrating radar (GPR) and sediment-core data allow to propose a model with six different stages of spit evolution, summarizing the development of northern Sylt since around 5000 BP. This model challenges the currently widely accepted hypothesis of a constant coastal retreat of northern Sylt during the last 5000 years. Former eolian deflation surfaces, preserved as erosional unconformities, indicate that the land surface of the spit tends to be in equilibrium with a given sea level. This results either in erosion during falling stages of the sea level, or in vertical aggradation during periods of sea-level rise. As sediment availability is an important prerequisite for spit aggradation during base-level rise, artificial stabilization of migrating dunes and exceptionally high coastal dunes, which prevent sand blow-out from the beach, thus reducing vertical spit aggradation during sea-level rise. A future sea-level rise, therefore, will cause not only enhanced erosion on the western coast, but also the flooding of the spit by marine inundation arising from the backbarrier bay.

5.1. Introduction

Barrier islands are the result of sediment availability, sea-floor topography and the interactions of waves and currents. They represent highly dynamic coastal systems, react very fast to changing conditions, and therefore contain a valuable, high-resolution sedimentary record of sea-level fluctuations and climate changes. Whereas stratigraphic

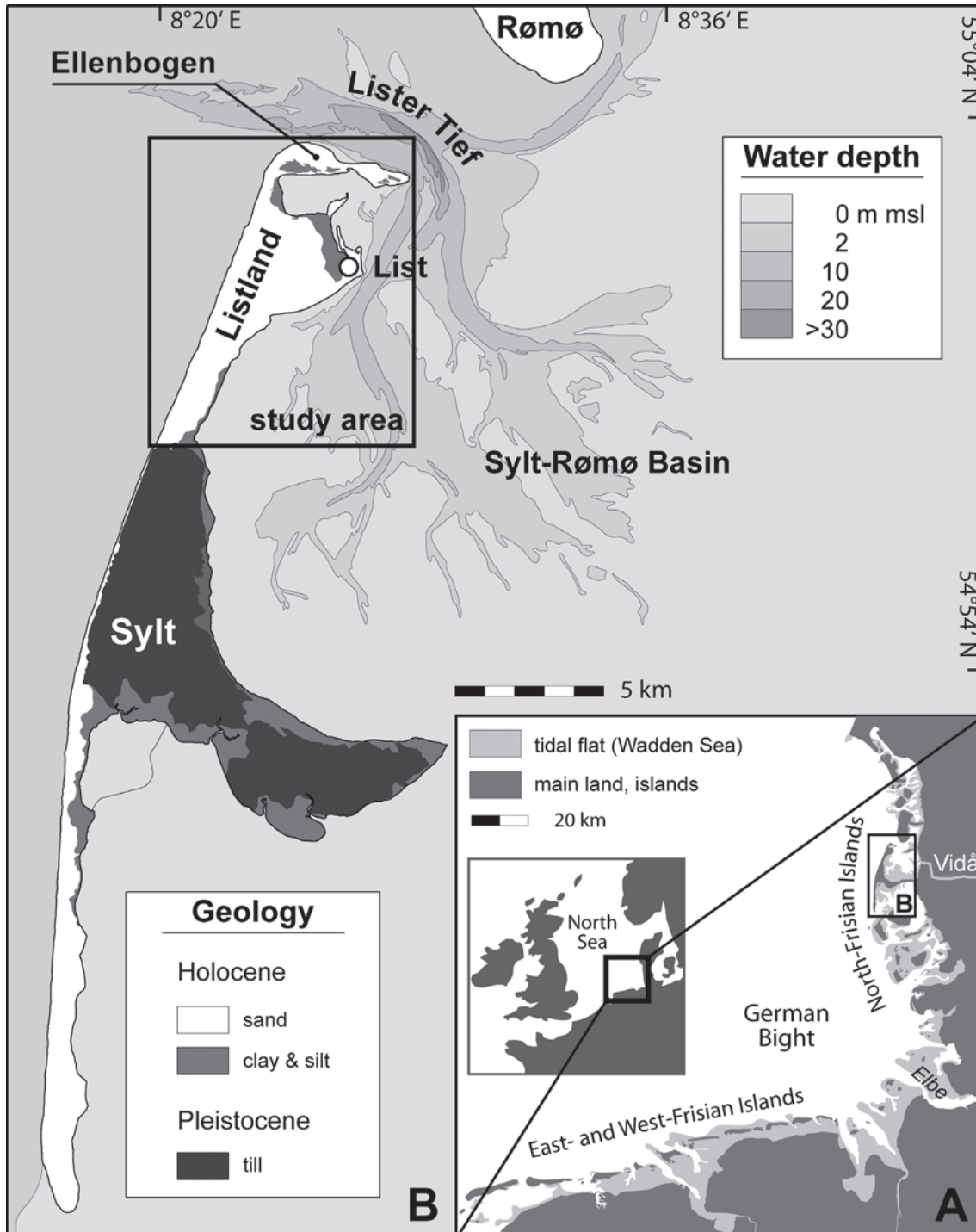


Figure 5.1: **A:** The southern North Sea (German Bight) with the barrier-island chain of the East-, West-, and North-Frisian Islands. The location of Sylt is marked with a box. **B:** Simplified geological map of Sylt (modified after Dietz & Heck, 1952b). Sylt has a core of predominantly Pleistocene moraine deposits. Two Holocene spit systems extend to the North and to the South. The northern spit, the „Listland“ terminates towards the North with a hooked spit, the „Ellenbogen“. On the eastern side of Sylt is a broad tidal bay, the „Sylt-Rømø Basin“, which is connected to the North Sea by the „Lister Tief“. The study area is marked with a box. Bathymetric data are from Neide (1977a, 1977b).

investigations of these settings along the North Sea coast in the past were almost completely based on sediment cores, which only allow for a punctual insight into the sediment succession. The development of GPR, however, enabled high-resolution spatial analyses of the shallow subsurface, leading to a detailed reconstruction of sediment geometries and facies distribution in space.

The investigated barrier system of Sylt belongs to an island chain lining the coast of the southern North Sea. Sylt is the largest of these islands. Two barrier spits, attached to a core of moraine deposits, shape a highly elongated island. The stratigraphy of the southern spit system is well-known (Gripp, 1968; Harck, 1972, 1974; Hoffmann, 1974; Köster, 1979; Ahrendt, 1992; Newig, 1995) and reflects a complex sedimentary architecture, involving at least one small Pleistocene moraine core south of the main moraine core of Sylt. The knowledge about the stratigraphic architecture of the northern spit is, however, based almost completely on cores drilled in the first third of the 20th century (Gripp & Simon, 1940). Stratigraphic models based on these data, geomorphological investigations, and historical maps imply that the spit must have experienced a complex development during the last 5000 years. As documented by historical maps and reports, and based on the modern rate of coastal retreat, this barrier system experienced a significant coastal retreat during the last centuries (Mager, 1927; Zausig, 1939; Bantelmann, 1967; Newig, 1980, 1995, 2004; Ahrendt & Thiede, 2001; Ahrendt, 1993; Bayerl & Higelke, 1994). Since the middle of the 20th century, the rate of coastal retreat has been increased (Ahrendt, 1993). These observations were extended to the widely accepted assumption of a post-glacial coastal retreat of more than 10 km during the last 5000 years (Gripp & Simon, 1940; Köster, 1974; Ahrendt & Thiede, 1992). More recent investigations, however, revealed that the development of the barrier in the past was rather characterized by the alternation of erosional events as well as phases of progradation and growth than by a continuously coastal retreat (see Chapter 3). Additionally, significant sediment redeposition played an important role in shaping the modern barrier spit (see Chapter 4).

This study aims to unravel the complex late Holocene development of the barrier system of Sylt. A new stratigraphic model for the northern barrier spit of Sylt is presented, based on high-resolution GPR data, sediment cores, and an age framework obtained from AMS ^{14}C -datings. Recorded sediment geometries allow to propose a new model for the paleogeographic reconstruction showing the different evolutionary stages of the spit during the last 5000 to 6000 years.

5.2. Study area

Sylt, the largest of the Frisian Islands that line the coast of Denmark, Germany, and the Netherlands (Fig 5.1A), is a north-south striking island, 15 km off the German coast near the border with Denmark. The island contains a core of Saalian and Elsterian moraines (Fig. 5.1B), as well as reworked tertiary sediments (Meyn, 1876; Gripp, 1915; Gripp & Becker, 1940; Gripp & Dittmer, 1941; Petersen, 1978; Schwarzer, 1984). During the latest Holocene, large sandy spit systems developed, attached to the northern as well as to the southern edge of the moraine core (Gripp & Simon, 1940), shaping a barrier system, some 38 km long. With a tidal range of 1.6 to 2.2 m (Hundt, 1957; Pejrup et al., 1997; Backhaus et al., 1998), the island is subjected to a semidiurnal upper microtidal to lower mesotidal regime as per definition of Hayes (1979). The average wave height is 1.0 to 1.25 m. During large storms,

waves build up to 6 m (Ahrendt, 1993). Westerly winds are dominant (Hundt, 1957; Müller, 1980; Draga, 1983; Ahrendt, 2001) and the average wind speed is around 6 m / s (Gierloff-Emden, 1961). Two different longshore currents trigger a net sediment transport from the moraine core towards the North and the South (Gripp, 1944; Dietz & Heck, 1952a).

5.2.1 Geomorphology and geology

The northern spit of Sylt is morphologically subdivided into the main spit, the so called „Listland“, and a small hooked spit, the „Ellenbogen“, which forms the northern termination of Sylt (Fig 5.1B). Sedimentary architecture and development of the Ellenbogen are described in detail in Chapter 4.

Between the Listland and the Ellenbogen there is a small tidal bay, the „Königshafen“, which covers an area of 5.55 km² (Backhaus et al., 1998). The Königshafen is around 1.5 m deep during mean high tide (MHT), and runs dry to a large extend during ebb tide (Austen, 1990). With exception of a small area with mixed flats at its western edge, the Königshafen is a sand flat of medium sand with a median between 1.5 and 2.25 phi (Austen, 1992). Locally, gravel and boulder are found in the Königshafen, which are attributed to hypothetic moraine sediments occurring in the shallow subsurface (Hagmeier & Kändler, 1927; Kolumbe, 1933). Gripp & Simon (1940) proposed that the tidal bay of the Königshafen developed as a recess. According to the the Königshafen developed during a phase of enhanced sediment delivery which has led to an accelerated northward-growth of the spit up to the Lister Tief where spit growth turned into easterly direction. A north-south striking cross section through the Königshafen provided by Bayerl & Higelke (1994) shows a lens-shaped clay layer at a depth of 1 to 3 m below mean sea level (bsl). The clay is interpreted as mud flat deposits, underlain by sand-flat sediments.

East of the spit, there is the tidal bay of the Sylt-Rømø Basin, which cover 400 km² (Bayerl & Köster, 1998). It is connected to the North Sea by the „Lister Tief“, an up to 40.5 m deep and 2.8 km wide tidal inlet. Since the construction of two dams in 1927 and 1948, water exchange between the basin and the North Sea has been restricted to the Lister Tief, where current velocities of up to 1.3 m / s were measured (Backhaus et al., 1998). The sediments of the Sylt-Rømø Basin are predominantly sands with a median between 3 and 2 phi (Bayerl et al., 1998a). As a consequence of an eolian sand input into the basin along the eastern coast of Sylt, coarser sediments locally occur (Goldschmidt et al, 1993; Bayerl et al., 1998b). Pejrup et al. (1997) investigated the sediment budget of the Sylt-Rømø Basin and considered that basin acts as a net sink for fine-grained material. Stones and pebbles found in the Sylt-Rømø Basin last from ancient beach ridges in the Königshafen and from tertiary sediments exposed at cliffs near the southern border of the tidal bay (Köster & Ricklefs, 1998). Only 3 % of the area of the Sylt-Rømø Basin is mudflat with more than 50 % silt and clay (Bayerl et al., 1998a). Bayerl et al. (1998b) assumed that the tidal flat of the Sylt-Rømø Basin had not undergone a profound change since 3000 BP, because older clay deposits are situated near the surface, and younger tidal-flat sediments only reached a thickness of several decimeter.

The marine Holocene of the northern barrier spit of Sylt, as recorded in borings, is 45 m thick (Bayer & Higelke, 1994; Ahrendt & Pesch, 2001). Holocene sediments consist of sand and gravel with interbedded layers of clay and peat (Fig. 5.2A). Based on the color of the sediment, Gripp & Simon (1940) distinguished two Holocene

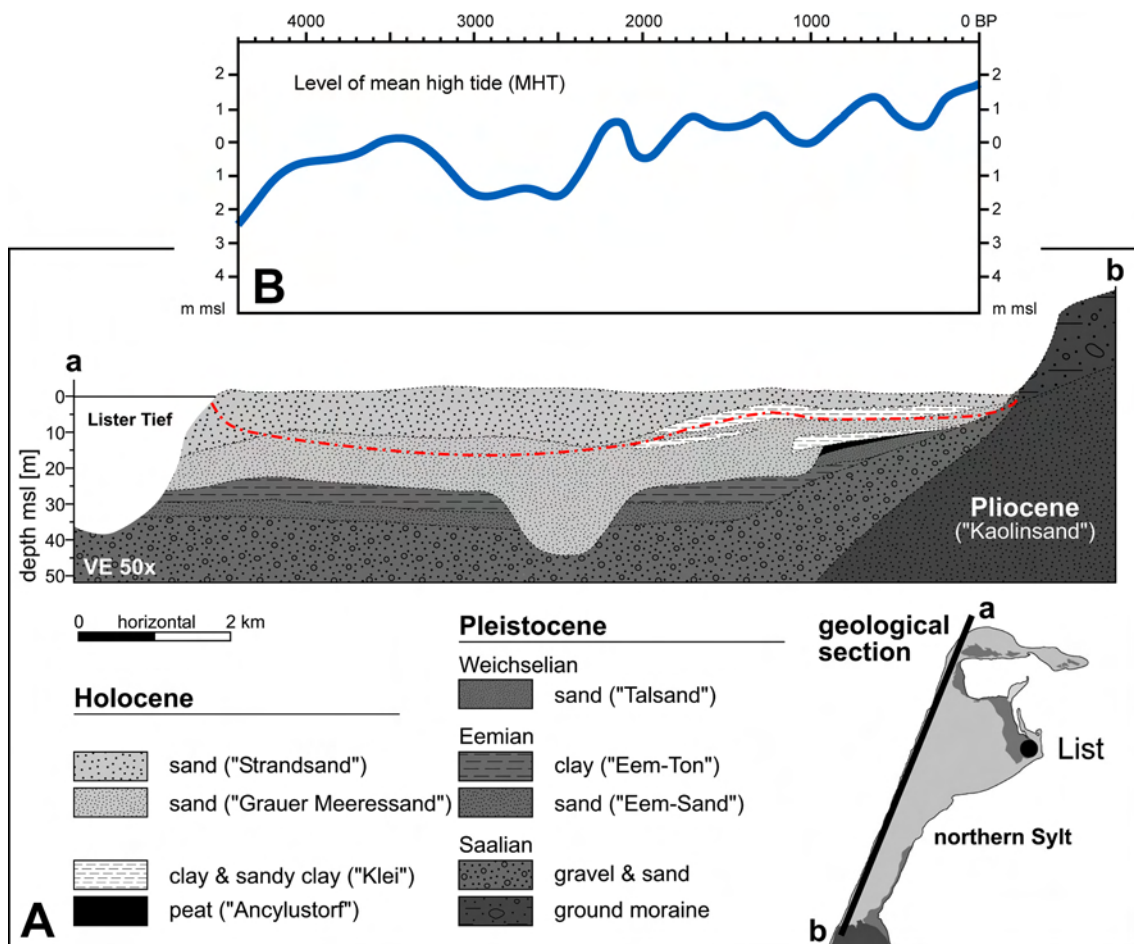


Figure 5.2: **A:** Geological cross section of northern Sylt, modified after Gripp & Simon (1940). The position of the profile is shown in the small inset map. Holocene sediments consist of sand, clays and peat. They unconformably overlie pre-Holocene clays, sands and gravels. Red dashed line indicates investigation depth achieved in this study. **B:** Sea-level curve for the southern North Sea area (after Behre, 2007). The graph indicates the level of mean high tide (MHT).

marine sand units. The lower unit, named „Grauer Meeressand“ (gray marine sand), unconformably rests onto Eemian clays, Elsterian ground moraines, sands and gravels of Saalian age, as well as Weichselian sands. The Grauer Meeressand unit contains interbedded clay horizons that show an onlap geometry against the moraine core of the island. Such horizons are interpreted to reflect short-term sea-level fluctuations (Gripp & Simon, 1940; Hoffmann, 1969, 1980; Bartholdy & Pejrup, 1994; Streif, 1990b, 2002). The Grauer Meeressand is overlain by the second marine sand unit, the yellowish „Strandsand“ unit, interpreted as beach deposits by Gripp & Simon (1940). This unit reaches down to a depth of between 5 and 15 m, and thickens towards the North. Gripp & Simon (1940) interpreted the color change between the two marine sand units as caused by the oxidation of pyrite, and not as a primary sedimentary feature. Sediments are interpreted to have been formed in a northward growing and backstepping spit. As shown in Figure 5.2A, Gripp and Simon (1940) depicted a channel-shaped erosion reaching down to a depth of 45 m bsl. This incision was interpreted to be a precursor of the Lister Tief by Gripp & Simon (1940). Newig (1995) proposed that it was formed during sea-level lowstand by the Danish River Vidå (Wiedau), and afterwards, during the early post-glacial transgression, served as a main tidal inlet.

The youngest sedimentary unit of northern Sylt consists of eolian dune sands, that cover the Listland and the Ellenbogen and reach a height of up to 34 m above

sea level (asl). Priesmeier (1970) proposed based on geomorphological studies that dune migration is cyclic: according to his these, a new generation of dunes accumulated every 300 years at the western coast and subsequently started migrating towards the East. Based on aerial photographs, Priesmeier (1970) calculated that after 900 to 1000 years, each dune chain had passed the northern spit and was blown into the Sylt-Rømø Basin. Newig (1995) assumed that extended dune development on Sylt started not earlier than the Late Middle Ages, during the 14th and 15th century, and Hansen (1877) remarked that extended dune development on the Listland started after a great storm surge in 1362. Extended dune fields on the moraine core were assumed to be only a few hundred years old (Averdieck & Hummel, 1974). The eolian dunes of the Ellenbogen belong to the youngest dune generation (Priesmeier, 1970), and they are therefore not older than 300 years. Lindhorst et al., (in prep., Chapter 4), however, showed that these dunes are fore-dune ridges, genetically related to erosional scarps in the subsurface of the Ellenbogen.

5.2.2 Late Holocene development of northern Sylt

The post-glacial return of marine conditions to the present position of the island gives a maximum age of these depositional systems. Behre (2007) noted that the sea reached the present coast in the southern North Sea area around 7500 BP, and Hoffmann (2004) found out that the Holocene transgression in coastal northwestern Germany took place around 8000 BP. Flemming (2002) remarked that the initial transgressive coastal retreat transformed into aggradation or regressive progradation during the mid-late Holocene, around 6000 BP. Eisma, et al. (1981) assumed that the southern German Bight became fully marine around 7000 BP, Wiermann (1966) ascribed the first occurrence of salt marsh deposits at the northwestern German coast to the time around 5500 BP. For the study area, this correlates with results of Willkomm (1980) who investigated peat horizons overlapping on the moraine core of Sylt. He found the first indication of the approaching sea for around 5500 BP. The same peat horizons were attributed to the Atlantikum by Gripp & Simon (1940) and dated to around 7000 to 6000 BP by Hoffmann (1985). Averdieck (1980) assumed the beginning of large peat development in the area of Sylt for the early Atlantikum.

Archeological age estimations of stone tools found on northern Sylt, indicate a Neolithic age for the Listland (Harck, 1972, 1974). In northern Germany, the Neolithic period is dated as approximately 6500 to 4200 BP (Behre, 1995; Litt et al., 2001). Based on geomorphological investigations, Priesmeier (1970) assumed a maximum age of the northern spit of 5500 to 6000 years.

In the area of northern Sylt, significant clay layers occur at depths of 2.5 to 2 m bsl and around 1 m asl. The lower clay layer was deposited before 4000 BP, the upper clay between 3500 and 2500 BP (Hoffmann, 1985). Absolute age dates are provided by Bayerl et al. (1998a), who revealed that the clay layer drilled in the Königshafen at a depth of 2 to 3.5 m bsl, dated back to 3640 – 3750 BP. The surface of the upper clay, situated at a depth of 0.6 to 1.3 m asl, was vegetated and settled around 2000 BP (Bantelmann, 1975; Kossack et al., 1975; Hoffmann, 1980, 1985). In no area of Sylt any sediments are known from the time between 2000 BP and short before 1000 BP (Hoffmann, 1984). The youngest clay deposition took place not before the 14th century, as parts of the today's tidal flats were used as range lands (Müller & Fischer, 1938; Hoffmann, 1985; Bayerl, 1992).

The Ellenbogen is considered to be significantly younger than the Listland (Gripp

& Simon, 1940; Priesmeier, 1970; Harck, 1972, 1974). Based on historical maps, Newig (1995) assumed that it was formed during the 17th century. New radiocarbon ages, however, showed that the Ellenbogen hooked spit already existed around 1300 BP (see Chapter 4).

5.2.2 Late Holocene sea-level rise and glacial isostatic adjustment

Numerous sea-level curves were compiled for the southern North Sea region, based on archeological, geological, and hydrographical data (Menke, 1976; Jelgersma, 1979; Streif, 1990a, 2002; de Groot et al., 1996; Behre, 2003, 2004, 2007; Gehrels et al., 2006). None of these sea-level curves, however, relies on data from Sylt. Behre (2007) presented the most recent compilation of data. This sea-level curve shows a fast rise with a rate of 1.25 cm per year until 7000 BP, when sea level reached a position of 7 m lower than today. Between 7000 BP and 3400 BP, the rate decreased to 0.14 cm per year, reaching a level of 2 m below present sea level. After a sea-level drop of 2 m around 3000 BP, small-scale sea-level fluctuations of 0.5 to 1.5 m occurred, superimposed on an overall sea-level rise with a rate of 0.11 cm per year (Behre, 2003).

Menke (1976) interpreted bogs which form the supposed short-term sea-level highstand deposits (Behre, 2007) as deposits of more humid and stormier periods. Such an interpretation is supported by numerical models of Langenberg et al. (1999), showing that between 1955 and 1993 the winter high-water level on the German North Sea coast increased by 1 to 2 mm per year through sole atmospheric forcing. For the Holocene, Linke (1981) found periods with significant higher storm surges that well correlated with short-term sea-level highstands in the curve of Behre (2007).

Data from southern Denmark, 60 km north of Sylt, provided by Gehrels et al. (2006), indicate a continuous sea-level rise between 3500 BP and 1500 BP and a possible lowering of around 0.5 m between 1500 and 1000 BP. However, they did not find any indication for a late Holocene sea-level highstand in north western Europe as supposed by Mörner (1976).

The question of the rate of post-glacial isostatic adjustment and local tectonic movements has not been fully answered yet for the investigated area. Based on the position of the top of the Eemian sediments, Menke (1976) derived a long-term rate of subsidence in the range of 11 cm per century for the northwest German North Sea coast. A map of recent vertical movements compiled by Frischbutter (2001), shows that the study area is located near the zero isobase, indicating no active vertical movement nowadays.

5.3. Methods

Sediment geometries were investigated by means of GPR surveys. GPR permits a non-invasive investigation of the shallow subsurface. The method is based on the transmission of high-frequency electromagnetic pulses and the reception of energy, reflected at electromagnetic discontinuities in the subsurface (Bristow et al., 1996; Blindow et al., 1997; Annan, 2001; Neal, 2004). GPR surveys for this study were performed using a GSSI 3000 radar system (Geophysical Survey Systems Inc.) and antenna frequencies of 100 and 200 MHz. In general, penetration depth in geological materials increases with decreasing antenna frequency (Jol, 1995; Neal, 2004). However, in the study area, frequencies lower than 100 MHz did not yield an increase

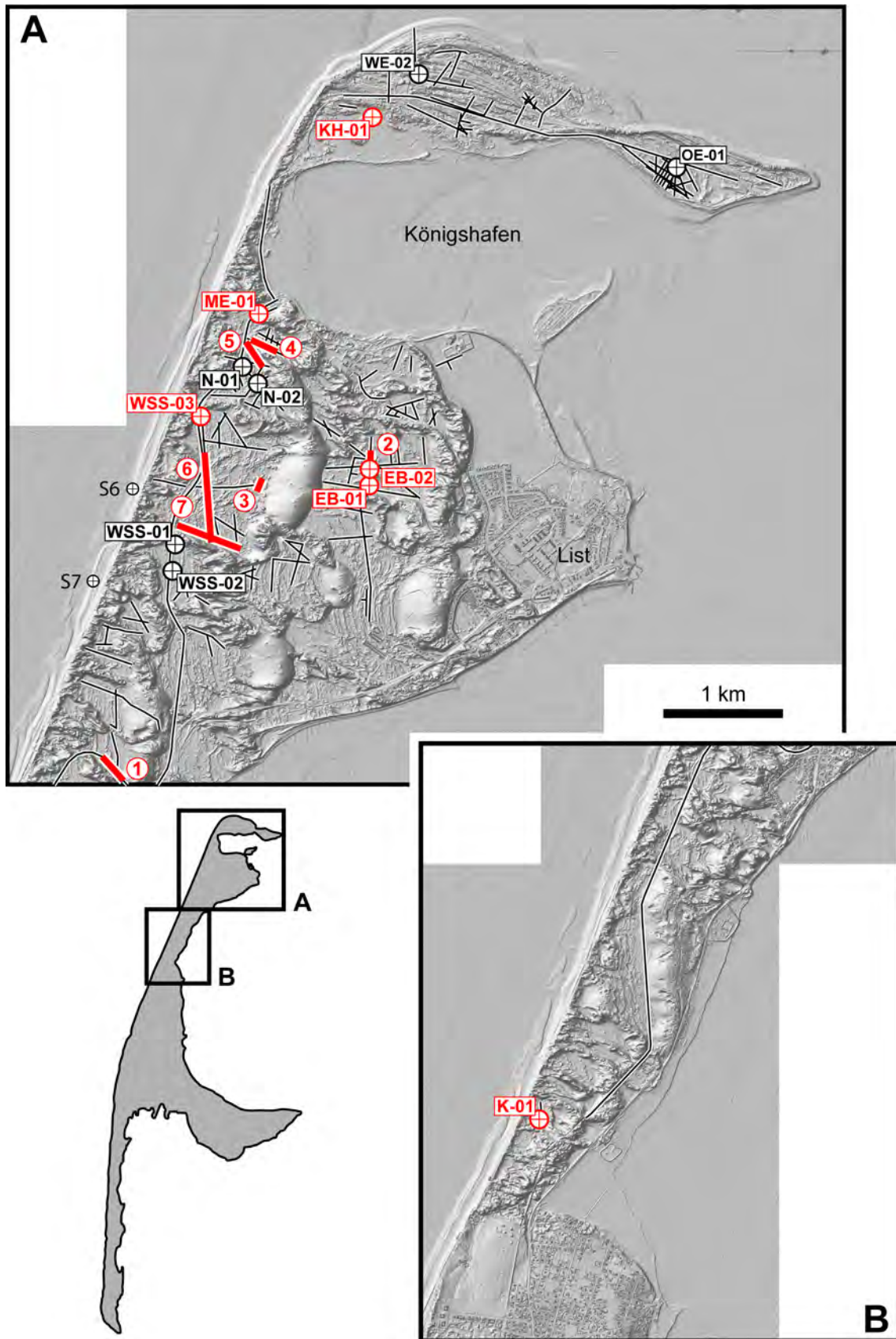


Figure 5.3: Terrain model of northern Sylt, based on airborne LIDAR measurements during low-tide by ALR (Husum) in 2002. Thin lines show position of GPR lines gathered for this study, bold red lines mark GPR lines 1 to 7 presented in the text. Whereas red circles indicate locations of sediment cores described in this chapter, black circles refer to cores presented in Chapter 3 and 4 respectively. S6 and S7 mark locations of cores described by Gripp & Simon (1940) and referred to in this text.

in penetration depth. This is probably due to pore-water salinity increasing with depth, causing higher signal attenuation.

To minimize tilting effects caused by non-vertical radar beam orientation (Lehman & Green, 2000), GPR surveys were mostly restricted to the wide interdune slacks on northern Sylt. Individual profile lengths up to 4000 m were achieved. Data were obtained in survey mode using a survey wheel as distance trigger. Trace increment (space in-between shot points) was set to 5 cm for the 200 MHz antenna and to 10 cm for the 100 MHz antenna. Manufacturer settings for frequency filtering and no stacking were applied during data collection.

To enhance signal-to-noise ratio, processing of the data using the software ReflexW (Sandmeier, 2006) comprises frequency-filtering, down-the-trace, and trace-to-trace stacking. Migration was done using the fk-migration algorithm after Stolt (1978). For each profile, a topographic correction was made to restore different terrain altitudes, and to deskew reflector geometries. Data required for topographic correction were obtained in the field using either a Ashtek ProMark II or a Leica GPS 1200 differential global-positioning system. Vertical accuracy of the Ashtek system is up to 0.15 m, and up to 0.01 m with the Leica system (manufacturer specifications).

Common mid-point measurements, usually aimed to obtain radar-wave velocities in the subsurface, failed on Sylt, because prerequisites were not fulfilled, such as laterally largely homogenous underground with nearly sub-horizontal strata or occurrence of a shallow reflector, traceable over at least a few tens of meters (Kruk et al., 1999; Jol & Bristow, 2003). Radar-wave velocities were determined by the analysis of diffraction hyperbolas and direct correlation of sediment core to radar data. Values of radar-wave velocities were in the range of 0.06 m / ns for water saturated sands, and of 0.12 m / ns for dry dune sands. These values correspond to radar-wave velocities determined in previous studies for saturated and dry sand respectively (Blindow et al., 1997; Jol & Bristow, 2003; Neal, 2004)

To link GPR with sedimentological data, vibracores down to a depth of maximal 11.75 m below the surface were drilled at selected positions along the radar lines (Fig 5.3). Sediment cores were sampled every 5 cm (1 cm thick samples) for further laboratory analyses. A Quantachrome Cilas 1180L laser diffraction particle size analyzer was used for grain-size analysis. Grains coarser than 2000 μm were removed from samples prior to measuring. Grain-size classes and sample statistics were performed using the computer program Gradistat (Blott & Pye, 2001) and self-programmed routines. All statistical grain-size parameters mentioned here are based on the graphical method by Folk and Ward (1957).

Age assignments are based on radiocarbon dating of mollusk shells. Samples were measured at the Leibniz-Labor für Altersbestimmung und Isotopenforschung, Kiel.

5.4. Results

5.4.1 Reflection geometries

The concept of radar-facies interpretation summarized in Chapter 2, allows to classify the numerous reflection geometries recorded in the GPR data. Radar facies (R_f) are characterized by shape and dip of reflections, relationship between reflections,





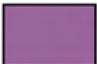
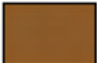
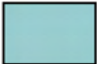
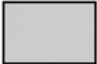
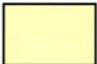
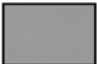
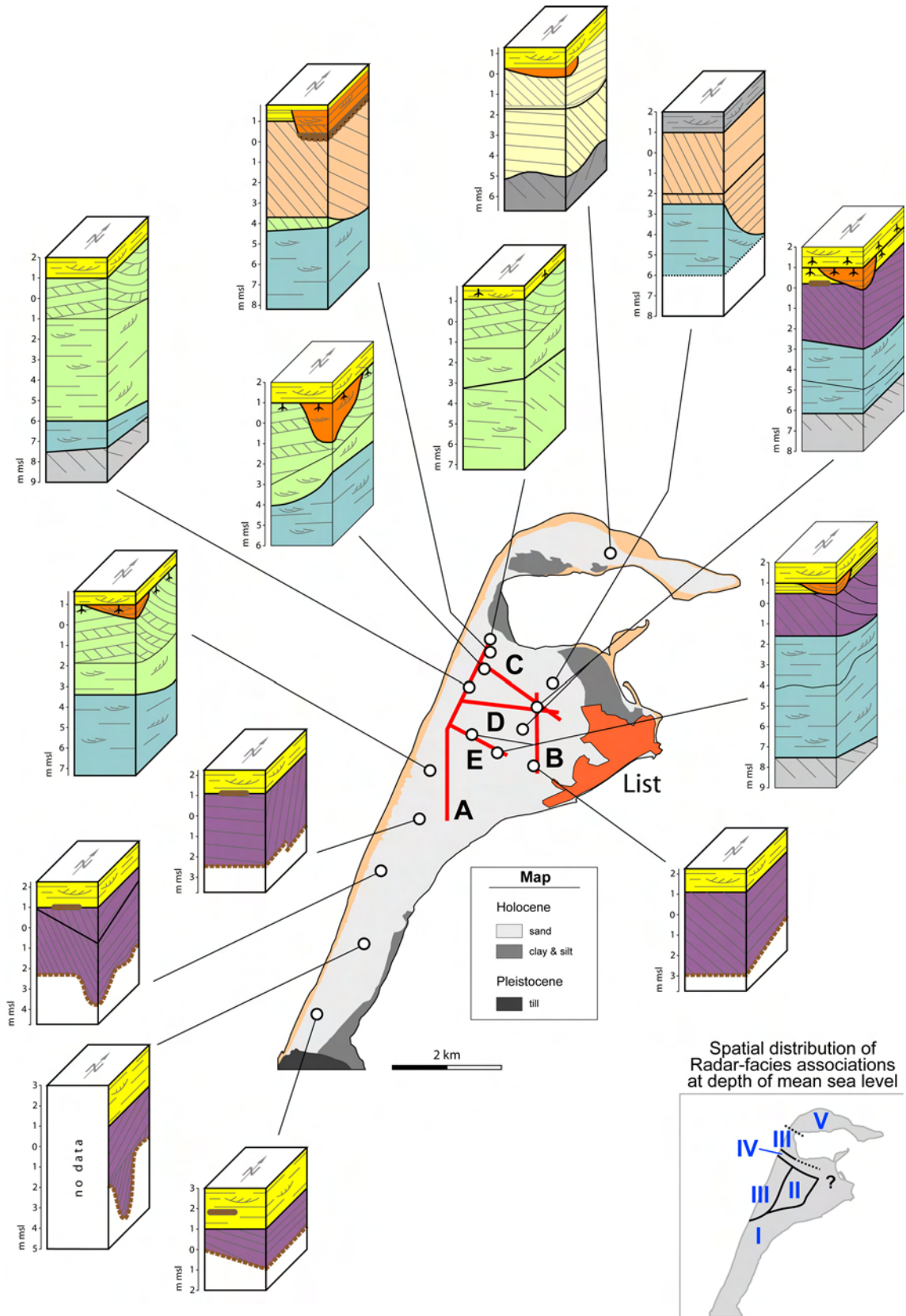
	Reflection pattern	Interpretation
	Rf-k: subparallel to parallel or wavy to concave curved	young eolian cover, in parts with soil development, truncated at top by recent deflation surface
	Rf-j: cut-and-fill structure, base truncates underlying reflections, internal reflections are wavy to concave curved	cut-and-fill structure, interpreted as scour channel leading to wash-over fans on the lee-side of the spit
	Rf-h: E-dipping at 6-8°, oblique tangential, topsets partly erode, bottomsets, unit forms channel and is up to 6 m thick	major cut-and-fill structure shaping an up to 6 m depth channel that crosses the Listland, interpreted as filled tidal inlet.
	Rf-g: contains different reflection patterns (for detailed description see Chapter 3), reflections showing landward dip of 1-2° are bundled by erosional unconformities into sigmoidal shaped, N-dipping packages, in greater depths wavy and concave curved reflections occur that look similar to Rf-d, but are terminated against underlying strata by an erosional unconformity	N-prograding spit sequence, build up of welded swash-bars bundled by erosional unconformities of different magnitude (For detailed description see Chapter 3), deeper strata are attributed to the shoreface.
	Rf-f: E- to SE-dipping at <15°, oblique tangential, topsets partly erode, bottomsets exist, unit forms several hundred meters wide, shallow channel	major wash-over deposits, predominantly consisting of well sorted dune and beach sands
	Rf-e: horizontal to subhorizontal, attenuating or shielding reflections from underlying strata, causes ringing in the GPR data	clay and silty clay, interpreted as tidal flat and interdune ponds sediments respectively
	Rf-d: concave curved or parallel to subparallel, partly gently dipping towards the N, large erosional unconformities separate spit growth increments	intertidal and subtidal sediments of prograding spit (undifferentiated)
	Rf-c: NE-dipping at <10°, oblique tangential, topsets eroded, bottomsets not observed, unit at least 6 m thick	NE-directed cross-bedding, genesis unclear, probably pre-spit sediments of early transgression
Additional radar facies for Ellenbogen hooked spit (detailed description see Chapter 4)		
	Rf-b: contains two reflection patterns, separated by erosional unconformity. Upper unit: oblique divergent to sigmoidal shaped, dip 5-10° alongshore, and 0.5 to 5° seaward. Lower unit: oblique divergent, sigmoidal or wavy shaped, dip 5-8° shore-normal and 0.5 to 5° alongshore	prograding hooked-spit sequence, containing foreshore (beach drift) and shoreface sediments
	Rf-a: SE-dipping at 5-8°, oblique tangential, topsets eroded, bottomsets not observed	SE-dipping strata interpreted as remnants of tidal inlet associated flood delta

Table 5.1: Key to radar facies (Rf) in GPR data from northern Sylt. Note that Rf-g and Rf-b summarize reflection patterns described more detailed in Chapters 3 and 4.

Figure 5.4 (next page): A: Reflection geometries in the study area. Columns show typical reflection geometries in GPR data from northern Sylt. Note that columns present reflection geometries with regard to GPR line orientation, namely north-south as well as west-east. Colors indicate radar facies according to key from Table 5.1; depth readings refer to German mean sea level (msl). Red lines indicate orientation of Profiles A-E provided in Figures 5.10 and 5.11. Geological map modified after Dietz & Heck (1952b). **B:** Spatial distribution of radar-facies associations (RfA) on northern Sylt at mean sea level.



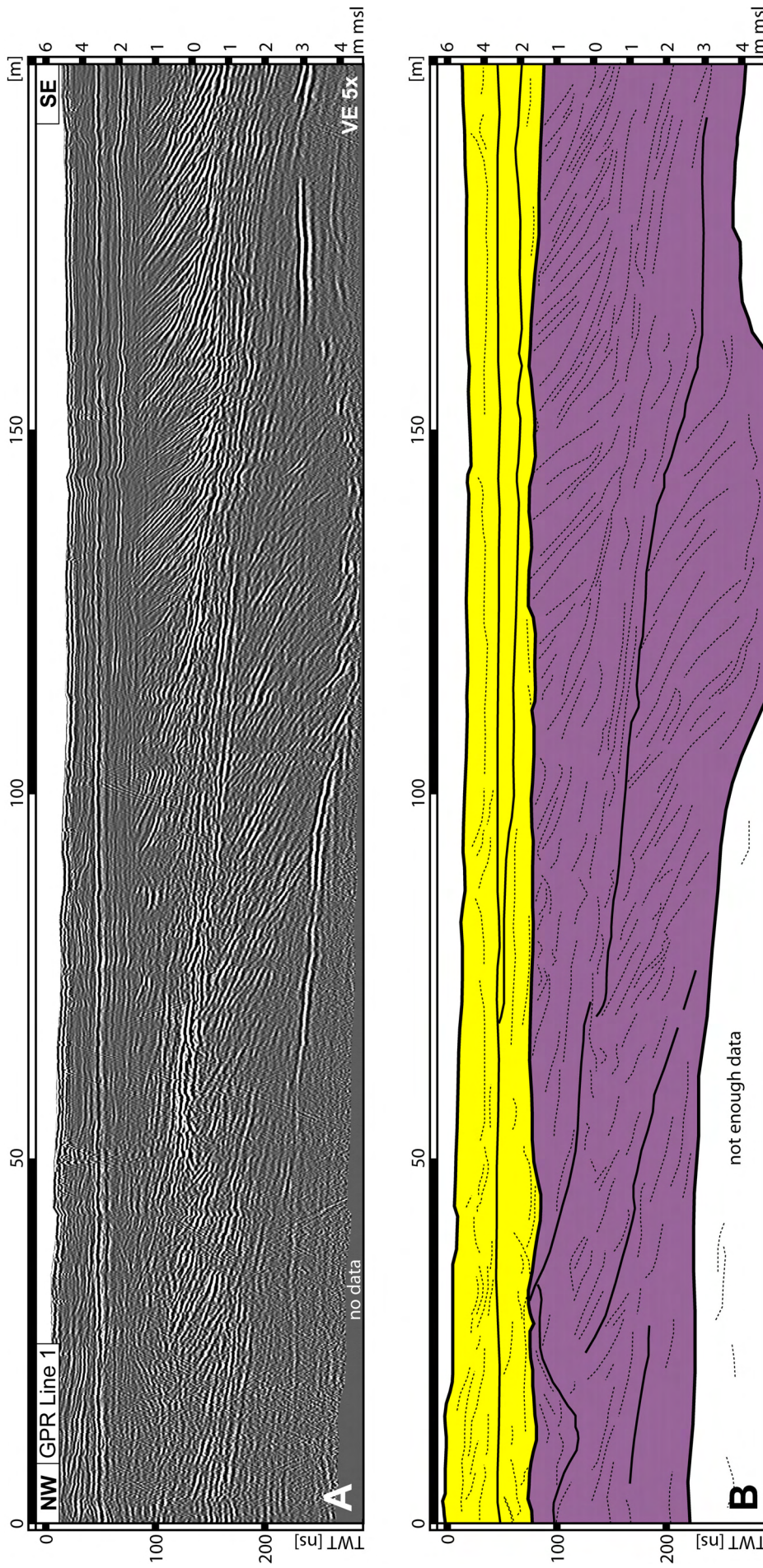


Figure 5.5: **A:** GPR Line 1 measured with a 200 MHz antenna. For location see Figure 5.3. Horizontal and concave curved reflections dominate down to a depth of 1.3 m asl. Between 1.3 m asl and 4 m bsl, the section is characterized by up to 3 m thick packages of eastward-dipping reflections, downlapping onto the underlying erosional unconformities. At a depth of 3 to 4 m bsl there is a reflection attenuating underlying radar reflections and causing signal ringing. **B:** Line drawing and interpretation of GPR section provided in A. Horizontal and concave curved strata in the upper part of the profile are interpreted as eolian sediments overlying an erosional unconformity at a depth of 1.3 m asl. This unconformity represents a former eolian deflation surface. Eastward-dipping strata beneath are washover deposits. The dominant reflection at a depth of 3 to 4 m bsl is probably caused by the surface of a thick clay layer.

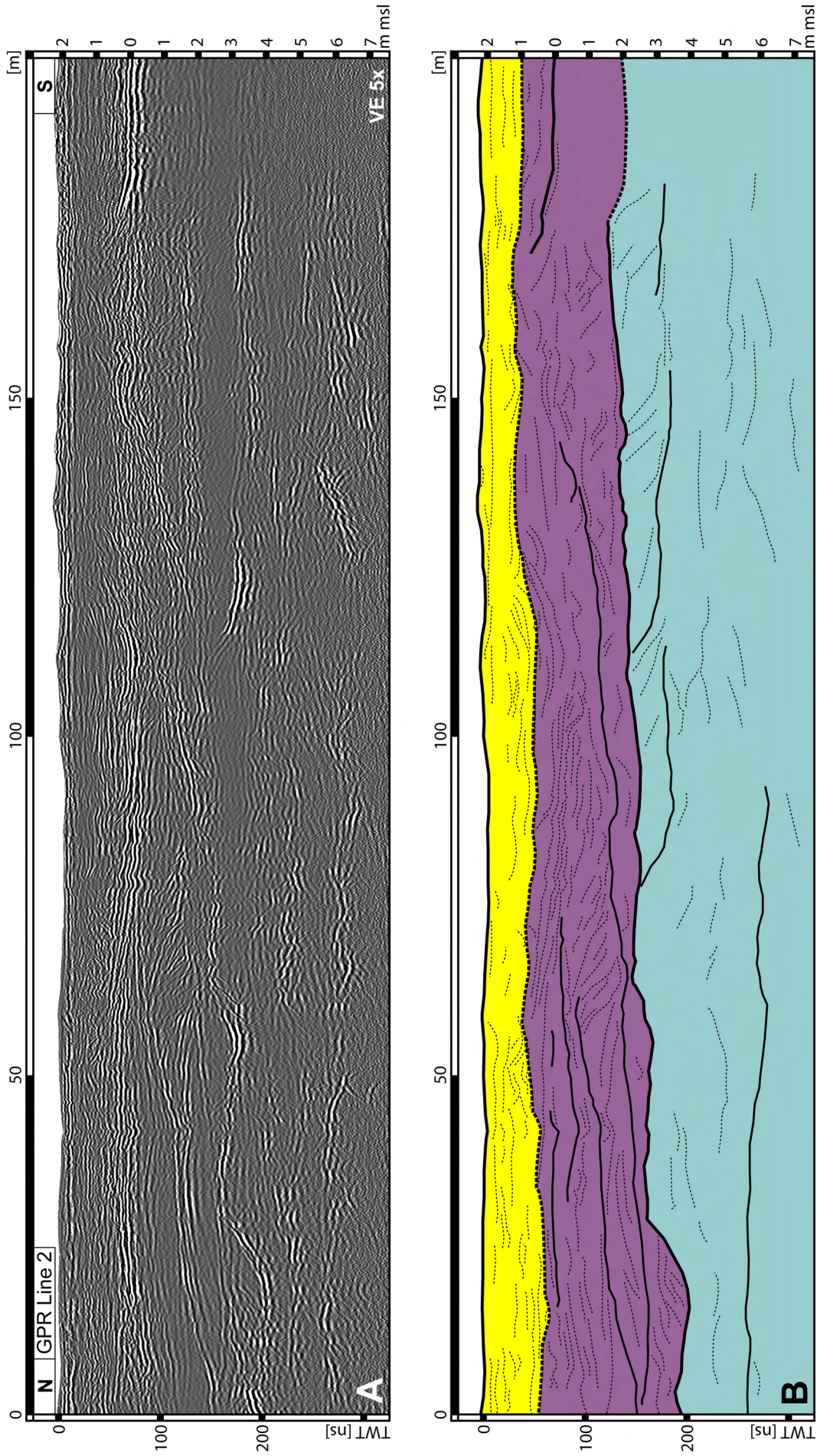


Figure 5.6: A: GPR Line 2. Data were obtained with a 200 MHz antenna, and show ground penetration down to 7 m bsf. For location compare Fig. 5.3. Down to mean sea level, horizontal or concave curved reflections dominate. Erosional unconformities are visible in depths of 1 m asl and at mean sea level. **(to be continued)**

reflection continuity and amplitude, and can be associated to a distinct sedimentary facies or a particular depositional process. Using the identified radar facies (Tab. 5.1), characterizing sediment geometries of selected study-area parts were mapped in the GPR lines and summarized in Figure 5.4A. Five different radar-facies combinations were defined, herein termed radar-facies associations (RfA). Each of them is typical for a specific part of the study area (Fig. 5.4B).

Radar-facies association „I“

This radar-facies association occurs in the southern and eastern part of the Listland (Fig. 5.4B). RfA-I contains the Rf-e, Rf-f, and Rf-k. It is characterized by Rf-e reflections at a depth between 3 m bsl and mean sea level, that are unconformably overlain by east- to southeastward-dipping reflections of Rf-f (Fig. 5.5). At a depth of 1 m asl, these east- to southeastward-dipping reflections are truncated by an erosional unconformity. Strata above this unconformity are of Rf-k, with local intercalations of horizons containing Rf-f reflections. Strata below the Rf-e reflections are not imaged in the GPR lines due to signal attenuation. In some parts, the surface defined by the Rf-e reflections form depressions down to a depth of 5 m bsl. These cut-and-fill structures form northwest-southeast striking, channel-shaped structures that are filled by lateral accretion of sediment bodies.

Radar-facies association „II“

RfA-II, which occurs in the central part of the Listland (Fig. 5.4B), is characterized by east- to southeastward-dipping Rf-f reflections, down to a depth of 1.5 to 3 m bsl, where they show a downlap configuration onto a wavy shaped erosional unconformity (Figs. 3.12, 5.6). The eastward- to southeastward-dipping reflections are truncated at mean sea level by an erosional unconformity. Strata above this unconformity are of Rf-k, with intercalations of Rf-e reflections. In parts, cut-and-fill structures occur (Rf-j). Below the east- to southeastward-dipping Rf-f reflections, reflections of Rf-d are imaged in the GPR. These reflections are bundled into northward-dipping packages that are up to 5 m thick (Fig. 5.6) and traceable laterally over more than 500 m by unconformities. The lowermost unit consists of northeastward-dipping Rf-c reflections that are truncated by an erosional unconformity at a depth of 6 to 10 m bsl (Fig. 5.7). Northeastward-dipping reflections are traceable down to a depth of 19 m bsl. Diffraction hyperbolas at the erosional unconformity probably indicates the occurrence of coarse grained sediment at this interface.

Radar-facies association „III“

Sedimentary architecture and genesis of RfA-III are described in detail in Chapter 3. RfA-III, present in the western part of the Listland (Fig. 5.4B), contains northward-dipping sigmoidal shaped reflections (Fig. 3.6) that bundle packages of weak Rf-g reflections dipping towards the southeast (Fig. 3.9). Cut-and-fill structures (Rf-j) occur down to a depth of 2 m bsl. Below the Rf-g reflections, there are concave curved reflections and horizontal or gently northward-dipping reflections of Rf-d, which are separated by a significant erosional unconformity (Fig. 5.4A). This

(continued from previous page): Note the high amplitude reflection between 175 and 200 m of the profile, at mean sea level, that attenuates underlying reflections. Below mean sea level there are southward-dipping reflections, separated by an unconformity from wavy to concave curved reflections. **B:** Line drawing and interpretation of GPR section provided in A. Horizontal and upward curved strata down to mean sea level reflects eolian sedimentation. Two erosional unconformities in depths of 1 m asl and at mean sea level are interpreted to reflect former eolian deflation surfaces. Below mean sea level, there is a further erosional unconformity, gently dipping towards the North.

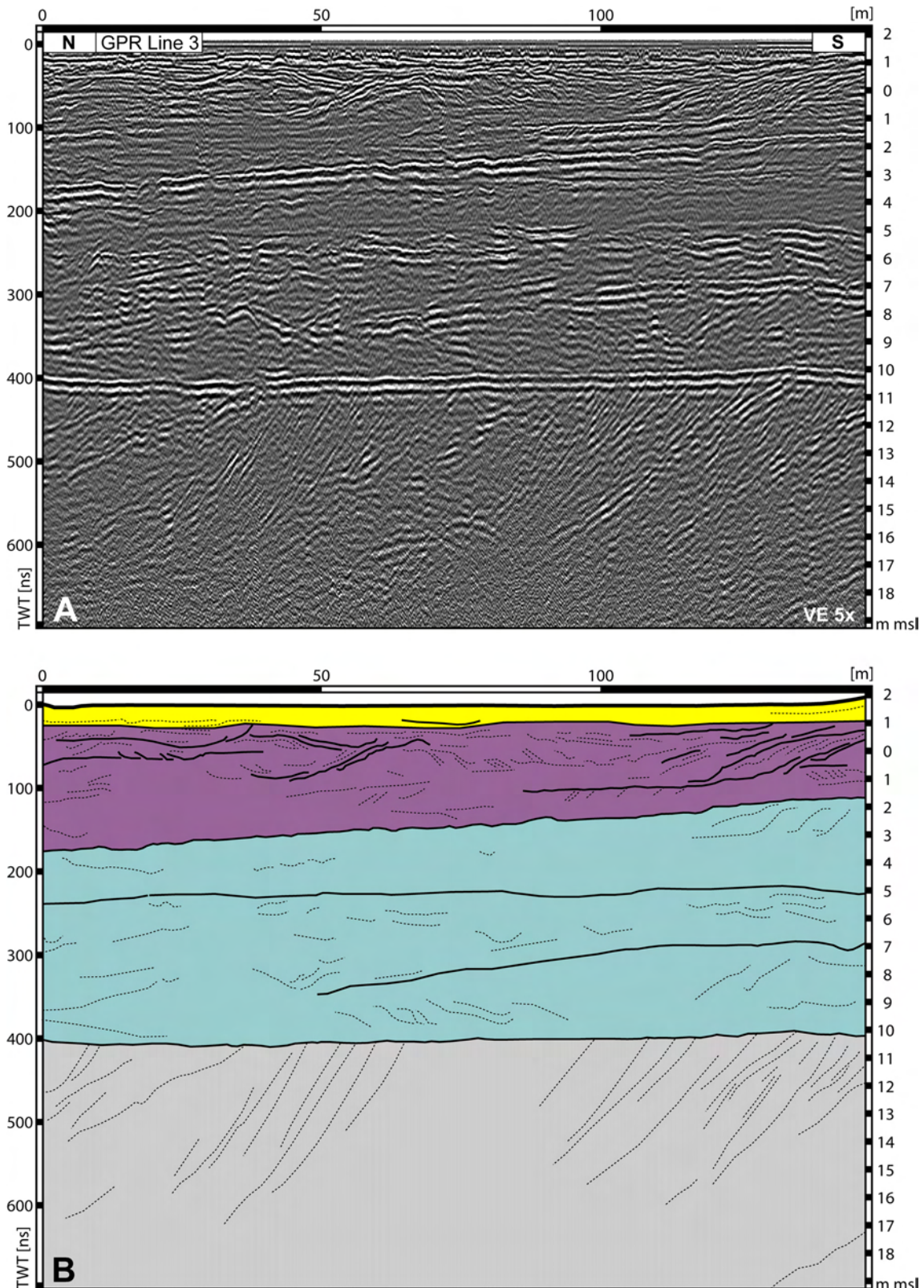


Figure 5.7: **A:** GPR Line 3, obtained with a 100 MHz antenna. For location see Figure 5.3. Note high-amplitude reflection at a depth of 10 m bsl, caused by an unconformity that truncates northward-dipping strata, which are traceable down to a depth of at least 16 m bsl, probably 19 m bsl. **B:** Line drawing and interpretation of GPR section provided in A. The uppermost meter of the profile reflects eolian sediments that overly a former eolian deflation surface. Strata below the deflation surface are interpreted as lateral accreted channel fill, associated with a large washover fan towards the east. Strata below a depth of 2 to 3.5 m bsl are interpreted to be associated with initial spit formation. The erosional unconformity at a depth of 10 m bsl probably reflects the spit basement. It truncates northeastward-dipping strata, interpreted as deposited during the early post-glacial marine transgression.

unconformity dips towards the west and northwest and is imaged in GPR data shown in Figures 3.9 and 3.10. Strata above this unconformity are attributed to the Rf-g as they are genetically related to the swash-bar system described in Chapter 3. The lowermost unit of RfA-III, which is only recorded in some of the GPR surveys, consists of weak Rf-c reflections and indicates strata dipping towards the northeast (Fig. 3.8). These reflections are truncated at the top by an erosional unconformity at a depth of 8 to 10 m bsl. Another distinct erosional unconformity exists at a depth of 1 m asl, and is overlain by Rf-k reflections (Fig. 3.10).

Radar-facies association „IV“

RfA-IV only occurs in a small northwest-southeast striking segment in the northern part of the Listland (Fig. 5.4B). This RfA is characterized by southeastward-dipping, up to 6 m thick Rf-h reflections (Fig. 5.8), forming the infill of a major erosional feature that truncates underlying northward-dipping packages of Rf-g and Rf-d reflections (Fig. 5.9). The northern-edge of the cut-and-fill structure is eroded by strata that belong to RfA-II. Rf-h reflections are truncated at a depth of 1 m asl by an erosional unconformity. Strata above this unconformity show planar or concave

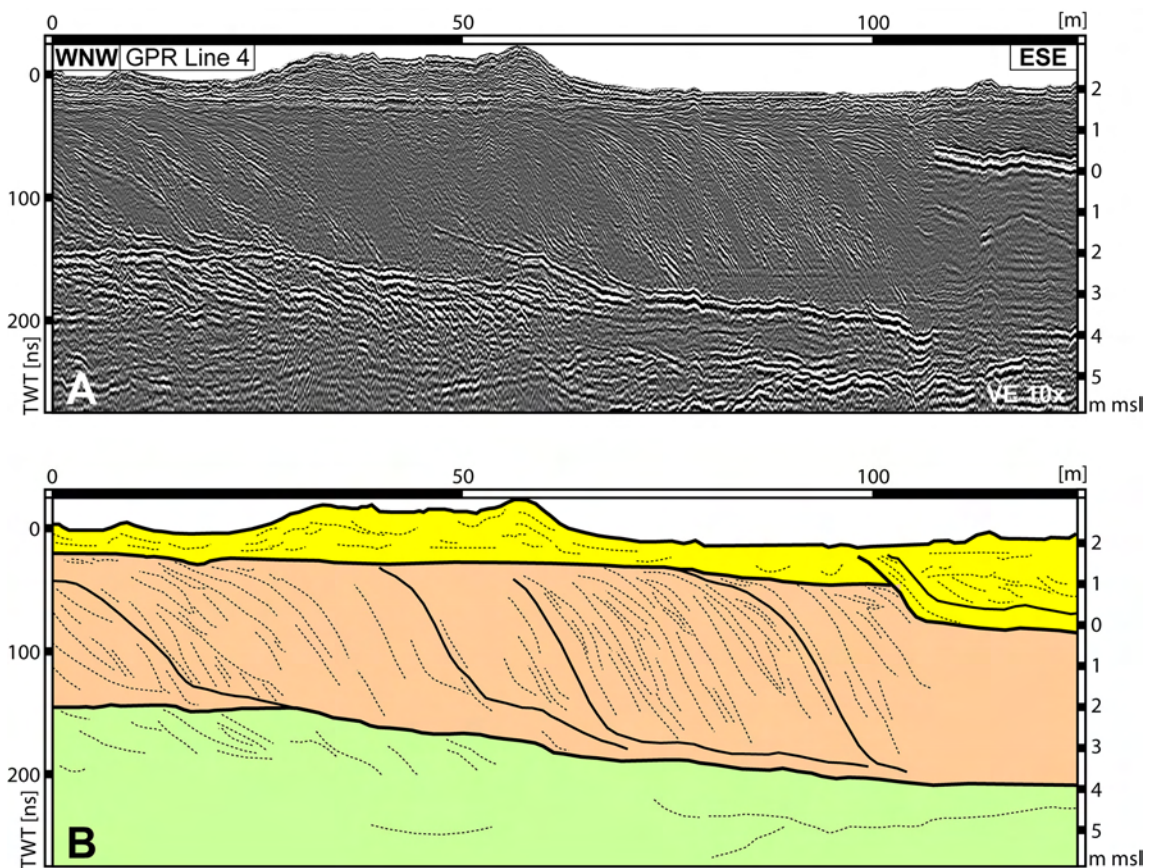


Figure 5.8: **A:** GPR Line 4 (200 MHz antenna) showing a ground penetration down to a depth of 6 m bsl. For location see Figure 5.3. Eastward-dipping reflections, unconformably overlying horizontal, concave curved, or eastward-dipping strata, predominate in this line. Eastward-dipping strata are truncated at a depth of 1 to 1.5 m asl by an erosional unconformity. Note high amplitude reflections around 120 m of the profile at mean sea level. **B:** Line drawing and interpretation of GPR section provided in A. Below a former eolian deflation surface, at a depth of 1 to 1.5 m asl, eastward-dipping strata are interpreted as tidal-inlet fill. The base of this tidal inlet is erosive and truncates underlying strata that exhibit eastward-dipping or are horizontal stratified. These strata are attributed to a system of welded swash bars. A clay layer, at mean sea level around meter 120 of the profile, is interpreted as deposited during a marine incursion from the Königshafen, which is situated towards the northeast.

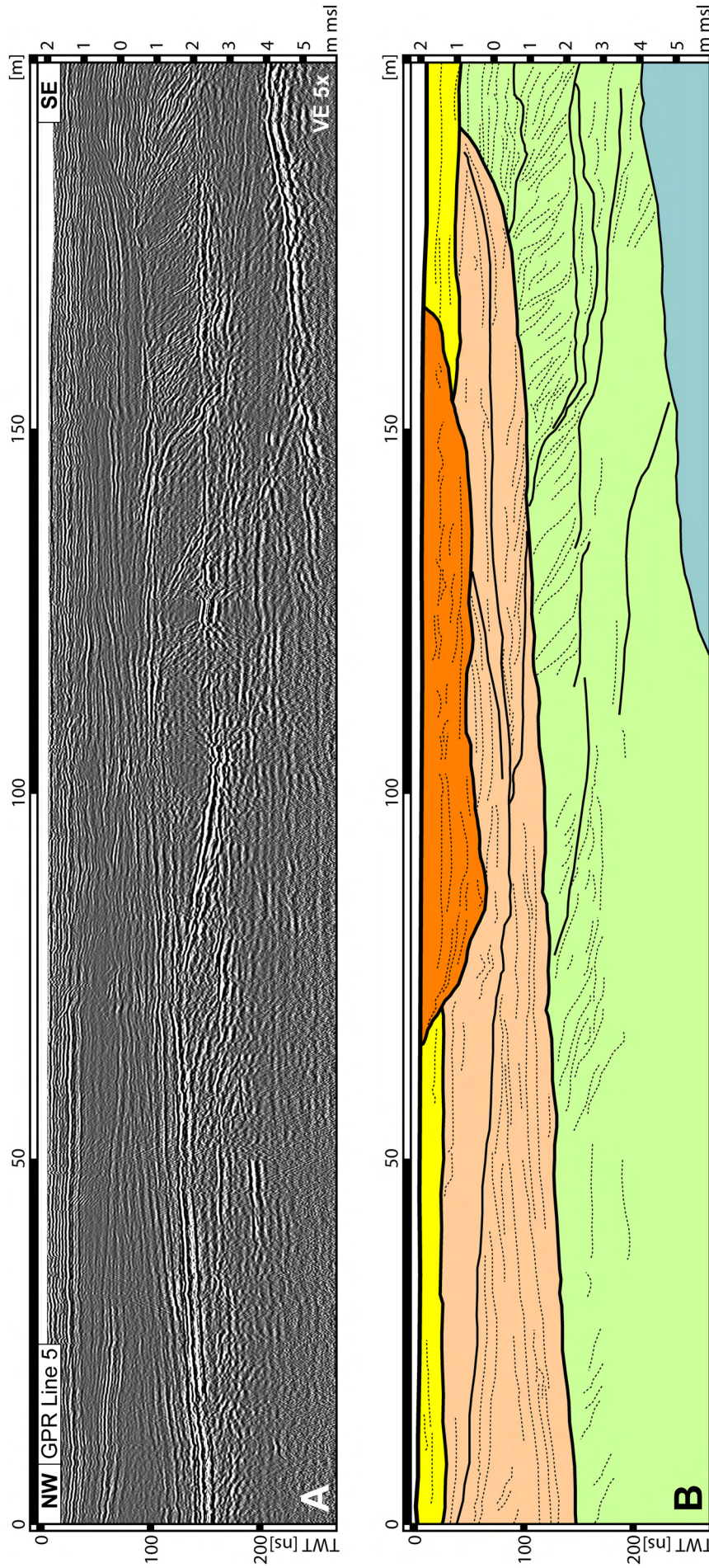


Figure 5.9: A: GPR Line 5 (200 MHz antenna) with a ground penetration down to 5 m bsl. For location see Figure 5.3. Between 60 and 160 m of the profile there is a cut-and-fill structure which internally also reveals horizontal reflections. Reflections below 1 m asl are subdivided by an erosional unconformity, gently dipping towards the northeast along the profile, from 1 m asl to 2 m bsl. Strata above the unconformity exhibit horizontal or concave curved reflections. Reflections beneath the unconformity, however, show a southeasterly-directed dip. B: Line drawing and interpretation of GPR section. The cut-and-fill structure in the middle part of the profile is interpreted as former eolian deflation surface at a depth of 1 m asl. Strata above this unconformity are eolian deposits. The cut-and-fill structure in the middle part of the profile is interpreted as scour channel, former feeding a washover fan situated to the east. Strata below 1 m asl, exhibit two different stratification patterns. First, there are horizontal to concavely curved strata that represent the fill of a large channel, reaching down to 2 m bsl. This channel probably was part of a former tidal inlet (compare Fig. 5.8). Second, strata below the erosive channel base show an easterly-directed internal bedding. These strata are part of a system of welded swash-bars, interpreted as spit-recovery sequence.

curved Rf-k reflections. GPR data exhibits a cut-and-fill structure (Rf-j) in the northwest-part of the Listland, reaching down to mean sea level (Fig. 5.8). The fill shows Rf-e reflections in the lower part and Rf-j reflections in the upper part. The structure is truncated at the top by an erosional unconformity at a depth of 0.5 to 1 m asl, and a second cut-and-fill structure (Rf-j) that reaches up to the surface.

Radar-facies association „V“

RfA-V summarizes the reflection geometries observed on the Ellenbogen hooked spit and described in detail in Chapter 4. Down to mean sea level, planar and concave curved reflections of Rf-k occur (Fig. 4.7). These reflections show interfingering with underlying Rf-b reflections. Rf-b comprises of alongshore-dipping reflections down to a depth of 2 m bsl and predominantly seaward-dipping reflections below, down to a depth of 4 to 6 m bsl. A seaward-dipping erosional unconformity separates the different reflection patterns from each other. Cut-and-fill structures (Rf-j) occur down to a depth of 0.5 m bsl (Fig. 4.6). The base of the Ellenbogen exhibits southeastward-dipping Rf-a reflections (Fig. 4.10) that are interpreted as sand bodies of a former tidal inlet. These strata are truncated at a depth of 4 to 6 m bsl by an erosional unconformity.

5.4.2 Stratigraphic cross sections

Cross sections through northern Sylt, constructed based on several GPR lines, reveal the different architectural elements of the spit. Two north-south striking sections are provided in Figure 5.10 and 5.11A. A northwest-southeast striking section is depicted in Figure 5.11B, and two west-east sections are shown in Figures 5.11C, and 5.11D respectively. As not all sections are directly covered by GPR lines, data from adjacent GPR surveys were incorporated and projected onto the line. Due to covering by high dunes, some parts of the profiles do not provide usable data, and were therefore left blank in the cross sections. The base of the Holocene, at a depth of 25 to 45 m bsl (Gripp & Simon, 1940), was not reached by GPR (Fig. 5.2A).

Profile A

Profile A (Fig. 5.10) is 4000 m long and extends parallel to the modern shoreline. Imaged depth varies in-between 1 m bsl at the ends of the profile and 15 m bsl between meters 1600 and 2300 of the profile. This reflects different antenna frequencies used during GPR survey, the varying thickness of the freshwater lens with different distance to the shoreline, and – in the southern part of the profile – the occurrence of clay horizons. Along the profile, every deeper subsurface reflections are truncated at a depth of 1 m asl by an erosional unconformity, which extends along the entire profile. Another major erosional unconformity, truncated at mean sea level at meter 3200 of the profile, subdivides the profile into northern and southern part.

The northern part of Profile A, between meters 0 and 3200, is characterized by a system of sigmoidal shaped, northward-dipping erosional unconformities, that bundle weak reflections with different dip orientations. With exception of the segment between meters 350 and 560, the profile consists of RfA-III, which is described more detailed in Chapter 3. Between meters 350 and 560, there is a major cut-and-fill structure, showing internal structures that are lenticular shaped or reflectors that are dipping towards the North. This reflection pattern is assigned to RfA-IV and shapes a northwest-southeast striking channel (Figs. 5.4, 5.5, and 5.6). The northern edge of this structure is truncated by reflections assigned to Rf-II.

The southern part of Profile A shows some patchy distributed Rf-e reflections, located at depths of mean sea level and 1 m bsl respectively, attenuating the GPR signal. Structures beneath are horizontal or gently northward-dipping unconformities that separate packages showing Rf-d reflections. The southern part of Profile A is build of RfA-II.

GPR data presented in Figure 5.12 cover a 780 m long segment of Profile A. Data were collected with a 100 MHz antenna and have a ground penetration down to 14 m bsl. Down to a depth of 4 to 9 m bsl, the GPR line shows northward-dipping unconformities, truncating packages that exhibit low-amplitude reflections. Two types of unconformities can be distinguished, based on their shape: Unconformities of the first type show a sigmoidal shape and dip down to a depth of 3 m bsl where they run nearly horizontal for 100 to 200 m. Unconformities of the second type dip down to a depth of 4 to 9 m bsl, where they are traceable for several hundred meters. The unconformities and the nearly transparent regions in-between are assigned to Rf-g. Strata below 4 to 9 m bsl show Rf-d reflections and are truncated at the top by the former described Rf-g reflections. Below 9 m bsl, reflections of Rf-c are imaged by the GPR.

The lowermost unconformity in Profile A (Fig. 5.10) forms the interface between underlying RfA-III and overlying RfA-I. Strata below this unconformity are dipping towards the northeast (Rf-c) and are imaged by GPR in several areas of the spit (compare Figs. 5.7, 5.11D, 5.11E, and 5.13). As mentioned above, GPR data show diffraction hyperbolas, probably caused by pebbles or boulders, at this unconformity (Fig. 5.7). This interpretation is supported by Gripp & Simon (1940) who described the occurrence of coarse sands and pebbles below a depth of 8 to 10 m (drillings S6 and S7 in Gripp & Simon, 1940). All deep unconformities are truncated around meter 1700 of the profile by northward-dipping reflections.

Profile B

The north-south running Profile B is 1550 m long. Significant unconformities are imaged all along the profile at depths of 1m asl and around mean sea level. In the southern part of the profile, between meters 1000 and 1550, widespread Rf-e reflections are imaged at mean sea level, which shield reflections from strata beneath. Below mean sea level, the profile is dominated by northward-dipping erosional unconformities that bundle reflections of Rf-d. A northward-dipping erosional unconformity between profile meters 350 and 75 truncates underlying Rf-d reflections. Strata above this unconformity show eastward-dipping Rf-f reflections. Between the north-end of the profile and 120 m, a significant northward-dipping erosional unconformity truncates underlying Rf-d reflections. Reflections above this unconformity are of Rf-j, forming a large cut-and-fill structure. Because no west-east striking GPR lines are available here, the exact geometrical shape of this reflections is unclear.

The main part of Profile B, between meters 350 and 1000, reflects RfA-II. However, between the north-end and meter 350 of the profile radar facies of RfA-IV dominate, whereas the southern part of the profile, in-between meters 1000 and 1550 of the profile, is attributed to RfA-I.

Profile C

Profile C provides a 2000 m long northwest-southeast striking cross section, based on GPR data obtained with a 200 MHz antenna. Investigated depth is down to

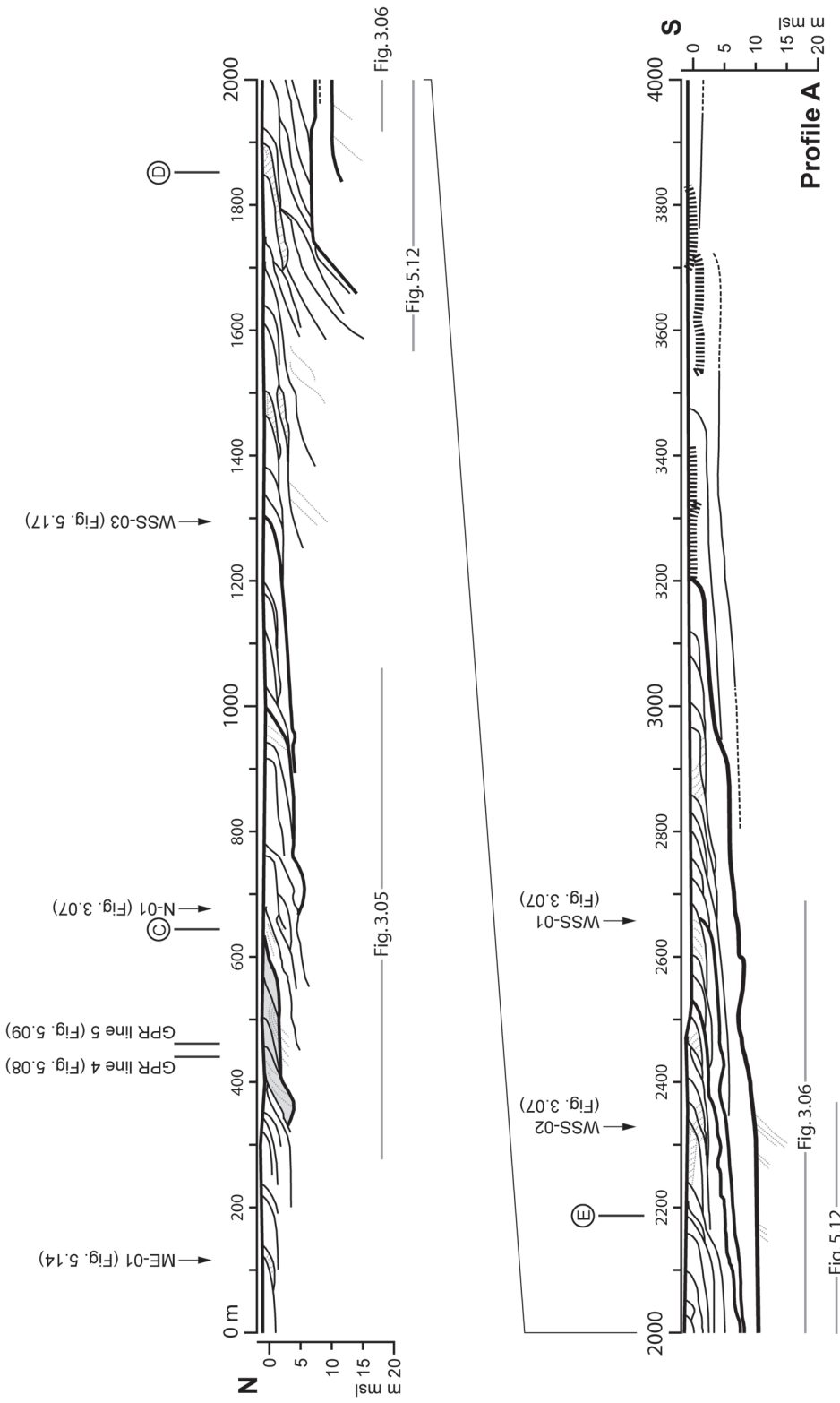


Figure 5.10: The north-south oriented Profile A (VE 10 x). For location of profile line see Figure 5.4. In addition to the position of sediment cores recovered along the profile line, several GPR lines, oriented perpendicular or parallel to the strike of the profile, and the positions of Profiles C - E are indicated. Decreasing penetration depth towards the northern end of the profile is attributed to increasing salt content of the groundwater. To the South, however, penetration decreases due to signal attenuation by clay layers (dashed bold lines) in the shallow subsurface. Note the erosive structure interpreted as former tidal inlet between profile meters 300 and 600. The major unconformity, dipping towards the North from meter 3200 of the profile (bold line), is interpreted as contact between RfA-I – in southeasterly direction – and RfA-III – towards the North. Thin dashed lines indicate internal structuring of sediment packages.

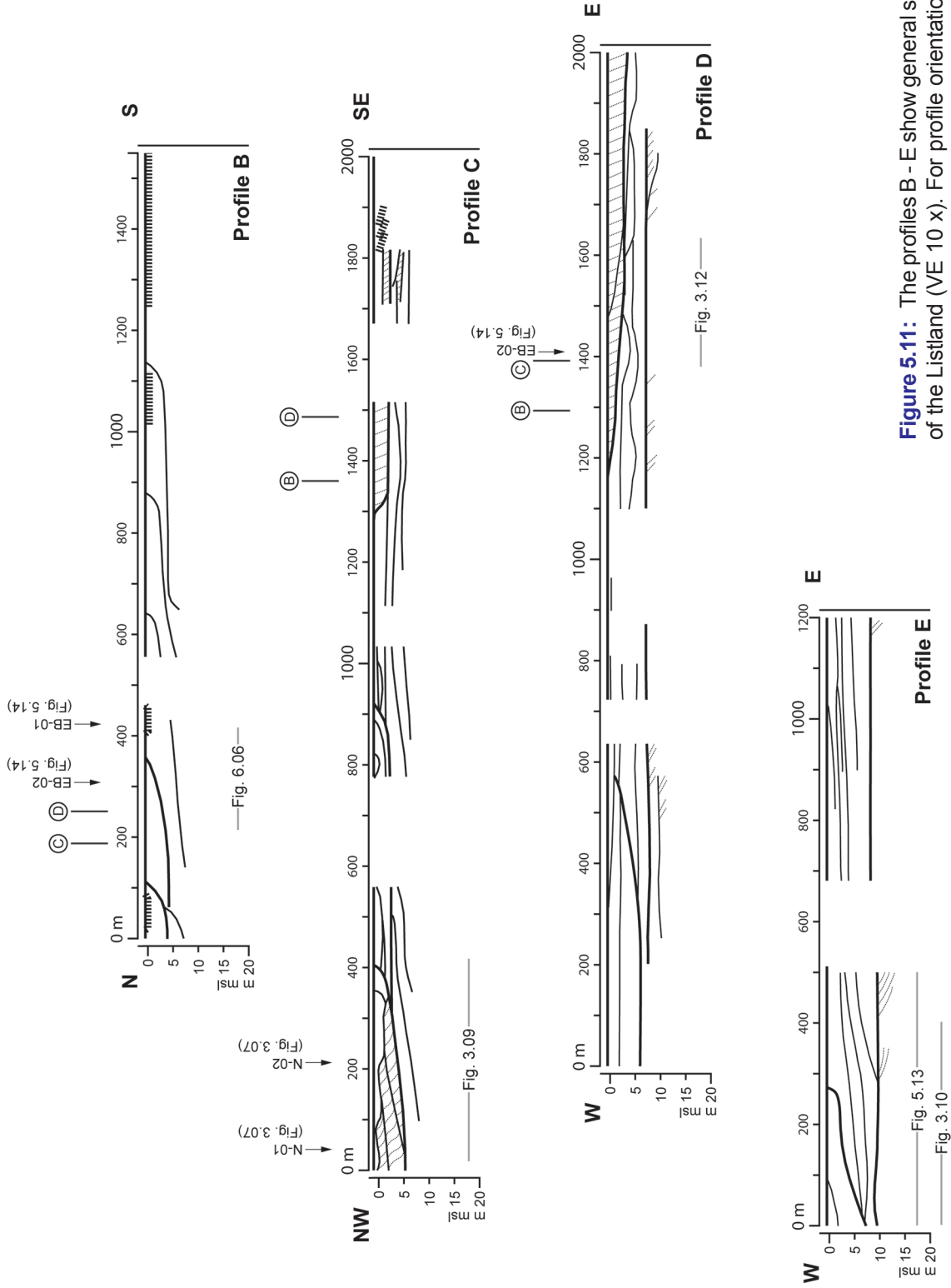
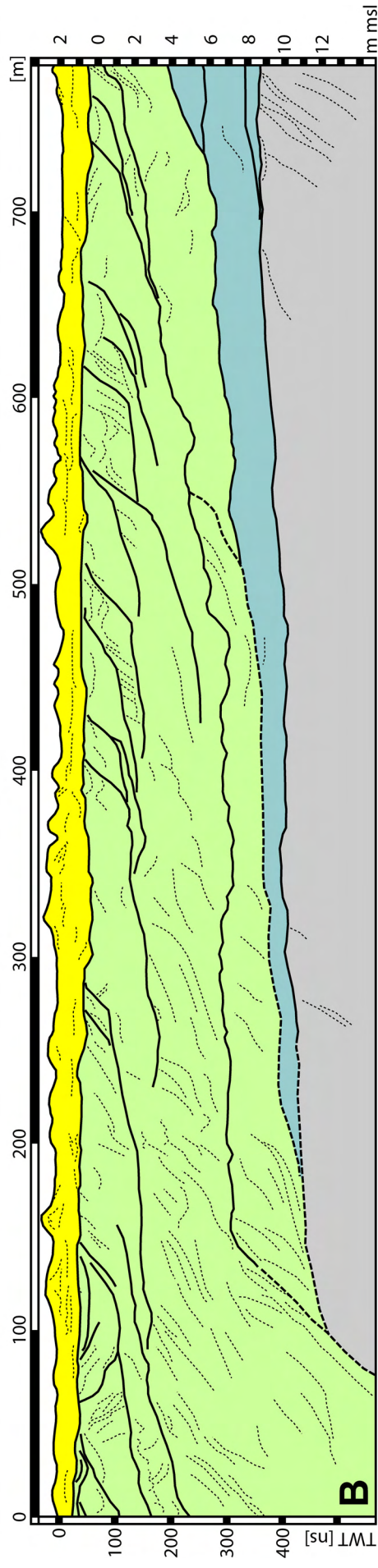
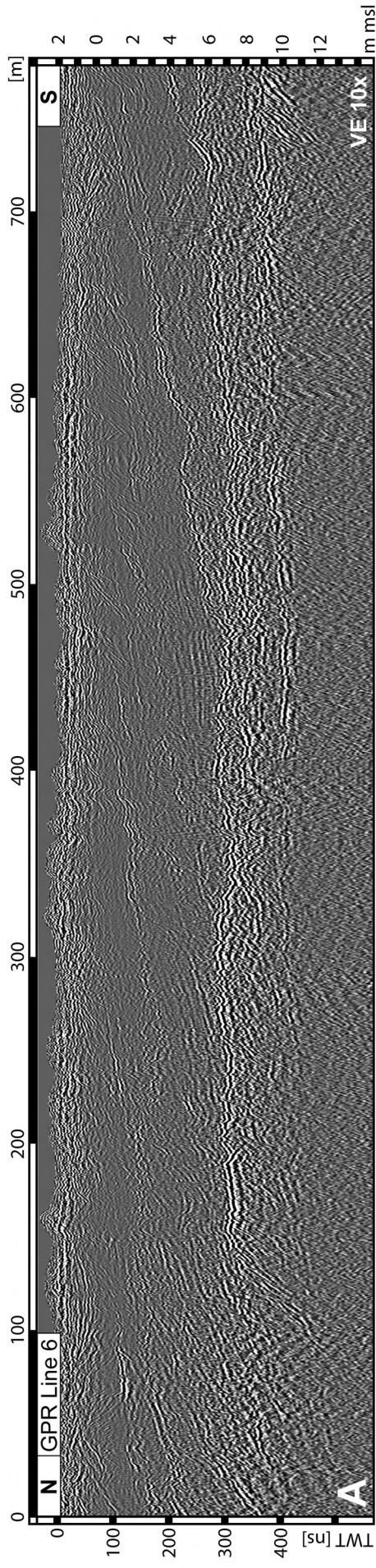


Figure 5.11: The profiles B - E show general sediment geometries of the Listland (VE 10 x). For profile orientation see Figure 5.4.



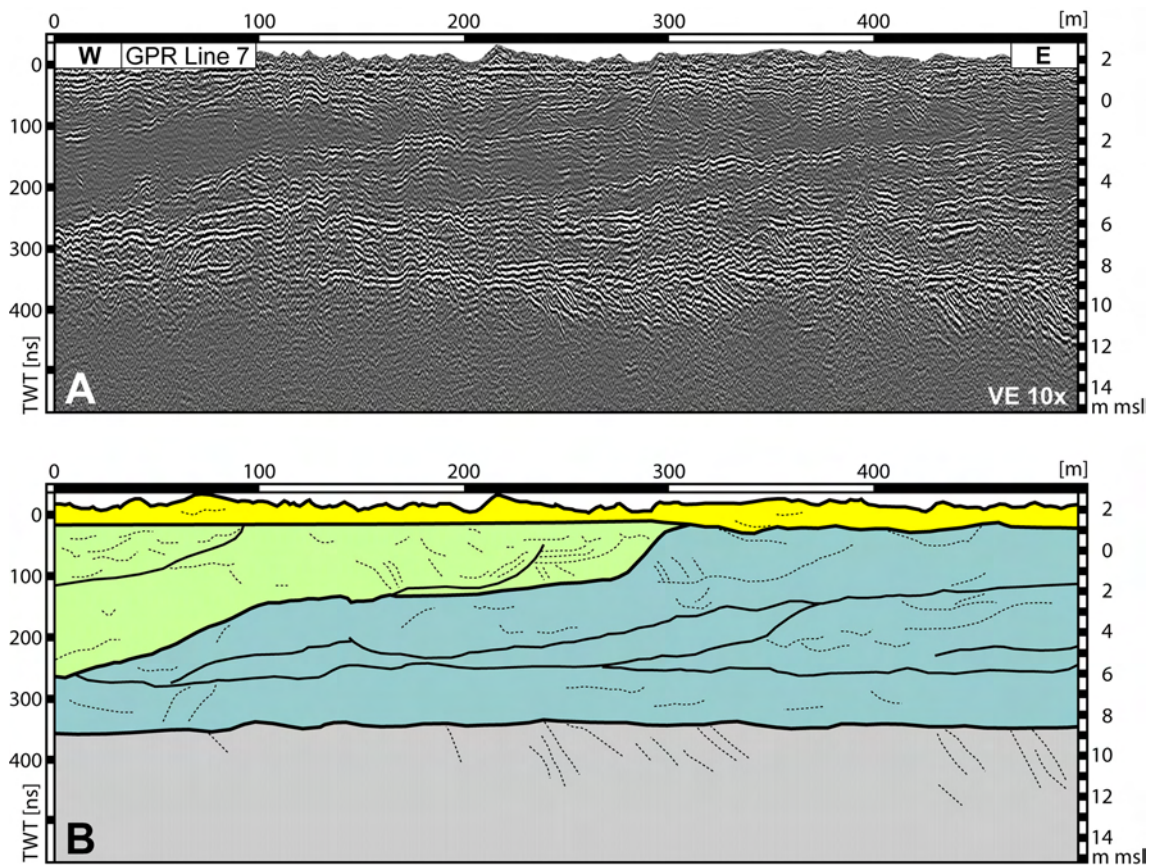


Figure 5.13: **A:** GPR Line 7 (100 MHz antenna) with a ground penetration down to 12 m bsl. For location see Figure 5.3. Westward dipping reflections dominate below an erosional unconformity at a depth of around 1 m asl. These reflections are truncated by a second erosional unconformity, dipping towards the western end of the profile, where it reaches a depth of 6 m bsl. An erosional unconformity is also imaged at a depth of 9 m bsl. This unconformity truncates eastward-dipping reflections, imaged down to a depth of 12 m bsl. **B:** Line drawing and interpretation of GPR section provided in A. Eolian strata, unconformably overlaying a former deflation surface, are imaged down to a depth of around 1 m asl. Beneath there are concave curved strata, bundled by erosional unconformities into westward-dipping sediment packages. These strata are interpreted as sediments of the initial spit, and in the western half of the GPR line are eroded by a westward-dipping unconformity. Strata above this unconformity are transparent in the GPR image or show an eastward-dip. These are sediments of the swash-bar system, associated to RfA-III. The erosional unconformity at a depth of 9 m bsl is interpreted to reflect the contact between northeastward-dipping sediments deposited during an early stage of the post-glacial marine transgression and sediments attributed to the spit. These sediments dipping towards the northeast probably correlate with the „Grauer Meeressand“ unit defined by Gripp & Simon (1940).

Figure 5.12 (previous page): **A:** GPR Line 6 (100 MHz antenna) shows a ground penetration down to 13 m bsl. For location see Figures 5.3 and 5.10. A major erosional unconformity is imaged along the line at a depth of 1 m asl. Strata above this unconformity show horizontal bedding. Below the unconformity there are northward-dipping reflections bundled by northward-dipping, sigmoidally shaped erosional unconformities. Two types of unconformities can be distinguished. One type reaches down to a depth of 3 to 4 m bsl, the other reaches down to at least 6 m bsl, where it can be traced over more than 500 m. At a depth of 8 to 10 m bsl, there is another unconformity that truncated northward-dipping strata, imaged down to a depth of 12-13 m bsl. **B:** Line drawing and interpretation of GPR section provided in A. Whereas eolian sediments are imaged down to a depth of 1 m asl, strata beneath are attributed to the system of welded swash bars, interpreted as spit-recovery sequence. Northward-dipping strata below the erosional unconformity at a depth of 8 to 10 m probably correlate with the „Grauer Meeressand“ unit defined by Gripp & Simon (1940), and are interpreted to reflect sediments of an early stage of the post-glacial marine transgression. These sediments may form the basement of the spit. Note erosive truncation of deeper strata at meter 130 of the profile.

around 7 m bsl. Below a depth of 3 – 4 m bsl, the section is characterized by gently dipping unconformities that bound Rf-d reflections. Dip-direction is towards the northwest, between meters 0 and 1000 of the profile, and towards the southeast, from meter 1000 onwards. Strata above these unconformities refer to Rf-g in the northwest-part of the profile (Fig. 3.9) and to Rf-f in the southeast-part respectively. Near the southeast-end of the profile Rf-e reflections occur.

Three different radar-facies associations are imaged in Profile C. Reflections between meters 0 and 400 of the profile are attributed to RfA-II, reflections between meters 400 and 1400 refer to Rf-III, and between meters 1400 and 2000 RfA-I occurs.

Profile D

The 2000 m long Profile D strikes west-east. GPR data obtained with antenna frequencies of 100 and 200 MHz allow to image structures down to a depth of 11 m bsl. Four significant erosional unconformities exist. The uppermost unconformity, at a depth of 1 m asl, truncates all underlying reflections and is imaged along the profile. Strata above this unconformity show Rf-k reflections. Around meter 550 of the profile there is the second unconformity that dips towards the western-end of the profile, where it reaches a depth of 6 m bsl. Above this unconformity there are reflections attributed to Rf-g. Strata beneath are of Rf-d and truncated by the unconformity. The third unconformity dips towards the east-end of the profile, starting from meter 1200 of the profile. Strata above this unconformity show reflections of Rf-f, dipping towards the east or southeast (Fig. 3.12). Strata below the unconformity are attributed to Rf-d. The lowermost unconformity, at a depth of 8 m bsl truncates northeastward-dipping reflections of Rf-c.

Profile D shows RfA-III between the west-end and meter 550 of the profile. The part of the profile in-between meter 550 and the east-end is attributed to Rf-III.

Profile E

West-east striking Profile E has a length of 1200 m. The profile incorporates GPR data obtained with frequencies of 100 and 200 MHz. Strata down to a depth of 12 m bsl are investigated. There are three significant erosional unconformities. The first is imaged along the profile and truncates underlying reflections at a depth of 1 m asl. The second unconformity, between meters 0 and 350, dips towards the west-end of the profile. Reflections above this unconformity are attributed to Rf-g, whereas Rf-d reflections are beneath. The third unconformity is located at a depth of 8 to 10 m bsl. This unconformity truncates northeastward-dipping reflections of Rf-c. Strata above are of Rf-d.

Radar facies between the western-end of the profile and meter 350 are attributed to RfA-II. The rest of Profile E exhibits RfA-II.

GPR Line 7 provided in Figure 5.13 was obtained with a 100 MHz antenna. Structures down to a depth of 12 m bsl are imaged. The GPR line is characterized by westward-dipping unconformities that bundle reflections of Rf-d. All reflections are truncated at a depth of around 1 m asl by an erosional unconformity. Above some Rf-k reflections are imaged. Between 0 and meter 240 of the profile there is a steep westward-dipping erosional unconformity truncating underlying strata. This unconformity reaches down to a depth of 6 m bsl at the western-end of the profile. Strata above this unconformity show reflections of Rf-g. At a depth of 8 to 9 m, there is an unconformity that truncates northeastward-dipping Rf-c reflections.

5.4.3 Grain-size data

Sediment cores with lengths between 480 and 1175 cm were drilled at selected locations on the northern spit (Fig. 5.3). Grain-size parameters for the six cores described herein are provided in Table 5.2. Additionally core data used are from sediment cores OE-01 and WE-02, presented in Chapter 4.

Core EB-01

The core is 480 cm long and reaches down to a depth of 2.50 m bsl (Fig. 5.14A-C). Dark grey stained intervals at 40 and 100 cm depth contain plant debris, and one small shell fragment occurs at a depth of 350 cm. Based on the mean grain size (Fig. 5.14A), four intervals exist in the core. The first interval reaches up to a core depth of 340 cm (1.1 m bsl), the second interval ranges from 340 to 235 cm core depth (1.1 to 0.05 m bsl), and the third interval from 235 to 30 cm core depth (0.05 m bsl to 2.0 m asl). The uppermost 30 cm of the core (2.0 m asl to the surface) form the fourth interval.

Grain size data reveal that the first interval is characterized by an overall coarsening upward trend. A horizon with significant finer grained sediments is located at a depth of around 400 cm. The second interval shows three horizons with significant finer grained sediments. These layers are exhibited in the core as light-grey colored clayey layers, up to 7 cm thick and separated from each other by yellow sand. The third interval shows minor variations in grain-size compared to the rest of the core and no clear grain-size trend. Finer grained sediments characterize the upper 30 cm of the core, forming the fourth interval.

The sorting data (Fig. 5.14B) reflect the four intervals previously defined. In the first interval, the sorting of the sediment shows strong variations, but at the same time an overall upward trend towards better sorted sediments occurs. The second interval is characterized by an overall upward trend towards better sorted sediments. The fine-grained horizons described for the mean grain size show the worst sorting

Core		Mean grain size (phi)					
ID	length	maximum		minimum		average	
EB-01	480 cm	1.66	medium sand	7.57	fine silt	2.74	fine sand
EB-02	480 cm	1.55	medium sand	5.66	coarse silt	1.87	medium sand
K-01	860 cm	1.62	medium sand	7.61	fine silt	3.50	very fine sand
KH-01	1085 cm	1.67	medium sand	5.10	coarse silt	2.23	fine sand
ME-01	865 cm	1.70	medium sand	5.22	coarse silt	2.97	very fine sand
WSS-03	1175 cm	1.55	medium sand	5.24	coarse silt	2.08	fine sand

Core		Sorting (phi)					
ID	length	maximum		minimum		average	
EB-01	480 cm	0.58	moderately well sorted	3.07	very poorly sorted	1.41	poorly sorted
EB-02	480 cm	0.58	moderately well sorted	2.74	very poorly sorted	0.91	moderately sorted
K-01	860 cm	0.56	moderately well sorted	2.94	very poorly sorted	1.55	poorly sorted
KH-01	1085 cm	0.49	moderately sorted	2.90	very poorly sorted	0.97	moderately sorted
ME-01	865 cm	0.47	well sorted	3.13	very poorly sorted	1.57	poorly sorted
WSS-03	1175 cm	0.46	well sorted	3.34	very poorly sorted	0.89	moderately sorted

Core		Skewness of the frequency distribution (phi)					
ID	length	maximum		minimum		average	
EB-01	480 cm	-0.25	coarse skewed	0.77	very fine skewed	0.36	very fine skewed
EB-02	480 cm	0.04	symmetrical	0.70	very fine skewed	0.39	very fine skewed
K-01	860 cm	-0.04	symmetrical	0.74	very fine skewed	0.36	very fine skewed
KH-01	1085 cm	0.01	symmetrical	0.74	very fine skewed	0.33	very fine skewed
ME-01	865 cm	-0.04	symmetrical	0.78	very fine skewed	0.44	very fine skewed
WSS-03	1175 cm	0.00	symmetrical	0.74	very fine skewed	0.38	very fine skewed

Table 5.2: Characteristic grain-sizes parameters for sediment cores. For core locations see Figure 5.3. Cores are presented in Figures 5.14 to 5.17.

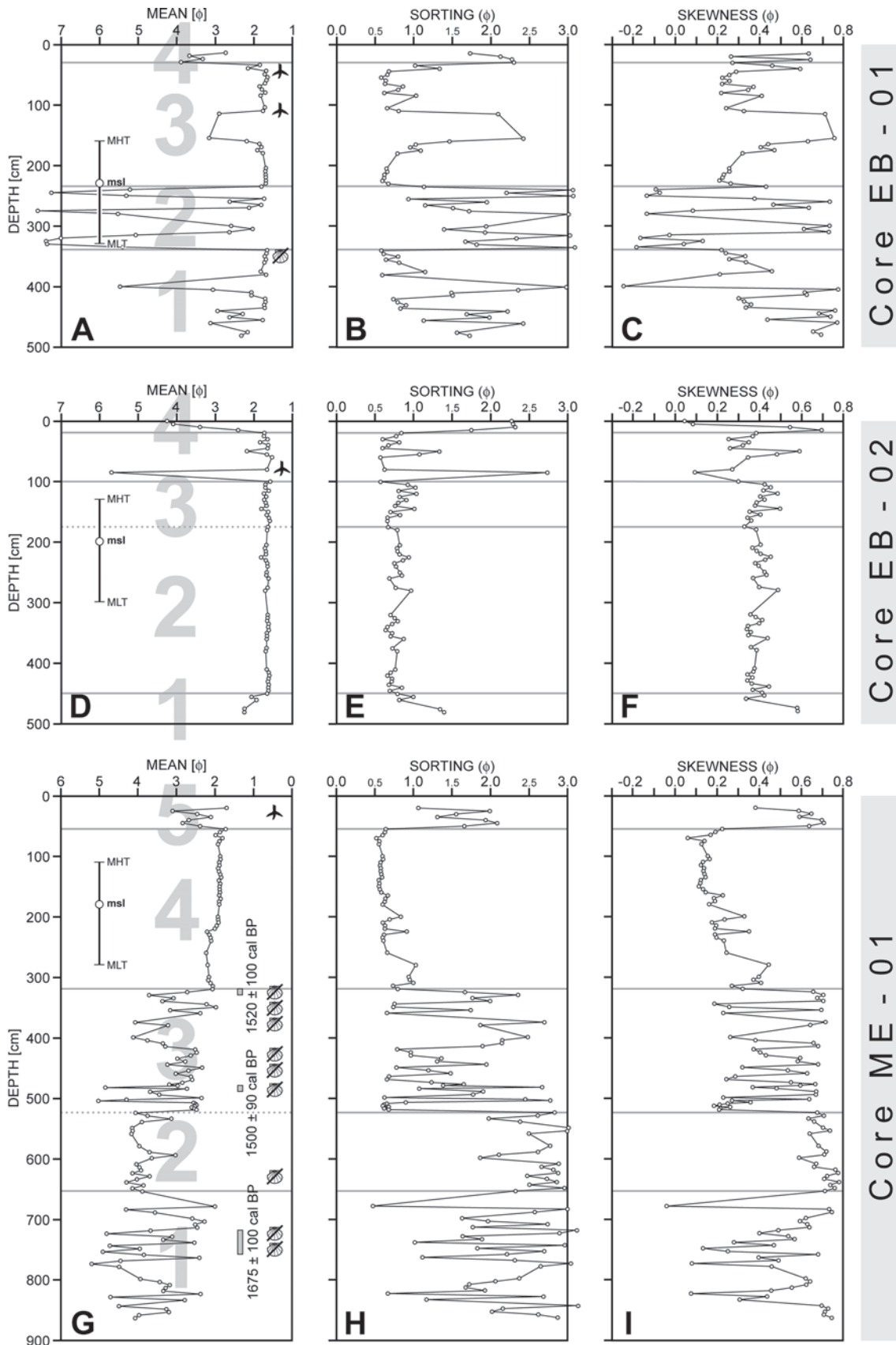


Figure 5.14: Grain-size data of Cores EB-01, EB-02, and ME-01. **A, D, G:** Mean grain size provided in phi. The bar on the right side of the grain-size curve shows the recent intertidal range with respect to msl. Position of root- or shell-bearing horizons is indicated. For core ME-01, available results of ¹⁴C-dating are presented on right side of the curve; vertical grey bars mark sampled depth ranges. **B, E, H:** Sorting of the investigated sediment samples. The sorting is based on grain-size classes in phi. **C, F, I:** Skewness of the frequency distribution, based on grain-size classes in phi.

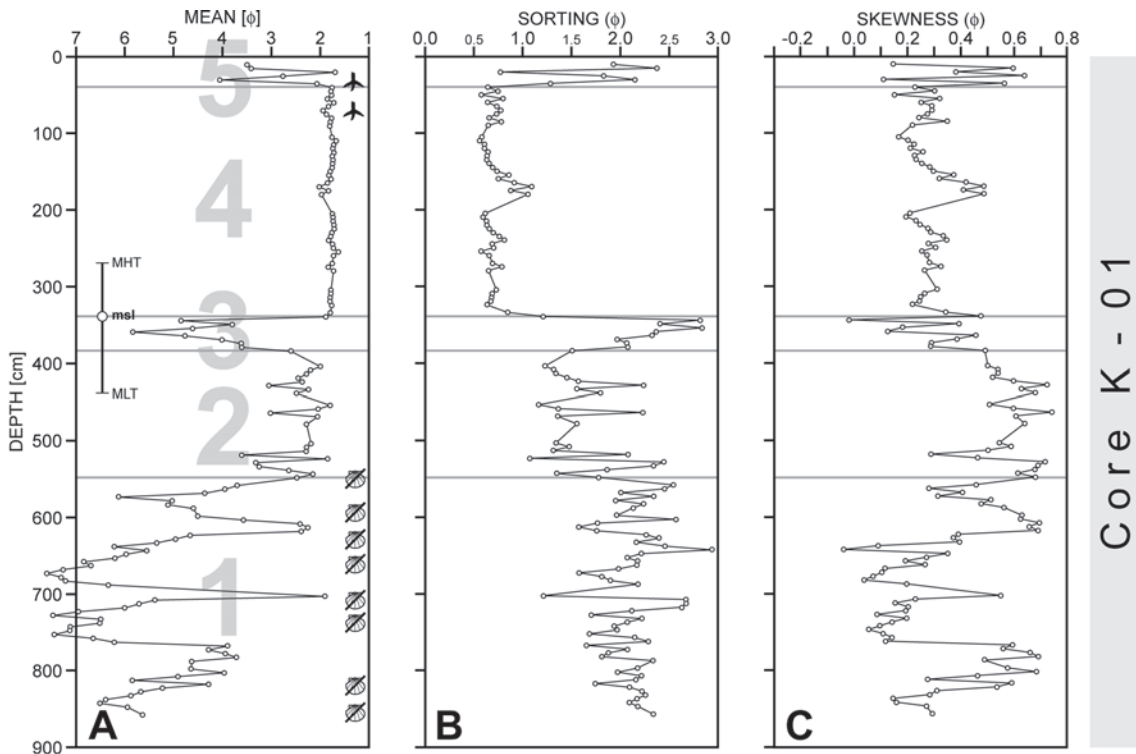


Figure 5.15: Grain-size data of Core K-01. Core location is depicted in Figure 5.3. **A:** Mean grain size provided in phi. For legend compare Figure 5.14. **B:** Sorting of the investigated sediment samples. **C:** Skewness of the frequency distribution.

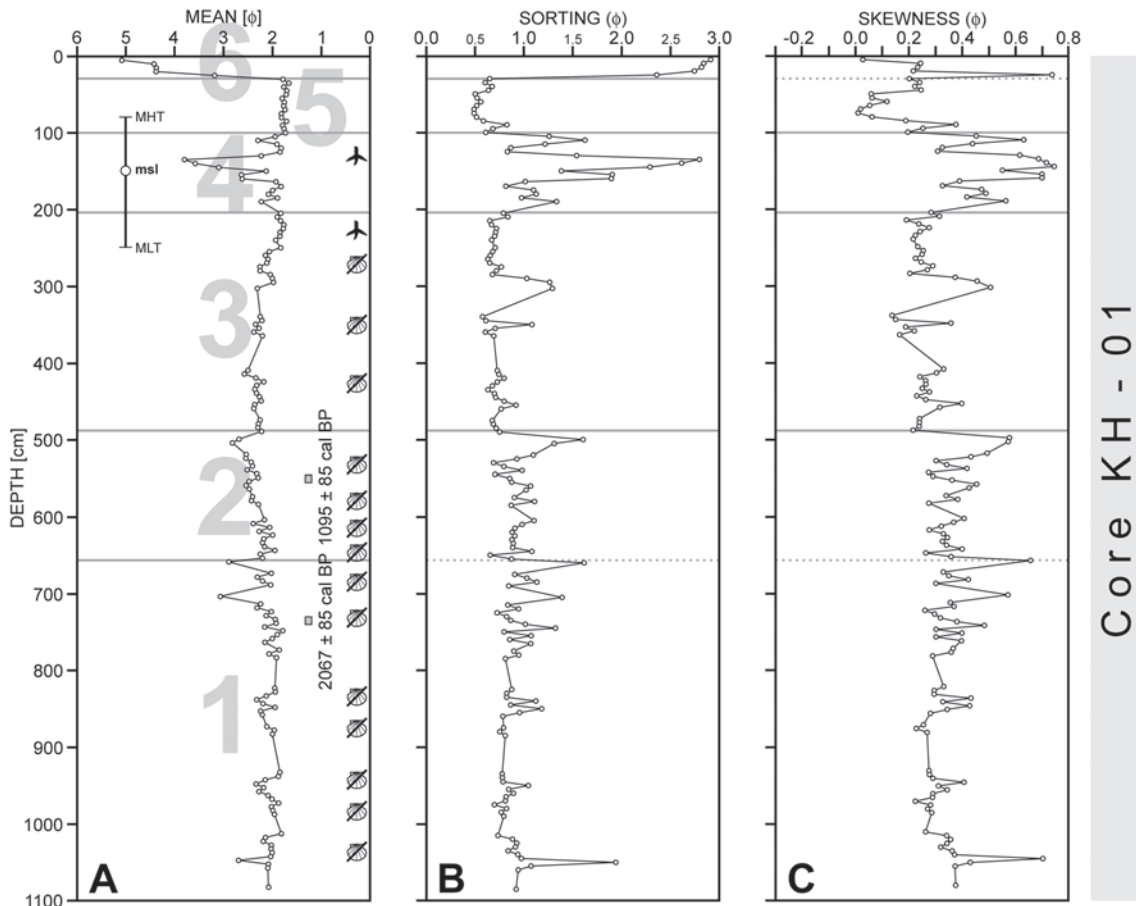


Figure 5.16: Grain-size data of Core KH-01. Core location is depicted in Figure 5.3. **A:** Mean grain size provided in phi. Results of ¹⁴C-dating are presented. For legend see Figure 5.14. **B:** Sorting of the investigated sediment samples. **C:** Skewness of the frequency distribution.

of the core. In the third interval no clear trend is shown by the sorting data. The fourth interval exhibit an upward trend towards better sorted sediments.

The skewness of the frequency distribution (Fig. 5.14C) mirrors the previously described four intervals too. In the first interval, there exist an overall trend towards a more symmetrical grain-size distribution. The second interval, reveal strong variations, whereas finer skewed intervals correlate with the horizons that are composed of finer grained sediments. The third and the forth interval exhibit no clear trend in the skewness data.

Core EB-02

The core is 480 cm long and reaches down to a depth of 2.80 m bsl (Fig. 5.14D-F). Root fragments were found at a depth of 80 cm, no shell fragments occur in the core. The curves for mean grain size (Fig. 5.14D) and sorting of the sediment (Fig. 5.14E) defines five intervals in the core. The first interval reaches up to 450 cm core depth (2.50 m bsl). The second interval ranges from 450 to 175 cm core depth (2.50 m bsl to 0.25 m asl), the third from 175 to 100 cm core depth (0.25 to 1.00 m asl), the fourth from 100 to 15 cm core depth (1.00 to 1.85 m asl), and finally the fifth interval comprises the uppermost 15 cm of the core.

The mean grain size exhibits a coarsening-upward trend in the first interval. The second interval shows only little variations in mean grain size, and the third interval shows a slightly upward fining. The fourth interval has a horizon with fine-grained material at the base and an overall slightly fining upward trend above. The fine-grained horizon contains the root fragments. The fifth interval is characterized by a fining-upward trend.

The sorting data for Core EB-02 exhibits a clear upward trend towards better sorted sediments in the first interval. The second interval shows no clear trend and only little variations in sediment sorting. The third interval, however, exhibits a clear upward trend towards poorer sediment sorting. The fine-grained horizon at the base of the fourth interval contains the less sorted sediment of the core. The fifth interval shows an upward trend towards poorer sorting of the sediment.

The skewness of the frequency distributions (Fig. 5.14F) reflects the previously defined five intervals in Core EB-02. The first interval is characterized by an upward trend towards a more symmetrical grain-size distribution. The second interval shows little variations in the skewness data and no clear trend. The third interval, which shows a comparably constant mean grain size, exhibits a significant upward trend towards a positive skewed grain-size distribution. In the forth interval, data show strong variations, and an overall upward trend towards positive skewness. The uppermost interval, which starts 15 cm below the surface, is characterized by a drop to a symmetrical grain-size distribution at the surface.

Core ME-01

The core (Fig. 5.14G-I) is 865 cm long and reaches down to a depth of 6.88 m bsl. At a depth of 30 cm, root fragments are found. Numerous layers with shell fragments occur between 325 cm and the bottom of the core. Variations in mean grain-size and sorting define five intervals in this core (Fig. 5.14G, H). The first interval is between the base of the core and a core depth of 655 cm (4.75 m bsl). The second interval ranges from 655 to 525 cm core depth (4.75 to 3.45 m bsl), the third from 525 to 320 cm core depth (3.45 to 1.4 m bsl), and the forth from 320 to 55 cm core

depth (1.4 m bsl to 1.25 m asl). The fifth interval comprises the upper 55 cm of the core (from 1.25 to 1.8 m asl).

The first interval is characterized by significant variations of the mean grain size, mantled by a coarsening-upward trend. Both of the second and the third interval show an overall coarsening upward trend. The fourth interval is significantly coarser grained and shows much less variations in mean grain size than the previously described intervals. A slightly fining upward is visible. The fifth interval exhibits no clear trend, but is finer grained than the fourth interval.

In Core ME-01, coarser grained sediments are better sorted than sediments with a finer mean grain size. The lowermost interval shows no clear trend but strong variations in sediments sorting. The second interval exhibits very poorly sorting, whereas comparable little variations in sorting exist. The third interval is characterized by a strong varying sorting curve with no clear trend. The fourth interval shows good sorting of the sediment and an overall upward trend towards better sorting. A break in the sorting curve marks the lower limit of the fifth interval, which is characterized by a poorer sorting of the sediments than the fourth interval.

Skewness of the frequency distribution for Core ME-01 (Fig. 5.14I) exhibits trends that are largely comparable to the sorting trends. In general, strong variations in sorting correlate with strong variations in skewness, with poorer sorted sediments being more skewed than better sorted sediments. Whereas the first three intervals do not reflect a clear trend, the fourth interval shows a clear upward trend towards a more symmetrical grain size distribution.

Core K-01

The core is 860 cm long and reaches down to a depth of 5.20 m bsl (Fig. 5.15A-C). Horizons bearing roots are located at depths of 35 and 75 cm. Between 550 cm depth and the bottom of the core there are numerous horizons with mollusk shells. Grain size data define five intervals in Core K-01 (Fig. 5.15A). The first interval is between the bottom of the core and a depth of 550 cm (2.10 m bsl). The second interval is between 550 and 385 cm core depth (2.10 to 0.45 m bsl), followed by the third interval from 385 to 340 cm core depth (0.45 m bsl to mean sea level), and the fourth between 340 and 40 cm core depth (mean sea level to 3.00 m asl). The fifth interval comprises the upper 40 cm of the core (3.00 to 3.40 m asl).

The first interval, showing an overall coarsening-upward, is characterized by an interlayering of finer and coarser sediments. There are three horizons that comprise sediment with a mean grain size in the range of silt. The basal contact of these horizons shows an abrupt change from coarser to finer sediments. The upper contact, however, exhibits a gradual transition towards coarser grained sediments. The second interval reveals no clear trend, and the third interval comprises sediments with a mean grain size in the range of coarse silt. Both intervals show a gradual transition from coarser to finer sediments at the base and an abrupt transition from finer to coarser sediments at the top. The fourth interval shows no clear trend and only negligible variations in mean grain size. Mean grain size in the fifth interval exhibits an overall fining upward.

The first interval shows only minor variations in mean grain size (Fig. 5.15B). Two trends are visible. Up to 705 cm core depth (3.65 m bsl) there is an upward trend towards better sorting of the sediment. The upper part of the interval, between 705 and 550 cm core depth, shows a trend towards poorer sorting. The second interval

exhibits strong variations in sorting, but no clear trend. The third interval is characterized by a strong upward trend towards poorly sorted sediment. There are only little variations in the fourth interval. The uppermost interval of the core shows strong variations and a superposed upward trend towards poorer sorting.

Skewness of the frequency distribution (Fig. 5.15C) shows two trends in the first interval: Up to 640 cm depth (3.00 m bsl) there is a trend towards a more symmetrical grain-size distribution, and between 640 and 550 cm depth sediments show a finer skewed grain-size distribution. The second interval exhibits an upward trend towards finer skewing of the sediment up to 430 cm core depth. Above, sediments tend to a more symmetrical grain-size distribution. The third interval shows an upward trend towards more symmetrical distributed grain sizes. The fourth interval is characterized by comparably little variations in skewness and shows no clear overall trend. The fifth interval exhibits strong variations and no clear trend.

Core KH-01

Core KH-01 (Fig. 5.16A-C) is located near the southern margin of the western Ellenbogen. No GPR measurements were possible at this location due to ground salinization by ephemeral flooding of the area during storms. The core is 1085 cm long and reaches down to a depth of 9.35 m bsl. Shell fragments are found along the core, up to a core depth of 270 cm (1.20 m bsl). In depths of 135 and 233 cm (0.15 m asl, 0.83 m bsl) plant fragments exist. Variations of the mean grain size define six intervals (Fig. 5.16A) in the core. The first interval reaches up to 660 cm core depth (5.10 m bsl), the second interval ranges from 660 to 490 cm core depth (5.10 to 3.45 m bsl), the third from 490 to 205 cm core depth (3.45 to 0.55 m bsl), the fourth from 205 to 100 cm core depth (0.55 m bsl to 0.50 m asl), and the fifth interval ranges from 100 to 30 cm core depth (0.50 to 1.2 m asl). The upper 30 cm of the core define the sixth interval.

Grain-size data show that the first interval contains two weakly expressed fining-upward cycles (1010 to 940 and 940 to 845 cm core depth). The second interval is characterized by a slightly overall fining-upward trend, whereas the third interval exhibits an overall coarsening-upward trend. In the fourth interval, at a core depth of around 150 cm, a significantly finer grained layer occurs. The fifth interval has a constant mean grain size, and sediments of the sixth interval are significantly finer than the rest of the core.

Sorting (Fig. 5.16B) and grain-size distribution in Core KH-01 show a distinct correlation, coarser sediments being generally better sorted than finer sediments. Sediments up to 800 cm core depth (6.50 m bsl) show less sorting variations than sediments between 800 and 490 cm core depth (up to 3.40 m bsl). However, a distinct trend that would characterize intervals 1 and 2, is not visible. The third interval is characterized by fewer variations in grain size compared to the sediments below. The fourth interval is partly poorly sorted, the corresponding parts are significantly finer grained. The fifth interval shows less variations in grain-size, and sediments of the sixth interval are very poorly sorted.

In Core KH-01 finer grained samples are generally finer skewed than coarser grained samples (Fig. 5.16C). Up to 490 cm core depth (intervals 1 and 2), there is no distinct trend in the skewness data. The third interval shows a weak trend towards a more symmetrical grain-size distribution. The fourth interval exhibits significantly finer skewed sediments. The sediments of the fifth interval are characterized by a

nearly symmetrical grain-size distribution. Except for one sample that shows a very fine skewed grain-size distribution, there is no difference in skewness between the fifth and the sixth interval.

Core WSS-03

Core WSS-03 (Fig. 5.17A-C) is 1175 cm long and reaches down to a depth of 9.85 m bsl. With exception of three horizons bearing root fragments at 10, 100-125, and 180 cm core depth, no fossils appear in Core WSS-03. Grain size data subdivide the core into five intervals (Fig. 5.17A). The first interval is from the bottom of the core up to 780 cm core depth (5.90 m bsl). The second interval ranges from 780 and 715 cm core depth (5.90 to 5.25 m bsl), the third from 715 to 560 cm core depth (5.25 to 3.70 m bsl), and the fourth from 560 to 105 cm core depth (3.70 m bsl to 0.85 m asl). The fifth interval is between 105 cm core depth and the land surface (0.85 to 1.90 m asl).

The first interval is characterized by a weak fining-upward trend of mean grain size. The second interval shows a coarsening upward. The third interval exhibits only little variations in mean grain size. The fourth interval is characterized by a poorly developed coarsening-upward trend and negligible variations of the mean grain size, except three horizons of finer sediments (around 435, 395 and 370 cm core depth). In the fifth interval, sediment coarsens upward.

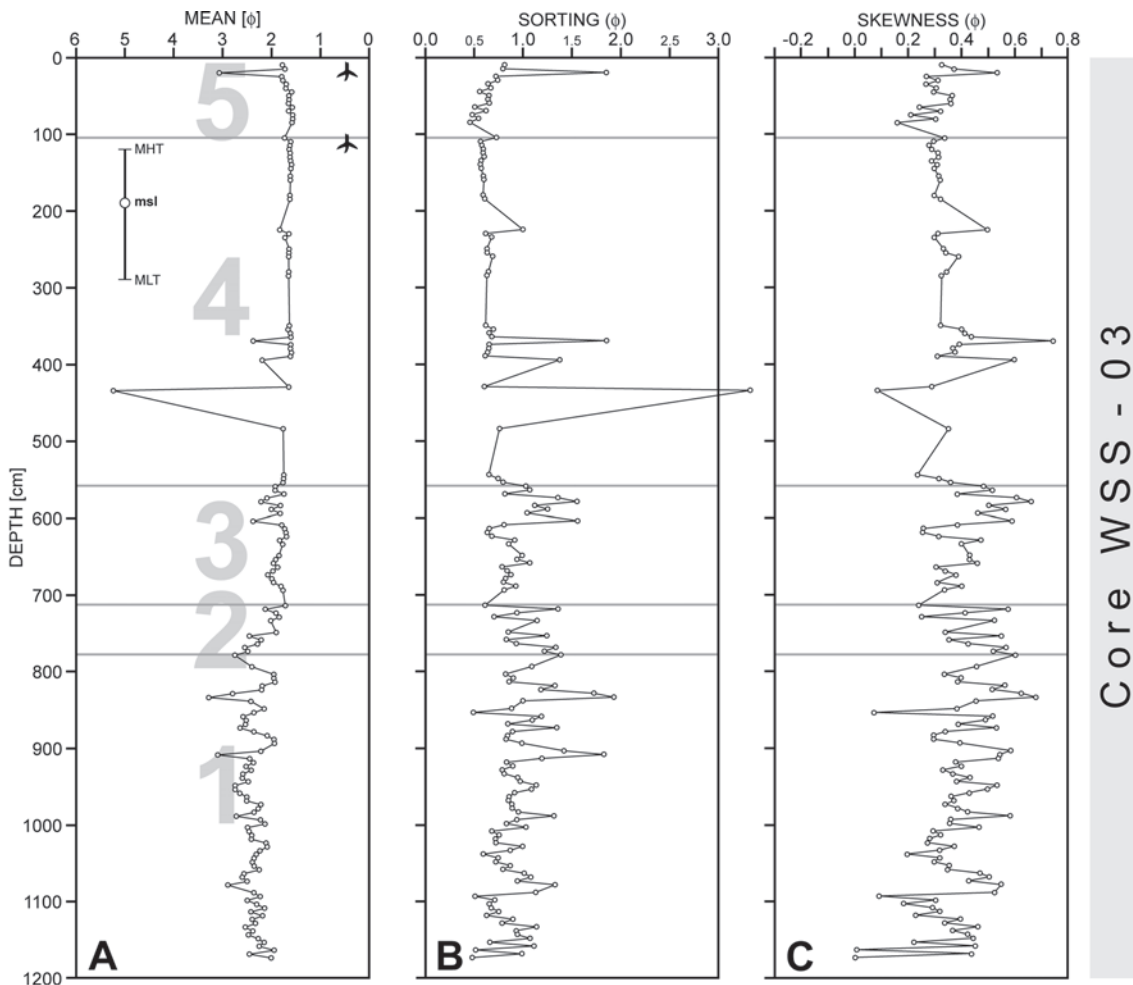


Figure 5.17: Grain-size data of core WSS-03. Core location is depicted in Figure 5.3. **A:** Mean grain size provided in phi. Note that no carbonate was found in the core. For legend see Figure 5.14. **B:** Sorting of the investigated sediment samples **C:** Skewness of the frequency distribution.

Sediments sorting (Fig. 5.17B) reflects the trends described for the mean grain-size. The first interval shows an overall upward trend towards less sorted sediments. The second interval is characterized by an upward trend towards better sorting. The third interval shows a trend towards less sorted sediments. With exception of the fine-grained layer, the fourth interval has only minor sorting variations and an overall trend towards better sorted sediments. The fine grained layer at 435, 395 and 370 cm core depth show poor respectively very poor sorting. The fifth interval shows an upward trend towards poorer sorting.

The five intervals are also mirrored by the skewness of the frequency distribution (Fig. 5.17C). The first interval is characterized by an upward trend towards finer skewed grain size distributions, the second interval shows a contrary trend, whereas the third interval again exhibits an upward trend towards finer skewed sediments. The fourth interval shows no clear trend. Sediments of the fifth interval are characterized by an upward trend towards finer skewed grain size distributions.

5.4.4 AMS ^{14}C -dates

AMS ^{14}C -datings were performed on mollusk shell debris from cores ME-01, KH-01 (Tab. 5.3), and OE-01 (described in Chapter 4, compare Tab. 4.3). Conventional ^{14}C -ages were calibrated using the program Calib 5.0 (Stuiver & Reimer, 1993) and marine calibration data from Hughen et al. (2004). As the local reservoir effects are unknown, and can be, however, assumed to be slightly different from the global reservoir age correction (Nadeau, Leibniz Laboratory, Kiel, pers. comm.), no reservoir corrections were applied to the data. Therefore, provided ^{14}C -ages should be regarded as maximum ages.

In Core KH-01 from the western Ellenbogen near the edge of the Königshafen (Fig. 5.3), a sample from a core depth of 550 to 560 cm (Fig. 5.16) revealed an age of 1008 – 1179 cal BP (averaged to 1095 ± 85 cal BP). The other sample, from a core depth of 730 to 740 cm, gave an age of 1981 – 2153 cal BP (averaged to 2067 ± 85 cal BP).

In Core ME-01 (Fig. 5.14) from the north-edge of the Listland and SW of the Königshafen, a sample from a core depth of 320 to 330 cm provided an age of between 1415 and 1623 cal BP (averaged to 1520 ± 100 cal BP). In 480 to 490 cm core depth, dating assigns an age of 1409 – 1588 cal BP (averaged to 1500 ± 90 cal BP), and in 720 to 760 cm core depth of the profile an age of 1579 – 1772 cal BP (averaged to 1675 ± 100 cal BP). GPR data indicate that the two younger ages are from the same sedimentary package, and there is an erosional unconformity between the second and the third sampled interval.

Interval	Sample	Lab. ID	^{14}C age	Res. corr.	95.4 % (2σ) cal age ranges		
Core ME-01						rounded	
320 - 330 cm	mollusk	KIA 31635	1575 ± 30 yr BP	not applied	1415 - 1623 cal BP	1520 ± 100 cal BP	327 - 535 AD
480 - 490 cm	mollusk	KIA 31636	1555 ± 25 yr BP	not applied	1409 - 1588 cal BP	1500 ± 90 cal BP	362 - 541 AD
720 - 760 cm	mollusk	KIA 31637	1695 ± 25 yr BP	not applied	1579 - 1772 cal BP	1675 ± 100 cal BP	178 - 371 AD
Core KH-01							
550 - 560 cm	mollusk	KIA 33890	1145 ± 25 yr BP	not applied	1008 - 1179 cal BP	1095 ± 85 cal BP	771 - 942 AD
730 - 740 cm	mollusk	KIA 33889	2035 ± 25 yr BP	not applied	1981 - 2153 cal BP	2067 ± 85 cal BP	204 - 32 BC

Table 5.3: Radiocarbon ages obtained by AMS ^{14}C -dating of marine mollusk shells from Cores KH-01 and ME-01 (compare Figs. 5.14G, 5.16A). Calibration of conventional ^{14}C -ages were performed using the software Calib 5.0 (Stuiver & Reimer, 1993). Marine calibration data are from Hughen et al. (2004). As the local reservoir effects are unknown, no reservoir correction was applied to the data.

5.5. Discussion

5.5.1 Stratigraphy

Based on the reflection geometries, the northern spit of Sylt can be subdivided into five different zones (Fig. 5.4), each characterized by a distinct radar-facies association (Fig. 5.4B). In the Listland, only strata below the recent deflation surface are considered for this study and the recent system of migrating dunes was not analyzed in detail.

Prominent geometrical feature of RfA-I and RfA-II are up to 4 m thick packages of east to southeast dipping reflections (Rf-f), located between 1 m asl and 3 m bsl (Fig. 5.5). These packages thicken towards the East, and overlie deeper strata above an irregular contact. Core K-01 (Fig. 5.15), obtained near the contact of the spit to the moraine core, reveals that these sediments show a mean grain size around 2 phi and only little variations in sorting and skewness. Additional information is provided by Cores EB-01 and EB-02 (Figs. 5.14A-F), drilled through sediments that exhibit a similar reflection pattern in the GPR (Figs. 5.11, 3.12). Both cores show only little variations in grain-size, a comparable degree of good sorting, and a positively skewed grain-size distribution. The east- to southeastward-dipping Rf-f reflections are interpreted as numerous large-scale washover bodies, based on the reflection geometries, the external shape of the sediment packages, and the lack of paleosols.

In the zone characterized by RfA-I (southern part of the spit and the areas around List (Fig. 5.4B), the washover sediments unconformably overlie strata that cause multiple reflections in the GPR data and attenuate reflections from deeper strata (Rf-e, compare Fig. 5.5). These reflections are located at a depth of 2.5 to 4 m bsl, and are traceable over a distance of several kilometers along the spit. Core K-01 shows that these horizons consist of silt (phi 5 to 7), are up to 1 m thick, and are interbedded by thin horizons of medium sand. Comparable reflections are imaged in GPR Line 2 between 180 m and the southern end of the profile (Fig. 5.6). However, strata beneath are here still imaged by the GPR, and the reflections extend only over a limited distance along the profile and are not traceable over several kilometers as in the zone of RfA-I. Core EB-01 shows that the Rf-e reflections imaged in GPR Line 2 are also associated with silt layers. Based on these results, Rf-e reflections are in general interpreted as caused by very fine grained layers in the subsurface.

Two different Rf-e types are imaged in the data: The first type correlates with 5 to 10 cm thick, patchy distributed horizons of silt, that are located at depths between mean sea level and 2 m asl. The second type is caused by up to 1 m thick sandy clay layers, extending over several kilometers, and are located at depths between mean sea-level and 4 m bsl. The first type is often associated with horizontal or concave curved strata of Rf-k. These strata are interpreted by Lindhorst et al. (in press, Chapter 3) as young eolian sediments with interbedded paleosols. Therefore, these silts are interpreted as deposits of ephemeral interdune ponds. The second type correlates with the clay sediments described by Gripp & Simon (1940), and is interpreted as backbarrier mud flat deposits. Summarizing, RfA-I is considered as former backbarrier depositional environment with large scale washovers, overlying thick, fine-grained mud-flat sediments.

Washovers attributed to RfA-II overlie sediments that show concave curved or parallel reflections, gently dipping towards the North (Rf-d). Rf-d reflections occur all

over the Listland (e.g. Figs. 5.6, 5.7), whereas this reflection pattern occurs near the surface in the central part and in greater depths near the coast as shown by Profiles C, D, E (Fig. 5.11). Erosional unconformities bundle the Rf-d reflections into 3 – 4 m thick packages (Figs. 5.6, 5.13). Profile C (Fig. 5.11) shows that the erosional unconformities exhibit a curved strike, dipping towards the northwest in the western-part of the Listland, and the northeast in the eastern part respectively. The Rf-d reflections are interpreted to represent sediments of a prograding spit subdivided into packages by erosion surfaces (compare Chapter 3).

Spit growth increments downlap onto a major erosional unconformity at a depth of 8 to 10 m bsl (Figs. 5.7, 5.11, 5.12, 5.13). Strata below this unconformity are of Rf-c, characterized by northeastward-dipping planar cross-beds with a thickness of at least 6 m (Fig. 5.7). Diffraction hyperbolas, imaged in the GPR data, indicate the occurrence of coarser material along this surface. The high-amplitude reflection, probably caused by a large electromagnetic contrast at the erosional unconformity, is a further indicator for a significant change of the material properties as caused by a shift in grain size. Gripp & Simon (1940) described the occurrence of coarse sand and pebbles below a depth of 8 to 10 m in drillings near GPR Line 6 (Figs. 5.3, 5.12). Their stratigraphic cross section (Fig. 5.2A) assigned these strata to the „Grauer Meeressand“ unit, which is unconformably overlain by the younger „Strandsand“ unit. With the data available, it can not be resolved, if these two units are genetically related – as assumed by Gripp & Simon (1940) – or if the „Grauer Meeressand“ unit represent marine sediments of a pre-spit stage. An independent genesis of the „Grauer Meeressand“ unit is indicated by the major erosional unconformity which truncates the northeastward-dipping cross beds, the downlap geometries of younger spit sediments onto these unconformity, and the abrupt termination of the „Grauer Meeressand“ unit towards the North (compare Profile A, Fig. 5.10). It can be speculated whether the „Grauer Meeressand“ unit would consist of sediments that were deposited during the early post-glacial marine transgressive period. During this phase, high amounts of sediment were eroded on the shelf and relocated towards the coastal areas. After Flemming (2002), the early transgressive stage of coastal evolution in general is characterized by a seaward progradation of the coast rather than vertical aggradation of barrier systems. This could explain the different sediment geometries of these strata, compared to the younger spit sediment.

Stratigraphy and genesis of the western part of the Listland are discussed in detail in Chapter 3, so that only a short summary is to be presented here. Reflection geometries imaged in this part of the spit are summarized as RfA-III, which occurs over a distance 3500 m along the western coast of the Listland (Fig. 5.4B), and is cross-cut by a northwest-southeast striking zone with RfA-IV. RfA-III is dominated by northward-dipping sigmoidal shaped reflections that bundle packages of weak reflections dipping towards the southeast. Two categories of sigmoidal shaped reflections are imaged in the GPR data and interpreted as erosional unconformities caused by storms of different magnitude. Two types of erosional surfaces can be distinguished. The one which can be traced over a distance of more than 1000 m along the spit reaches down to a depth of 7 m bsl, and is interpreted as caused by rare severe storms. Surfaces of the other type, interpreted as caused by annual storms, reach down to 2 – 3 m bsl, and can be traced over 150 to 200 m (compare Chapter 3). Weak reflections in-between the unconformities represent swash bars that are welded to the beach leading to spit progradation. Cut-and-fill structures, reaching down to a depth of 2 m bsl, intersect the swash-bar system, and are interpreted as scour channels feeding washover fans lying towards the East. The

swash-bar system unconformable overlies older spit sediments, and is separated from these sediments by a major unconformity which extends along the recent shoreline and dips towards the northwest (Figs. 5.10 and 5.11). Core data (Fig. 3.7) reveal that sediments overlying these unconformity are significantly finer grained than sediments above and below. These sediments are therefore interpreted as transported in suspension during severe storms, and settled as the storm ceased (Lindhorst et al., in press, Chapter 3). Sediments with a similar grain-size distribution, associated with a major unconformity, occur in Core OE-01 from the Ellenbogen (Fig. 4.12A), and are also interpreted as settled suspension load (see Chapter 4).

Several cores were drilled through bodies of RfA-III. Grain-size data of Core WSS-03 (Fig. 5.17) reflect a fining upward sequence up to 5.9 m bsl (first interval), a coarsening upward up to 3.70 m bsl (second and third interval), and comparable stable grain-size conditions up to the surface. Sorting and skewness data also reflect a significant change around 3.70 m bsl. A similar transition is recorded in the grain-size data of Core ME-01 (Fig. 14). Here, sediments below 1.4 m bsl (first to third interval) show stronger variations in mean grain size, and are less sorted and more skewed than sediments above this level (fourth level). This change is considered to have been caused by the transition from a foreshore to a shoreface depositional environment. Better sorting in the shoreface can be attributed to sorting effects by waves and intertidal currents. Poorer sorting in the foreshore, however, can be achieved by ephemeral beach-normal sediment relocation during severe storms. Sediments showing comparable grain-size characteristics were drilled on the Ellenbogen (Core OE-01, Fig. 4.12A-C) and reflect fair-weather sedimentation in the foreshore, and storm driven sedimentation in the shoreface respectively (Chapter 4).

RfA-IV occurs in an elongated, northwest-southeast striking area south of the Königshafen (Fig. 5.4B). It is dominated by Rf-h, eastward-dipping reflections that form an up to 6 m thick package, reaching down to a depth of 4 to 5 m bsl (Fig. 5.8). These reflections image the sedimentary fill of a large channel-shaped structure, which has been eroded into the swash-bar system of RfA-III (Figs. 5.9, 5.10). The northern flank of the channel is not preserved in the western part of the Listland, because the eastward-dipping Rf-h reflections are truncated by RfA-III (compare Fig. 5.4B). In the eastern part of the Listland, GPR measurements north of RfA-IV are hindered by the Königshafen. Due to reflection geometries and the external shape of the cut-and-fill structure, the Rf-h reflections are considered as channel fill. The channel is interpreted to reflect a former tidal inlet, which existed between the recent Königshafen and the Listland. The time of closure of this tidal inlet is estimated by radiocarbon dates of Core ME-01. This core was drilled through sediments of RfA-III that truncate the inlet fill towards the North. These sediments yielded an age of 1675 ± 100 cal BP at a depth of 5.40 – 5.80 m bsl, indicating that the closure of the tidal inlet occurred before 1700 BP.

RfA-V summarizes the reflection geometries observed on the northern termination of Sylt, the Ellenbogen. The stratigraphy of the Ellenbogen is described in detail in Chapter 4. The Ellenbogen which shows a hooked spit geometry probably serves as a sink for material eroded at the moraine core of Sylt and the western coast of the Listland. Eroded material, transported along the main-spit shore northerly-directed, is redirected by tidal currents at the Lister Tief. Subsequently, the material forms beach drifts, migrating easterly-directed along the northern coast of the Ellenbogen. Beach-drift sedimentation, occasionally interrupted by storms leading to coast-normal sediment redeposition, trigger the growth of the Ellenbogen hooked spit. Rare severe

storms cause profound erosion of the hooked spit and the development of extended erosional surfaces that scarp into the backshore. These backshore scarps act as a trap for blown sand and allow the formation of embryonic dunes and subsequently the formation of fore-dune ridges oriented largely parallel to the northern coast of the Ellenbogen. The eolian genesis of the fore-dune ridges on the Ellenbogen is reflected by the very constant mean grain-size (around 1.7 phi), only minor variations in sorting, and the occurrence of paleosols (Figs. 4.12D, F). Radiocarbon dates from Core OE-01 (Fig. 4.12A) indicates that the processes leading to the development of the hooked spit were already active at $1300 \text{ BP} \pm 60 \text{ cal BP}$. Based on these data, the initiation of the hooked spit development is assumed to mark the moment of an increased erosion of the main spit. GPR and core data indicate that the eastern Ellenbogen incorporated parts of a former flood tidal delta (compare Chapter 4), which existed around $2250 \text{ BP} \pm 90 \text{ cal BP}$. The eastern Ellenbogen as a supra-tidal geomorphologic feature has been existing at least since around $720 \pm 60 \text{ cal BP}$, because strata at the dated depth were probably located above mean-sea level according to the sea-level curve of Behre (2007, Fig. 5.2B). For the western Ellenbogen, radiocarbon dating of sediments from Core KH-01 (Fig. 5.16A) shows that sediments at a depth of 5.80 to 5.90 m bsl were deposited around $2067 \pm 85 \text{ cal BP}$, and sediments at a depth of 4.00 to 4.10 m bsl around $1095 \pm 85 \text{ cal BP}$. This significant age gap between adjacent strata is interpreted as caused by an erosional event at or shortly before $1095 \pm 85 \text{ cal BP}$. Significant changes in sorting and skewness of the grain-size distributions and the beginning of a fining upwards cycle at a depth of 5.10 m bsl probably mark the location of the hypothetical erosional unconformity. During the last century, the Ellenbogen experienced significant growth, as shown by comparison of historical maps (Fig. 4.2C). This reflects the enhanced erosion of the western coast in the 20th century reported by Hundt (1957) and Ahrendt (1993).

GPR data from the Listland show that at least the upper 0.5 m of the sedimentary succession yields horizontal or concave curved reflections (Rf-k) in the data. These sediments are interpreted as deposited by accumulation of eolian sand, trapped due to a rise of the groundwater table (compare Chapter 3). GPR data furthermore indicate that these eolian sediments are separated from underlying strata by an erosional unconformity. This surface is considered to represent a former eolian deflation surface in the sense of Stokes (1968), Kinsman (1969), and Fryberger et al. (1988), and is assumed to have developed under comparable stable sea-level conditions. Root remnants found in the cores and interpreted as paleosols support this hypothesis (Figs., 5.14, 5.15, 5.17). In the Listland, eolian deflation surfaces occur at depths of around 1.5 m bsl, 0.5, 1.0, and 0.6 m asl. The first two surfaces are only preserved in areas assigned to RfA-II, and are located in the central part of the Listland (Fig. 5.4). The deflation surface at a depth of 1 m asl occurs all over the Listland. The shallowest deflation surface is restricted to the area north of RfA-IV. On the Ellenbogen, no unequivocal paleo-deflation surface is recorded, but it should be noticed that the recent interdune land surface of the Ellenbogen is located at around 1.3 m asl, 0.5 to 0.7 m lower than in the Listland. This probably reflects the greater horizontal and vertical extension of the freshwater aquifer in the Listland compared to the Ellenbogen.

With the data available it is not resolvable, when the development of the recent eolian dune system started. For the oldest dunes on northern Sylt, Priesmeier (1970) supposed an age of around 1000 years. Behre (2007) assumed the last period of longer stable sea-level conditions for the time between 1700 and 1300 BP, followed

by a sea-level lowering for additionally 300 years, till 1000 BP. This could give an age estimation of 1000 to 1700 years for the extended eolian deflation surface detected at a depth of 1 m asl all over the Listland.

Figure 5.2A presents the north-south striking cross section provided by Gripp & Simon (1940) showing the contact between the clay deposits near the moraine core and the unconformable overlying sands of the „Strandsand“ unit significantly thickening towards the North. Reflection geometries presented in Figure 5.4, Profile A (Fig. 5.10) and Profile E (Fig. 5.11) indicate that the recent shoreline is not oriented parallel to the genetically build spit axis, which rather strikes northeast-southwest. This implies that the section of Gripp & Simon (1940) is not oriented parallel to the spit axis and that it cross-cuts sediments of the spit (mostly RfA-III) and sediments of the former backbarrier region (RfA-I). The unconformity between the clays and the „Strandsand“ unit near the moraine core is therefore the contact between tidal-flat clays and sands deposited by easterly-directed washovers. Sands of the „Strandsand“ unit further to the North, however, must be attributed to the system of welded swash-bars described in Chapter 3.

5.5.2 Development of northern Sylt

Figure 5.18 presents a new model for the development of northern Sylt during the latest Holocene, based on GPR and core data. The model consists of six stages, reflecting the proposed development of the spit during the past 5000 years.

Stage 1 (approximately 5000 to 3500 BP)

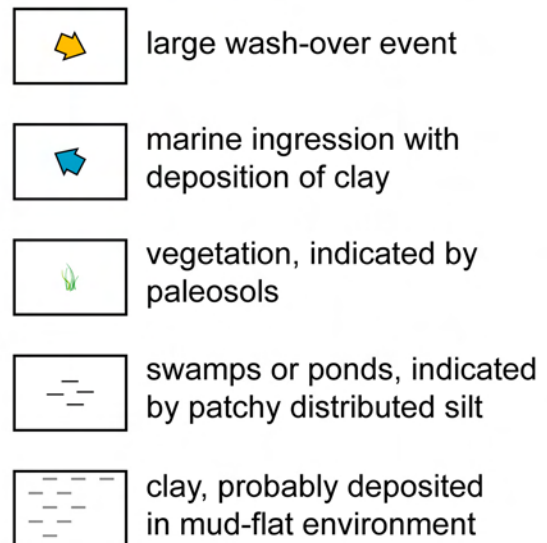
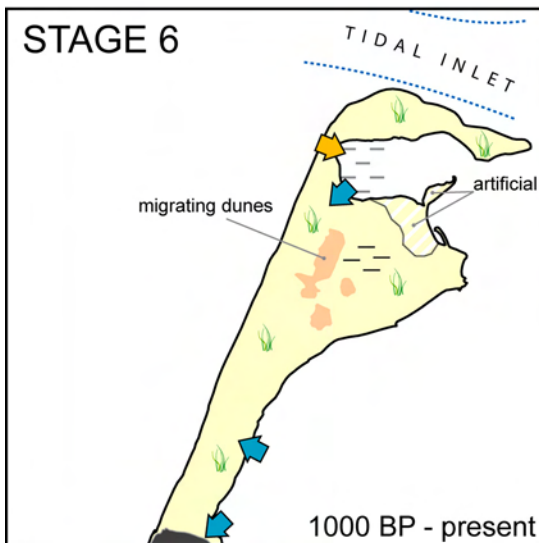
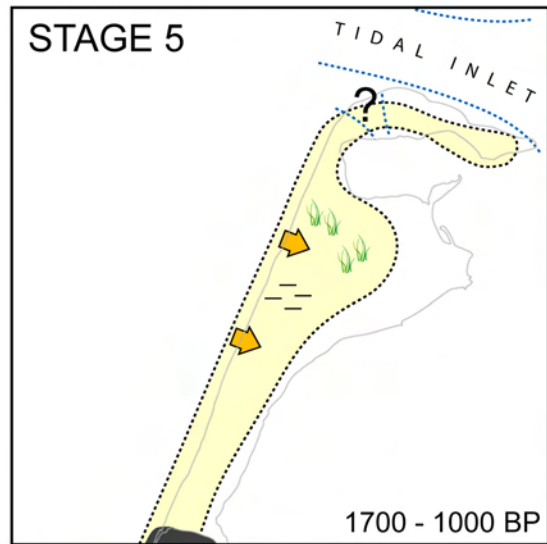
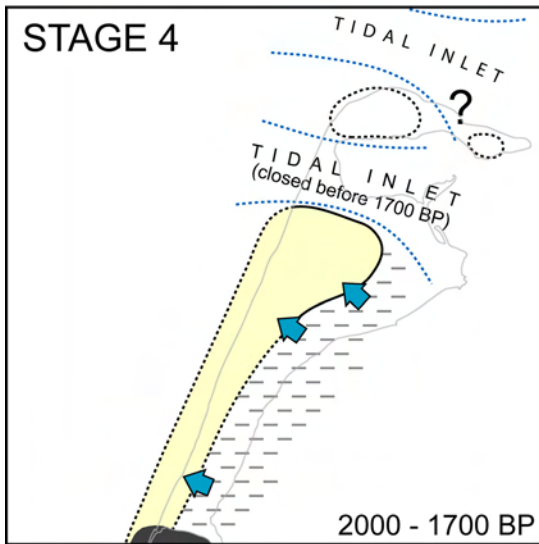
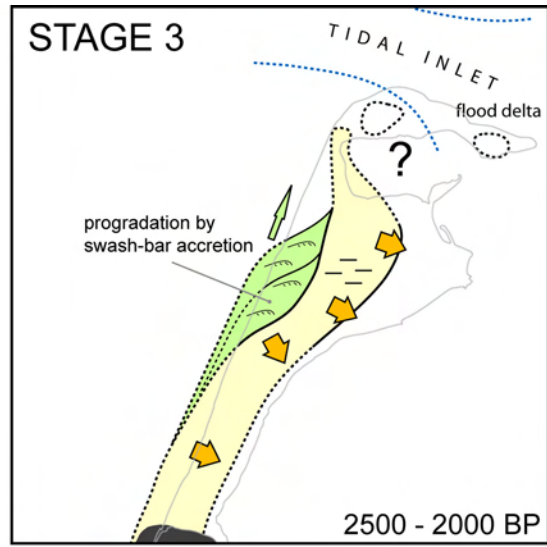
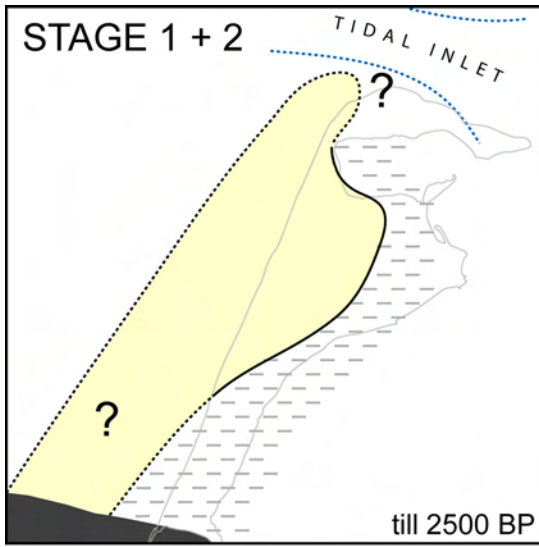
During this oldest stage a slow sea-level rise occurred, with a rate of around 0.14 cm per year (Behre, 2007; Fig. 5.2B). Initial development of the northern spit probably dates back to around 5000 BP, since this is the age of the oldest clay deposits found around Sylt (Hoffmann, 1985; Bayerl, 1992). These clays are assigned to tidal flats, and therefore must have been deposited in a sheltered embayment. As the barrier spit of Sylt consists of eroded moraine material to a great proportion, the moraine probably extended further to the west than today.

Around 4200 BP, at the end of the Neolithic period (Litt et al., 2001), the spit extended at least up to the Königshafen, as indicated by younger Neolithic stone tools found in the Listland (Harck, 1972, 1974). A second evidence for such a large spit is the occurrence of a thick clay layer in the Königshafen that dates back to around 3700 BP (Bayerl et al., 1998a). A north-south extension of the spit comparable to present day extension thus can be assumed for the time around 3700 BP. The clay was probably deposited in a small tidal bay, a precursor of the Königshafen, as distribution of the clay horizon, although it cannot be discarded that the clays were locally eroded.

The assumed eastern limit of the spit is indicated by the first occurrence of clayey layers in the upper 10 m of the sedimentary succession, indicating a former backbarrier setting. The position of the western shoreline around 3500 BP still remains speculative.

Stage 2 (3500 to 2500 BP)

The second stage is characterized by a sea-level lowering of around 2 m (Behre, 2007) (Fig. 5.2B). An eastward-dipping erosional unconformity located in parts of the eastern Listland at a depth of maximal 3 m bsl (Profile D, Fig. 5.11) is probably be attributed to continued erosion during sea-level lowering and lowstand.



Stage 3 (2500 to 2000 BP)

A sea-level rise by around 2 m (Fig. 5.2B) triggered formation of a ravinement surface with a deep-reaching erosion on the western coast of the spit at the beginning of Stage 3. Subsequently, spit recovery by welding of swash bars took place, a process described in detail by Lindhorst et al. (in press, Chapter 3). The data available do not enable to resolved if the increase in sediment supply that allowed for beach progradation, and therefore spit recreation, was caused by enhanced erosion of the moraine core further to the South, or sediment redeposition from eroded parts of the spit.

Whereas erosion was the dominating process at the western coast at the beginning of this stage, the area of the lee-side of the spit including the proximal tidal flats near the moraine core, experienced significant sedimentation by washover events (Fig. 3.12). GPR data show that washover sediments in the northern part of the Listland overlie the erosional unconformity directly, which was formed during the previous sea-level lowstand (Figs. 5.6, 5.11). To the South, however, washover deposits are underlain by clayey horizons, interpreted as tidal flat sediments of the backbarrier region (Fig. 5.5). The large east-west extension of these washover fans (Fig. 5.11) and their thickness of up to 3 m probably indicate that storms were more intense than today, when washover fans on Sylt have a comparably limited extension. A similar hypothesis was proposed by Donnelly et al. (2004) for large-scale washover fans in backbarrier regions at the coast of New Jersey. Washovers deposited in the time interval of the 6th and the 14th century were significantly larger than recent washovers, which is interpreted to reflect a stronger storm intensity in the past. Wang & Horwitz (2007) presented washover deposits associated with barrier islands along the coasts of northern Florida. The investigated sediments were deposited in the backbarrier bay during multiple hurricanes in 2004 and 2005. The great thickness of the sediments of up to 2 m, is interpreted to result from the accommodation space available in the backbarrier bay.

At the position of the recent eastern Ellenbogen, a flood tidal delta attributed to a precursor of the Lister Tief existed during this stage, as indicated by the occurrence of southeastward-dipping strata at the basement of the Ellenbogen (Fig. 4.10). Radiocarbon data provide an age of 2250 ± 90 cal BP for these sediments. At the today's position of the western Ellenbogen, ^{14}C -data from Core KH-01 provide an age of 2067 ± 85 cal BP for sediments in a core depth of 730 – 740 cm. This corresponds to a depth of 5.80 – 5.90 m bsl and indicates that these sediments

Figure 5.18 (previous page): Model showing the development of northern Sylt since around 5000 BP in six stages. **Stage 1 (from approximately 5000 to 3500 BP):** Initial development of the spit assumable dates back to approximately 5000 BP. Around 3700 BP, the spit reaches a north-south extension, comparable to present day values. Clay is deposited in a sheltered embayment, a precursor of the Königshafen. **Stage 2 (3500 to 2500 BP):** Continued erosion due to a sea-level drop by approximately 2 m leads to the development of an erosional unconformity at a depth of 2 to 3 m bsl. **Stage 3 (2500 to 2000 BP):** Profound erosion took place at the western coast of Sylt. Subsequently, spit recovery by welding of swash bars occurs. The lee-side of the spit experiences significant sedimentation by large washover fans. A tidal delta exists at the position of the today's eastern Ellenbogen during this stage. **Stage 4 (2000 to 1700 BP):** A new tidal inlet develops between the Listland and the Königshafen and closes again before 1700 BP. **Stage 5 (1700 to 1000 BP):** Washovers indicate at least one period with stronger storms in early Stage 5. Subsequently, a long period of stable sea-level allows for the development of an eolian deflation surface at 1 m asl. Significant spit growth occurs, leading to the initial development of the Ellenbogen latest around 1300 BP. **Stage 6 (1000 BP to present):** Significant erosion took place at the western coast, combined with growth of the Ellenbogen. An up to 1.5 m thick eolian succession accumulates onto the Listland.

were deposited in a water depth of several meters, as sea level around 2000 BP is given 2 m below the present day level by Behre (2007, Fig. 5.2B). Because no GPR data exist for core KH-01, the nature of these sediments has to remain speculative. A possible scenario is the development of submarine shoals at the position of the western Ellenbogen around that time. It is proposed that the spit extended up to the Königshafen, sheltering the small bay from the influence of the open sea and protecting the clay of the Königshafen, which was deposited during Stage 1, from erosion.

Bayerl (1992) noted that the backbarrier region of Sylt was settled, at least in parts, around 2000 BP. This is in line with the lower sea-level position indicated by Behre (2007) for this time. GPR data show that washover sediments in the eastern Listland, attributed to early Stage 3, are truncated at mean sea level by an erosional unconformity, interpreted as eolian deflation surface. This is corroborated by the patchy occurrence of clayey sand on top of this surface (Fig. 5.6) which are interpreted as remnants of interdune pond or swamp deposits.

Stage 4 (2000 to 1700 BP)

During Stage 4 a new tidal inlet developed between the Listland and the Königshafen under conditions of sea-level rise (Fig. 5.2B). In the data this structure is imaged as large cut-and-fill structure, which internally shows easterly-directed cross-bedded sediments with a maximum thickness of 5 to 6 m (Figs. 5.8, 5.9). As the fill of this supposed tidal inlet is eroded by younger strata towards the North, the moment of closure can be determined by ^{14}C -data of Core ME-01 (Fig. 5.14) as having occurred around 1675 ± 100 cal BP. This corresponds to a highstand in the sea-level curve of Behre (2007). Increased sediment supply by northerly-directed longshore currents probably triggered the closure of the tidal inlet. On the lee side of the spit, rising sea level led to a marine incursion reflected by the widely distribution of a clay layer, which is several cm thick, located at mean sea level, and overlaying sandy spit sediments (Figs. 5.4, 5.8).

Stage 5 (1700 to 1000 BP)

Stage 5 is characterized by a long period of comparable stable sea-level conditions with a sea level position 1 m below the present-day level, followed by a time of a 1 m sea level fall (Fig. 5.2B). The long period of stable sea level accounted for the development of an eolian deflation surface located 1 m below the present surface that is imaged in GPR data all over the Listland as an unconformity. Patchy distributed clay layers deposited in interdune ponds and plant remnants situated 1 m below the present surface (Figs. 5.14A, B and Fig. 5.17) indicate a longer period of stable groundwater conditions for this stage.

Small scour channels imaged in the GPR data indicate at least one period with stronger storms and coupled washover events. These channels were truncated at a depth of 1 m asl by the eolian deflation surface, nevertheless, they had been already cut into eolian sediments, that were probably accumulated as a consequence of a rising groundwater table during Stage 4. The associated washover events should be attributed to early Stage 5.

After closure of the tidal inlet between the Königshafen and the Listland, the spit prograded towards the North, presumably up to the position of the recent Lister Tief. The development of the initial Ellenbogen, is very likely, as ^{14}C -ages of Core OE-01 indicate easterly-directed beach-drift sediments at a depth of 2 m bsl for the time around 1300 ± 60 cal BP.

Stage 6 (1000 BP to present)

Stage 6 is characterized by retreat of the western coast, combined with growth of the hooked spit of the Ellenbogen. Strong erosion at the western coast of the spit is documented by historical reports and maps (Hundt, 1957; Newig, 1980, 1995, 2004; Ahrendt, 1994, 2001; Ahrendt & Thiede, 2001). Major land losses were especially reported for the time between 900 and 500 BP (Woebcken, 1924). This correlates with a phase of rising sea-level (Behre, 2007, Fig. 5.2B) and probably marks the beginning of accelerated growth of the hooked spit (see Chapter 4), which serves as a sediment sink for material eroded from the main spit. The age of the eastern Ellenbogen is around 720 ± 60 cal BP for beach sediments 150 – 190 cm below the surface.

The upper meter of the sedimentary succession of the spit consists of eolian sands which accumulated on top of an erosional unconformity. Whereas the erosional unconformity is interpreted as eolian deflation surface, developed during Stage 5, the accumulation of eolian sands reflects a rise of the groundwater table (Chapter 3), which is hydrodynamically coupled to the sea level.

Some small marine inundations occurred during Stage 6 leaving thin clay horizons overlying the sands. The timing of these events is unclear, but Bayerl (1992) noted that the youngest clay sedimentation around northern Sylt did not start before the 14th century. This probably can give a maximum age for these sediments.

5.6. Summary and conclusions

This study has shown that the barrier system of Sylt has undergone a complex evolution. The stratigraphic architecture of this spit down to a depth of 12 m bsl is summarized in Figure 5.19. Northeastward-dipping strata interpreted as sediments of the early Holocene marine transgressive period form the basement of the spit. These strata, that exhibit at least up to 6 m thick planar cross-beds, are truncated at a depth of 10 m bsl by an erosional unconformity. Northeastward-prograding sediments of the initial spit form the second unit. Erosional unconformities subdivide these sediments into up to 3 m thick, sedimentary packages that downlap onto the underlying strata. Delimiting surfaces are interpreted to reflect erosional phases. In the western part, sediments of the early spit are truncated by a major unconformity, which dips towards the west and northwest. Sediments above this unconformity are considered as spit-recovery sequence, consisting of welded swash-bars, shoreface deposits, and filled scour channels linked to washover fans. Spit recovery was interrupted for several times by severe storms, as indicated by major erosional unconformities. A major erosional surface also truncates sediments in the eastern part of the spit. This surface dips towards the East and reaches a depth of 3 m bsl at the easternmost part of the spit. It reflects a sea-level lowstand between 3500 and 2500 BP and is overlain by large washover fans indicating an easterly-directed sediment transport. Washover sediments are truncated at mean sea level by an eolian deflation surface. Patchy distributed clay layers are interpreted to reflect interdune swamp and pond deposits. A second eolian deflation surface, located at a depth of 1 m asl, is attributed to stable sea-level conditions between 1700 and 1000 BP. Paleosols associated with this surface indicate that this deflation surface was vegetated. An overall sea-level rise during the last 1000 years is recorded by a sequence of up to 1.5 m thick eolian sediments that overlie the former deflation

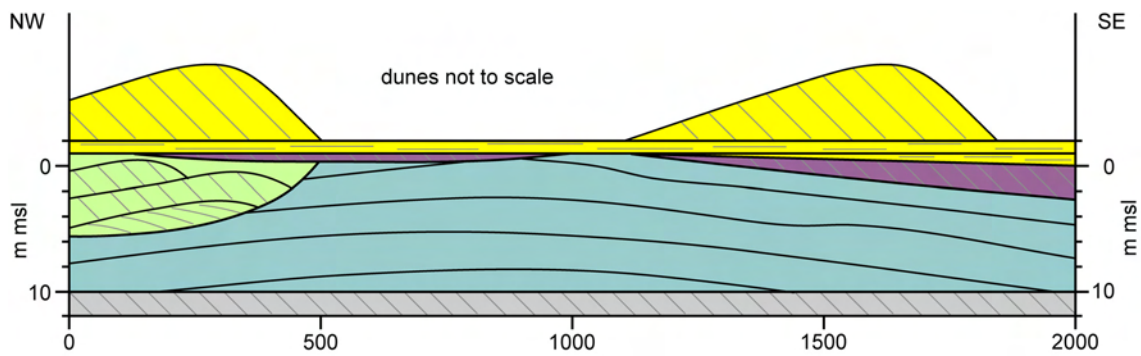


Figure 5.19: Model summarizing the stratigraphic architecture of the Listland down to a depth of 12 m bsl. Northeastward-dipping strata, truncated by an erosional unconformity at a depth of around 10 m bsl, probably represent sediments of an early stage of the post-glacial marine transgression. The erosional unconformity is overlaid by sediments of the initial spit. Spit growth increments, gently dipping towards the North, reflect interruptions in spit growth. Sediments of the initial spit are truncated towards the West by a westward-dipping unconformity. Sediments above this unconformity are attributed to a spit-recovery sequence, and consist mainly of welded swash-bars. Sediments in the eastern part of the spit are truncated by an eastward-dipping erosional unconformity, which reaches a depth of 3 m bsl. Large washover sediments on top of this surface show easterly-directed cross beds. Two significant former eolian deflation surfaces are present on northern Sylt, located around mean sea level and at a depth of 1 m asl respectively. The uppermost sedimentary unit of the spit is formed by an up to 1.5 m thick layer of eolian sediments. These sediments are accumulated due to a rise of the groundwater table, subsequently followed by trapping of eolian sand. Movement of large sand dunes occurs on top of the recent deflation surface.

surface. Until today, a new deflation surface has developed. Large sand dunes migrate towards the East on this surface, not affecting older sediments that are preserved due to high groundwater table.

In contrast to the moraine core, which underwent continuous vertical erosion during the Holocene, the surface of the spit system reacts to sea-level changes either by erosion during falling stages of the sea level or by vertical aggradation during periods of sea-level rise, respectively.

6

Conclusions and outlook

The aims of this study were to reveal the sedimentary architecture of the northern barrier spit of Sylt in high resolution, to develop a new model for the genesis of this spit system and to determine the basic sedimentary processes that formed the spit. An integrated approach with ground-penetrating radar (GPR) and sedimentological data was used. This method, continuously adapted and improved during the study, now provides a powerful tool for sedimentological studies in coastal settings. This chapter summarizes the results, adds some remarks and gives a short outlook for future investigations in the studied area.

6.1 Methods applied

It has been shown that the combination of GPR and sedimentological investigations is an efficient tool for sedimentary research in the coastal setting. In addition to the advantages of the method, limits and pitfalls are also highlighted. Near the shoreline, salty groundwater hinders GPR measurements, and clay and silt in the subsurface lead to reduced penetration depth or completely mask deeper strata. Nevertheless, there is no other technology which enables such fast and high-resolution survey capabilities as provided by GPR. However, it turned out that a stratigraphic model could not rely on sole GPR data, but also had to contain the results of sedimentological investigations which contribute information about sedimentary facies and absolute age. In Chapter 2, a detailed description of field work, potential pitfalls, different processing strategies and interpretation steps is provided. It can serve as a vademecum for future investigations in the coastal setting.

6.2 Geology of northern Sylt

Linking GPR data to sedimentology, the principle sedimentary processes were identified that led to the present sedimentary architecture of the investigated barrier spit.

Radiocarbon dates were used to propose a new model for the development of northern Sylt during the latest Holocene. The investigated spit system is geomorphologically subdivided into a large, recurved main spit (named „Listland“) and a small hooked spit which forms the northward termination of the system (the „Ellenbogen“). Data indicates that the formation of the Ellenbogen hooked spit, that nowadays serves as a downstream sink for eroded material from the main spit, times the beginning of net erosion of the main spit. During the last decades, sediment delivery to the hooked spit increased by a factor of approximately 2 to 3, probably due to extended beach nourishment at the main spit. The effects of this increase in sediment supply can be studied in a great detail and make the Ellenbogen spit an ideal natural laboratory for studies dealing with sediment dynamic and beach development in a microtidal to lower mesotidal regime.

Data from the main spit, the Listland, revealed that swash bars were an important building block of the investigated spit system. This contrasts with widely accepted beach models, which underline the predominance of seaward-dipping foreshore bedding in beach architecture. Observed swash-bar bodies are delimited by erosive surfaces, which are interpreted as the result of storm events triggering erosion, sediment reworking, and sediment export out of the nearshore zone. Sediment transfer back to the beach was achieved through swash-bar growth during fair-weather periods. Swash-bar accretion itself resulted in a northward and a substantial westward spit-beach progradation. The interpreted processes have been summarized in a six-stage model which shows the whole cycle of beach progradation, erosion, recovery and sediment preservation by sea-level rise. These results show that the evolution of the spit is much more complex than previously stated, and not only characterized by a continuous eastward retreat. The data indicates that at least 700 m of seaward beach progradation occurred. There are, however, no age dates available so far to pinpoint this period of spit growth. Furthermore, the example of the dominance of swash-bar bedding over seaward-dipping planar foreshore bedding does not seem to be a very common pattern in the geological record of beach deposits.

The development of the hooked spit, the Ellenbogen, is controlled by the interplay of fair-weather beach-drift migration and erosion by storms of different magnitude. Whereas sediment transport by beach-drift migration serves as the most important mechanism of beach progradation, storms are responsible for the relocation of material from the foreshore to the shoreface. The development of fore-dune ridges, oriented parallel to the shoreline, is initialized by the formation of a scarp in the backshore that serves as a trap for windblown sand. Colonization by plants stabilizes the embryonic dune and supports the further growth of the ridge by continued trapping of wind-blown sand.

Northeastward-prograding sediments of the initial spit form the second unit. Erosional unconformities subdivide these sediments into up to 3 m thick, sedimentary packages that downlap onto the underlying strata. Delimiting surfaces are interpreted to reflect erosional phases. In the western part, sediments of the early spit are truncated by a major unconformity, which dips towards the west and northwest. Sediments above this unconformity are interpreted as spit-recovery sequence, consisting of welded swash-bars, shoreface deposits, and filled scour channels linked to washover fans. Spit recovery was several times interrupted by severe storms, as indicated by major erosional unconformities. A major erosional surface also truncates sediments in the eastern part of the spit. This surface dips towards the East and reaches a depth of 3 m bsl at the easternmost part of the spit. It reflects a sea-level

lowstand between 3500 and 2500 BP and is overlain by large wash-over fans indicating an easterly-directed sediment transport. Washover sediments are truncated at mean sea level by an eolian deflation surface. Patchy distributed clay layers are interpreted to reflect interdune swamp and pond deposits. A second eolian deflation surface, located at a depth of 1 m asl, is attributed to stable sea-level conditions between 1700 and 1000 BP. Paleosols associated with this surface indicate that these deflation surface was vegetated. An overall sea-level rise during the last 1000 years is recorded by a sequence of up to 1.5 m thick eolian sediments that overlie the former deflation surface. Today, a new deflation surface has developed. Large sand dunes migrate towards the East on this surface, without affecting older sediments that are preserved due to the high ground-water table.

This study has shown that the barrier system of Sylt has undergone a much more complex evolution than previously thought. Northeastward-dipping strata, interpreted as sediments of the early Holocene marine transgressive period, form the basement of the spit. A model, comprising six stages of subsequent spit development, has been presented in Chapter 5. Stage 1, lasting from 5000 to 3500 BP, is characterized by the initial development of the spit. Around 3700 BP, the spit reached a north-south extension comparable to present day values. The position of the western shoreline during this period has to remain speculative. Continued erosion due to a sea-level drop by approximately 2 m took place during Stage 2, between 3500 and 2500 BP. The erosion surface that developed during this phase is still preserved in parts of the spit. Profound coastal retreat took place at the western coast of Sylt during early Stage 3, between 2500 and 2000 BP. Subsequently, spit recovery through welding of swash bars occurred. Contemporaneously, the lee-side of the spit experienced significantly sedimentation by large wash-over fans, covering sediments of the sandy spit and fine-grained tidal-flat deposits. At the end of Stage 3, sea-level dropped and the backbarrier region was partly settled. Stage 4 (2000 to 1700 BP) is characterized by the development of a tidal inlet between the Listland and the Ellenbogen. This feature closed before 1700 BP. During early Stage 5, which lasted from 1700 to 1000 BP, washover sediments indicate at least one period with stronger storms. Subsequently, a long period of stable sea-level allowed for the development of an eolian deflation surface at 1 m above present sea level, associated with interdune ponds, and soil development. Significant spit growth, leading to the initial development of the Ellenbogen, occurred latest around 1300 BP. During Stage 6, from 1000 BP onwards to the present, enhanced erosion took place at the western coast, combined with significant growth of the Ellenbogen. Major land losses are especially reported for the time between 900 and 500 BP. Throughout the Listland, an eolian succession, up to 1.5 m thick, accumulated.

On barrier spits, such as the investigated system, the coupling of groundwater table to sea-level position results either in erosion of the spit surface, during falling stages of the sea level, or in vertical aggradation, during periods of sea-level rise. Availability of sediment to be transported with wind is a necessary prerequisite for spit aggradation during base-level rise. Nowadays, when dunes on northern Sylt are artificially stabilized by plants, and coastal dunes are forced to form a high barrier on the western coast, no vertical spit aggradation is possible any longer, due to sediment starvation. A lowering of the ground-water table, triggered for example by the increased pumping of drinking water, will additionally enhance this effect. Future sea-level rise, therefore, will result in both, enhanced erosion on the western coast and flooding of the spits surface by marine incursion from the lee side of the spit.

6.3 Outlook

Although the results presented in this study enabled a detailed view of the late Holocene development of northern Sylt, there are still open questions, leaving space for further investigations. In the following, I will address some of these questions to give suggestions for future work in this area.

- The accretion of swash bars turned out to be an important factor in barrier-beach growth along the recurved spit. Nevertheless, it was beyond the scope of this study to reconstruct the controlling factors that determine whether swash bars are present and recorded in beach deposits. However, the observation that spit growth can be achieved through swash-bar accretion may be a key for developing a concept of enhanced coastal protection under future conditions of accelerated sea-level rise. Sand nourishment in a distal beach area may be more efficient than beach nourishment in the backshore setting, as practiced along the coast of Sylt nowadays.
- GPR data has revealed an excellent storm record in the western Listland. However, due to the absence of material datable with the radiocarbon method, the time period covered by this record still remains unclear. Luminescence dating, using optical or thermal stimulated luminescence of quartz grains, would offer new data, and probably could make this paleoclimate record accessible.
- The eolian dunes that cover northern Sylt probably bear an important archive of wind-field changes during the last centuries. GPR here provides a method to access these data. Potential results could be of great importance for paleoclimatic models dealing with changes in wind speed and predominant wind direction along the coast of the southern North Sea.
- The nature of the northeastward-dipping strata that underlie the Listland in a depth of 10 m below mean sea level is still unclear. Though data presented in Chapter 5 makes it possible to propose an early postglacial genesis for these strata, further investigations are necessary to prove this interpretation. New data would not only shed new light on the formation of these strata, but also lead to a better understanding of the early transgression history along the coast of the southern North Sea. In this context, an integration of land based GPR data and marine sparker data could be a promising approach.

References

- AAGAARD, T., NIELSEN, J., AND GREENWOOD, B., 1998. Suspended sediment transport and nearshore bar formation on a shallow intermediate-state beach. *Marine Geology*, 148, 203-225.
- AHRENDT, K., 1992. Entwicklung und Sedimenthabitus des Hörnum- und Vortrapptiefs. *Meyniana*, 44, 53-65.
- AHRENDT, K., 1993. Sedimentdynamik an der Westküste Sylts (Deutsche Bucht / Nordsee). *Meyniana*, 45, 161-179.
- AHRENDT, K., 1994. Geologie und Küstenschutz am Beispiel Sylt. *Berichte aus dem Forschungs- und Technologiezentrum Westküste*, 4, 135 pp.
- AHRENDT, K., 2001. Expected effect of climate change on Sylt island: results from a multidisciplinary German project. *Climate Research*, 18, 141-146.
- AHRENDT, K. AND THIEDE, J., 1992. Entwicklung und Sedimenthabitus des Hörnum- und Vortrapptiefs. *Meyniana*, 44, 53-65.
- AHRENDT, K. AND PESCH, R., 2001. Das GIS als Methode für die Rekonstruktion geologischer Entwicklungen - Beispiel Sylt/Deutsche Bucht. *Meyniana*, 53, 5-30.
- AHRENDT, K. AND THIEDE, J., 2001. Naturräumliche Entwicklung Sylts – Vergangenheit und Zukunft. In: Daschkeit, A., Schottes, P. (eds.), *Sylt – Klimafolgen für Mensch und Küste*, Springer, Berlin, pp. 69-112.
- AIGNER, T. AND REINECK, H.-E., 1982. Proximity trends in modern storm sands from the Helgoland Bight (North Sea) and their implications for basin analysis. *Senckenbergiana Maritima*, 14, 183-215.
- ALLEN, J.R.L., 1982. *Sedimentary structures: their character and physical basis*. Volume 1. *Developments in Sedimentology*. Elsevier, Amsterdam, 593 pp.
- ALTEKÖSTER, C.A., 2004. *Untersuchungen zur Reproduzierbarkeit von Bodenradarmessungen*. Dissertation, Universität Bonn, 189 pp.
- ANNAN, A.P., 1999. *Practical processing of GPR data*. Sensors and Software Inc., Mississauga, Canada, 16 pp.
- ANNAN, A.P., 2001. *Ground-penetrating radar workshop notes*. Sensors and Software Inc., Mississauga, Canada, 192 pp.
- ANNAN, A.P., 2005. *Ground-penetrating radar*. In: Butler, D.K. (ed.), *Near-surface geophysics*. Society of Exploration Geophysicists, Tulsa, pp. 357-438.
- ANNAN, A.P. AND DAVIS, J.L., 1976. Impulse radar sounding in permafrost. *Radio Sciences*, 11, 383-394.

- ANNAN, A.P. AND DAVIS, J.L., 1992. Design and development of a digital ground-penetrating radar system. In: Pilon, J. (ed.), Ground penetrating radar. Geological Survey of Canada Papers, 90, 15-23.
- ANTHONY, D. AND MØLLER, I., 2002. The geological architecture and development of the Holmsland barrier and Rinkøbing Fjord area, danish North Sea coast. *Geografisk Tidsskrift, Danish Journal of Geography*, 102, 27-36.
- ANTHONY, E.J., LEVOY, F., AND MONFORT, O., 2004. Morphodynamics of intertidal bars on a megatidal beach, Merlimont, Northern France. *Marine Geology*, 208, 73-100.
- ANWAR, J., 1974. Der holozäne Meeressand im Seegebiet westlich von Sylt zwischen Kampen und Rantum (Ausgangsmaterial und Sedimentation). *Meyniana*, 24, 43-55.
- ASPRION, U., 1998. Ground-penetrating radar (GPR) analysis in aquifer-sedimentology: case studies, with an emphasis on glacial systems of SW Germany. *Tübinger Geowissenschaftliche Arbeiten, Reihe A*, 43, 105 pp.
- ASPRION, U. AND AIGNER, T., 1997. Aquifer architecture analysis using ground-penetrating radar: Triassic and Quaternary examples. *Environmental Geology*, 31, 66-75.
- AUSTEN, I., 1990. Geologisch-sedimentologische Kartierung des Königshafens (List auf Sylt) und Untersuchungen seiner Sedimente. Diplomarbeit, Universität Kiel, 99 pp.
- AUSTEN, I., 1992. Geologisch-sedimentologische Kartierung des Königshafens (List/Sylt). *Meyniana*, 44, 45-52.
- AVERDIECK, F.-R., 1980. Geobotanik des Sylter Holozäns. In: Kossack, G., Harck, O., Newig, J., Hoffmann, D., Willkomm, H., Averdieck, F.-R., Reichstein, J. (eds.), *Archsum auf Sylt. Part 1, Römisch-Germanische Forschungen*, 39, pp. 147-172.
- AVERDIECK, F.-R. AND HUMMEL, P., 1974. Zum Aufbau und Alter des Heidsandes auf Sylt. *Meyniana*, 24, 9-25.
- BACKHAUS, J., HARTKE, D., HÜBNER, U., LOHSE, H., AND MÜLLER, A., 1998. Hydrographie und Klima im Lister Tidebecken. In: Gätje, C., Reise, K. (eds.), *Ökosystem Wattenmeer*, Springer, Berlin, pp. 39-54.
- BAKER, P.L., 1991. Response of ground-penetrating radar to bounding surfaces and lithofacies variations in sand barrier sequences. *Exploration Geophysics*, 22, 19-22.
- BANO, M. AND GIRARD, J.-F., 2001. Radar reflections and water content estimation of aeolian sand dune. *Geophysical Research Letters*, 28, 3207-3210.
- BANTELMANN, A., 1967. Die Landschaftsentwicklung an der schleswig-holsteinischen Westküste – dargestellt am Beispiel Nordfriesland; eine Funktionschronik durch fünf Jahrtausende. *Wachholtz, Neumünster*, 97 pp.
- BANTELMANN, A., 1975. Die frühgeschichtliche Marschensiedlung beim Elisenhof in Eiderstedt. *Landschaftsgeschichte und Baubefunde. Studien zur Küstenarchäologie Schleswig-Holsteins, Series A*, 1, 190 pp.
- BARTHOLDY, J. AND PEJRUP, M., 1994. Holocene evolution of the Danish Wadden Sea. *Senckenbergiana Maritima*, 24, 187-209.
- BASSON U., 1992. Mapping of moisture content and structure of unsaturated sand layers with ground-penetrating radar. PhD-Thesis, Tel-Aviv University, 80 pp. (in Hebrew with English abstract).
- BAYERL, K., 1992. Zur jahreszeitlichen Variabilität der Oberflächensedimente im Sylter Watt nördlich des Hindenburgdammes. Dissertation, Berichte aus dem Forschungs- und Technologiezentrum Westküste der Universität Kiel, 2, 134 pp.
- BAYERL, K. AND HIGELKE, B., 1994. The development of northern Sylt during the latest Holocene. *Helgolander Meeresuntersuchungen*, 48, 145-162.

- BAYERL, K. AND KÖSTER, R., 1998. Morphogenese des Lister Tiedebeckens. In: Gätje, C., Reise, K. (eds.), *Ökosystem Wattenmeer*, Springer, Berlin, 25-29.
- BAYERL, K., KÖSTER, R., AND MURPHY, D., 1998a. Verteilung und Zusammensetzung der Sedimente im Lister Tidebecken. In: Gätje, C., Reise, K. (eds.), *Ökosystem Wattenmeer*, Springer, Berlin, pp. 31-38.
- BAYERL, K., AUSTEN, I., KÖSTER, R., PEJRUP, M., AND WITTE, G., 1998b. Dynamik der Sedimente im Lister Tidebecken. In: Gätje, C., Reise, K. (eds.), *Ökosystem Wattenmeer*, Springer, Berlin, pp. 127-159.
- BEHRE, K.-E., 1995. Die Entstehung und Entwicklung der Natur- und Kulturlandschaft der ostfriesischen Halbinsel. In: Behre, K.E. and van Lengen, H. (eds.), *Ostfriesland – Geschichte und Gestalt einer Kulturlandschaft*, Wilhelmshaven, pp. 5-37.
- BEHRE, K.-E., 2003. Eine neue Meeresspiegelkurve für die südliche Nordsee: Transgressionen und Regressionen in den letzten 10,000 Jahren. *Probleme der Küstenerforschung im südlichen Nordseegebiet*, 28, 9-63.
- BEHRE, K.-E., 2004. Coastal development, sea-level change and settlement history during the later Holocene in the Clay District of Lower Saxony (Niedersachsen), northern Germany. *Quaternary International*, 112, 37-53.
- BEHRE, K.-E., 2007. A new Holocene sea-level curve for the southern North Sea. *Boreas*, 6, 82-102.
- BERES, M. AND HAENI, F.P., 1991. Application of ground-penetrating-radar methods in hydrogeologic studies. *Ground Water*, 29, 375-386.
- BLINDOW, N., RICHTER, T., AND PETZOLD, H., 1997. Bodenradar. In: Knödel, K., Krümmel, H., Lange, G. (eds.), *Handbuch zur Erkundung des Untergrundes von Deponien und Altlasten*. Bundesanstalt für Geowissenschaften und Rohstoffe, Springer, Berlin, pp. 369-403.
- BLOTT, S.J. AND PYE, K., 2001. Gradistat: a grain size distribution and statistics package for the analysis of unconsolidated sediments. *Earth Surface Processes and Landforms*, 6, 1237-1248.
- BOOTHROYD, J.C., 1985. Tidal inlets and tidal deltas. In: Davis, R.A. (ed.), *Coastal sedimentary environments*, Springer, Heidelberg, Berlin, New York, pp. 445-532.
- BRENNINKMEYER, B., 1976. Sand fountains in the surf zone. In: Davis, R.A., Ethington, R.L. (eds.), *Beach and nearshore sedimentation*, SEPM Special Publication, 24, pp. 69-91.
- BRESSAU, S., 1984. Zur Hydrogeologie der Insel Sylt. In: Degens, E.T., Hillmer, G., Spaeth, C. (eds.), *Exkursionsführer Erdgeschichte des Nordsee- und Ostseeraumes*, Geologisch-Paläontologisches Institut der Universität Hamburg, Hamburg, pp. 383-390.
- BRISTOW, C.S., 1995. Facies analysis in the Lower Greensand using ground-penetrating radar. *Journal of the Geological Society*, London, 152, 591-598.
- BRISTOW, C.S. AND JOL, H.M., 2003. An introduction to ground-penetrating radar (GPR) in sediments. In: Bristow, C.S. and Jol, H.M. (eds.), *Ground-penetrating radar in sediments*. Geological Society, London, Special Publications, 211, pp. 1-7.
- BRISTOW, C.S., PUGH, J., AND GOODALL, T., 1996. Internal structure of Aeolian dunes in Abu Dhabi determined using ground-penetrating radar. *Sedimentology*, 43, 995-1003.
- BRISTOW, C.S., CHROSTON, P.N., AND BAILEY, S.D., 2000. The structure and development of foredunes on a locally prograding coast: insights from ground-penetrating radar surveys, Norfolk, UK. *Sedimentology*, 47, 923-944.
- BUYNEVICH, I.V. AND FITZGERALD, D.M., 2003. High-resolution subsurface (GPR) imaging and sedimentology of coastal ponds, Maine, USA: implications for Holocene back-barrier evolution. *Journal of Sedimentary Research*, 3, 559-571.

- BUYNEVICH, I.V., FITZGERALD, D.M., AND VAN HETEREN, S., 2004. Sedimentary records of intense storms in Holocene barrier sequences, Maine, USA. *Marine Geology*, 210, 135-148.
- BUYNEVICH, I.V., FITZGERALD, D.M., AND GOBLE, R.J., 2007. A 1500 yr record of North Atlantic storm activity based on optically dated relict beach scarps. *Geology*, 35, 543-546.
- CAMPBELL, C.V., 1967. Lamina, laminaset, bed and bedset. *Sedimentology*, 8, 7-26.
- CARTER, R.W.G., 1986. The morphodynamics of beach-ridge formation: Magilligan, northern Ireland. *Marine Geology*, 73, 191-214.
- CHAMLEY, H., 1990. *Sedimentology*. Springer, Berlin, 285 pp.
- CHEEL, R.J. AND LECKIE, D.A., 1992. Coarse-grained storm beds in the upper cretaceous Chungo Member (Wapiabi Formation), southern Alberta, Canada. *Journal of Sedimentary Petrology*, 62, 933-945.
- CLEMMENSEN, L.B., ANDREASEN, F., NIELSEN, S.T., AND STEN, E., 1996. The late Holocene coastal dunefield at Vejers, Denmark: characteristics, sand budget and depositional dynamics. *Geomorphology*, 17, 79-98.
- CLEMMENSEN, L.B., PYE, K., MURRAY, A., HEINEMEIER, J., 2001. Sedimentology, stratigraphy and landscape evolution of a coastal dune system, Lodbjerg, NW Jutland, Denmark. *Sedimentology*, 48, 3-27.
- CLEMMENSEN, L.B., BJØRNSSEN, M., MURRAY, A., AND PEDERSEN, K., 2007. Formation of aeolian dunes on Anholt, Denmark since AD 1560: A record of deforestation and increased storminess. *Sedimentary Geology*, 199, 171-187.
- CLIFTON, H.E., 1969. Beach lamination – nature and origin. *Marine Geology*, 7, 553-559.
- CLIFTON, H.E., HUNTER, R.E., AND PHILLIPS, R.L., 1971. Depositional structures and processes in the non-barred high-energy nearshore. *Journal of Sedimentary Petrology*, 41, 651-670.
- CLOUGH, J.W., 1976. Electromagnetic lateral waves observed by earth-sounding radars. *Geophysics*, 41, 1126-1132.
- COLLINSON, J., MOUNTNEY, N., AND THOMPSON, D., 2006. *Sedimentary Structures*. 3rd edition, Terra Publishing, Harpenden, 292 pp.
- CONYERS, L.B. AND GOODMAN, D., 1997. *Ground-penetrating radar: an introduction for Archaeologists*. Altamira Press, London.
- COSTAS, S., ALEJO, I., RIAL, F., LORENZO, H., AND NOMBELA, M.A., 2006. Cyclical evolution of a modern transgressive sand barrier in northwestern Spain elucidated by GPR and aerial photos. *Journal of Sedimentary Research*, 76, 1077-1092.
- DALY, J., MCGEARY, S., AND KRANTZ, D.E., 2002. Ground-penetrating radar investigation of a late Holocene spit complex: Cape Henlopen, Delaware. *Journal of Coastal Research*, 18, 274-286.
- DAVIDSON-ARNOTT, R.G.D. AND GREENWOOD, B., 1976. Facies relationships on a barred coast, Kouchibouguac Bay, New Brunswick, Canada. In: Davies, R.A. and Ethington, R.L. (eds.), *Beach and nearshore sedimentation*, SEPM Special Publication, 24, 149-168.
- DAVIS, J.L. AND ANNAN, A.P., 1989. Ground-penetrating radar for high-resolution mapping of soil and rock Stratigraphy. *Geophysical Prospecting*, 3, 531-551.
- DAVIS, R.A., 1985. Beach and nearshore zone. In: Davis, R.A. (ed.), *Coastal sedimentary environments*. Springer, New York, pp. 379-444.
- DAVIS, R.A., 1994. Barrier island systems – a geologic overview. In: Davis, R.A. (ed.), *Geology of Holocene barrier island systems*, Springer, Heidelberg, Berlin, pp. 1-46.

- DAVIS, R.A. AND HINE, A.C., 1989. Quaternary geology and sedimentology of the barrier island and marshy coast, west-central Florida, USA. International Geological Congress, Fieldtrip Guidebook No. T375. American Geophysical Union, Washington DC, 38 pp.
- DE GROOT, TH.A.M., WESTERHOFF, W.E., AND BOSCH, J.H.A., 1996. Sea-level rise during the last 2000 years as recorded on the Frisian Islands (the Netherlands). *Mededelingen Rijks Geologische Dienst*, 57, 69-78.
- DIETZ, C. AND HECK, H.-L., 1952a. Geologische Karte von Deutschland, Erläuterungen zu den Blättern Sylt-Nord und Sylt-Süd. Landesanstalt für Angewandte Geologie, Kiel. 123 pp.
- DIETZ, C. AND HECK, H.-L., 1952b. Geologische Karte von Deutschland, Insel Sylt. Landesanstalt für Angewandte Geologie, Kiel.
- DONNELLY, J.P., BUTLER, J., ROLL, S., WENGREN, M., AND WEBB, T., 2004. A backbarrier overwash record of intense storms from Brigantine, New Jersey. *Marine Geology*, 210, 107-121.
- DRAGA, M., 1983. Eolian activity as a consequence of beach nourishment – observations at Westerland (Sylt), German North Sea coast. *Zeitschrift für Geomorphologie*, 45, 303-319.
- DUKE, W.L., 1990. Geostrophic circulation of shallow marine turbidity currents? The dilemma of paleo-flow patterns in storm-influenced prograding shoreline systems. *Journal of Sedimentary Petrology*, 60, 870-883.
- EIDNER, M., 2006. Analyse des Informationsgehaltes von 3D-Georadardaten. *Freiberger Forschungshefte, Reihe C*, 103 pp.
- EISMA, D., MOOK, W.G., AND LABAN, C., 1981. An early Holocene tidal flat in the Southern Bight. *Special Publications of the International Association of Sedimentologists*, 5, 229-237.
- ELIOT, I., FULLER, M., AND SANDERSON, P., 1998. Historical development of a fore-dune plain at Desperate Bay, Western Australia. *Journal of Coastal Research*, 14, 1187-1201.
- ELLIOTT, T., 1986. Siliciclastic shorelines. In: Reading, H.G. (ed.), *Sedimentary environments and facies*. Blackwell Scientific Publications, Oxford, pp. 155-188.
- EMERY, D. AND MYERS, K.J., 1996. *Sequence stratigraphy*. Blackwell Science, London, 297 pp.
- FETTER, C.W., JR., 1972. Position of the saline water interface beneath oceanic islands. *Water Resource Research*, 8, 1307-1315.
- FISHER, E., McMECHAN, G.A., ANNAN, A.P., AND COSWAY, S.W., 1992. Examples of reverse-time migration of single channel, ground-penetrating radar profiles. *Geophysics*, 57, 577-586.
- FISHER, S.C., STEWARD, R.R., AND JOL, H.M., 1996. Ground-penetrating radar (GPR) data enhancement using seismic techniques. *Journal of Environmental Engineering & Geophysics*, 1, 89-96.
- FITZGERALD, D.M. AND VAN HETEREN, S., 1999. Classification of paraglacial barrier systems: coastal New England, USA. *Sedimentology*, 46, 1083-1108.
- FITZGERALD, D.M., PENLAND, S., AND NUMMEDAL, D., 1984. Control of barrier island shape by inlet sediment bypassing: East Frisian Islands, West Germany. *Marine Geology*, 60, 355-376.
- FITZGERALD, D.M., BALDWIN, C.T., IBRAHIM, N.A., AND HUMPHRIES, S.M., 1992. Sedimentologic and morphologic evolution of a beach-ridge barrier along an indented

- coast – Buzzard Bay, Massachusetts. In: Fletcher, C.H., Wehmiller, J.F. (eds.), *Quaternary coasts of the United States – marine and lacustrine systems*, SEPM Special Publications, 48, pp. 65-75.
- FLEMMING, B.W., 2002. Effects of climate and human interventions on the Evolution of the Wadden Sea depositional system (Southern North Sea). In: Wefer, G., Berger, W., Behre, K.-E., Jansen, E. (eds.), *Climate development and history of the North Atlantic Realm*, Springer, Berlin, Heidelberg, pp. 399-413.
- FOLK, R.L. AND WARD, W.C., 1957. Brazos River bar (Texas): a study in the significance of grain size parameters. *Journal of Sedimentary Petrology*, 27, 3-26.
- FORKMANN, B., 2006. Geschichte, Grundlagen und Zukunft des GPR. *Mitteilungen der Deutschen Geophysikalischen Gesellschaft, Sonderband II/2006*, 3-21.
- FREELAND, R.S., YODER, R.E., AMMONS, J.T., AND LEONARD, L.L., 2002. Integration of real-time global positioning with ground-penetrating radar surveys. *Applied Engineering in Agriculture*, 18, 647-650.
- FRISCHBUTTER, A., 2001. Recent vertical movements. In: Garetsky, R.G., Ludwig, O., Schwab, G., Stackebrandt, W. (eds.), *Neodynamics of the Baltic Sea depression and adjacent areas*. Brandenburgische Geowissenschaftliche Beiträge, Landesamt für Geowissenschaften und Rohstoffe Brandenburg, pp. 27-32.
- FRYBERGER, S.G., SCHENK, C.J., AND KRYSSTINIK, L.F., 1988. Stokes surfaces and the effects of near-surface groundwater-table on aeolian deposition. *Sedimentology*, 35, 21-41.
- FÜCHTBAUER, H., 1958. Die Schüttungen im Chatt und Aquitan der deutschen Alpenvorlandsmolasse. *Eclogae Geologicae Helvetiae*, 51, 928-941.
- FÜCHTBAUER, H., 1988. Sandsteine. In: Füchtbauer, H. (ed.), *Sedimente und Sedimentgesteine*, Schweizerbart, Stuttgart, pp. 97-184.
- GAERTNER, H. AND WITTKA, T., 1997. Reflexionsseismik. In: Knödel, K., Krümmel, H., Lange, G. (eds.), *Handbuch zur Erkundung des Untergrundes von Deponien und Altlasten*. Bundesanstalt für Geowissenschaften und Rohstoffe, Springer, Berlin, pp. 620-670.
- GAWTHORPE, R.L., COLLIER, R.E.L., ALEXANDER, J., BRIDGE, J.S., AND LEEDER, M.R., 1993. Ground-penetrating radar: application to sandbody geometry and heterogeneity studies. In: North, C.P., Prosser, D.J. (eds.), *Characterization of fluvial and aeolian reservoirs*. Geological Society Special Publications, London, 73, pp. 421-432.
- GEHRELS, W.R., SZKORNIK, K., BARTHOLDY, J., KIRBY, J.R., BRADLEY, S.L., MARSHALL, W.A., HEINEMEIER, J., AND PEDERSEN, J.B.T., 2006. Late Holocene sea-level changes and isostasy in western Denmark. *Quaternary Research*, 66, 288-302.
- GIBBS, A.E. AND DAVIS R.A., 1991. Development and stratigraphy of Three Rooker Bar; a recently emergent barrier island, Pinellas County, Florida. *Proceedings of the GCSSEPM Foundation, 12th Annual Research Conference, Houston*, 84-90.
- GIERLOFF-EMDEN, H.G., 1961. Luftbild- und Küstengeographie am Beispiel der deutschen Nordseeküste. *Schriftenfolge des Institutes für Landeskunde und Raumforschung*, 4, 118 pp.
- GOLDSCHMIDT, P., BAYERL, K., AUSTEN, I., AND KÖSTER, R., 1993. From the Wanderdünen to the Watt – coarse grained aeolian sediment transport on Sylt, Germany. *Zeitschrift für Geomorphologie*, 37, 171-178.
- GRASMUECK, M., WEGER, R., AND HORSTMAYER, H., 2003. How dense is dense enough for a real 3D GPR survey? *Conference Proceedings Volume, Society of Exploration Geophysics*, 4 pp.

- GREENWOOD, B., AAGAARD, T., AND NIELSEN, J., 2004. Swash Bar Morphodynamics in the Danish Wadden Sea: Sand Bed Oscillations and Suspended Sediment Flux during an Accretionary Phase of the Foreshore Cycle. *Geografisk Tidsskrift*, 104, 15-30.
- GRIPP, K., 1915. Über das marine Altmiocän im Nordseebecken. *Neues Jahrbuch für Mineralogie, Geologie und Paläontologie*, 41, 1-59.
- GRIPP, K., 1944. Entstehung und künftige Entwicklung der Deutschen Bucht. *Archiv der deutschen Seewarte und des Marineobservatoriums*, 63, 1-44.
- GRIPP, K., 1968. Zur jüngsten Erdgeschichte von Hörnum/Sylt und Amrum mit einer Übersicht über die Entstehung der Dünen in Nordfriesland. *Die Küste*, 16, 76-117.
- GRIPP, K. AND BECKER, W., 1940. Untersuchungen über den Aufbau und die Entstehung der Insel Sylt: II. Mittel-Sylt. *Westküste*, 2, 71-84.
- GRIPP, K. AND DITTMER, E., 1941. Die Entstehung Nordfrieslands. *Die Naturwissenschaften*, 29, 577-581.
- GRIPP, K. AND SIMON, G., 1940. Untersuchungen über den Aufbau und die Entstehung der Insel Sylt: I. Nord-Sylt. *Westküste*, 2, 1-70.
- GUPTA, S. AND ALLEN, P.A., 1999. Fossil shore platforms and drowned gravel beaches: evidence for high-frequency sea-level fluctuations in the distal alpine foreland basin. *Journal of Sedimentary Research*, 69, 394-413.
- HAGMEIER, A. AND KÄNDLER, R., 1927. Neue Untersuchungen im nordfriesischen Wattenmeer und auf den fiskalischen Austernbänken. *Wissenschaftliche Meeresuntersuchungen, N.F. Abt. Helgoland*, 16, 1-90.
- HANSEN, C.P., 1877. *Chronik der Friesischen Uthlande*. Lühr & Dircks, Garding, 319 pp.
- HARCK, O., 1972. Steinzeitfunde im Listland und auf der Hörnum Halbinsel auf Sylt. *Offa*, 29, 5-19.
- HARCK, O., 1974. Zur Datierung des Listlandes und der Hörnum Halbinsel auf Sylt. *Meyniana*, 24, 69-72.
- HAYES, M.O., 1975. Morphology of sand accumulation in Estuaries. In: Cronin, L.E. (ed.), *Estuarine Research*, vol. 2, *Geology and Engineering*, Academic Press, New York, pp. 3-22.
- HAYES, M.O., 1979. Barrier island morphology as a function of tidal and wave regime. In: Leatherman, S.P. (ed.), *Barrier islands from the Gulf of St. Lawrence to the Gulf of Mexico*. Academic Press, New York, pp. 1-27.
- HAYES, M.O., 1980. General morphology and sediment patterns in tidal inlets. *Sedimentary Geology*, 26, 139-156.
- HAYES, M.O. AND BOOTHROYD, J.C., 1969. Storms as modifying agents in the coastal environment. *SEPM Eastern Section Field Trip Guidebook*, 245-265.
- HESP, P.A., 1988. Morphology, dynamics and internal stratification of some established foredunes in southeast Australia. *Sedimentary Geology*, 55, 17-41.
- HESP, P.A., 1999. The beach backshore and beyond. In: Short, A.D. (ed.), *Handbook of beach and shoreface morphodynamics*, Wiley, Chichester, pp. 145-169.
- HINE, A.C., 1979. Mechanisms of berm development and resulting beach growth along a barrier spit complex. *Sedimentology*, 26, 333-351.
- HIROKI, Y. AND TERASAKA, T., 2005. Wavy lamination in a mixed sand and gravel foreshore facies of the Pleistocene Hosoya Sandstone, Aichi, central Japan. *Sedimentology* 52, 65-75.

- HOFFMANN, D., 1969. The marine Holocene of Sylt – discussion of the age and facies. *Geologie en Mijnbouw*, 48, 343-347.
- HOFFMANN, D., 1971. Zur Geologie d. Seegebietes westl. von Sylt. *Meyniana*, 21, 25-31.
- HOFFMANN, D., 1974. Zum geologischen Aufbau der Hörnumer Halbinsel auf Sylt. *Meyniana*, 23, 63-68.
- HOFFMANN, D., 1980. Küstenholozän zwischen Sylt und Föhr. *Römisch-Germanische Forschungen*, 39, 85-130.
- HOFFMANN, D., 1984. Das Holozän der Insel Sylt. In: Degens, E.T., Hillmer, G., Spaeth, C. (eds.), *Exkursionsführer Erdgeschichte des Nordsee- und Ostseeraumes*, Geologisch-Paläontologisches Institut der Universität Hamburg, Hamburg, pp. 335-352.
- HOFFMANN, D., 1985. The Holocene marine transgression in the region of the North Frisian Islands. *Eiszeitalter und Gegenwart*, 35, 61-69.
- HOFFMANN, D., 2004. Holocene landscape development in the marshes of the West Coast of Schleswig-Holstein, Germany. *Quaternary International*, 112, 29-36.
- HOUSER, C. AND GREENWOOD, B., 2007. Onshore migration of a swash bar during a storm. *Journal of Coastal Research*, 23, 1-14.
- HOUSER, C., GREENWOOD, B., AND AAGAARD, T., 2006. Divergent response of an intertidal swash bar. *Earth Surface Processes and Landforms*, 31, 1775-1791.
- HUBBARD, S.S., PETERSON, J.E., MAJER, E.L., ZAWISLANSKI, P.T., WILLIAMS, K.H., ROBERTS, AND J., WOBBER, F., 1997. Estimation of permeable pathways and water content using tomographic radar data. *The Leading Edge*, 16, 1623-1628.
- HUGHEN, K.A., BAILLIE, M.G.L, BARD, E., BAYLISS, A., BECK, J.W., BERTRAND, C., BLACKWELL, P.G., BUCK, C.E., BURR, G., CUTLER, K.B., DAMON, P.E., EDWARDS, R.L., FAIRBANKS, R.G., FRIEDRICH, M., GUILDERTSON, T.P., KROMER, B., McCORMAC, F.G., MANNING, S., BRONK RAMSEY, C., REIMER, P.J., REIMER, R.W., REMMELE, S., SOUTHON, J.R., STUIVER, M., TALAMO, S., TAYLOR, F.W., VAN DER PLICHT, J., AND WEYHENMEYER, C.E., 2004, *Marine04 – marine radiocarbon age calibration, 0–26 cal kyr BP*. *Radiocarbon*, 46, 1059-1086.
- HUISKES A.H.L, 1979. Biological Flora of the British Isles: *Ammophila arenaria* (L.) Link. *Journal of Ecology*, 67, 363-382
- HUNDT, C., 1957. Die Abbruchursachen an der Nordwestküste des Ellenbogens auf Sylt. *Die Küste*, 6, 3-38.
- HUNTER, R.E., CLIFTON, H.E., AND PHILLIPS, R.L., 1979. Depositional processes, sedimentary structures, and predicted vertical sequences in barred nearshore systems, southern Oregon coast. *Journal of Sedimentary Petrology*, 49, 711-726.
- INGLE, J.C., 1966. The movement of beach sand – an analysis using fluorescent grains. Elsevier, New York, 221 pp.
- JELGERSMA, S., 1979. Sea-level changes in the North Sea basin. In: Oele, E., Schüttenhelm, R.T.E., Wiggers, A.J. (eds.), *The Quaternary history of the North Sea*. *Acta Universitatis Upsaliensis. Symposia Universitatis Upsaliensis annum quingentesimum celebrantis*, 2, 233-248.
- JOL, H.M., 1995. Ground-penetrating radar antennae frequencies and transmitter powers compared for penetration depth, resolution and reflection continuity. *Geophysical Prospecting*, 43, 693-709.
- JOL, H.M. AND SMITH, D.G., 1991. Ground-penetrating radar of northern lacustrine deltas. *Canadian Journal of Earth Sciences*, 28, 1939-1947.
- JOL, H.M. AND BRISTOW, C.S., 2003. GPR in sediments: advice on data collection, basic processing and interpretation, a good practice guide. In: Bristow, C.S., Jol, H.M. (eds.),

Ground-penetrating radar in sediments. Geological Society, London, Special Publications, 211, pp. 9-27.

JOL, H.M., SMITH, D.G., AND MEYERS, R.A., 1996. Digital ground penetrating radar (GPR): a new geophysical tool for coastal barrier research (examples from the Atlantic, Gulf and Pacific coasts, U.S.A). *Journal of Coastal Research*, 12, 960-968.

JOL, H.M., LAWTON, D.C., AND SMITH, D.G., 2002. Ground-penetrating radar: 2D and 3D subsurface imaging of a coastal barrier spit, Long Beach, WA, USA. *Geomorphology*, 53, 165-181.

KEARY, P. AND BROOKS, M., 1991. An introduction to geophysical exploration. Blackwell Scientific Publications, Boston. 272 pp.

KIM, J.-H., CHO, S.-J., AND YI, M.-J., 2007. Removal of ringing noise in GPR data by signal processing. *Geosciences Journal*, 11, 75-81.

KING, C.A.M. AND WILLIAMS, W.W., 1949. The formation and movement of sand bars by wave action. *The Geographical Journal*, 113, 70-85.

KINSMAN, D.J.J., 1969. Modes of formation, sedimentary associations, and diagnostic features of shallow-water and supratidal evaporites (in *Evaporites and petroleum*). *The American Association of Petroleum Geologists Bulletin*, 53, 830-840.

KNAPP, R.W., 1990. Vertical resolution of thick beds, thin beds and thin-bed cyclotherms. *Geophysics*, 55, 1183-1190.

KNAPP, R.W., 1991. Fresnel zones in the light of broad-band data. *Geophysics*, 56, 354-359.

KNIGHT, R. AND TERCIER, P., 1997. The role of ground-penetrating radar and geostatistics in reservoir description. *The Leading Edge*, 16, 1576-1582.

KNÖDEL, K., KRUMMEL, H., AND LANGE, G., 1997. *Handbuch zur Erkundung des Untergrundes von Deponien und Altlasten*, Bundesanstalt für Geowissenschaften und Rohstoffe, Springer, Berlin. 1102 pp.

KOLUMBE, E., 1933. Ein Beitrag zur Kenntnis der Entwicklungsgeschichte des Königshafens bei List auf Sylt. *Wissensch. Meeresunters., N.F. Abt. Kiel*, 21, 116-130.

KOSSACK, G., HARCK, O., AND REICHSTEIN, J., 1975. Zehn Jahre Siedlungsforschung in Archsum auf Sylt. *Berichte der Römisch-germanischen Kommission*, Berlin, 55, 261-377.

KÖSTER, R., 1974. Geologie des Seegrundes vor den Nordfriesischen Inseln Sylt und Amrum. *Meyniana*, 24, 27-41.

KÖSTER, R., 1979. Dreidimensionale Kartierung des Seegrundes vor den Nordfriesischen Inseln. In: *Deutsche Forschungsgemeinschaft (ed.), Sandbewegung im Küstenraum – Rückschau, Ergebnisse und Ausblick, ein Abschlußbericht*, pp. 146-168.

KÖSTER, R. AND RICKLEFS, K., 1998. Sediments and suspended matter in the Sylt-Rømø tidal area: a summary of results collected in the „SWAP“-project. *Seckenbergiana maritime*, 29, 101-109.

KOSTIC, B. AND AIGNER, T., 2007. Sedimentary architecture and 3D ground-penetrating radar analysis of gravelly meandering river deposits (Neckar Valley, SW Germany). *Sedimentology*, 54, 789-808.

KOSTIC, B., BECHT, A., AND AIGNER, T., 2005. 3-D sedimentary architecture of a Quaternary gravel delta (SW-Germany): implications for hydrostratigraphy. *Sedimentary Geology*, 181, 143-171.

KRUK, J. VAN DER, SLOB, E.C., AND FOKKEMA, J. T., 1999. Background of ground-penetrating radar measurements. *Geologie en Mijnbouw*, 77, 177-188.

- KUMAR, N. AND SANDERS, J.E., 1974. Inlet sequence – a vertical succession of sedimentary structures and textures created by the lateral migration of tidal inlets. *Sedimentology*, 21, 491-532.
- KUMAR, N. AND SANDERS, J.E., 1976. Characteristics of shoreface storm deposits: modern and ancient examples. *Journal of Sedimentary Petrology*, 46, 145-162.
- LANGENBERG, H., PFIZENMAYER, A., VON STORCH, H., AND SÜNDERMANN, J., 1999. Storm-related sea-level variations along the North Sea coast: natural variability and anthropogenic change. *Continental Shelf Research*, 19, 821-842.
- LEHMANN, F. AND GREEN, A.G., 1999. Semiautomated georadar data acquisition in three dimensions. *Geophysics*, 64, 719-731.
- LEHMANN, F. AND GREEN, A.G., 2000. Topographic migration of georadar data: implications for acquisition and processing. *Geophysics*, 65, 836-848.
- LINDHORST, S., BETZLER, C., HASS, H.C., FÜRSTENAU, J., AND FEINDT, S., 2006. The Holocene stratigraphy of Sylt Island (German Bight): new insights revealed by ground-penetrating radar (GPR). *Sediment 2006*, Göttingen, Schriftenreihe der deutschen Geologischen Gesellschaft, 45, 112.
- LINDHORST, S., BETZLER, C., AND HASS, H.C., in press. The sedimentary architecture of a Holocene barrier spit (Sylt / German Bight): swash-bar accretion and storm erosion. *Sedimentary Geology*.
- LINDHORST, S., FÜRSTENAU, J., HASS, H.C., AND BETZLER, C., in prep. Anatomy of a hooked spit.
- LINKE, G., 1981. Ergebnisse und Aspekte zur Klimaentwicklung im Holozän. *Geologische Rundschau*, 70, 774-783.
- LITT, T., BRAUER, A., GOSLAR, T., MERKT, J., BALAGA, K., RALSKA-JASIEWICZOWA, M., STEBICH, M., AND NEGENDANK, J.F.W., 2001. Correlation and synchronization of lateglacial continental sequences in northern central Europe based on annually laminated lacustrine sediments. *Quaternary Science Reviews*, 20, 1233-1249.
- MAGER, F., 1927. Der Abbruch der Insel Sylt durch die Nordsee (Eine historisch-geographische Untersuchung). *Veröffentlichungen der Schleswig-Holsteinischen Universitätsgesellschaft*, 8, 1-199.
- MARGRAVE, G.F., 2001. Direct Fourier migration for vertical velocity variations. *Geophysics*, 66, 1504-1514.
- MASSARI, F. AND PAREA, G.C., 1988. Progradational gravel beach sequences in a moderate-to high-energy, microtidal marine environment. *Sedimentology*, 35, 881-913.
- MASSELINK, G., KROON, A., AND DAVIDSON-ARNOTT, R.G.D., 2006. Morphodynamics of intertidal bars in wave-dominated coastal settings – a review. *Geomorphology*, 73, 33-49
- MAUZ, B. AND BUNGENSTOCK, F., 2007. How to reconstruct trends of late Holocene relative sea level: A new approach using tidal flat clastic sediments and optical dating. *Marine Geology*, 237, 225-237.
- MCCUBBIN, D.G., 1982. Barrier-island and strand-plain facies. In: Scholle, P.A., Spearing, D. (eds.), *Sandstone depositional environments*, AAPG Memoir, 31, 247-258.
- MENKE, B., 1976. Befunde und Überlegungen zum nacheiszeitlichen Meeresspiegelanstieg (Dithmarschen und Eiderstedt, Schleswig-Holstein). *Probleme der Küstenforschung im südlichen Nordseegebiet*, 11, 145-161.
- MEYN, L., 1876. Geognostische Beschreibung der Insel Sylt und ihrer Umgebung nebst einer geognostischen Karte im Maassstabe von 1:100.000. *Abhandlungen zur geologischen Spezialkarte von Preussen und den thüringischen Staaten*. Berlin.

- MIALL, A.D., 1991. Hierarchies of architectural units in terrigenous clastic rocks, and their relationship to sedimentation rate. In: Miall, A.D., Tyler, N. (eds.), *The three-dimensional facies architecture of terrigenous clastic sediments and its implications for hydrocarbon discovery and recovery*. Concepts in Sedimentology and Palaeontology, SEPM, Tulsa, 3, pp. 6-12.
- MILITZER, H. AND WEBER, F. (eds.), 1985. *Angewandte Geophysik. Band 2*, Springer, Wien, New York, 379 pp.
- MITCHUM, R.M., VAIL, P.R., AND SANGREE, J.B., 1977. Stratigraphic interpretation of seismic reflection patterns in depositional sequences. In: Payton, C.E. (ed.), *Seismic stratigraphy – applications to hydrocarbon exploration*. AAPG Memoir, 26, pp. 117-123.
- MØLLER, I. AND ANTHONY, D., 2003. A GPR study of sedimentary structures within a transgressive coastal barrier along the Danish North Sea coast. In: Bristow, C.S., Jol, H.M. (eds.), *Ground penetrating radar in sediments*. Geological Society, London, Special Publications, 211, pp. 55-65.
- MOORE, L.J., JOL, H.M., KRUSE, S., VANDERBURGH, S., AND KAMINSKY, G.M., 2004. Annual layers revealed by GPR in the subsurface of a prograding coastal barrier, southwest Washington, U.S.A. *Journal of Sedimentary Research*, 74, 690-696.
- MÖRNER, N.-A., 1976. Eustatic changes during the last 8,000 years in view of radiocarbon calibration and new information from the Kattegatt Region and other Northwestern European coastal areas. *Palaeogeography, Palaeoclimatology, Palaeoecology*, 19., 63-85.
- MÜLLER, F. AND FISCHER, O., 1938. *Sylt. Das Wasserwesen an der schleswig-holsteinischen Nordseeküste, Teil 2. Die Inseln*, 7, Berlin, 304 pp.
- MÜLLER, M.J., 1980. *Handbuch ausgewählter Klimastationen der Erde*. Forschungsstelle Bodenerosion der Universität Trier, Trier, 346 pp.
- NEAL, A., 2004. Ground-penetrating radar and its use in sedimentology: principles, problems and progress. *Earth-Science Reviews*, 66, 261-330.
- NEAL, A. AND ROBERTS, C.L., 2000. Applications of ground-penetrating radar (GPR) to sedimentological, geomorphological and geoarchaeological studies in coastal environments. In: Pye, K., Allen, J.R.L. (eds.), *Coastal and estuarine environments: sedimentology, geomorphology and geoarchaeology*. Geological Society, London, Special Publications, 175, pp. 139-171.
- NEAL, A., RICHARDS, J., AND PYE, K., 2002. Structure and development of shell cheniers in Essex, southeast England, investigated using high-frequency ground-penetrating radar. *Marine Geology*, 185, 435-469.
- NEAL, A., PONTEE, N.I., PYE, K., AND RICHARDS, J., 2002. Internal structure of mixed-sand-and-gravel beach deposits revealed using ground-penetrating radar. *Sedimentology*, 49, 789-804.
- NEIDE, H., 1977a. *Küstenkarte 1:25000 - 0916 K List*. Landesvermessungsanstalt Schleswig-Holstein, Kiel.
- NEIDE, H., 1977b. *Küstenkarte 1:25000 - 1016 K Kampen*. Landesvermessungsanstalt Schleswig-Holstein, Kiel.
- NEWIG, J., 1980. Sylt im Spiegel historischer Karten. In: Kossack, G., Harck, O., Newig, J., Hoffmann, D., Willkomm, H., Averdick, F.-R., Reichstein, J. (eds.), *Archsum auf Sylt. Part 1. Römisch-Germanische Forschungen*, 39, pp. 64-84.
- NEWIG, J., 1995. Zur langfristigen Gestaltänderung der Insel Sylt. *Kölner Geographische Arbeiten*, 66, 121-138.

- NEWIG, J., 2004. Die Küstengestalt Nordfrieslands im Mittelalter nach historischen Quellen. In: Schernewski, G., Dolch, T. (eds.), *Coastline Reports*, 1, pp. 23-36.
- NIEDORODA, A.W., SWIFT, D.J. P., HOPKINS, T.S., AND MA, C.-M., 1984. Shoreface morphodynamics on wave-dominated coasts. *Marine Geology*, 60, 331-354.
- NIEDORODA, A.W., SWIFT, D.J. P., AND HOPKINS, T.S., 1985. The shoreface. In: Davis, R.A. (ed.), *Coastal sedimentary environments*, Springer, New York, 533-623.
- NIELSEN, L.H., JOHANNESSEN, P.N., AND SURLYK, F., 1988. A late Pleistocene coarse-grained spit-platform sequence in northern Jylland, Denmark. *Sedimentology*, 35, 915-937.
- NOON, D.A., STICKLEY, G.F., AND LONGSTAFF, D., 1998. A frequency-independent characterisation of GPR penetration and resolution performance. *Journal of Applied Geophysics*, 40, 127-137.
- OERTEL, G.F., 1975. Post Pleistocene island and inlet adjustment along the Georgia coast. *Journal of Sedimentary Petrology*, 45, p.150-159.
- OLHOEFT, G.R., 1998. Electrical, magnetic, and geometric properties that determine ground-penetrating radar performance. *Proceedings of GPR '98, Seventh International Conference on Ground Penetrating Radar*, Kansas, University of Kansas, 177-182.
- OVERBECK, F., 1975. *Botanisch-geologische Moorkunde*. Wachholtz, Neumünster, 719 pp.
- PEJRUP, M., LARSEN, M., AND EDELVANG, K., 1997. A fine-grained sediment budget for the Sylt-Rømø tidal basin. *Helgoländer Meeresuntersuchungen*, 51, 253-268.
- PETERSEN, M., 1978. Inseln vor der östlichen Nordseeküste. *Die Küste*, 32, 94-109.
- PIPAN, M., FORTE, E., DAL MORO, G., SUGAN, M., AND FINETTI, I., 2003. Multifold ground-penetrating radar and resistivity to study the stratigraphy of shallow unconsolidated sediments. *The Leading Edge*, 22, 876-881.
- POWERS, M.H., 1997. Modeling frequency-dependent GPR. *The Leading Edge*, 16, 1657-1662.
- PRIESMEIER, K., 1970. Form und Genese der Dünen des Listlandes auf Sylt. *Schriften des Naturwissenschaftlichen Vereins für Schleswig-Holstein*, 40, 11-51.
- PRINGLE, J.K., WESTERMAN, A.R., CLARK, J.D., GARDINER, A.R., AND CORBETT, P.W.M., 2000. 3-D GPR surveying with vertical radar profiling (VPR) of petroleum reservoir outcrop analogues. *EAGE 62nd Conference*, Glasgow, Scotland.
- PSUTY, N.P., 1992. Spatial variations in coastal foredune development. In: Carter, R.W.G., Curtis, T.G.F., Sheehy-Skeffington, M.J. (eds.), *Coastal dunes – geomorphology, ecology and management for conservation*, Balkema, Rotterdam, pp. 3-13.
- PYE, K., 1990. Physical and human influences on coastal dune development between the Ribble and Mersey estuaries, northwest England. In: Nordstrom, K.F., Psuty, N.P., Carter, R.W.G. (eds.), *Coastal dunes – form and processes*, Wiley, Chichester, pp. 339-359.
- READING, H.G., 1996. Introduction. In: Reading, H.G. (ed.), *Sedimentary environments: processes, facies and stratigraphy*, 3rd edition, Blackwell, Oxford, pp. 1-4.
- REYNOLDS, J.M., 1997. *An introduction to applied and environmental geophysics*. Wiley, Chichester, 796 pp.
- ROBINSON, D.A. AND FRIEDMAN, S.P., 2001. Effect of particle size distribution on the effective dielectric permittivity of saturated granular media. *Water Resources Research*, 37, 33-40.

- ROBINSON, E.S. AND ÇORUH, C., 1988. Basic Exploration Geophysics. Wiley, Chichester, 576 pp.
- SANDMEIER, K.J., 2006. ReflexW manual, version 4.2. Karlsruhe, 209 pp.
- SCHNEIDER, W.A., 1978. Integral formulation for migration in two dimensions and three-dimensions. *Geophysics*, 43, 49-76.
- SCHWARTZ, R.K., 1982. Bedform and stratification characteristics of some modern small-scale washover sand bodies. *Sedimentology*, 29, 835-849.
- SCHWARZER, K., 1984. Das Morsum-Kliff und seine Ausbreitung unter den nördlich vorgelagerten Wattsedimenten. In: Degens, E.T., Hillmer, G., Spaeth, C. (eds.), *Exkursionsführer Erdgeschichte des Nordsee- und Ostseeraumes*, Geologisch-Paläontologisches Institut der Universität Hamburg, Hamburg, pp. 251-282.
- SHERIFF, R.E., 1977. Limitations on resolution of seismic reflections and geologic detail derivable from them. In: Payton, C.E. (ed.), *Seismic stratigraphy – applications to hydrocarbon exploration*. AAPG Memoir, 26, pp. 3-14.
- SHERIFF, R.E. AND GELDART, L.P., 1995. *Exploration Seismology*, 2nd edition. University Press, Cambridge, 592 pp.
- SMITH, D.G. AND JOL, H.M., 1995. Ground-penetrating radar: antenna frequencies and maximum probable depths of penetration in Quaternary sediments. *Journal of Applied Geophysics*, 33, 93-100.
- SMITH, D.G., MEYERS, R.A., AND JOL, H.M., 1999. Sedimentology of an upper-mesotidal (3.7 m) Holocene barrier, Willapa Bay, SW Washington, U.S.A. *Journal of Sedimentary Research*, 69, 1290-1296.
- STOKES, W.L., 1968. Multiple parallel truncation bedding planes – a feature of wind-deposited sandstone formations. *Journal of Sedimentary Petrology*, 38, 510-515.
- STOLT, R.H., 1978. Migration by Fourier transform. *Geophysics*, 43, 23-48.
- STREIF, H., 1990a. Quaternary sea-level changes in the North Sea, an analysis of amplitudes and velocities. In: Brosche, P., Sündermann, J. (eds.), *Earth's rotation from eons to days*. Springer, Heidelberg, pp. 201-214.
- STREIF, H., 1990b. Das ostfriesische Küstengebiet – Nordsee, Inseln, Watten und Marschen. *Sammlung geologischer Führer*, Borntraeger, Berlin, Stuttgart, 57, 376 pp.
- STREIF, H., 2002. The Pleistocene and Holocene development of the southeastern North Sea basin and adjacent coastal areas. In: Wefer, G., Berger, W., Behre, K.-E., Jansen, E. (eds.), *Climate development and history of the North Atlantic Realm*, Springer, Berlin, Heidelberg, pp. 387-397.
- STUIVER, M. AND REIMER, P.J., 1993. Extended ¹⁴C-database and revised CALIB radiocarbon calibration program. *Radiocarbon*, 35, 215-230.
- SWITZER, A.D., BRISTOW, C.S., AND JONES, B.G., 2006. Investigation of large-scale washover of a small barrier system on the southeast Australian coast using ground-penetrating radar. *Sedimentary Geology*, 183, 145-156.
- TAIRA, A. AND SCHOLLE, P.A., 1979. Discrimination of depositional environments using settling tube data. *Journal of Sedimentary Petrology*, 49, 787-800.
- TANNER, W.F., 1995. Origin of beach ridges and swales. *Marine Geology*, 129, 149-161.
- THOMPSON, W.O., 1937. Original structures of beaches, bars, and dunes. *Geological Society of America Bulletin*, 48, 723-752.
- TISCHLER, M., COLLINS, M.E., AND GRUNWALD, S., 2002. Integration of ground-penetrating radar data, global positioning systems, and geographic information systems to create

- three-dimensional soil models. Ninth International Conference on Ground-Penetrating Radar (GPR 2002), Santa Barbara, USA. SPIE Proceedings Series, The International Society for Optical Engineering, 313-316.
- TÖPPE, A., 1994. Beschleunigter Meeresspiegelanstieg. Hansa – Schifffahrt, Schifffbau, Hafen, Hamburg, 131, 78-82.
- TRONICKE, J., DIETRICH, P., WAHLIG, U., AND APPEL, E., 2002. Integrated surface georadar and crosshole radar tomography: a validation experiment in braided stream deposits. *Geophysics*, 67, 1516– 1523.
- VAN DAM, R.L., 2001. Causes of ground-penetrating radar reflections in sediment. PhD-Thesis, Vrije Universiteit, Amsterdam, 110 pp.
- VAN DAM, R.L. AND SCHLAGER, W., 2000. Identifying causes of ground-penetrating radar reflections using time-domain reflectometry and sedimentological analyses. *Sedimentology*, 47, 435-449.
- VAN DAM, R.L., SCHLAGER, W., DEKKERS, M.J., AND HUISMAN, J.A., 2002. Iron oxides as a cause of GPR reflections. *Geophysics*, 67, 536-545.
- VAN DER KRUK, J., SLOB, E.C., AND FOKKEMA, J.T., 1999. Background of ground-penetrating radar measurements. *Geologie en Mijnbouw*, 77, 177-188.
- VAN HETEREN, S. AND VAN DE PLASSCHE, O., 1997. Influence of relative sea-level change and tidal-inlet development on barrier-spit stratigraphy, Sandy Neck, Massachusetts.
- VAN HETEREN, S., FITZGERALD, D.M., BARBER, D.C., KELLEY, J.T., AND BELKNAP, D.F., 1996. Volumetric analysis of a New England barrier system using ground-penetrating radar and coring techniques. *Journal of Geology*, 104, 471-483.
- VAN HETEREN, S., FITZGERALD, D.M., MCKINLAY, P.A., AND BUYNEVICH, I.V., 1998. Radar facies of paraglacial barrier systems: coastal New England, USA. *Sedimentology*, 45, 181-200.
- VAN STRAATEN, L.M.J.U., 1965. Coastal barrier deposition in South- and North-Holland, in particular in the areas of Scheveningen and IJmuiden. *Mededelingen Van de Geologische Stichting*, 17, 41-75.
- WANG, P. AND HORWITZ, M.H., 2007. Erosional and depositional characteristics of regional overwash deposits caused by multiple hurricanes. *Sedimentology*, 54, 545-564.
- WIDESS, M.B., 1973. How thin is a thin bed? *Geophysics*, 38, 1176-1180.
- WIERMANN, R., 1966. ¹⁴C-Datierungen zum zeitlichen Ablauf der marinen Transgression bei Schüttsiel (Nordfriesland). *Meyniana*, 16, 117-122.
- WIGGINS, J.W., 1984. Kirchhoff integral extrapolation and migration of nonplanar data. *Geophysics*, 49, 1239-1248.
- WILLIS, A.J., 1989. Coastal dunes as biological system. *Proceedings of the Royal Society of Edinburgh*, 96B, p.17-36.
- WILLIS, A.J., FOLKES, B.F., HOPE-SIMPSON, J.F., AND YEMM, E.W., 1959. Braunton Burrows: the dune system and its vegetation. Part II. *Journal of Ecology*, 47, 249-288.
- WILLKOMM, H., 1980. Radiokohlenstoff- und ¹³C-Untersuchungen zur Torfentwicklung und Meerestransgression im Bereich Sylt-Föhr. In: Kossack, G., Harck, O., Newig, J., Hoffmann, D., Willkomm, H., Averdieck, F.-R., Reichstein, J. (eds.), *Archsum auf Sylt. Part 1, Römisch-Germanische Forschungen*, 39, pp. 131-146.
- WOEBCKEN, C., 1924. *Deiche und Sturmfluten an der deutschen Nordseeküste*. Friesen-Verlag, Bremen, Wilhelmshaven, 232 pp.
- YILMAZ, O., 1987. Seismic data processing. *Investigations in Geophysics*. Society of Exploration Geophysics, Tulsa, 526 pp.

YOUNG, R.A., DENG, Z., AND SUN, J., 1995. Interactive processing of GPR data. *The Leading Edge*, 14, 275-280.

ZÄUSIG, F., 1939. Veränderungen der Küsten, Sände, Tiefs und Watten der Gewässer um Sylt nach alten Seekarten, Seehandbüchern und Landkarten seit 1585. *Geologie der Meere und Binnengewässer*, 3, 401-505.

ZIEKUR, R., 2000. Georadar in der Bodenkunde. *Geologisches Jahrbuch*, 52, 9-34.

Danksagung

Angefangen hat alles mit dem Vorschlag meines Doktorvaters, Christian Betzler, doch mal die Dünen auf Sylt mit dem Georadar zu untersuchen. Die ersten Geländeversuche, noch mit der unhandlichen SIR-10B, waren überaus erfolgreich und so entstand aus der ersten Idee schnell ein Kooperationsprojekt mit Christian Hass vom Alfred-Wegener Institut für Meeres- und Polarforschung, das auf Sylt eine Forschungsstation betreibt.

Ein so umfangreiches Projekt wie eine Dissertation wäre niemals möglich, ohne die Unterstützung und Hilfe vieler freundlicher und lieber Menschen...

Christian, für diese erste Idee, vor allem aber für die Möglichkeit, aus dieser Idee ein eigenes Projekt zu formen, stets meinen eigenen Weg zu gehen, und dabei doch immer unterstützt und betreut zu werden, dafür danke ich Dir sehr. Auch natürlich für Deine stete Diskussionsbereitschaft und unendliche Stunden des Korrekturlesens.

Dir, Christian, einen ebenso herzlichen Dank für Deine Betreuung, Deine stete Bereitschaft zu ewigen Diskussionen am Telefon, die Unmengen an Korngrößenanalysen, die gemeinsamen Bohrtage, und vor allem für Deine logistische Unterstützung, ohne die das Projekt nie möglich gewesen wäre.

Der Universität Hamburg danke ich für finanzielle Unterstützung durch ein Promotionsstipendium im Rahmen der Graduiertenförderung der Stadt Hamburg. Dieses Stipendium verschaffte mir die Möglichkeit, mich voll und ganz auf die Arbeit an der Dissertation zu konzentrieren. Ebenso danke ich der Deutschen Forschungsgemeinschaft für die finanzielle Unterstützung der Arbeiten im Rahmen des Projektes „GeoSylt“ (Be1272/15-2) und dem AWI für weitere finanzielle Mittel zur Durchführung der Laboruntersuchungen.

Der Familie Diedrichsen als Listlandeigentümer danke ich sehr herzlich für Ihre Erlaubnis im Listland und auf dem Ellenbogen arbeiten zu dürfen.

Ein herzlicher Dank an das Amt für ländliche Räume (ALR) in Husum und an das Landesamt für Umwelt- und Naturschutz (LANU) in Kiel für die Unterstützung unseres Projektes. Herrn Schaller, Herrn Hinrichsen und Herrn Jensen vom ALR danke ich für die Überlassung digitaler Geländedaten die mir die Arbeiten im Gelände sehr erleichtert haben, und den Einblick in das Bohrchiv des ALR, Frau Behm für zahlreiche Genehmigungen, in den Naturschutzgebieten auf Sylt arbeiten zu dürfen.

Für die Möglichkeit, auf dem Gelände des Standortübungsplatzes List Radarmessungen und Bohrungen vorzunehmen danke ich sehr herzlich Herrn Kapitän-Leutnant Lamps, Herrn Mallasch und Herrn Brodersen. Ihnen, Herr Brodersen, möchte ich darüber hinaus sehr herzlich danken: für zwei wunderbare Tage mit Kaffee und der absolut nicht selbstverständlichen Überlassung einiger Schlüssel.

Ali Deghani und Christian Hübscher vom Geophysikalischen Institut der Uni Hamburg danke ich für ihre stete Bereitschaft, mich für meine Geländearbeiten mit zusätzlichen Antennen und GPS-Geräten auszustatten.

Ein besonderer Dank geht an Frau Mumm und Frau Kessenich vom AWI in List für die Möglichkeit, im Gästehaus des AWI zu wohnen und dafür, dass man sich dort immer fast wie zu Hause fühlt.

Für tatkräftige Unterstützung auf dem Gebiet der Logistik und im Institutsalltag danke ich sehr herzlich Wolfgang Weitschat. Für das Anfertigen von Ausrüstungsgegenständen vielen Dank an Rainer Knut und Jan Stoffledt von der Werkstatt. Martina Pabst und Eva Koziarski vielen Dank für stete Hilfe im Dschungel des Bibliothekswesens.

Miriam Römer und David Jaramillo-Vogel, tausend Dank an Euch für die tatkräftige Hilfe im Gelände und hier in Hamburg, für das Abwandern zahlloser Profilkilometer mit dem GPS, die Tage mit dem Bohrgerät und eine unvergessliche Zeit auf Sylt. Für tatkräftige Hilfe im Gelände danke ich auch ganz herzlich Jan Grundmann, Johan Klages, Tobias Bauer, Volker Wagner und Annette Heddaeus.

Merle Benišek, Dir einen ganz lieben Dank: dafür dass Du das tägliche Doktoranden-„Leid“ mit mir geteilt hast und für Deine stete moralische Unterstützung (und natürlich auch für tatkräftige Mithilfe im Gelände).

Ein Dank, der mir besonders wichtig ist, geht an Jörn Fürstenau und Susanne Feindt: Euch beiden, Susi und Jörn, danke ich für wunderbare, unvergessliche Tage auf Sylt, für unschätzbare Hilfe im Gelände, für Eure stete Unterstützung und Diskussionsbereitschaft (und natürlich auch für zwei hervorragende Diplomarbeiten).

Irina Tchaiko, für das Korrekturlesen in letzter Minute einen lieben Dank an Dich. Ebenfalls für Korrekturlesen einen lieben Dank an Stefanie Graumann.

Der persönlichste Dank gilt zunächst meinen Eltern, Dr. Dagmar und Michael Lindhorst, für die stete, bedingungslose Unterstützung meines Studiums und für Euren unerschütterlichen Glauben an mich und die Dinge, die ich tue. Und dann meiner Freundin Tomoko Kogure für ausdauerndes Korrekturlesen bis zum letzten Augenblick - vor allem aber für das Verständnis, das Du meinem ja doch etwas merkwürdigen Alltag, während der ganzen Jahre meines Studiums hindurch, stets entgegengebracht hast - und vor allem für Deinen unauffälligen Rückhalt die ganze Zeit - ohne den wäre diese Arbeit sicher niemals fertig geworden ...